ADVANCES IN VANADIUM AND POLYOXOMETALATE REDOX FLOW BATTERIES

Thesis submitted for the degree of Doctor of Philosophy

by

Matthäa Verena Holland-Cunz

Chemistry - School of Natural and Environmental Sciences, Newcastle University

Newcastle upon Tyne NE1 7RU, United Kingdom

December, 2018

Das schönste Glück des denkenden Menschen ist,

das Erforschliche erforscht zu haben

und das Unerforschliche ruhig zu verehren.

--- Johann Wolfgang von Goethe --

Abstract

Electrochemical energy storage is one of the few options to store the energy from intermittent renewable energy sources like wind and solar. Redox flow batteries are such an energy storage system, which has favourable features over other battery technologies, for example, solid state batteries, due to their inherent safety and the independent scaling of energy and power content. However, because of their low energy density, low power density, and the cost of components such as redox species and membranes, commercialised RFB systems like the all-vanadium chemistry cannot make full use of the inherent advantages over other systems. This thesis shows a comparison of promising cell chemistries with the aim to elucidate which redox system is most favourable in terms of energy density, power density and capital cost. Additionally, the choice of solvent and the selection of inorganic or organic redox couples with the entailing consequences are discussed. The sluggish redox kinetics of the VO^{2+}/VO_2^+ couple limit the power density of the VRFB, which increases the footprint of the power converters and increases capital costs. During recent years, much research has been carried out in the field of heterogeneous catalysis, but this is now approaching its limits. In this work, homogeneous catalysis was conducted to improve the system. The kinetics of the VO^{2+}/VO_2^+ redox reaction have been investigated in 1M sulphuric and 1 M phosphoric acid by cyclic voltammetry, chronoamperometry, electrochemical impedance spectroscopy and flow battery tests. It was found that in 1 M phosphoric acid the electron transfer constant k_0 is up to 67 times higher than in 1 M sulphuric acid and an over-potential dependent difference in electron transfer constant was observed and explained. This study shows that the redox kinetics of the VO^{2+}/VO_2^+ can be considerably accelerated by altering the chemical environment of the vanadium ions, and that this effect can also be transferred into a flow battery. However, the prevailing technology, the all-vanadium system, comprises low energy and low power densities, therefore, the chemistry of polyoxometalates, $[SiW_{12}O_{40}]^{4-}$ and $[PV_{14}O_{42}]^{9-}$, as nano-sized electron shuttles was investigated. It is shown that these POMs exhibit fast redox kinetics (electron transfer constant $k_0 \approx 10^{-2}$ cm s^{-1} for $[SiW_{12}O_{40}]^{4-}$), thereby enabling high power densities; in addition, they feature multi-electron transfer, realizing a high capacity per molecule; they do not cross cation exchange membranes, thus eliminating self-discharge through the separator; and they are chemically and electrochemically stable as shown by *in-*

situ nuclear magnetic resonance spectroscopy. In flow battery studies the theoretical capacity (10.7 Ah L^{-1}) could be achieved under operating conditions with Coulombic efficiency of 94%. Very small losses occurred due to residual oxygen in the system. Options to improve the energy density of the system are discussed.

Acknowledgments

I would like to express my very special gratitude to SIEMENS AG for supporting me and providing the funding for the work. They also gave me the opportunity to present my work at the 22nd Topical Meeting of the International Society of Electrochemistry in Tokyo, which was a great benefit to me and an experience I will always remember.

I would like to thank my supervisor Prof. Ulrich Stimming for accepting me as his PhD student, for giving me the opportunity to attend conferences and to write publications.

I would like to express my gratitude to Libby Gibson for taking time out from her busy schedule to help me, for her encouragement and understanding. I greatly appreciate the support received through Martin Cooke for his support and encouraging words.

I would like to thank Nuria Garcia-Araez and Benjamin Horrocks for taking time to be my examiners.

My research would have been impossible without the support of Jochen Friedl. It was a pleasure to work with him and I want to thank him for his supervision. Without his support this PhD would not have been possible.

My sincere thanks to Prof. William McFarlane and Corrine Wills for their support and constructive feedback concerning NMR spectroscopy.

I would like to thank Felix for his support in the lab, together with his patience and reliability. Many thanks to all members of the group; they all were good colleagues and I enjoyed working with them.

I would like to thank my amazing sister, Katharina, for her encouragement, empathy and for always being there to help and support me. I am grateful to my parents for the support they provided me through my entire life and who have always believed in me.

I am also grateful to my friends who have supported me along the way, especially to Chris and Mark for proofreading my thesis and to my best friend, Alexandra, who is always there for me and I can count on in every situation.

And finally and most importantly, I would like to thank my beloved husband Nils. I look forward to our future together and all the paths ahead and places on earth we will explore together.

Table of Contents

List of figures

List of tables

Abbreviations and symbols

ΔU cell voltage

A surface area

a(Ox) activities of the oxidized species

a(Red) activities of the reduced species

A^{BET} Brunauer–Emmett–Teller surface area

ACA alloxazine 7/8-carboxylic acid

A^{DL} surface area of the electrode determined by EIS

AQDS 9,10-anthraquinone-2,7-disulphonic acid

ARPA-E Advanced Research Projects Agency-Energy

ASR area-specific resistance

A_{wet} wetted surfaced area

BET Brunauer–Emmett–Teller

BMI^+ 1-butyl-3-methylimidazolium

BODIPY boron-dipyrromethene

bp basal plane

Bu_4NClO_4 tetrabutylammonium perchlorate

c concentration

CA chronoamperometry

C_d differential capacitance

C_{DL} double layer capacitance

CE counter electrode

CLFC co-laminar flow cell

CNTs carbon nanotubes

c_{ox} concentration of oxidised species

CPE constant phase element

c_{red} concentration of reduced species

CV cyclic voltammetry

D diffusion coefficient

d distance between charge

DHAQ 2,6-dihydroxyanthraquinone

DOE Department of Energy

$D_{ox/red}$ diffusion coefficient for redox species

E energy density

E_{bat} energy content in a battery

EC ethylene carbonate

EDL electrochemical double layer

EDLSC electrochemical double layer supercapacitors

EES electrochemical energy storage

$E_{F,EL}$ Fermi energy of (metal) electrolyte

$E_{F,Me}$ Fermi energy of (metal) electrode

EIS electrochemical impedance spectroscopy

EMC methyl ethyl carbonate

ep edge plane

E_{SC} energy of supercapacitor

F Faraday constant

f frequency

FC fuel cell

FEC fluoroethylene carbonate

HER hydrogen evolution reaction

HOMO highest occupied molecular orbital

HOR hydrogen oxidation reaction

I current

i imaginary number

I_0 exchange current

I_F Faradaic current

I_{NF} non-Faradaic current

I_{peak} peak current

j current density

j_0 exchange current density

k_0 electron transfer constant

k_B Boltzmann's constant

LIB lithium ion battery

$LiPF_6$ lithium hexafluorophosphate

LUMO lowest occupied molecular orbital

m weight of the electrode

MEA membrane electrode assembly

methyl-viologen N,N'-dimethyl-4,4-bipyridinium dichloride

MSE mercurous sulphate reference electrode

n number of transferred electrons per molecule

$NaHClO_4$ Sodium perchlorate

NASA National Aeronautics and Space Administration

NMR Nuclear magnetic resonance spectroscopy

OCP open circuit potential

OER oxygen evolution reaction

ORR oxygen reduction reaction

PC propylene carbonate

PCET proton coupled electron transfer

POM polyoxometalate

PS electrode potential step

Q charge

Q constant phase element

$Q^{anolyte}$ theoretical capacity of anolyte

$Q^{catholyte}$ theoretical capacity of catholyte

$Q^{discharge}$ discharge capacity

Q^{exp} experimental capacity

Q_{in} amount of charge during charge

Q_{out} amount of charge during discharge

Q^{theo} theoretical capacity

$q^{theo,g}$ theoretical specific capacity per gram

$q^{theo,v}$ theoretical specific capacity per volume

r hydrodynamic radius

R ideal gas constant

R_{CT} charge transfer resistance

R_{diff} diffusion resistance

RE reference electrode

R_{elec} electronic resistance

RFB redox flow battery

R_{mass} mass transport resistance

R_{mem} membrane resistance

R_{Ohm} Ohmic resistance

RT room temperature

RTILs room temperature ionic liquids

R_{total} total resistance

R_u uncompensated resistance

R_uC_{DL} cell time constant

SC supercapacitor

SCE saturated calomel electrode

SHE standard hydrogen electrode

SOC state of charge

SSB solid-state battery

T temperature

TASt (vinylbenzyl)trimethylammonium perchlorate

TBA PF_6 Tetrabutylammonium hexafluorophosphate

TBAOTf tetrabutylammonium trifluoromethanesulfonate

$TEABF_4$ tetraethylammonium tetrafluoroborate

TEGSt (vinyl-benzyl)-triethylene glycol monomethyl ether

TEMPO 2, 2, 6, 6-tetramethylpiperidine-1-oxyl

TEMPTMA N,N,N-2,2,6,6-heptamethylpiperidinyl oxy-4-ammonium chloride

U potential

$U^{0'}$ formal potential

U_0 standard potential

U_{OCV} open circuit potential

U^{ox} potential of the oxidation peak

U^{red} potential of the reduction peak

v scan rate

V volume

$V(acac)_3$ vanadium (III) acetylacetonate

V_{charge} charge voltage

$V_{discharge}$ discharge voltage

VRFB all-vanadium redox flow battery

WE working electrode

Z'' imaginary part of the impedance

Z impedance

z integer

Z' real part of the impedance

Z_w Warburg element

α constant phase element parameter

$\alpha_{a/c}$ anodic/cathodic transfer coefficient

ΔU potential difference

ε_0 permittivity of free space

ε_r dielectric constant

η dynamic viscosity

η over-potential

η_{CE} Coulombic efficiency

η_{EE} energy efficiency

η_{VE} voltage efficiency

Λ electrochemical reversibility parameter

μ_e electrochemical potential

σ Warburg coefficient

χ electronegativity

ω angular frequency

Publications

1. M. V. Holland-Cunz*, F. Cording*, J. Friedl and U. Stimming, *Front. Energy*, 2018, **12**, 198–224. (*equal contribution)

2. M. V. Holland-Cunz, J. Friedl and U. Stimming, *J. Electroanal. Chem.*, 2017, 0–1.

3. J. Friedl*, M. V. Holland-Cunz*, F. Cording, F. L. Pfanschilling, C. Wills, W. McFarlane, B. Schricker, R. Fleck, H. Wolfschmidt and U. Stimming, *Energy Environ. Sci.*, 2018, **11**, 3010–3018. (*equal contribution)

4. J. Friedl, M. V. Holland-Cunz, R. Fleck, B. Schricker, H. Wolfschmidt and U. Stimming, *Upscaling of an asymmetric Polyoxometalate Redox Flow Battery.* Submitted.

CHAPTER 1. INTRODUCTION

Electrochemical energy storage is one of the few options to store the energy from intermittent renewable energy sources like wind and solar. Redox flow batteries (RFBs) are such an energy storage system, which has favourable features over other battery technologies, e.g. solid state batteries, due to their inherent safety and the independent scaling of energy and power content. However, because of their low energy density, low power density, and the cost of components such as redox species and membranes, commercialised RFB systems like the all-vanadium chemistry cannot make full use of the inherent advantages over other systems. In principle, there are three pathways to improve RFBs and to make them viable for large scale application: First, to employ electrolytes with higher energy density. This goal can be achieved by increasing the concentration of redox species, employing redox species that store more than one electron or by increasing the cell voltage. Second, to enhance the power output of the battery cells by using high kinetic redox species, increasing the cell voltage, implementing novel cell designs or membranes with lower resistance. The first two means reduce the electrode surface area needed to supply a certain power output, thereby bringing down costs for expensive components such as membranes. Third, to reduce the costs of single or multiple components such as redox species or membranes. To achieve these objectives it is necessary to develop new battery chemistries and cell configurations.

In the second chapter, a comparison of promising cell chemistries is focused on, be they all-liquid, slurries or hybrids combining liquid, gas and solid phases. The aim is to elucidate which redox-system is most favourable in terms of energy density, power density and capital cost. Besides, the choice of solvent and the selection of inorganic or organic redox couples with the entailing consequences are discussed [1].

One of the remaining challenges and the main drawback is the low power density (< 0.1 W cm^{-2}) of the all-vanadium redox flow battery (VRFB), caused by sluggish kinetics of the redox reactions. To alleviate this drawback, many studies tried to heterogeneously catalyse the redox reactions. However, up to now, there is no consensus in the literature which of the two half-cell reactions, the V^{2+}/V^{3+}- or the VO_2^+/VO^{2+}-reaction, features the higher rate constant [2]. In the literature, rate constants of the two half-cell reactions spread over four orders of magnitude [3]. This uncertainty in the literature is due to two factors:

- An apparent catalytic effect appears when porous electrode materials are investigated with linear or cyclic voltammetry. The porosity reduces the separation between anodic and cathodic peak suggesting enhanced kinetics when indeed only an interplay of enlarged electrochemical surface area and impeded diffusion within the porous electrode is present;
- The Faradaic current I_F is proportional to both wetted surface area A_{wet} and the rate constant k_0: $I_F \propto A_{wet}\, k_0$. As both parameters vary with electrode composition, it is often difficult to distinguish catalytic from surface area effects.

The VO^{2+}/VO_2^+ redox reaction takes place in the catholyte solution of the VRFB. The sluggish redox kinetics of the VO^{2+}/VO_2^+ couple limit the power density of the VRFB, which increases the footprint of the power converters and increases capital costs. Therefore, catalysis of the redox reaction and a deeper understanding of its intricate reaction pathways is desirable. This complex situation was unravelled by using a procedure based on electrochemical impedance spectroscopy. Combining these results and X-ray photoelectron spectroscopy it was shown that surface functional groups such as hydroxyl, carbonyl and carboxyl increase the wetted surface area A_{wet}, increase the rate constant k_0 for the V^{2+}/V^{3+}-redox reaction but decrease k_0 for the VO_2^+/VO^{2+}-redox reaction [3,4]. Many attempts have already been made to improve the system by heterogeneous catalysis but it was shown that in comparison to the V^{2+}/V^{3+} redox reaction, the VO^{2+}/VO_2^+ couple cannot be catalyzed by oxygen functional groups on carbon electrodes [2–5]. The research hypothesis in this work is to increase the power density of the catholyte of the VRFB by homogeneous catalysis. Therefore, investigations by homogeneous catalysis of the VO_2^+/VO^{2+}-redox reaction by replacing the commonly employed sulphate ions by phosphate ions were conducted (see fourth chapter) [6].

Many attempts have been made to improve the application RFB in various directions as presented in chapter two but every system reaches its limits sooner or later. Organic redox couples can be low cost and made from abundant elements, and they offer greater variability than metallic redox couples due to their tuneable structure. A great number of organic redox couples were presented in recent years, with capital cost of metallic RFB chemistries being the main driver for their development. As most studies have been restricted to laboratory cell operation, insights into scale-up with larger cell areas and bigger

electrolyte volumes and long-term cycling are currently not available [7]. The research hypothesis in this thesis is to increase the power and energy density of the electrolyte by applying polyoxometalates as a new class of redox electrolyte which combines the tuneability of organic molecules with the stability of metal ions. POMs offer an enormous variation in topology, size, electronic properties and elemental composition [8] which are perfect properties for application in RFBs. Because the power and energy density of VRFBs are restricted because of the sluggish kinetics and the transfer of a single electron per vanadium ion only, POMs are promising candidates for RFB because of the following properties: (1) POMs are large ions and therefore might not permeate through membrane, which would decrease capacity loss; (2) fast redox kinetics with high electron transfer constants are expected due to the small solvent reorganization energy of POMs, which would lead to high current densities; (3) POMs are reducible and re-oxidizable, which increases the capacity per molecule; (4) POMs are soluble and stable and (5) their composition can be modified, which allows easy adjustment of their redox behaviour. In chapter five two POMs, $[SiW_{12}O_{40}]^{4-}$ and $[PV_{14}O_{42}]^{9-}$ as nano-sized electron shuttles are presented and electrochemically investigated for application as asymmetric electrolytes in RFBs [9]. Options to improve the system are discussed.

An overview about the used electrochemical techniques are given in the third chapter.

Chapter 2. Redox flow batteries - Concepts and chemistries for cost-effective energy storage

2.1 Principles of operation for redox flow batteries

Electrochemical energy storage (EES) devices store energy for later use. To clearly showcase the unique features of RFBs (redox flow batteries), they and their principles will be contrasted with three other devices: electrochemical double layer supercapacitors (EDLSCs), solid-state batteries (SSBs), and fuel cells (FCs). These four archetypes capitalize on different physical and chemical principles, not even all of them employ redox reactions to store energy, and are therefore suitable for diverse EES applications. Examples for these applications are balancing and stabilizing the electricity grid [10], electric vehicles [11,12] and mobile consumer electronics [13,14]. Schematics of these four devices are shown in Figure 1.

EDLSCs (Figure 1 (a)) work on the principle that a potential difference ΔU at an electrode-electrolyte interface, which establishes itself due to the different Fermi energies of (metal) electrode $E_{F,Me}$ and electrolyte $E_{F,EL}$, is balanced by accumulating charges. Cations or anions in the electrolyte form an electrochemical double layer (EDL), conglomerating in order to keep the electrochemical potential μ_e across the interface constant [15,16]. Charges in the electrode, counterbalanced by charges in the electrolyte form a capacitor with a differential capacitance C_d equal to

$$C_{\mathrm{d}} = \frac{\mathrm{d}Q}{\mathrm{d}(\Delta U)} = \frac{\varepsilon_{\mathrm{r}}\varepsilon_0 A}{d} \qquad (1)$$

with accumulated charge Q, distance between charges d, dielectric constant ε_{r}, permittivity of free space ε_0 and electrochemically active surface area A.

High specific capacitances of 10^{-5} F cm^{-2} are reported in the literature for carbon electrodes in aqueous electrolytes [17], because the first layer of charges is very close to the electrode (some Ångströms), and carbon can have a high gravimetric surface area ($\sim$1000 m g^{-1}) [18–20]. The energy E_{SC} of an EDLSC, which is stored entirely in the electrochemical double layer, is given by

$$E_{\mathrm{SC}} = \frac{1}{2} C_{\mathrm{D}} \Delta U^2 \qquad (2)$$

The maximum voltage ΔU is limited by the oxidative and reductive stability of the system comprising electrodes and electrolyte. Organic electrolytes and room temperature ionic liquids (RTILs) can sustain higher voltages than water (approx. 1.23 V) [21,22]. In commercial EDLSCs propylene carbonate or acetonitrile are used as solvent with quaternary ammonium salts as supporting electrolyte, their maximum voltage is typically 2.8 V. Storage of energy in the double layer as only principle limits the energy density of EDLSCs to some Wh kg^{-1}, however, the build-up of the electrochemical double layers is a very fast process. This enables high power density for EDLSCs, in the order of 10 kW kg^{-1} [21].

As shown in Figure 1(b), SSBs also comprise two electrodes and an electrolyte (plus separator), but their energy is not stored in the ECDL, but in the electrodes. The energy content in SSBs is given by the product of the charge that can be transferred, the capacity *Q*, and the potential difference at which electrons flow through the external circuit:

$$E_{\mathrm{Bat}} = Q \Delta U \qquad (3)$$

Atom density in condensed matter is roughly 10^{23} atoms per gram [23], which entails a high capacity *Q* for SSB because the active material is present at a very high concentration. This is a significant difference to RFBs, as we will see later. This can be illustrated for the example of a lithium metal electrode [24,25]. At a mass of roughly 7 u, each lithium atom can be oxidised to give a monovalent cation:

$$\mathrm{Li} \rightleftharpoons \mathrm{Li^+} + \mathrm{e^-} \quad U^0 = -3.04\ \mathrm{V\ vs.\ SHE} \qquad (4)$$

The standard potential U_0 of this reaction is at -3.04 V vs. the Standard Hydrogen Electrode (SHE). Hence, a lithium anode could store a theoretical specific capacity of $q_{\mathrm{Li}}^{\mathrm{theo,g}}$ = 3660 mAh g^{-1} or $q_{\mathrm{Li}}^{\mathrm{theo,v}}$ = 2061 mAh cm^{-3}. Due to the problems associated with lithium metal anodes [26], graphite is commonly employed as host material for the anode in a lithium ion battery (LIB). Because carbon is heavier than lithium, and six carbon atoms are

required to store one lithium cation, the theoretical capacity of carbon is lower at $q_{\mathrm{C}}^{\mathrm{theo,g}}$ = 372 mAh g^{-1}.

$$\mathrm{LiC_6} \rightleftharpoons \mathrm{C_6} + \mathrm{Li^+} + \mathrm{e^-} \quad U^0 = -2.94\ \mathrm{V\ vs.\ SHE} \qquad (5)$$

Cathodes for LIBs are typically lithium metal oxides such as $LiCoO_2$ ($q_{\mathrm{LCO}}^{\mathrm{theo,g}}$ = 170 mAh g^{-1}) or $LiFePO_4$ ($q_{\mathrm{LFP}}^{\mathrm{theo,g}}$ =150 mAh g^{-1}). As intercalation reactions into these cathodes take place at a high potential, e.g. 0.7 V vs. SHE for $LiCoO_2$, the energy density of a LIB can be high (approx. 200 Wh kg^{-1}) [24].

Intercalation reactions are not conversion or alloying reactions, which limits the stress the electrodes experience during charge or discharge. As LIBs rely entirely on the intercalation of lithium ions into interstitial sites of host lattices, high cycle lives are possible.

The combination of high capacity, high voltage and high stability make LIB the premier choice for electric vehicles and consumer electronics. One of the major current challenges is safety, as the employed organic electrolyte has a large combustion enthalpy and can therefore explode violently.

FCs oxidize some fuel (hydrogen, methanol, ethanol, carbon, etc.) at the anode while reducing an oxidant (oxygen) at the cathode, see Figure 1 (c) [27]. The reaction product (H_2O, CO_2, etc.) is exhausted. The energy is stored in the chemical bonds of the fuel, which is pumped from external tanks into the power converter and the electrodes contain catalysts which facilitate the oxidation of fuel or the reduction of oxygen. Advantages of FCs are the high energy density of the fuel (ethanol stores 6.4 kWh L^{-1}) and their versatility in accepting various types of fuel. Also, FCs converting hydrogen are local-zero emission, a big advantage for FC electric vehicles when looking at the detrimental impact of internal combustion engine fumes on human health [12]. One of the main challenges are the sluggish redox reactions at anode and cathode. In acidic media on platinum, which is one of the best catalysts for the hydrogen related reaction, the hydrogen oxidation reaction (HOR) has an exchange current density of 1 mA cm^{-2} [28]. Therefore, large over-potentials are required to obtain a substantial current from anode. For the oxygen reduction reaction (ORR) typically no exchange current density but a kinetic current is given [29,30]. It is agreed however, that the activity for the ORR is orders of magnitude lower than that of the hydrogen evolution

reaction (HER) on platinum. This is thought to be mostly due to the high stability of reaction intermediates such as adsorbed oxygen and adsorbed hydroxyl [31]. To obtain a current density of 200 mA cm^{-2} (at 1 bar O_2 and H_2 pressure) in a low temperature FC, the resting potential of 1.23 V is reduced to 0.78 V [16]. This kinetic limitation renders FCs low power devices.

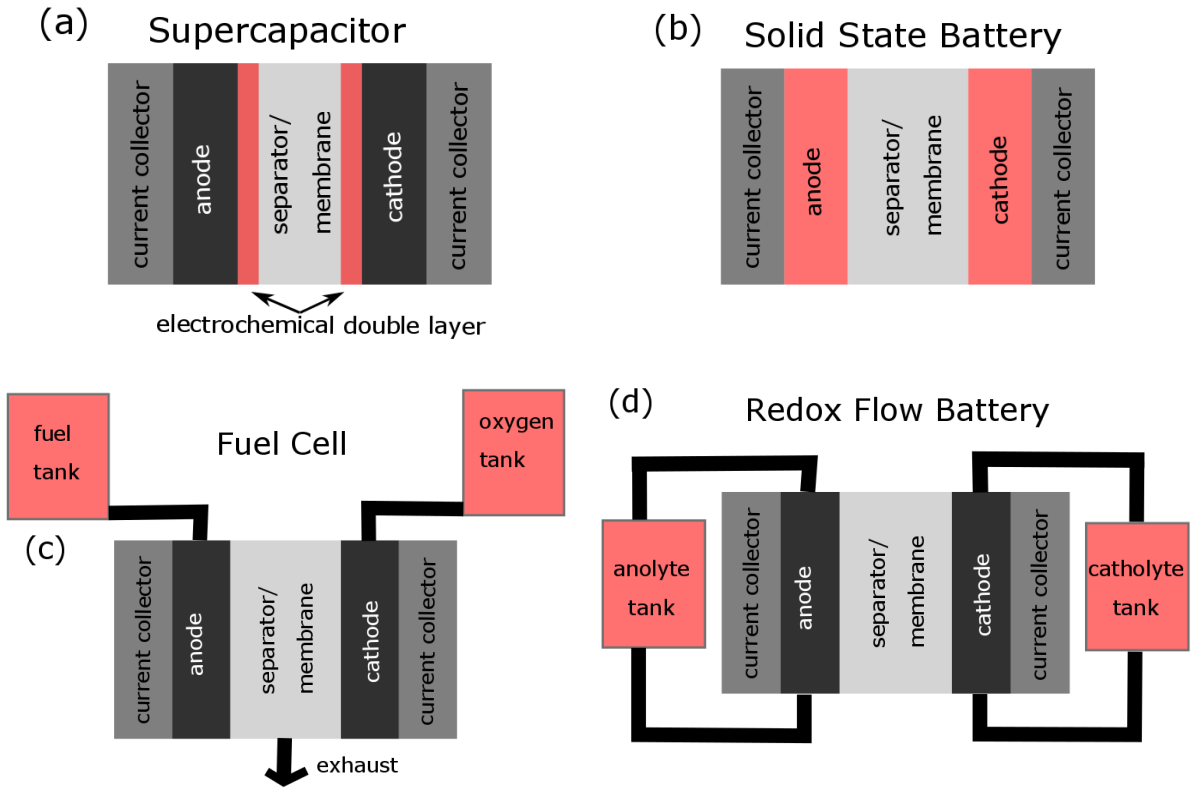

Figure 1 Schematics of different electrochemical energy storage devices. The location where the active material is stored is highlighted in red. (a) Supercapacitor, (b) solid state battery, (c) fuel cell, and (d) redox flow battery.

RFBs share many characteristics with FCs, as can be seen in Figure 1 (c) and (d). Like FCs, RFBs store the active material in tanks which is then pumped to the anode or cathode for charge transfer. One of the differences is that the reaction products are not discarded in a RFB, but kept in their respective streams and pumped back into the anolyte and catholyte tanks. As a RFB is a secondary battery, the discharged species can be re-charged. For that the polarity of the RFB is reversed, the anode is now reducing the anolyte redox species, the cathode is oxidizing the catholyte redox species (against electrochemical conventions). While a FC can use liquid (ethanol, methanol, liquid nitrogen) and gaseous fuels (compressed hydrogen), a RFB will usually operate with dissolved redox molecules, it stores its energy entirely in solution. For the energy density of the RFB equation (3) holds. The charge of the

RFB is determined by how many redox molecules are in solution (governed by concentration *c*), and number of transferred electrons per molecule *n*:

$$Q = n\,c\,F \tag{6}$$

Because typical concentrations are in the order of one mole of redox molecules per litre ($6\ 10^{23}\ L^{-1} \approx 6\ 10^{20}\ cm^{-3}$) and only a single electron is transferred for most RFB chemistries ($n = 1$), the charge contained in the liquid electrolyte is approximately two orders of magnitude lower than for SSBs ($10^{23}\ cm^{-3}$). However, storing energy in a liquid has many conceivable advantages, some of which are shared with FCs: The electrolyte can be easily exchanged by draining and refilling. This could be employed to replace faulty or aged electrolyte or to upgrade the battery with a more advanced electrolyte, or to instantaneously recharge a battery. Also, it enables the scalability of RFBs: The size of the tanks determines the charge *Q* that is stored in the battery and therefore the battery's energy content. The power is determined by the size of the membrane electrode assembly (MEA). This means that RFBs can be easily adapted to specific needs, either by changing the size of the tanks, or by altering the size of electrodes and membranes (or the number of cells). The power density of a RFB, which is normalized to the geometric surface area of the MEA, is limited by four resistances that introduce a potential drop in the cell:

$$R_{\mathrm{total}} = R_{\mathrm{elec}} + R_{\mathrm{mem}} + R_{\mathrm{CT}} + R_{\mathrm{mass}} \tag{7}$$

The total resistance R_{total} is the sum of the resistances caused by the electronic resistance R_{elec} between the various components (e.g. between current collector and electrode), the membrane resistance R_{mem}, the charge transfer resistances on anode and cathode R_{CT} and the mass transport resistance R_{mass}. Because R_{elec}, R_{mem} and R_{mass} are related to the engineering of the MEA [32,33], only R_{CT} is briefly covered here:

$$R_{\mathrm{CT}} = \frac{R\,T}{n\,F\,A\,j_0} = \frac{R\,T}{n^2\,F^2\,A\,k_0\,c} \tag{8}$$

with the ideal gas constant *R*, temperature *T*, Faraday constant *F* and electron transfer constant k_0. Because k_0 can spread over several orders of magnitude, from facile couples

such as ferrocene/ferrocenium with $k_0 \approx 1$ cm s^{-1} [34] to sluggish ones such as the VO^{2+}/VO_2^+ redox reaction with $k_0 \approx 10^{-6}$ cm s^{-1} [3,4], this fundamental parameter is of high importance for the power of a RFB. Maximizing it could lead to high-power RFBs, but current technology, such as the all-vanadium RFB (VRFB) provides only about 70 mW cm^{-2}.

With these principles established, the sequence in energy density and power density shown in the Ragone plot (Figure 2) can be understood: supercapacitors (SCs) store energy only in the electrochemical double layer, by placing charges in a potential field, which gives small energy densities. RFBs store energy in redox couples in liquid form, which entails a lower density of charge carriers than in SSBs. Lastly FCs store energy in the chemical bonds of either the lightest element (H_2), or hydrocarbons (ethanol, methanol, gasoline) which makes them high-energy density devices. However, because the reactions in a FC are sluggish (ORR, HOR), they are low power devices. The intercalation reactions that take place in LIBs are faster than the redox reactions occurring RFBs, making the latter slower than the former. SCs exhibit the highest power density, because the formation of the double layer is a purely physical process and no electron transfer is taking place.

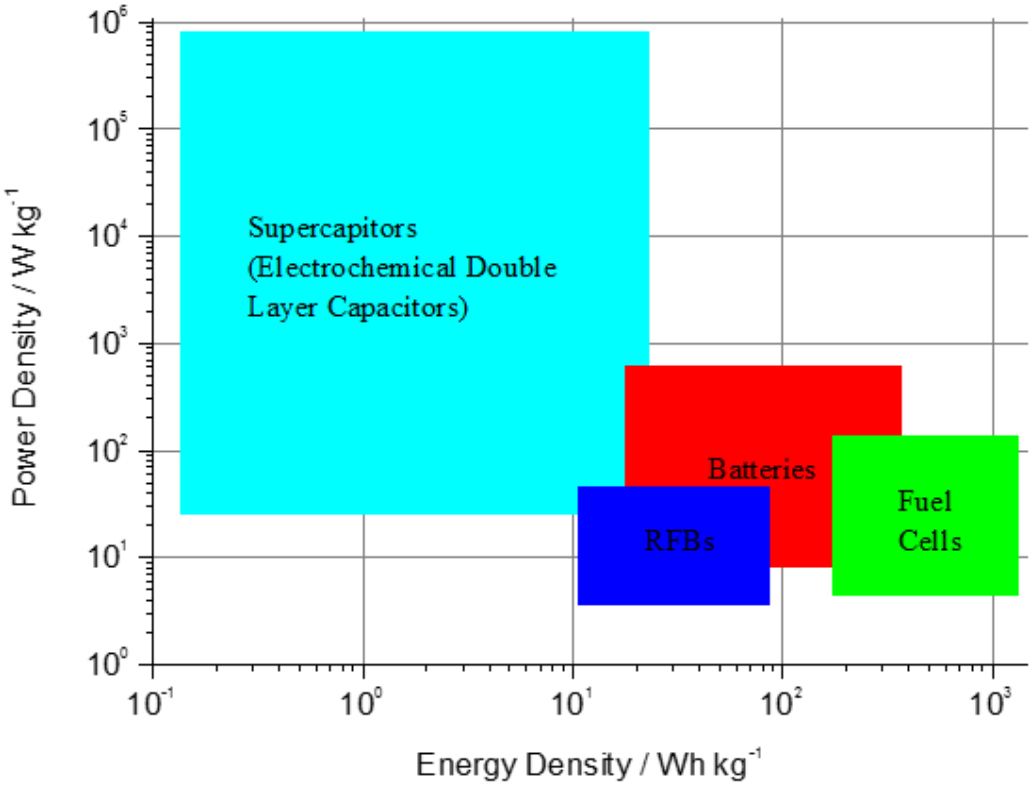

Figure 2 Ragone plot for four electrochemical devices: supercapacitors, batteries, redox flow batteries and fuel cells.

2.2 CRITERIA FOR TECHNOLOGY

A typical RFB cell consists of two electrode compartments divided by a separator. The separator is commonly an ion exchange membrane which prevents the crossover of active species between half-cells but allows the movement of ions between electrode compartments for the balancing of charge. The positive and negative electrolyte are stored in external tanks and are pumped into each half-cell. The electrodes of a RFB are normally inert, serving as the site for the redox reactions of the active species only which remain soluble in the electrolyte. Upon exiting the electrode compartments, the electrolytes are returned to the storage tanks to be re-circulated through the cell. Individual RFB cells can be connected in series to produce cell stacks by the use of conductive bipolar plates which connect one cell to another. The array of cell stacks, stored electrolyte and the balance of plant constitute a complete RFB system. The balance of plant includes all other components necessary for operation of a RFB: pumps, plastic plumbing and tanks, a power conditioning system and systems for battery monitoring and control [35]. Figure 3 illustrates the creation of a RFB system through the building up of individual cells into modular stacks.

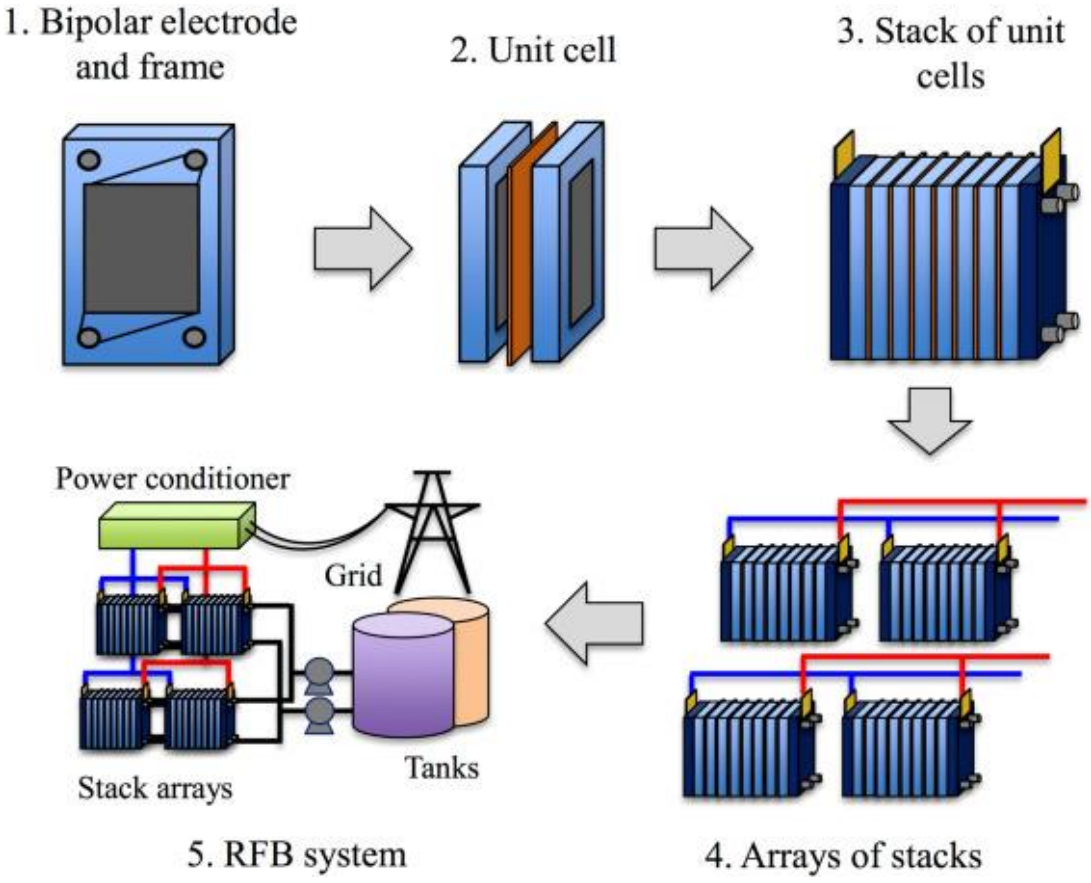

Figure 3 Figure illustrating the creation of a RFB system through the building up of individual cells into modular stacks [36].

RFBs can be subdivided into “true” RFBs and hybrid RFBs (see section 3.3 for further detail). In short, true RFBs utilise inert electrodes and redox species that remain in solution. Examples of classical true RFBs are the iron-chromium [37], bromine-polysulphide [38], and the VRFB [39]. A schematic of the VRFB is shown in Figure 4. The operation of a hybrid RFB involves a phase change during the cell reaction. An example is the zinc-bromine system in which the plating and dissolution of zinc at the anode occurs upon charge and discharge respectively [40].

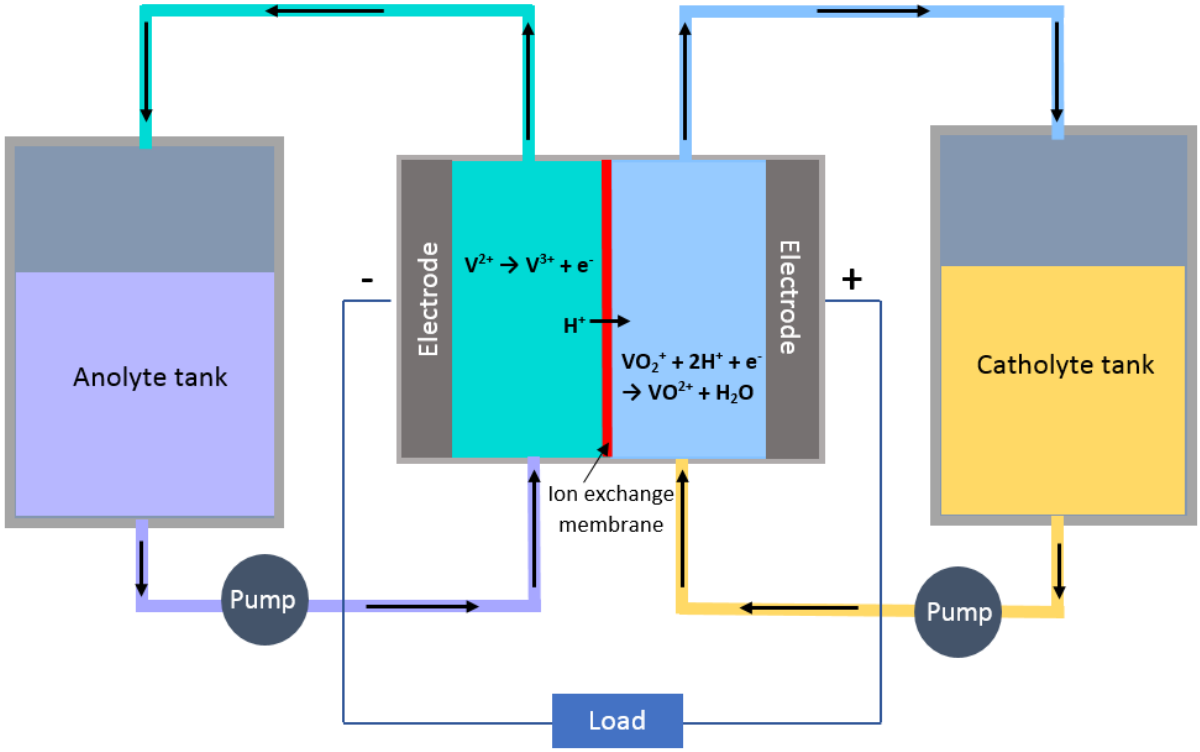

Figure 4 A schematic diagram of the all-vanadium RFB in discharge mode.

The efficiency of a RFB can be characterised by several parameters. Firstly, the Coulombic efficiency η_{CE} which is the ratio of the current transferred upon discharge to the current transferred upon charge.

$$\eta_{CE} = \frac{Q_{out}}{Q_{in}} \cdot 100\% \qquad (9)$$

with Q_{out} the amount of charge during discharge and Q_{in} the amount of charge during charge. Low values indicate a crossover of active species between electrode compartments causing self-discharge, or side reactions that consume charge. Another parameter is the

voltage efficiency η_{VE}, defined as the ratio of the average discharging voltage $V_{discharge}$ to the average charging voltage V_{charge}.

$$\eta_{\mathrm{VE}} = \frac{V_{\mathrm{discharge}}}{V_{\mathrm{charge}}} \cdot 100\%. \quad (10)$$

Activation over-potentials deriving from the reaction kinetics, mass transport over-potentials and Ohmic losses are all sources of a discrepancy between the charging and discharging voltage (see equation (6)). The Coulombic efficiency η_{CE} multiplied by the voltage efficiency η_{VE} yields the energy efficiency η_{EE} of a RFB which indicates how much of the energy that is supplied to the battery during charging can be extracted upon discharge.

$$\eta_{\mathrm{EE}} = \eta_{\mathrm{CE}} \cdot \eta_{\mathrm{VE}} \cdot 100\%. \quad (11)$$

RFBs have several benefits over conventional secondary batteries. For instance, external storage of the electrolyte prevents the self-discharge of the stored solutions. Further, as the electrodes are not subjected to continuous plating or intercalation reactions, electrode deterioration is minimised. When a conventional battery undergoes repeated charge/discharge cycles, the electrode materials expand and contract which results in their degradation over time [41]. Thus, the lifetime can be much improved when there is no phase change at the electrodes during cycling, as in a RFB. The predicted lifetime for a RFB tends to exceed ten years and the VRFB is rated at 10 000 cycles [42].

The life-limiting component of a RFB is typically the cell stack. Wearing of the membranes separating the electrode compartments is a source of performance degradation and for the VRFB in particular, the cell stack is expected to have a lifetime of ten to 15 years for a RFB undergoing 1000 charge/discharge cycles per year [43]. The electrolyte storage tanks, plumbing, structural components, power electronics and controls of a RFB should have longer useful lifetimes [42], but pump replacement may also be required periodically. The crossover of active species between the half-cells due to an inefficiency of the separator is a source of capacity fade and as such, a degree of electrolyte maintenance may be necessary. However, with stack and pump replacement, VRFBs can operate for more than 20 years [43]. Hazards relating to the operation of RFBs include the use of flammable, toxic and/or

corrosive electrolytes. While the flowing electrolytes aid heat dissipation and RFBs such as the VRFB classically used aqueous solutions, flammability should be a consideration if a RFB electrolyte is based on a non-aqueous solvent. Further, acidic supporting electrolytes are typically used which necessitates the use of acid-resistant components and toxicity associated with active species is of concern in the event of leakages.

It is often noted that cost is currently prohibitive for the widespread deployment of RFBs for energy storage. The cost of a RFB system includes numerous components: the cell stacks including separators, electrolyte solutions, storage tanks, power-electronics equipment, the control system, pumps, valves and plumbing as well as the cost of assembly and installation costs [41]. A target capital cost of $100 per kWh has been suggested for large-scale grid storage of energy from renewable sources [44], while a recent cost analysis that considered the VRFB set a base case capital cost of $380 per kWh for a 1 MW/12 MWh system [45]. Both the electrolyte and the cell stack and membrane are implicated as substantial contributors to the capital cost of VRFBs [45,46]. The cost of the electrolyte is dependent on the price of vanadium per kg, while the acidic and oxidising environment of the VRFB requires the use of hardwearing yet costly Nafion ion exchange membranes. Thus, at the electrolyte level, possible improvements to the capital cost of RFBs relative to the VRFB could come from the use of lower-cost active materials and RFB chemistries that allow less expensive porous separators to be used. The different RFB chemistries have been summarised in several recent review papers [7,47–52] and there is a myriad of published reactions for the positive and negative electrode (see Table 1). Aqueous metal-based chemistries are complemented by both reports of non-aqueous RFBs and the emergence of active species based on organic molecules, as alternatives to the traditional and widely tested RFBs are continually devised. The themes of non-aqueous electrolytes versus aqueous electrolytes and non-metallic RFBs versus metal-ion chemistries are discussed herein.

2.3 Various concepts, all-liquids, gas/liquid, semi-solid, slurries, redox mediators

Since their inception in the 1970s at NASA, various combinations of electrolyte/electrode phases have been investigated for RFBs [47,49,50]. Classic examples, like the Fe-Cr system [53] or the VRFB [39,54,55] use two liquid electrolytes, anolyte and catholyte, to store energy. This all-liquid form exhibits all the advantages and disadvantages related to liquid electrolytes stated

in the introduction: lower concentration of charge carriers than in the solid state but a capacity that is only limited by the size of the tank (and the cost of the electrolyte).

The gaseous phase is lighter than liquid electrolytes, and oxygen, if it can be taken from the atmosphere, is almost free of costs. This motivated the design of a V-O_2 RFB or vanadium/air RFB as presented by Hosseiny *et al*. [56]. This embodiment of a gas/liquid RFB hybrid employs the V^{2+}/V^{3+} redox couple as anolyte, and the oxygen evolution reaction (OER) and the ORR as cathode. The battery published suffered from low η_{EE} (27% at 60°C), and the need for catalyst loading on the cathode. As this battery combines the more problematic half-cell of the VRFB [57,58] with the sluggish half-cell of a hydrogen-oxygen FC, the underwhelming performance can be understood.

Combinations of hydrogen electrodes with regular RFB catholytes ($H_2/2H^+$-VO^{2+}/VO_2^+ [59], $H_2/2H^+$-Fe^{2+}/Fe^{3+} [60], $H_2/2H^+$-Ce^{3+}/Ce^{4+} [61]) might have been born from the realisation that the HER contributed a substantial parasitic current in VRFB and Fe-Cr batteries [62,63]. The replacement of one liquid half-cell by $H_2/2H^+$ seems promising from a cost and energy density perspective, but problems such as Pt catalyst leaching into the cell and carbon corrosion by Ce^{3+}/Ce^{4+} have to be addressed [61].

Solid-liquid RFBs comprise one liquid half-cell and one metal electrode which typically undergoes a plating reaction [64]. One example is the zinc-bromine battery, that features a Zn or carbon plastic anode on which Zn is deposited during charge [65]. Metal electrodes allow an increase in energy density as compared to regular flow batteries, however, they also introduce the problems of regular batteries into the RFB: dendrite formation upon plating reactions that can lead to internal short-circuits and high self-discharge rates make it questionable whether liquid-solid hybrids are useful.

Slurries of lithium-metal-oxides are well-studied system due to their importance for LIBs. Under the moniker “semisolid flow batteries”, they were introduced for RFBs utilizing 20 vol% $LiCoO_2$ and 10 vol% $Li_4Ti_5O_{12}$ [66]. This concept allows for very high concentrations of redox species (estimated ranges from 20 to 80 mol L^{-1}) [67]. Conductive slurries are used as electrolyte, in which carbon forms a conductive network. The limited conductivity of these slurries (0.1 mS cm^{-1}) is one of the contemporary challenges of semisolid flow batteries [66,67].

A concept that does not rely on dissolved redox species, but instead on a solid active material that is stored in tanks: mediated flow batteries. In these the charge is transferred to the active material via redox-mediators such as ferrocene [68] or cobaltocene [69]. This type of flow battery utilises similar active materials as semisolid flow batteries but avoids the high viscosity and poor conductivity of slurries. To avoid losses the potentials of the redox mediators must closely match the (de-)intercalation potentials of the active material.

Another concept is the addition of a solid energy booster to the tank of a RFB [70]. This approach proposes that the redox transitions of the polymer polyaniline are accessed by a redox mediator, storing charge in the emeraldine-pernigraniline and leucoemeraldine-emeraldine redox transitions of the polymer. As redox-mediators, $Fe^{2+}/Fe^{3+}$and V^{3+}/VO^{2+} were employed at a concentration of 1 M. When polyaniline was combined with conductive carbon and abovementioned electrolytes the volumetric energy density was increased by a factor of three, compared to the base case with only iron and vanadium ions [70]. Current challenges are a “passivation” of polyaniline in certain redox state and sluggish kinetics of the V^{3+}/VO^{2+} couple.

The advantages and drawbacks of various RFB concepts are listed in Table 1.

Table 1 Summary of advantages and drawbacks of various RFB concepts.

Type	Advantages	Challenges	Ref.
Solid - liquid (e.g. Zn/Br)	• High energy density due to solid state.	• Internal short-circuits; • High self-discharge.	[65]
Slurries (e.g. $LiCoO_2$ / $Li_4Ti_5O_{12}$	• High energy density due to high concentration of redox species.	• Limited conductivity of the slurries; • High viscosities; • Potentially sluggish kinetics of non-dissolved species.	[66]
Mediated FB (Ferrocene as shuttle and $LiFePO_4$ as storage material)	• Low viscosity of shuttles • Good conductivity	• Limited variety of suitable redox mediators; • Complicated reaction mechanism;	[68,69]
Liquid-liquid (e.g. Fe/Cr)	• Capacity that is only limited by the size of the tank.	• Lower concentration of charge carriers than in the solid state.	[53]
Liquid-gaseous (e.g. V/O_2 or H_2/V)	• Low costs for gaseous species; • High concentrations of gaseous species can be reached, therefore high energy density,	• Low energy efficiency; • Self-discharge; • Oxygen gas permeation through membrane need for catalyst loading on electrode; • Pt leaching into the cell.	[56,59]

2.4 SOLVENT: AQUEOUS - NON-AQUEOUS

In most of the current RFB-systems, acidic, aqueous electrolytes are used. One disadvantage of electrochemical application in aqueous solutions is the electrolysis of water. The corresponding half-reactions can be described for acidic and basic solutions:

Cathodic reaction:

$$2\,H_3O^+ + 2\,e^- \rightarrow\ H_2\ +\ 2\,H_2O, \qquad (12)$$

$$2\,H_2O + 2\,e^- \rightarrow\ H_2\ +\ OH^-. \qquad (13)$$

Anodic reaction:

$$6\,H_2O \rightarrow\ O_2 + 4\,H_3O^+ + 4\,e^-, \qquad (14)$$

$$4\,OH^- \rightarrow\ O_2 + 2\,H_2O\ + 4\,e^-. \qquad (15)$$

The potential at which those reactions occur depends on the electrode material used. The thermodynamic potential window in which no reactions take place is 1.23 V. Out of this range, water electrolysis is promoted which leads to parasitic side reactions and therefore to efficiency loss and capacity imbalance in a full RFB. This limits the selection of electrochemical active species for an aqueous RFB. Furthermore, the application of aqueous electrolytes is restricted by the temperature range of 0 to 100°C. Mostly, sulphuric acid is added as supporting electrolyte to enhance the conductivity of the electrolyte without the addition of additional salts as supporting electrolyte.

Often, to ensure higher conductivity, hydrochloric acid is added to the aqueous electrolyte [71]. However, the dissociated chloride ions can promote corrosion processes, thus having a negative effect on the lifetime of the battery attachments. Chloride ions are not oxidizing agents themselves but they can influence the corrosive conditions and are able to catalyse the process depending on the used materials which results in higher maintenance costs [72].

The use of non-aqueous electrolytes is a possibility to enlarge the potential window and the temperature range. An example for an organic solvent used in a RFB is acetonitrile [73–76]. To obtain a reasonable conductivity, a supporting electrolyte like tetrabutylammonium hexafluorophosphate (TBA PF_6) or sodium perchlorate ($NaClO_4$) has to be added to the electrolyte, which can limit the potential window because of decomposition reactions [77]. Furthermore, these supporting electrolytes increase capital costs. The potential windows of acetonitrile with 0.1 M additive on a platinum electrode are from +3.0 V to -2.6 V vs. saturated calomel electrode (SCE) in the case of TBA PF_6 and from +1.8 V to -1.6 V vs. SCE in the case of $NaClO_4$ [78]. This suggests that the potential window can be enlarged in non-aqueous media but is limited by the decomposition of the additive. The useable temperature range of acetonitrile (anhydrous) is between -43.8 and 81.7°C which is beneficial for low

temperature applications. In general, solvents with nitrile groups have a good stability towards oxidizing and reducing conditions in electrochemical cells [78].

Another example for non-aqueous electrolytes are organic carbonates like propylene carbonate (PC), ethylene carbonate (EC) and methyl ethyl carbonate (EMC), which are well studied due to their application in LIBs [77,79]. Those solvents have the capability to dissolve salts such as tetrabutylammonium trifluoromethanesulfonate (TBAOTf) and lithium hexafluorophosphate ($LiPF_6$) to function as supporting charge carrier in the electrolyte.

The use of organic solvents could potentially require complex maintenance operations, especially if the organic solvent is hygroscopic and prone to water intake from the atmosphere which would lead to a decreased potential window. Acetonitrile, for example, is strongly hygroscopic and will readily absorb water from air if not stored under inert conditions. For technical application this would mean that the battery would have to run under nitrogen or argon gassing which would result in higher maintenance costs compared to the aqueous system. Also, non-aqueous solvents like acetonitrile corrode rubber and polymer materials which could damage the tubes the electrolyte are pumped through and the innards of the cell which would reduce the lifetime of the battery [72].

While intensifying maintenance requirements, electrolytes such as PC, EC, EMC, and others also carry a significant safety risk. This is aggravated in LIBs because they contain, besides the flammable electrolyte, oxidizing material in the form of the lithium-metal oxides that typically make up the cathode [80]. Therefore, two of the three elements of the combustion triangle (fuel and oxidant) are present in LIBs, and the addition of a heat source can lead to catastrophic failure. In a large scale RFB application of organic electrolytes, the fuel would be present in a much higher quantity than in a LIB, and surrounding oxygen in the atmosphere could function as oxidizer. Organic solvents are, in most cases, ecologically questionable and their application should be reduced as much as possible because, in spite of safety measures, solvents are released into the environment and have a polluting impact. For the synthesis of PCs, dichloromethane is used for which carcinogenic effect is suspected and it harms aquatic organisms (H-351, H-373) [81]. Acetonitrile as a solvent should be considered critically as well. Acetonitrile is absorbed by the digestive system, the skin, and the lungs and releases cyanide in the human body. Hence, poisoning symptoms of cyanide exposure

occur [82]. Due to these properties the toxicity of the used solvent must be taken into account when developing a battery [83].

The selection of a suitable solvent for conducting experiments requires careful consideration as the solvent can have a significant influence on the electrochemical properties of the redox couples. The standard potential of a reaction like

$$\mathrm{M}^{\mathrm{n}+} + n\,\mathrm{e}^{-} \rightleftharpoons \mathrm{M} \qquad (16)$$

depends on the solvent or on the solvation energy of the metal ion. For instance, the standard potential is shifted to more negative values in solvents in which the metal ion is solvated more strongly [72]. In some cases solvents have the capability to change the whole reaction mechanism, which affects the electrochemistry of a redox system. For example, a one-step reaction in water could be a two-step reaction in an organic solvent. Copper in the oxidation state I+ is unstable in water but is stabilized in acetonitrile, which means the reduction of Cu(II) to Cu(0) in water occurs at another potential than in acetonitrile. Besides, the permittivity and Lewis acidity of a solvent affects the standard potential of metal ions significantly. The electron transfer constant k_0, an important factor in electrochemistry, is affected by the solvent, too, due to its influence on the reorganization energy.

Another type of electrolyte that receives more and more attention to enhance the energy density of RFBs are room temperature ionic liquids [84]. They are solvents that consist entirely of ions, are non-volatile, non-flammable, chemically stable, and highly conductive [85]. Furthermore, if free of water, they make a huge potential window and temperature range accessible [86,87]. RTILs offer environmentally friendly properties and can be used as green solvents in electrochemical application, especially RFBs. There are two main types of RTIL: one is a mixture of $AlCl_3$ and quaternary ammonium chloride (R^+Cl^-) and the other type are salts of cations like 1-butyl-3-methylimidazolium (BMI^+), 1-ethyl-3-methylimidazolium, and 1-butyl-pyridinium and anions like BF_4^-,PF_6^-,CF_3COO^-,$CF_3SO_3^-$ and $(CF_3SO_2)_2N^-$. The potential window depends on the acidity and basicity of the solution, respectively. In the case of 1-butyl-3-methylimidazolium - PF_6^- , the potential window is 7.1 V [72]. Some properties can be adjusted by the anion and in which way the ligand coordinates to the metal centre. The

group of Anderson *et al*. investigated the aforementioned properties in copper ionic liquids [88]. $Cu\{NH_2CH_2CH_2OH\}_6[BF_4]_2$ showed the best results regarding viscosity, conductivity and electrochemical reversibility, and was liquid at 25°C, whereas the copper complex with one anion exchanged with triflate was solid at room temperature (RT). In addition the conductivity changes with the anion. With one 2-ethylhexanoate anion instead of tetrafluoroborate, the conductivity decreases from 6.8 to 0.586 mS cm^{-1} [89].

Membranes in RFBs are used to separate the liquid electrolyte compartments and are permeable ions to enable charge balancing [90,91]. The most important properties of those membranes are high ionic conductivity and low permeability towards the electrochemical active species to inhibit crossover of the catholyte into the anolyte and vice versa. In aqueous systems, a cation exchange membrane like Nafion is usually used [92]. However, anion-exchange membranes [93–95] or porous membranes [96] have also been used. In non-aqueous media polyethylene-based porous separators [79], anion-exchange membranes [74] and cellulose-based dialysis membranes [97] are reported.

The advantages and challenges of various types of electrolytes used in RFBs are tabulated in Table 2.

Table 2 Summary of advantages and challenges of various types of electrolytes used in RFBs.

Electrolyte	Advantages	Challenges	Ref.
Aqueous	• Environmentally friendly; • Inexpensive; • High conductivities; • Often high solubility for redox species.	• Small potential window • Restriction by temperature range • Corrosion processes by chloride ions;	[78]
Non-Aqueous	• Larger potential window than aqueous electrolytes; • Larger temperature range than aqueous electrolytes;	• Potential window limited by decomposition of additives; • Safety risks; • Low conductivity; • Environmental hazards; • Higher (maintenance) costs;	[77,81]
Room temperature ionic liquids	• Non-volatile; • Non-flammable; • Highly conductive; • Chemically stable; • Wide potential window; • Environmentally friendly?	• High viscosity; • High (maintenance) costs; • Low conductivity.	[85–87]

2.5 Redox centre: metallic - non-metallic

There are two types of metal-based batteries which can be distinguished between Me/Me^{z+} and $Me^{z+}/Me^{(z+1)+}$ systems (with integer *z*). An example for Me/Me^{z+} system is the Zn/Br_2 battery in which metallic Zn is deposited on the cathode during charging and Br^- ions are oxidised to elementary bromine simultaneously [40,65]. In this system the metal is an electrochemically active species and forms part of the electrode as well [98]. A problem that often occurs with this kind of battery is the formation of dendrites, which can lead to a short circuit when these protrusions pierce the separator [99,100].

An example for a $Me^{z+}/Me^{(z+1)+}$ system is the VRFB [101]. In this battery, the redox couples V^{3+}/V^{2+} and VO^{2+}/VO_2^+ are used. During charging V^{3+} is reduced to V^{2+} and VO^{2+} is oxidised to

VO_2^+ simultaneously. During the entire process, the ions remain dissolved and are not part of the electrode. The disadvantage of this type of system is the crossover of the ions across the membrane into the other half-cell which decreases the efficiency. In the case of different elements, the capacity is significantly reduced by the crossover and the associated irreversible contamination. Another point which limits the application is the limited solubility of the metal salts used. In the case of the VRFB, the maximum concentration of the VRFB electrolyte is 1.7 to 2 M vanadium if only sulphuric acid is used as supporting electrolyte [102]. It should also be mentioned that at higher concentrations, the V^{3+} and V^{2+} ions precipitate in the negative electrolyte if the temperature is lower than 10°C. While the solubility of V^{2+}, $V^{3+}$and VO^{2+} increases with increasing temperature, thermal precipitation of the VO_2^+ species into V_2O_5 occurs when the positive electrolyte is over 40°C [103]. The electrolyte of non-aqueous system contains a concentration of electrochemically active species from 0.01 M [74] to 2 M [79].

The locus of the redox reaction is the electrode surface and this is why the selection of the right electrode plays an important role. The electrode requirements for all systems are, in general, high conductivity, good resistance towards the chemical environment, mechanical stability towards compression, and inexpensive costs. In $Me^{z+}/Me^{(z+1)+}$ systems, commonly carbon-felt materials are used because they do not undergo any redox reaction within the stability window of water [3]. The surface of the electrode should be active towards the desired redox reactions and simultaneously inhibit unwanted side reaction such as the HER.

2.6 Review of battery chemistries

The development of novel chemistries for RFBs is a research area that attracts a tremendous amount of attention at the moment. Therefore, it is impossible to present a holistic compendium of all the (half-cell) chemistries investigated. The present chapter should be seen as complimentary to recently published reviews on the topic of chemistries for RFBs [7,47–52]. In this selection, chemistries that target the capital costs of RFBs are focused on, which is currently the main inhibitor for their wide-spread application. Avenues to achieve these cost-savings are: high capacity chemistries that allow for a reduction in footprint of the battery, high power chemistries that allow for a reduction in size of the cells and, therefore, reduce the footprint and costly materials such as membranes and low-cost molecules.

2.6.1 High energy density all-vanadium RFBs

2.6.1.1 VRFBs with increased concentration

As described, for VRFBs, V^{2+} and V^{3+} species in the negative half-cell precipitate below 10°C while VO_2^+ precipitates as V_2O_5 above 40°C in the positive half-cell which allows a maximum vanadium concentration of 2 M in the sulphuric acid electrolyte and limits the energy density to 25 Wh kg^{-1} [103]. Reformulation of the electrolyte is a possible way to access higher vanadium concentrations and increase energy density. Indeed, Li *et al*. demonstrated use of a mixed sulphate and chloride electrolyte that allowed a 2.5 M concentration of vanadium to be achieved [104]. This represented about a 70% increase in energy density relative to current sulphate-only systems. It was found that vanadium in all four oxidation states was stable in a solution of 2.5 M SO_4^{2-} and 6 M Cl^- from -5 to 40°C, and a subsequent study demonstrated the stability of VO_2^+ in solution at 50°C. The mixed electrolyte could, therefore, provide an extended operational temperature range of -5 to 50°C, compared to the 10 to 40°C temperature window that is allowable for VRFBs that use a supporting electrolyte of sulphuric acid only. The enhanced stability of V(V) is attributed to the formation of soluble, neutral vanadium-containing complexes of formula $VO_2Cl(H_2O)_2$ as the temperature approaches 20°C [104]. This was evidenced by use of the Amsterdam Density Functional program and by ^{51}V and ^{35}Cl nuclear magnetic resonance spectroscopy (NMR) analysis. Quantum calculations also indicates that in sulphate solution, V(V) exists as $[VO_2(H_2O)_3]^+$ which is converted to insoluble V_2O_5-$3H_2O$ at elevated temperatures. The solubility and stability of V^{3+} and VO^{2+} is also thought to be increased by the lower sulphate concentration of the mixed electrolyte relative to standard sulphate concentrations for VRFBs. When a 2.5 M vanadium solution in the mixed sulphate-chloride electrolyte was tested in a RFB cell, a stable performance with 87% energy efficiency over 20 days was achieved. Energy densities of >36 Wh L^{-1} were demonstrated for 2.5 M vanadium solutions in mixed electrolyte compared to around 22 Wh L^{-1} for 1.6 M vanadium solutions in 4.5 M sulphate electrolyte [103,104]. The formation of Cl_2 gas during cycling is a concern but it has been reported that no significant gas evolution is observed. It is possible to show that k_0 of the VO^{2+}/VO_2^+ reaction in 1 M H_3PO_4 is up to 67 higher than in 1 M H_2SO_4, which is attributed to a different chemical coordination in the electrolytes [6].

Electrolyte additives are also a possible measure that can be implemented to increase vanadium concentration and achieve higher energy densities for the VRFB. For instance, Roe

et al. recently investigated various stabilising additives for the purpose of preventing the thermal precipitation of VO_2^+ species [104,105] (Figure 5). Several inorganic additives were studied as it was noted that finding effective organic additives that had long-term stability was a challenge due to the high oxidising power of VO_2^+. Sodium pentapoly phosphate, K_3PO_4, H_3PO_4 and $(NH_4)_2SO_4$ were thus screened as stabilisers for 3 M supersaturated VO_2^+ solutions. H_3PO_4 (1wt%) was found to be most effective at maintaining VO_2^+ concentration at 30°C while a 1wt% H_3PO_4 + 2wt% ammonium sulphate formulation performed best at 50°C and was investigated further in cell cycling tests. Such stabilising behaviour could be attributed to the formation of V(V)-phosphate complexes and the increase in H^+ concentration due to phosphoric acid addition causing thermal precipitation of V(V) as V_2O_5 to become disfavoured. A 3 M VO_2^+ solution with 5 M total sulphate concentration and containing 1wt% H_3PO_4 + 2wt% ammonium sulphate demonstrated stable efficiencies over 90 charge/discharge cycles with a slight decrease in cell capacity observed [105]. No precipitation was evident during the experiments. A viable 3 M vanadium electrolyte could allow a 60% – 90% increase in energy density relative to the practical concentrations of 1.6 M – 1.8 M that are currently used in VRFBs.

A number of organic additives were proposed [106] and researchers found that amino acids [107], coulter dispersant [108], polyacrylic acid and its mixture with CH_3SO_3H [109] as well as fructose, mannitol, glucose, and D-sorbitol [110] and other [111] organic compounds could improve the temperature stability of the catholyte in the VRFB. However, Nguyen *et al*. studied the effect of additives glucose and ascorbic acid, and found that they only led to an apparently enhanced stability [111]. They claimed that the catholyte with organic molecules was more stable because these molecules were oxidised by the VO^{2+} ions, thereby reducing the state of charge (SOC) of the VRFB. As precipitation occurred at high SOCs, when the catholyte was mostly present as VO_2^+ and these additives effectively diminished the concentration of VO_2^+, the time until precipitation occurred was prolonged.

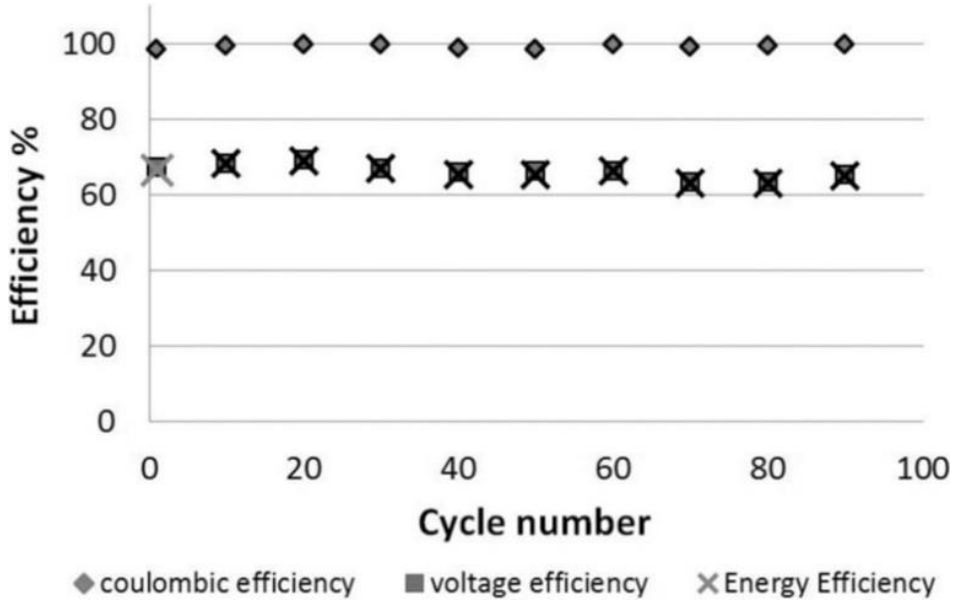

(**a**)

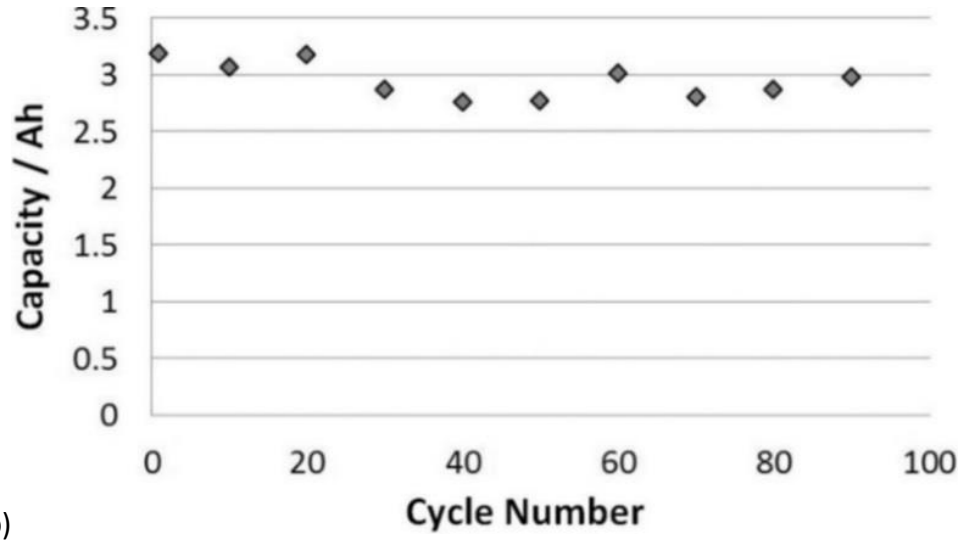

(**b**)

Figure 5 Performance data of a VRFB employing 3 M vanadium in 5 M total sulphate electrolyte with 1wt% H_3PO_4 + 2wt% ammonium sulphate additives. (a) Coulombic, voltage and energy efficiencies vs. cycle number; (b) capacity vs. cycle number [105].

2.6.1.2 VRFBs WITH INCREASED CELL VOLTAGE

The energy density of a RFB is proportional to the cell voltage, but for aqueous electrolytes the voltage is limited by the electrochemical window of water. In light of this, Liu *et al*. investigated a non-aqueous electrolyte for application in RFBs [73]. Vanadium (III) acetylacetonate ($V(acac)_3$) was dissolved in acetonitrile with tetraethylammonium tetrafluoroborate ($TEABF_4$) as the supporting electrolyte. The stability window for the system

was approximately 4 V (-2.5 V to 1.5 V vs. Ag/Ag^+) and within this voltage range, the analysis of $V(acac)_3$ by cyclic voltammetry (CV) showed peaks corresponding to V^{2+}/V^{3+} and V^{3+}/VO^{2+} redox couples. From the potentials of these reactions, a useful cell potential of 2.2 V for a RFB was calculated. The charge-discharge performance for a non-aqueous V^{2+}/V^{3+}-V^{3+}/VO^{2+} system was tested in an H-type glass cell. The separation between charging voltage and discharging voltage was around 3 V and Coulombic efficiencies η_{CE} near 50% were obtained for a 0.01 M $V(acac)_3$ solution. Nonetheless, the 4 V stability window of acetonitrile indicates the higher electrochemical window offered by non-aqueous solvents and it is noteworthy that both the V^{2+}/V^{3+} and V^{3+}/VO^{2+} redox couples revert to the same V^{3+} species upon discharge. This system saw further evaluation focusing on kinetics [112] (Figure 6), degradation mechanisms [113] and the influence of different solvents and supporting electrolytes [114,115].

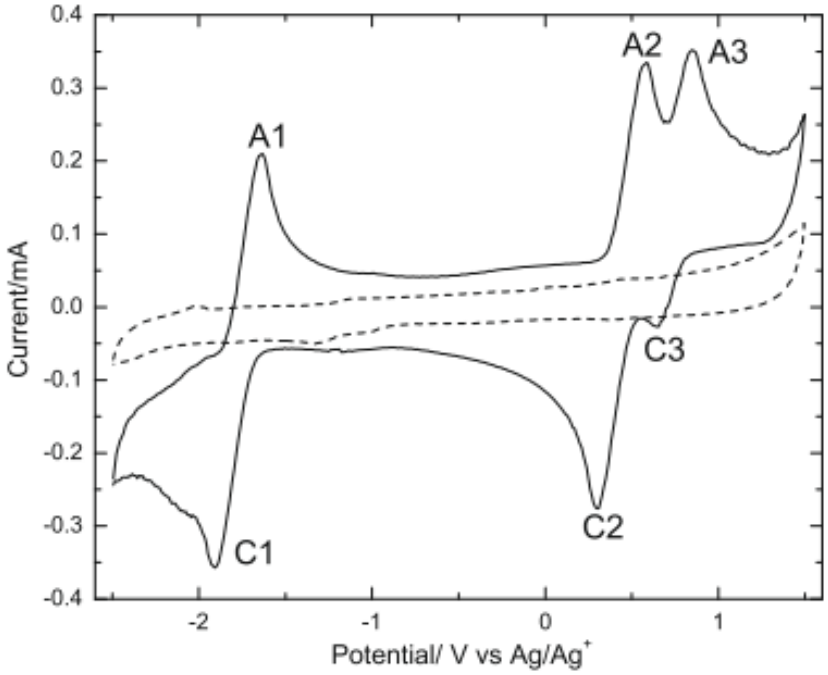

Figure 6 Cyclic voltammograms recorded at 0.5 V s^{-1} at a glassy carbon electrode in 0.5 M $TEABF_4$ in CH_3CN (dashed line) and 0.01 M $V(acac)_3$ and 0.5 M $TEABF_4$ in CH_3CN (solid line) (measurements were taken at room temperature) [112].

$$\text{A1 and C1: } V(acac)_3 + e^- \rightleftharpoons [V(acac)_3]^-, \quad (17)$$

$$\text{A2 and C2: } V(acac)_3 \rightleftharpoons [V(acac)_3]^+ + e^-, \quad (18)$$

RFBs that discharge to the same active species in both half-cells mitigate the issue of cross-contamination of half-cells resulting from active species crossover. In a similar way, a non-aqueous chromium acetylacetonate RFB was also investigated [116]. A cell potential of 3.4 V was indicated for a one-electron disproportionation reaction of $Cr(acac)_3$ in which $Cr^{III}(acac)_3$ was oxidised to $[Cr^{IV}(acac)_3]^+$ and reduced to $[Cr^{II}(acac)_3]^-$. The charge-discharge performance in an H-type cell of 0.05 M $Cr(acac)_3$ in acetonitrile with a 0.5 M $TEABF_4$ supporting electrolyte was evaluated. The cycling between 0 to 50% of the theoretical SOC yielded η_{CE} of 53 - 58% and η_{EE} of 21 - 22%. A non-aqueous RFB utilising manganese acetylacetonate was also later investigated [74]. A 1.1 V cell potential was indicated for a RFB based on $Mn^{III}(acac)_3/[Mn^{II}(acac)_3]^-$ and $Mn^{III}(acac)_3/[Mn^{IV}(acac)_3]^+$ redox couples. A cell containing 0.05 M $Mn(acac)_3$ in 0.5 M $TEABF_4$/acetonitrile supporting electrolyte showed a discharge plateau at around 0.3 V over ten cycles. An increase in η_{CE} from ~74% to ~97% was attributed to an unknown side reaction, while the η_{EE} remained at around 21% during cycling.

2.6.1.3 VRFBs WITH NOVEL REACTOR DESIGN

A co-laminar flow cell (CLFC) is a microfluidic device with a "membrane-less" design: achieving laminar flow in adjacent liquid streams allows two solutions to flow side by side with mixing occurring only by diffusion of active species between streams [117,118]. The prevention of turbulent mixing thus allows the two electrolytes to flow side by side in a CLFC, with ionic conduction still permitted but no requirement for a membrane, thereby omitting a significant cost contribution [45] and source of overvoltage through membrane resistance. A high power density RFB that utilises vanadium chemistry was presented in the form of a CLFC by Goulet *et al*. [118]. The high power density was mainly attributed to a novel *in operando* deposition method of carbon nanotubes (CNTs) that was applied to the flow-through porous carbon paper electrodes of the CLFC. This involved suspending the CNTs directly in the electrolyte that was to be flowed through the cell. The deposition of CNTs enhanced the electrochemical active surface area by adhering to the carbon paper electrodes and forming a conducting nano-porous layer. Further, an improvement in mass transport was indicated which was attributed to both the deposition of material directly in the reactant flow path and a reduced average pore size of the electrodes. The power density

of the flow cell subjected to CNT deposition was 2 W cm^{-2} (a typical power density for a RFB cell is 0.1 W cm^{-2} [41,118]). CLFCs are classed as microfluidic electrochemical cells and as such, it is noted that the cell is limited in scale. However, the addition of CNTs directly to the redox electrolyte presents as a simple and inexpensive method that lead to an enhancement of both the surface area and mass transport properties of the electrodes. A real-time image of the CLFC discharging with colour changes indicating the different vanadium ion oxidation states and a schematic of the construction of the cell are shown in Figure 7.

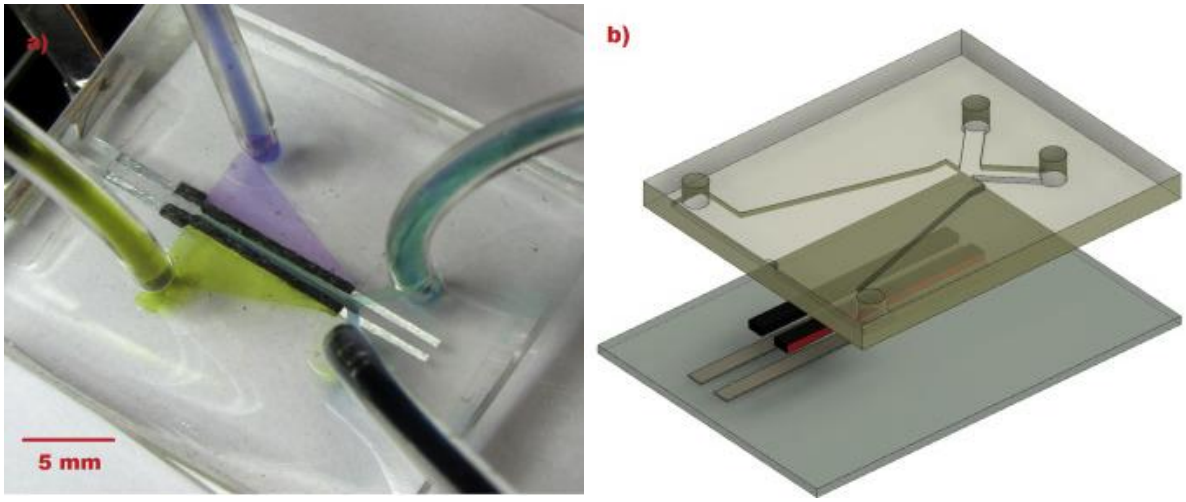

Figure 7 A co-laminar flow cell by Goulet *et al*. [118] (a) A real-time image of the CLFC discharging with colour changes indicating the different vanadium ion oxidation states; (b) a schematic of the construction of the cell (the flow-through cross-sectional area of the electrode is highlighted in red.

A tubular vanadium redox flow cell was presented by Ressel *et al*. [119]. This approach was chosen to enable reduced manufacturing costs and less shunt currents in a cell stack. The tubular cell was constructed from extruded current collectors and a welded tubular membrane, it was able to produce 70 mA cm^{-2} at a η_{EE} of 55%.

2.6.1.4 VANADIUM CHLORIDE/POLYHALIDE RFB

In order to avoid the precipitation of V_2O_5 at high temperatures, a RFB which used a polyhalide solution in the catholyte and a vanadium(II)/vanadium(III) chloride redox couple in the anolyte was developed [120]. The occurring reactions are

$$\mathrm{V^{2+}} \rightleftharpoons \mathrm{V^{3+}} + \mathrm{e^-} \qquad U^0 = -0.25\ \mathrm{V\ vs.\ SHE}, \qquad (19)$$

$$\mathrm{ClBr_2^-} + \mathrm{e^-} \rightleftharpoons 2\mathrm{Br^-} + \mathrm{Cl^-} \qquad U^0 = +1.04\ \mathrm{V\ vs.\ SHE}. \qquad (20)$$

During the charging process, the bromide ions in the positive half-cell are oxidised to the polyhalide ion Br_2Cl^-; the reaction between Br_2 and Cl^- leads to the Br_2Cl^- ion, while Cl_2 dissolved in a Br^- solution generates the Cl_2Br^- ion that has high oxidation potential. The application of those compounds in a vanadium chloride/polyhalide redox flow cell would lead to a cell potential of around 1.3 V. A CV was conducted on a graphite electrode and the authors claimed that the redox reaction of VCl_3/VCl_2 was reversible [120]. A correction for the high surface area and porosity of the electrode, which could elucidate k_0 [3], was not performed. A higher chloride ion concentration apparently shifts the peak potentials. In 8.48 M Cl^- supporting electrolyte, the anodic peak appears at a potential of −0.27 V vs. SHE (recalculated from SCE) and the corresponding cathodic peak at −0.33 V vs. SHE. Another advantage is that no hydrogen evolution is observed at potentials below the V(III) reduction peak which is favourable for the charging process in RFBs. A short-term cell test was conducted and the composition of the negative half-cell electrolyte was 1 M VCl_3 in 1.5 M HCl, while that of the positive half-cell electrolyte was 1 M NaBr in 1.5 M HCl. The η_{CE} and η_{VE} values were calculated as 83% and 80%, respectively. The long-term experiments to investigate the crossover across the membrane of electrolyte and the stability tests of the bromine–polyhalide mixture have to be conducted.

2.6.2 BROMINE-POLYSULPHIDE RFB

The bromine-polysulphide RFB was patented in 1984 [38]. Upon charge bromide ions are oxidised to bromine at the positive electrode which are complexed as the tribromide ion Br_3^- in solution, and the S_4^{2-} anion is reduced to S_2^{2-} at the negative electrode. Upon discharge the reverse occurs, with S_2^{2-} anions oxidised to the polysulphide anion S_4^{2-} at the anode and

bromine reduced to bromide ions at the cathode. The catholyte and anolyte originally reported were an aqueous 1 M NaBr solution saturated with bromine and a 2 M Na_2S solution, the optimal *pH* for the electrolytes being neutral or slightly basic *pH*, while a cation exchange membrane separated the half-cells to allow the transfer of Na^+ ions between the electrodes to complete the circuit [38]. The open circuit voltage of the system is around 1.5 V [50].

Anolyte*:*

$$\mathrm{S_4^{2-} + 2\,e^- \rightleftharpoons 2\,S_2^{2-}} \qquad U^0 = -0.265\ \mathrm{V\ vs.\ SHE.} \qquad (21)$$

Catholyte*:*

$$\mathrm{3\,Br^- \rightleftharpoons\ Br_3^- + 2\,e^-} \qquad U^0 = +1.09\ \mathrm{V\ vs.\ SHE.} \qquad (22)$$

The bromine-polysulphide RFB was investigated extensively by Regenesys Technologies Ltd. in the 1990s and early 2000s, leading to the production of three scales of bromine-polysulphide modules with 5 kW, 20 kW and 100 kW power output and a 1 MW pilot scale facility that was built at Aberthaw Power Station near Cardiff, United Kingdom [121]. Interest in the system culminated in the construction of a 15 MW/120 MWh demonstration plant at Little Barford power station, also in the United Kingdom. However, the plant was never fully commissioned and the funding for the technology was later withdrawn [122]. Problems encountered with the bromine-polysulphide system include cross-contamination of electrolyte solutions due to membrane inefficiency, possible deposition of sulphur species in the membrane, as well as concern over the formation of H_2S and Br_2 gases [50].

2.6.3 Zinc/polyiodide hybrid RFB

On the subject of higher energy density RFBs, Li *et al*. presented a zinc/polyiodide hybrid flow battery [123]. The aqueous electrolyte, a ZnI_2 solution in both compartments, was ambipolar; both the cationic and anionic ions were redox active which eliminated the need for counter ions. Further, the Zn^{2+} species also functioned as a charge carrier so a supporting electrolyte was not needed. Upon charge, zinc is deposited at the anode and polyiodide ions are formed in solution at the cathode while the reverse reactions occur upon discharge.

Anolyte:

$$\mathrm{Zn} \rightleftharpoons \mathrm{Zn^{2+}} + 2\,\mathrm{e^-} \qquad U^0 = +0.76\ \mathrm{V\ vs.\ SHE.} \tag{23}$$

Catholyte:

$$\mathrm{I_3^-} + 2\,\mathrm{e^-} \rightleftharpoons 3\,\mathrm{I^-} \qquad U^0 = +0.54\ \mathrm{V\ vs.\ SHE.} \tag{24}$$

A high η_{CE} of 99% was demonstrated in charge/discharge cycling using concentrations of ZnI_2 from 0.5 M to 3.5 M. Over 40 cycles, a 3.5 M ZnI_2 electrolyte showed no obvious efficiency or capacity decay. While η_{EE} was shown to decrease with higher ZnI_2 concentrations due to the increasing electrolyte resistance, a 5 M ZnI_2 solution reached an energy density of 167 Wh L^{-1} based upon the discharge energy density which approached the energy density of some LIBs. An electrolyte stability window of −20 to 50°C was reported. However, as discussed in a previous section for the zinc-bromine RFB, an issue with the operation of the Zn/Zn^{2+} redox couple was the formation of dendrites when zinc was deposited at the anode during charging which was observed in the zinc-polyiodide flow battery.

2.6.4 Semi-solid lithium slurry RFBs

Optimisation of the VRFB remains a compelling topic, but alternative RFB chemistries also garner attention in the pursuit of improved energy densities. For instance, concepts of LIBs are naturally carrying over into flow battery research. As well as the increased cell voltages allowed by the use of a non-aqueous electrolyte, LIB operation involves ionic transport within solid electrodes which allows greater storage of active species and higher energy densities. As such, a semi-solid flow cell utilising Li-ion chemistry and slurries of suspended electrode material was presented by Duduta *et al.* [66]. The electrolytes were semi-solid suspensions containing a nanoscale conducting carbon network that was formed by Ketjen black in alkyl carbonate/$LiPF_6$ solution, with micrometre-scale particles of electrode material (e.g. $LiCoO_2$) distributed throughout the network. The flowable suspensions that were demonstrated had up to 12 M active material concentration. A full-cell test using intermittent flow mode in which a single volume of the semi-solid suspensions was pumped into the cell, discharged and later displaced by a new volume gave a first demonstration of a fully operational semi-solid flow cell. Suspensions containing $LiCoO_2$ were utilised at the

cathode (20 vol% (10.2 M), 1.5% Ketjen black) and suspensions containing $Li_4Ti_5O_{12}$ were active at the anode (10 vol% (2.3 M), 2% Ketjen black), both in 1 M $LiPF_6$ in dimethyl carbonate. A η_{CE} of 73% and 80% was achieved in the first and second cycles. A calculated theoretical energy density for a semi-solid system utilising $LiCoO_2$ and $Li_4Ti_5O_{12}$ with 40vol% solid in each suspension at an average discharge voltage of 2.35 V was 397 Wh L^{-1}. More generally, it was estimated that optimised semi-solid flow cells utilising lithium intercalation compounds could have energy densities of 300 to 500 Wh L^{-1}. However, higher viscosity electrolytes are associated with increased parasitic energy losses, owing to the additional energy that is required to pump the electrolyte.

2.6.5 Redox active polymers for RFBs

The use of organic molecules or polymers as the active materials in RFBs are also gaining prominence in RFB research as such species can be synthesised from inexpensive organic raw materials. An all-polymer RFB utilising a polymer bearing the TEMPO moiety at the cathode and a viologen-based polymer at the anode was presented by Janoschka *et al*. [97]. The TEMPO unit (2,2,6,6-tetramethylpiperidine-1-oxyl) is a heterocyclic, stable radical nitroxide molecule that can be oxidised to an oxammonium cation, while viologens are dicationic 4,4'-bipyridine derivatives that can be reduced to monocationic radicals. Both polymers also contain quaternary ammonium units to aid solubility. A study of the redox properties of the polymers by CV indicated the TEMPO-containing polymer underwent oxidation to $TEMPO^+$ at 0.7 V vs. Ag/AgCl while the viologen polymer underwent a reduction at around −0.4 V vs. Ag/AgCl which corresponded to the formation of a monovalent radical $Viol^{+\bullet}$ species. The electrolyte for the all-polymer battery was an aqueous sodium chloride solution and a low-cost cellulose-based dialysis membrane was used to prevent crossover of the polymeric species but allow the movement of ions between half-cells. Figure 8 shows a schematic representation of the polymer-based RFB and the fundamental electrode reactions of the TEMPO and viologen radicals.

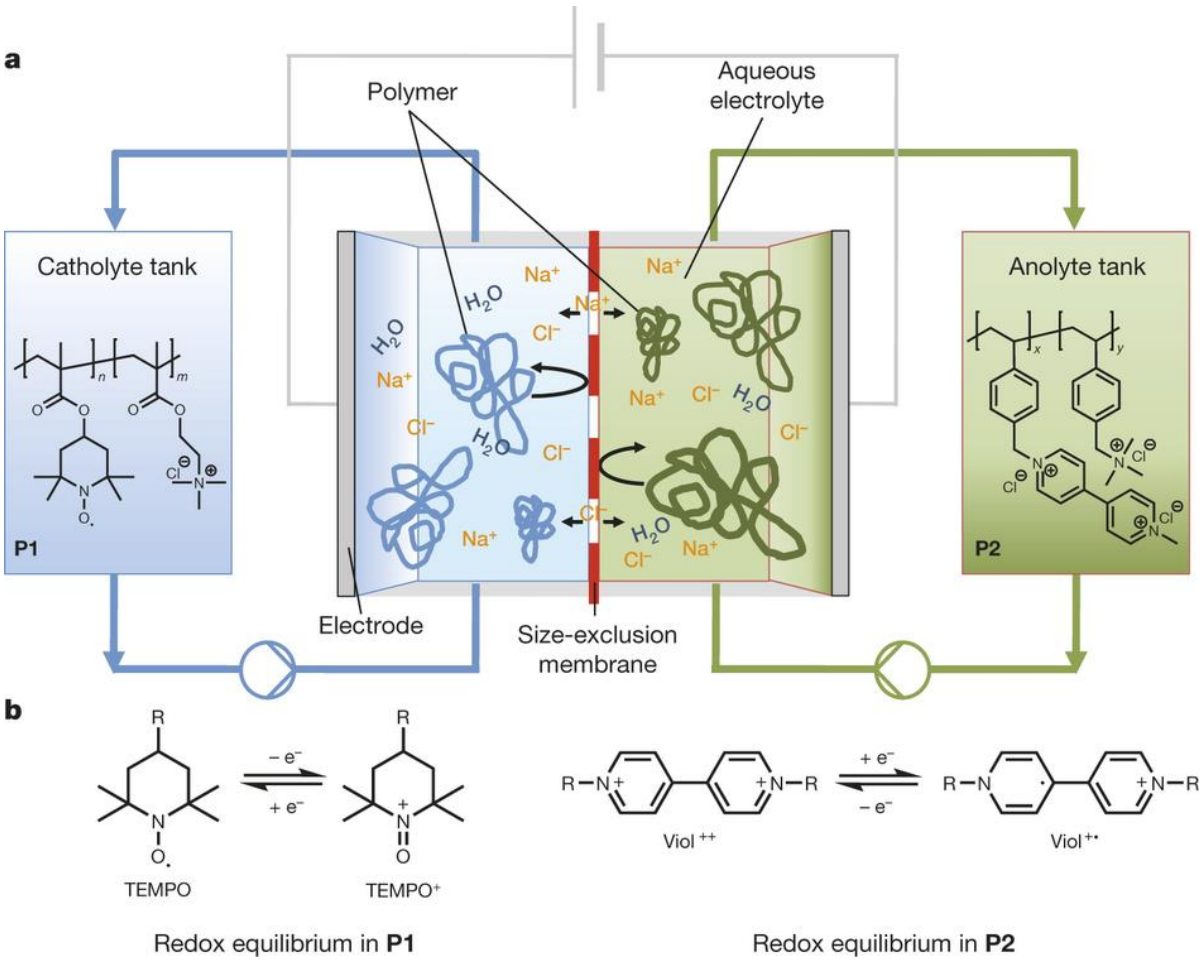

Figure 8 Schematic representation of the polymer-based RFB and the fundamental electrode reactions of the TEMPO and viologen radicals [97] (a) Polymer-based RFB, consisting of an electrochemical cell and two electrolyte reservoirs (A semipermeable size-exclusion membrane separates the anolyte and catholyte.); (b) the fundamental electrode reactions of the TEMPO and viologen radicals.

The open-circuit voltage in cell testing was 1.1 V and energy densities of around 10 Wh L^{-1} are reported for the polymer solutions. After 10 000 cycles, 80% of the initial capacity was retained in a static, unpumped cell. A faster capacity fade was observed in a pumped cell, thought to be attributable to oxidation of the viologen radical species by oxygen entering the electrolyte. The cytotoxicity of the redox-active polymers was also tested and compared with the cytotoxicity of VCl_3, $VOSO_4$ and two other cationic polymers, poly(L-lysine) and branched poly(ethylene imine), materials chosen because of their wide use. The TEMPO polymer showed less toxicity than the viologen polymer, while both polymers were less cytotoxic than poly(L-lysine), poly(ethylene imine) and the vanadium salts.

The use of size-exclusion membranes that prevent polymeric active species from crossing into the adjacent electrode compartment instead of more costly Nafion ion exchange

membranes illustrates a promising aspect of RFBs that utilise polymers. However, as the concentration or the molecular weight of a dissolved polymer increases, so too does the viscosity of a polymer solution. While for any RFB, a higher concentration of active species leads to a greater energy density, increasing the concentration of a polymer solution may be problematic as viscous solutions increase the energy cost of pumping the electrolytes. Thus, the advantage of the use of a size-exclusion membrane in a polymer RFB could be counterbalanced by the viscosity that is intrinsic to polymer solutions.

The use of TEMPO and viologen as small organic molecules in a RFB is an alternative to TEMPO and viologen-based polymers. For instance, a RFB that used aqueous solutions of TEMPTMA (*N,N,N*-2,2,6,6-heptamethylpiperidinyl oxy-4-ammonium chloride) (a TEMPO derivative) and methyl-viologen (*N,N'*-dimethyl-4,4-bipyridinium dichloride) had an energy density of 38 Wh L^{-1} for a theoretical cell voltage of 1.4 V and excellent capacity retention over 100 cycles [124].

Winsberg *et al*. presented a polymer-based RFB that utilised two polymers bearing the boron-dipyrromethene (BODIPY) unit [125] in propylene carbonate as solvent. CV of the monomer containing the BODIPY group showed two redox reactions at −1.51 V vs. $AgNO_3$/Ag and 0.69 V vs. $AgNO_3$/Ag which corresponded to reduction of the monomer to $BODIPY^-$ and oxidation to $BODIPY^+$ respectively. The BODIPY monomer was copolymerised with either TASt ((vinylbenzyl)trimethylammonium perchlorate) or TEGSt ((vinyl-benzyl)-triethylene glycol monomethyl ether) to generate two different polymers that could be used as the anolyte and catholyte in cell testing. Two static cell tests were performed (Figure 9). One employed poly(BODIPY-co-TEGSt) as anolyte with a further polymer that bore the TEMPO group used as the catholyte (poly(TEMPO-co-PEGMA). The second cell utilised poly(BODIPY-co-TASt) and poly(BODIPY-co-TEGSt) as the catholyte and anolyte respectively. A size-exclusion membrane separated the half-cells and a solution of 0.5 M tetrabutylammonium perchlorate (Bu_4NClO_4) in propylene carbonate was used as the supporting electrolyte. The TEMPO/BODIPY battery outperformed the all-BODIPY battery, with an average discharging voltage of 1.82 V and a η_{VE} and η_{EE} of 89% and 88% respectively. A η_{CE} of 99% was achieved over 100 cycles, with 70% of the initial discharge capacity preserved. The all-BODIPY system had a charging plateau at 2.06 V while the mean discharge voltage was 1.28 V leading to a

η_{VE} and η_{EE} of 62% and 55% respectively, with η_{CE} reaching 89%. The energy density of the electrolyte was 0.5 Wh L^{-1} for both polymer RFBs.

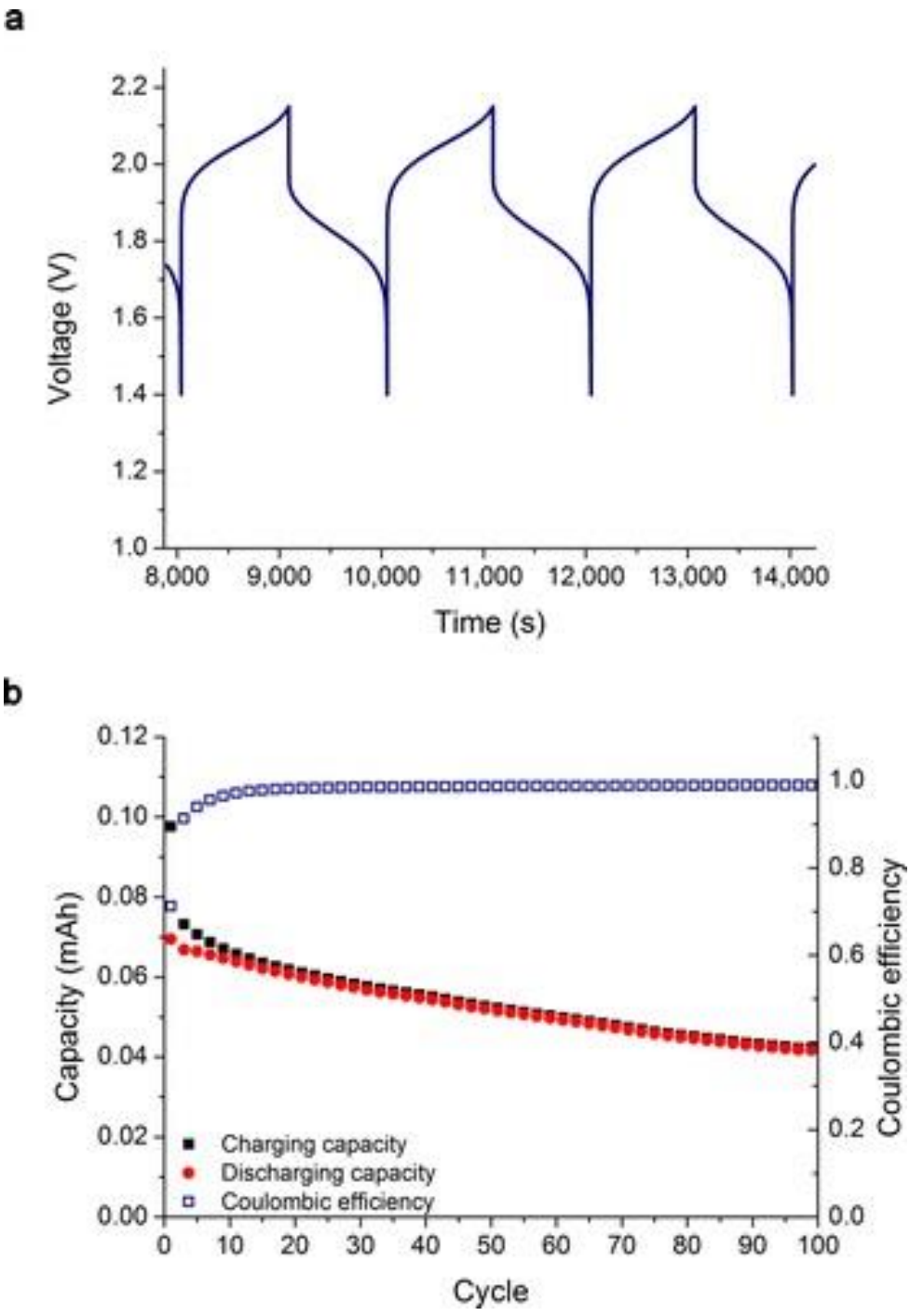

Figure 9 Performance data of a polymer-based RFB presented by Winsberg *et al*. [125]
(a) Representative charge/discharge curves of an all-organic polymer RFB using poly(TEMPO-co-PEGMA)and poly(BODIPY-co-TEGSt) operating in the range of 1.4 V and 2.15 V, showing cycles 3 to 5; (b) long-term battery cycling at a constant current of 0.25 mA (an electrolyte of propylene carbonate with 0.5 M Bu_4NClO_4 was used).

2.6.6 POLYOXOMETALATE RFB

Pratt *et al*. presented a flow battery containing vanadium- and tungsten-polyoxometalates (POMs), in which the POMs underwent multi-electron reactions [126,127]. POMs are suitable for electrochemical energy storage applications because they are often stable over a wide range of temperatures, exhibit multi-electron transfer with high kinetics [128]. Also, oxidation or reduction of POMs is usually accompanied by proton or cation transfer, a mechanism that avoids the generation of highly charged radicals [129]. In the publication by Pratt *et al*., two three-electron POM redox couples ($[SiV(V)_3W(VI)_9O_{40}]^{7-}$ / $[SiV(IV)_3W(VI)_9O_{40}]^{10-}$ and $[SiV(IV)_3W(VI)_9O_{40}]^{10-}$ / $[SiV(IV)_3W(V)_3W(VI)_6O_{40}]^{13-}$) were investigated for application as electrolyte in aqueous or non-aqueous media for RFBs.

The η_{CE} in aqueous solution was greater than 95% with a low capacity loss observed during more than 100 charge-discharge cycles and no decomposition of the molecule was reported [126]. The POM also dissolved in a non-aqueous electrolyte (0.5 M TBAOTf in propylene carbonate) and the non-aqueous system had a higher operating voltage (1.1 V, 0.3 V higher than the aqueous system) but a drop of η_{CE} (initially 87%, after ten cycles dropped by half) occurred. With a concentration of 20 mM POM and 0.5 M H_2SO_4, the observed current densities were one order of magnitude lower than in conventional RFBs. A reasonable approach to increase the current would be to enhance the POM concentration. The stability and costs were not reported. In the paper, the dimerization and eventual deposition of POMs containing W-ions at negative potentials was not discussed [126]. Keita and Nadjo reported that at negative potentials (approx. 1 V vs. SHE) in acidic solutions, POMs will modify the electrode surface [130]. The deposited material is usually a catalyst for the HER, thereby reducing the stability window of the electrolyte [131]. For $[SiW_{12}O_{40}]^{4-}$, the precursor for the redox active material used in Ref. [126], electrode coverages of 33 to 120 monolayers are reported [130].

A potential candidate for a POM catholyte was reported: $[Mn^{II}_3SiW_9O_{34}]^{7-}$ [128,132]. While this molecule was able to transfer six electrons at high potentials, by oxidising three Mn(II) to Mn(IV), the POM adsorbed on the electrode and was too difficult to synthesise to make upscaling reasonable.

Another symmetric POM RFB was presented by Liu *et al*. [133]. They employed $H_6[CoW_{12}O_{40}]$ in both anolyte and catholyte of an aqueous battery. The reactions for the anolyte were two

two-electron waves at −0.04 V vs. SHE and −0.16 V vs. SHE (in 1 M H_2SO_4, recalculated form the SCE) [134]. As catholyte, the single one-electron redox reaction of the Co(II)-heteroatom at 1.1 V vs. SHE was used. The POM was exceptionally soluble, up to 0.8 M, and 14 Ah L^{-1} were reached as capacity. However, for that result four times more catholyte volume than anolyte volumes were used (and above volumetric capacity is given for the anolyte) which was necessitated by the imbalance in charge transfer reactions at low and high potentials.

2.6.7 METAL-FREE ORGANIC-INORGANIC AQUEOUS RFBS BASED ON ANTHRAQUINONES

A RFB with quinones as aromatic redox-active organic molecules instead of redox-active metals was developed with the main objective to reduce capital costs [135]. The molecule used in the anolyte was 9,10-anthraquinone-2,7-disulphonic acid (AQDS) dissolved in 1 M H_2SO_4 (Figure 10). According to the authors, AQDS can be synthesized from cheap, conventional educts.

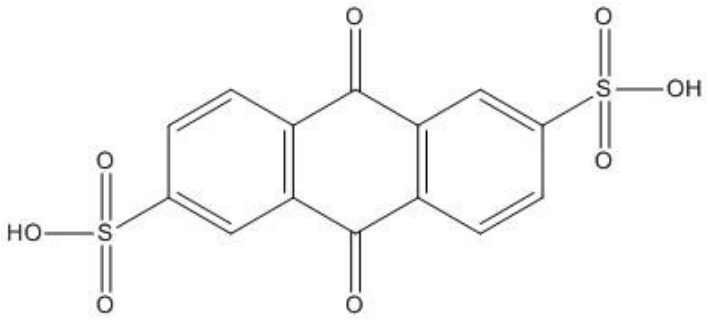

Figure 10 Chemical structure of 9,10-anthraquinone-2,7-disulphonic acid.

In the positive half-cell, the redox couple was Br_2/Br^- complementing the quinone/hydroquinone redox couple in the anolyte. For this type of battery, a tremendous power density of 1 W cm^{-2} was reported at a relatively low cell voltage of 0.86 V [136,137]. The storage capacity retention reached was more than 99% per cycle (99.90% per cycle over 40 cycles). These losses are thought to originate from the leakage of the anolyte, crossover of bromide, and destruction of redox species [138].

The theoretical capacity of 35 Wh L^{-1} cannot be reached in the cell; only 23 Wh L^{-1} could be realized. A possible explanation was provided by Carney *et al.*, who found intermolecular dimerization of AQDS at concentrations greater than 10 mM [139] . This behaviour is *pH*

dependent and might reduce the electrons that can be carried per AQDS molecule from two to one and a half in acidic media.

A further advantage is that the chemical and electrochemical properties of the AQDS molecules can be engineered by adding functional groups. Addition of a hydroxyl group reduces the standard potential of the redox reaction, thereby increasing the open circuit potential U_{OCV}. A CV of 1 mM solution of AQDS in 1 M sulphuric acid on a glassy carbon disk working electrode was conducted and a fast reversible two-electron two-proton redox reaction occurred. The peak separation was 34 mV and correspond to a two-electron process. The kinetic reaction rate constant k_0 was calculated to 7.25 10^{-3} cm s^{-1} which was greater than that found for other components used for RFBs such as V^{3+}/V^{2+} (compare Table 1).

The main advantages of the AQDS/Br system are low electrolyte costs and fast kinetics. The crossover of bromine into the negative half-cell could affect the lifetime and the stability of the organic compound should be investigated. The array of π-aromatic redox-active organic compounds constitutes a new opportunity for low-cost large-scale energy storage.

Another cell chemistry employing quinones is the 2,6-dihydroxyanthraquinone (DHAQ)/$Fe(CN)_6$ system in alkaline media [140]. At *pH* 14, the $Fe(CN)_6^{3-}$/ $Fe(CN)_6^{4-}$ avoids the use of the problematic Br_2/HBr employed in the acidic quinone chemistry [135], and the cell reaches a higher cell voltage of 1.2 V. The modest solubility of both DHAQ and $Fe(CN)_6$, however, limits the theoretical energy density to 9.2 Wh L^{-1}, of which 74% have been shown experimentally [140].

2.6.8 A RFB WITH AN ALLOXAZINE-BASED ORGANIC ELECTROLYTE

In this work an aqueous RFB utilizing an organic redox compound was reported. As electrochemically active molecule alloxazine, which was a tautomer of the isoalloxazine backbone of vitamin B_2 was used [141]. It could be obtained by a single-step coupling of o-phenylenediamine derivatives and alloxan with a yield of 95% at room temperature. The synthesis route was inspired by nature and the educts were reported to be inexpensive.

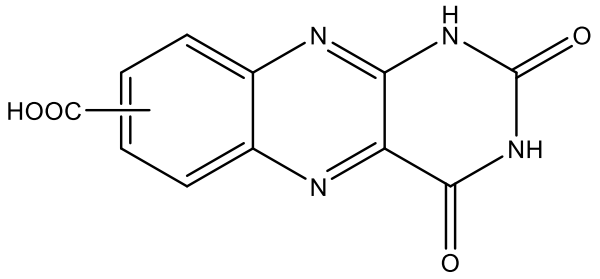

Figure 11 Alloxazine 7/8-carboxylic acid (ACA).

The alloxazine was functionalized with acarboxylic acid group (alloxazine 7/8-carboxylic acid (ACA), see Figure 11) to increase its solubility in aqueous solution. ACA was investigated by CV and the standard potential was −0.62 V vs. SHE. The rate constant was calculated from rotating-disc electrode measurement and determined to be $k_0 = 1.2 \pm 0.2\ 10^{-5}$ cm s^{-1}, which was an order of magnitude higher than that of the reactions of the VRFB [3]. The full-cell test was conducted using 0.5 M ACA (1.5 mmol) as the negative electrolyte and 0.4 M ferrocyanide (4.5 mmol) + 40 mM ferricyanide (0.46 mmol) as the positive electrolyte. Both solutions were adjusted to *pH* 14 by KOH. An excess concentration of the positive electrolyte was used to determine the electrochemical stability of the negative electrolyte. The resulting alkaline aqueous RFB exhibited an OCV of 1.2 V and η_{CE} and capacity retention reaching 99.7% and 99.98% per cycle, respectively. The alloxazine redox centre demonstrated a high electrochemical and chemical stability and a high solubility. It was shown in theoretical studies that structural modification such as adding electron-donating groups to the alloxazine could increase the battery voltage. This aza-aromatic molecule undergoes reversible redox reaction in aqueous electrolyte and constitutes a class of radical-free redox-active compounds for application in RFBs with high power density and low costs.

2.6.9 TEMPO-BASED CATHOLYTE FOR NON-AQUEOUS RFBS

Although only a catholyte was presented, due to its potential it was included in this review. A lithium hybrid flow battery containing TEMPO, a stable, heterocyclic nitroxide radical, as the organic active material was developed [79]. Figure 12 shows the redox reactions taking place in anolyte and catholyte. CVs were conducted in an electrolyte of 0.005 M TEMPO and 1.0 M $LiPF_6$ dissolved in EC/PC/EMC (4:1:5 by weight) and clear redox peaks in the potential range of 2.5 - 4.0 V of TEMPO were obtained. The peak separation of 61 mV at 10 mV s^{-1}

corresponds to a one-electron-transfer between the nitroxide radical and the oxoammonium cation.

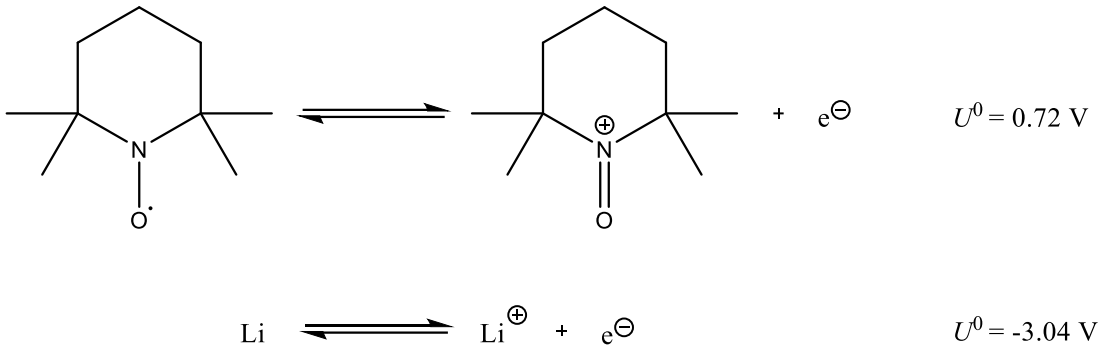

Figure 12 Redox reactions in the negative and positive electrolyte during charge and discharge in a hybrid TEMPO-Li RFB [79].

The electrochemical performance was tested in a non-aqueous hybrid RFB with a polyethylene-based porous separator. The anode was a hybrid anode consisting of lithium foil and graphite felt, and as cathode, a graphite felt was used. Both electrodes were compressed by 15%. An additive, fluoroethylene carbonate (FEC), was added to protect the Li anode. TEMPO was dissolved in a solution containing EC/PC/EMC (weight ratio of 4:1:5) and $LiPF_6$ as supporting electrolyte. The TEMPO based electrolyte was static within the anode compartment and was not flowed, whereas in the cathode compartment the electrolyte was circulated through the graphite felt at a flow rate of 50 mL min^{-1}. Galvanostatic charge/discharge cycling with various concentrations of TEMPO (0.8/1.2 M, 1.5/1.8 M, and 2.0/2.3 M) were conducted. Charge and discharge experiments were conducted and 100 cycles were obtained with a η_{CE} of 99%, a η_{VE} of 87% and a η_{EE} of 86%, and an average capacity retention of 99.8% per cycle were achieved. Due to high viscosities of the electrolytes, the flow cells were cycled at current densities of 2.5 mA cm^{-2} at 1.5 M and 1.0 mA cm^{-2} at 2.0 M.

The theoretical energy density of the system with 2.0 M TEMPO is 126 Wh L^{-1} and is much higher than that for a conventional VRFB. Due to the high energy density and overall voltage of 3.5 V, TEMPO is a promising candidate for flow batteries.

2.7 Overview of some redox reactions of importance for RFBs

The overview of some redox reactions of importance for RFBs is shown in Table 3. If approximate realised energy density is given, the energy content is calculated from the given publication. Chemistries not demonstrated in flow batteries were usually tested in a stationary cell configuration.

Table 3 Overview of redox reactions of importance for RFBs.

Redox couples	U^0 vs. SHE	Medium	k_0 / cm s^{-1}	Concentration	*n*	Energy content realised	Ref.
Br^-/Br_2	1.09 V	Aqueous			2	3 MWh	[40,142]
Zn/Zn^{2+}	-0.76 V	Aqueous	-		2		
Fe^{2+}/Fe^{3+}	0.77 V	Aqueous	$6\ 10^{-5}$	2 M	1	12 kWh in 1981	[143,144]
Cr^{2+}/Cr^{3+}	-0.41	Aqueous	$2.2\ 10^{-5}$	2 M	1		
VO^{2+}/VO_2^+	1.0 V	Aqueous	10^{-6}	1.6 – 2M	1	800 MWh contract signed in 2016	[3,145]
V^{2+}/V^{3+}	-0.25 V	Aqueous	10^{-6}	1.6 – 2M	1		
Br_3^-/Br^-	+1.09 V	Aqueous	$4\ 10^{-5}$	1 M NaBr saturated with Br	2	120 MWh in 2002	[50,146,147]
S_4^{2-}/S_2^{2-}	-0.265 V	Aqueous	$3\ 10^{-6}$	2 M Na_2S	2		
I_3^-/I^-	+0.54 V	Aqueous	-	5.0 M ZnI_2	2	Approx. 0.01 Wh in 2015	[123]
Zn/Zn^{2+}	-0.76 V	Aqueous	-	5.0 M ZnI_2	2		
Ce^{3+}/Ce^{4+}	+1.28 to +1.72 V	Aqueous	-	0.2 M Ce(III) methane sulfonate	1	Approx. 3 Wh in 2011	[148]

				(0.5 M methane sulfonic acid)			
Zn/Zn^{2+}	-0.76 V	Aqueous	-	1.5 M zinc methane sulfonate (0.5 M methane sulfonic acid)	2		
Mn^{2+}/Mn^{3+}	+1.3 V vs. Ag/AgCl	Aqueous	-	1 M $MnSO_4$ + 1.5 M $TiOSO_4$ (3 M H_2SO_4)	1	Approx. 20 Wh in 2015	149
Ti^{3+}/TiO_2^{2+}	∼-0.09 V vs. Ag/AgCl	Aqueous	-	1 M $MnSO_4$ + 1.5 M $TiOSO_4$ (3 M H_2SO_4)	1		
Fe^{2+}/Fe^{3+}	+0.77 V	Aqueous	$6\ 10^{-5}$	1 M $FeCl_2$ + 0.5 M $CdSO_4$ (3 M HCl)		No flow cell demonstrated.	150
Cd/Cd^{2+}	-0.40 V	Aqueous	-	1 M $FeCl_2$ + 0.5 M $CdSO_4$ (3 M HCl)	2		
$NiOOH/Ni(OH)_2$	0.490 V	Aqueous	-	1 M ZnO (10 M KOH)	2	Approx. 0.3Wh in 2007	151
$Zn/Zn(OH)_4^{2-}$	-1.215 V		-	1 M ZnO (10 M KOH)	2		
$V^{III}(acac)_3/[V^{IV}(acac)_3]^+$	+0.45 V vs. Ag/Ag^+	Non-aqueous	$1.\ 3\ 10^{-4}$	0.01 M	1	No flow cell demonstrated.	73,112

$V^{III}(acac)_3/[V^{II}(acac)_3]^-$	-1.8 V vs. Ag/Ag^+	Non-aqueous	-	(0.5 M $TEABF_4$ /acetonitrile)	1		
$Ru^{III}(acac)_3/[Ru^{IV}(acac)_3]^+$	+1.0 V vs. SCE	Non-aqueous	$3.4\ 10^{-3}$	0.1 M (0.5 M $TEABF_4$/ acetonitrile)	1	Approx 0.2 Wh in 2011	[152,153]
$Ru^{III}(acac)_3/[Ru^{II}(acac)_3]^-$	-0.85 V vs. SCE	Non-aqueous			1		
$Mn^{III}(acac)_3/[Mn^{IV}(acac)_3]^+$	+0.7 V vs. Ag/Ag^+	Non-aqueous	-	0.05 M (0.5 M $TEABF_4$/acetonitrile)	1	No flow cell demonstrated.	[74]
$Mn^{III}(acac)_3/[Mn^{II}(acac)_3]^-$	-0.4 V vs. Ag/Ag^+	Non-aqueous	-		1		
$Cr^{III}(acac)_3/[Cr^{IV}(acac)_3]^+$	+1.2 V vs. Ag/Ag^+	Non-aqueous	-	0.05 M (0.5 M $TEABF_4$/acetonitrile)	1	No flow cell demonstrated.	[112]
$Cr^{III}(acac)_3/[Cr^{II}(acac)_3]^-$/	-2.2 vs. Ag/Ag^+	Non-aqueous	-		1		
$[Ru^{II}(bpy)_3]^{2+}/[Ru^{III}(bpy)_3]^{3+}$	+1.0 V vs. Ag/Ag^+	Non-aqueous	-	0.02 M (0.1 M Et_4NBF_4/acetonitrile)	1	n.a.	[75]
$[Ru^{II}(bpy)_3]^{2+}/[Ru^{I}(bpy)_3]^+$	-1.6 V vs. Ag/Ag^+	Non-aqueous			1		

$[V(mnt)_3]^{2-}/[V(mnt)]^{-}$	0.856 V	Non-aqueous	-	0.02 M (0.1 M $TBAPF_6$/acetonitrile)	1	No flow cell demonstrated.	[154]
$[V(mnt)_3]^{2-}/[V(mnt)_3]^{3-}$	-0.227 V	Non-aqueous	-		1		
Fc/Fc^{+} (Fc = ferrocene)	0.041 V vs. Ag/Ag^{+}	Non-aqueous	-	0.01 M (1 M $TEAPF_6$/acetonitrile)	1	Approx. 0.3 mWh	[155]
Cc/Cc^{+} (Cc = cobaltocene)	-1.290 V vs. Ag/Ag^{+}	Non-aqueous	-		1		
Co^{II}(acacen)/ $[Co^{I}(acacen)]^{-}$	-0.2 V vs. Ag/Ag^{+}	Non-aqueous	-	0.01 M (0.1 M $TEAPF_6$/acetonitrile)	1	No flow cell demonstrated.	[156]
Co^{II}(acacen)/ $[Co^{III}(acacen)]^{+}$	-2.2 V vs Ag/Ag^{+}	Non-aqueous	-		1		
QCl_4/QH_2Cl_4 (QCl_4 = Tetrachloro-*p*-benzoquinone)	0.71 V	Aqueous	-	0.5 M $CdSO_4$ (1 M $(NH_4)_2SO_4$ + 0.5 M H_2SO_4)	2	Approx. 0.2 Wh	[157]
Cd/Cd^{2+}	-0.402	Aqueous	-		2		
BQDS/H_2BQDS (BQDS = 1,2-benzoquinone-3,5-disulfonic acid)	0.85 V	Aqueous	$1.55\ 10^{-4}$	0.2 M (1 M H_2SO_4)	2	Approx. 0.1 Wh	[158]

AQS/H_2AQS (AQS = anthraquinone-2-sulfonic acid)	0.09 V		$2.25\ 10^{-4}$	0.2 M (1 M H_2SO_4)	2		
TEMPO/$TEMPO^+$	0.30 V vs. Ag	Non-aqueous	-	0.1 M (1 M $NaClO_4$ /acetonitrile)	1	< 1mWh	[76]
N-methylphthalimide/ N-methylphthalimide$^{-\bullet}$	-1.30 V vs. Ag	Non-aqueous	-	0.1 M (1 M $NaClO_4$ /acetonitrile)	1		
TEMPTMA/ $TEMPTMA^+$	0.79 vs. AgCl/Ag	Aqueous	$4.2\ 10^{-3}$	2 M (in NaCl)	1	Approx. 0.6 Wh	[124]
Methyl $Viol^{2+}$/ Methyl $Viol^{+\bullet}$	-0.63 V vs. AgCl/Ag		$3.3\ 10^{-3}$		1		
Polythiophene/ $Polythiophene^+$	+0.5 V vs. Ag/Ag^+	Non-aqueous	-	Suspension of polythiophene (0.1 eq. L^{-1} of thiophene repeating units) (1 M $TEABF_4$ /propylene carbonate)	1	Approx. 1.5 mWh	[159]
Polythiophene/ $Polythiophene^-$	-2.0 V vs. Ag/Ag^+	Non-aqueous	-		1		

TEMPO/TEMPO^{+}	+0.7 V vs. Ag/AgCl	Aqueous	(4.5 ± 0.1) 10^{-4}	polymer solutions	1	Approx. 80mWh	[97]
$Viol^{2+}/Viol^{+\bullet}$	~-0.4 V vs. Ag/AgCl		(9 ± 2) 10^{-5}	(2 M NaCl)	1		
Poly(BODIPY)/ Poly(BODIPY)$^{+}$	0.69 V vs. $AgNO_3$/Ag	Non-aqueous	-	polymer solution (0.5 M Bu_4NClO_4/ propylene carbonate)	1	Approx. 0.006 mWh	[125]
Poly(BODIPY)/ Poly(BODIPY)$^{-}$	-1.51 V vs. $AgNO_3$/Ag	Non-aqueous	-		1		

2.8 Conclusions: What would be the ideal RFB?

The primary properties of the ideal RFB chemistry are high energy and power density, long-time stability and low capital costs. Secondary features are high efficiencies and safety, and low toxicity of the chemistries. However, the detail in these secondary features will not be discussed, because efficiencies are very much related to the issues power density and stability, and the ideal toxicity level is easily assessed: the ideal RFB chemistry is not harmful to the health of humans or the environment, such as claimed by the nanoFlowcell Holdings Ltd. for their undisclosed nanoFlowcell technology [160], which, due to its unverified claims, is regarded very sceptically by the scientific community.

Energy density: The (volumetric) energy density *E* for a RFB is given by the combination of equations (3) and (6). There are three parameters that can be adjusted to increase *E*: the number of electrons transferred per molecule *n,* the concentration *c*, and the cell voltage ΔU. For most molecules discussed in this chapter, *n* = 1, with some exceptions such as the AQDS and Br_2/Br^- systems which transfer *n* = 2 electrons [50,135,146] and POM systems with $n \geq 3$ [126,133]. In the latter case, this property is achieved only by employing heavy molecules (molar mass larger than 2000 g mol^{-1}). Due to the high solubility of POMs, this can increase the volumetric energy density, but hardly the gravimetric energy density. Highly charged species are often not stable, and therefore, multi-electron transfer is usually accompanied by proton transfer [128,129,161]. While this prevents the formation of radicals, balancing of protons adds an additional challenge to the system, if it does not operate at very low *pH*. As shown in section 3.4, the question of maximum cell voltage ΔU is intricately connected to the question of aqueous or non-aqueous chemistry. While the limit of ΔU in water is roughly 1.6 V, this value can be significantly higher in organic electrolytes. However, as the use of non-aqueous electrolytes comes with a serious penalty in terms or costs and ease of operation, the cell voltage has to be increased at least to 3 V in order to warrant drastic step [162].

Concentration *c* is probably the most freely adjustable parameter that determines the energy density. Employing slurries of lithium ion battery cathode materials concentrations as high as 12 M for the active material are reported [66]. Classical RFBs such as the VRFB reach concentrations of 1 – 3 M, often with the use of stabilisers or in concentrated acids.

Looking at the discussion of the three parameters above, something like the expected value can be defined in terms of volumetric energy density for an aqueous RFB: This cell transfers one electron n = 1 per molecule, anolyte and catholyte are present as c = 2 M solutions, and the cell voltage takes the maximum advantage of the stability window of carbon electrodes in water, $\Delta U = 1.6\ \mathrm{V}$. The result is a battery with energy density $E \approx 43\ \mathrm{W\ L^{-1}}$. Any RFB chemistry that features a higher volumetric energy content, while simultaneously satisfying the other constraints (power, cost, safety, efficiency), would be desirable.

Power density: The power that can be drawn from a battery is limited by the overvoltage $R_{\mathrm{total}}\ I$ that has to be applied to reach a certain current I. This total resistance R_{total}, often given as area-specific resistance (ASR) of the power converter, comprises the single resistances R_{elec}, R_{mem}, R_{CT}, and R_{mass} as given in equation (7). R_{elec} and R_{mass} are from the realm of power converter design and electrochemical engineering, and are, therefore, not discussed here [32,33,50,121]. The membrane resistance R_{mem} is determined by the membrane used or separator, but that is pre-determined by the chemistry used, for instance, the resistance of many types of membranes decreases after soaking in VO_2^+ containing solution [90,163]. Ideally, size-exclusion membranes [97] or fluorinated exchange membranes with high proton concentrations are used to keep R_{mem} low. In non-aqueous solvents or in neutral aqueous electrolytes, the membrane can have a significant contribution to the ASR. One major factor is the charge transfer resistance R_{CT} that depends on the employed redox couple. The electron transfer constant k_0 which determines R_{CT} (see equation (8)) spreads over more than three orders of magnitude for different redox couples used for RFBs (see Table 1). With c = 2 M $\mathrm{L^{-1}}$, n = 1 and k_0 = 0.001 cm $\mathrm{s^{-1}}$, the R_{CT} = 0.1 $\Omega \cdot \mathrm{cm^2}$ would contribute only minimally to the ASR for which an upper bound of 1.5 $\Omega \cdot \mathrm{cm^2}$ was given [162].

Long-time capacity stability is an obvious criterion for an RFB. In terms of the chemistry, this can be subdivided into cycling stability and chemical stability. The former is diminished by side-reactions during charge and discharge, and cross-over through the membrane. Only the fraction of electrolyte volume in the power converter is subjected to it. The latter, chemical stability, concerns either individual oxidation states or redox molecules themselves. For most of these phenomena, mitigation strategies can be found. For example, in a VRFB, hydrogen evolution takes place [63], ion-specific cross-over through the membrane occurs [164], and V^{2+} is oxidized by O_2. All these effects lead to an imbalance in the electrolyte, thus

anolyte and catholyte are not at the same SOC during battery operation. Re-mixing of the electrolytes or electrochemical rebalancing can be employed to mitigate this capacity loss [165]. More problematic is chemical instability, if the employed redox shuttles react to form other species. This is because even if the temporal capacity fade, such as for the bis((3-trimethylammonio)propyl)- ferrocene dichloride / bis(3-trimethylammonio)propyl viologen tetrachloride seems extremely low, at the reported 99.90%/d [166], the capacity has dropped to 70% of its initial value after one year.

Degradation effects that do not stem from the electrolytes can be due to membrane fouling [167], bipolar plate corrosion, and electrode ageing [5,57]. These are serious issues, but they could be remedied by replacing the cell stack which might be cheaper than replacing the electrolyte.

The ideal RFB chemistry features high Coulombic efficiency, however, ion crossover and side reactions can be tolerated if the battery is symmetric as in the case of the VRFB, and viable rebalancing strategies exist. Chemical instability cannot be tolerated, as even smallest decay rates add up very quickly.

The discussion of costs for a RFB is dominated by the goal set by the Advanced Research Projects Agency-Energy (ARPA-E) of the Department of Energy (DOE) of the United States to limit the capital cost to US$100 per kWh for widespread adoption [168,169]. Since then, a number of cost calculations for RFBs have appeared [45,162,168], comparing the costs for the various components. For the VRFB, Zhang *et al*. found that the electrolyte and the membrane were the major cost contributors [45]. However, it is also reasonable that when the main application of RFBs shifts from frequency regulation to grid storage, the ratio of power (kW) to energy content (kWh) will decrease, favouring longer storage times over power output. In that case, the contribution of the power converter will lose importance and the main cost factor will be the electrolyte. The cost for battery grade V_2O_5, a convenient benchmark, fluctuated a lot over the last decade, with maximum costs of US$28 kg^{-1} and minimum costs of US$8 kg^{-1} [170]. Assuming a cost of US$21.13 kg^{-1} for vanadium, the capital cost price tag for a 1 MW/12 MWh VRFB battery was put at US$400 kWh^{-1} [45]. Acknowledging that even at a power to energy ratio of 1:12, this value greatly exceeds the DOE's target. There are two conceivable pathways for capital cost reduction:

First, it is considered that the vanadium employed does not degrade over the course of the battery's lifetime. Therefore, it can be fully recuperated at end of operation, potentially with minimal purification necessary. The capital cost spent is, therefore, not lost but is merely an investment. With respect to recycling, the VRFB, and RFBs in general, have a clear advantage over LIBs in which the single components are more intimately entangled and cannot be separated easily.

The second possibility is to replace vanadium as active element by cheaper molecules. Substitution of vanadium by organic molecules that only contain cheap elements [97,125,135] is envisioned, or by replacing it with cheaper metals such as iron and chromium [171] or manganese [149]. Whatever the strategy, Darling *et al*. concluded that the active species should not cost more than US$5 kg^{-1} and the electrolyte not more than US$0.1 kg^{-1} (for aqueous systems) assuming a weight of not more than 150 g per mole of electrons stored [168]. They further concluded that while the design space for non-aqueous systems seemed wider than for aqueous chemistries, the additional costs for the electrolyte (must not cost more than US$5 kg^{-1}) imposed additional hurdles that needed to be taken by the chemistry such as ΔU > 3V and c > 4 M. Therefore, the conclusion is that the ideal system, in terms of cost, is either a combination of two aqueous redox couples that can be easily produced on large-scale and is cheaper than US$5 kg^{-1}, or that there is rethinking regarding the VRFB system, with the electrolyte not seen as something that is spent after the battery's operation, but as an investment that keeps its value, or might even increase in value during the operation of the battery.

CHAPTER 3. ELECTROCHEMICAL TECHNIQUES

3.1 CYCLIC VOLTAMMETRY

Cyclic voltammetry is a method to investigate the behaviour of an electrochemical system and to acquire qualitative and quantitative information about electrochemical reactions. For the first time in literature this technique was mentioned and described by Randles and Sevick in 1948 [172]. In this work CV was used to evaluate the suitability of POMs as electrolytes for RFBs to check their stability and to get semi-qualitative insights about the electrode-electrolyte system. Furthermore, the vanadium redox reactions were investigated by CV in various electrolytes.

CV is a reversal technique and an established standard procedure to investigate electrochemical processes that take place in an unstirred solution at the interface between electrolyte and electrode by using a three-electrode arrangement of working electrode (WE), reference electrode (RE) and counter electrode (CE). During CV the potential *U* is continuously cycled between two set potential limits, for example in aqueous solution the onset of hydrogen and oxygen evolution, or for a certain time at a variable scan rate $\frac{dU}{dt}$ and a potentiostat monitors the resulting current. This potential-time behaviour at the working electrode has got a triangular waveform, and an example for the current response over potential can be seen Figure 13. The actual voltammogram is the plot of the potential at the WE versus RE against the flowing current.

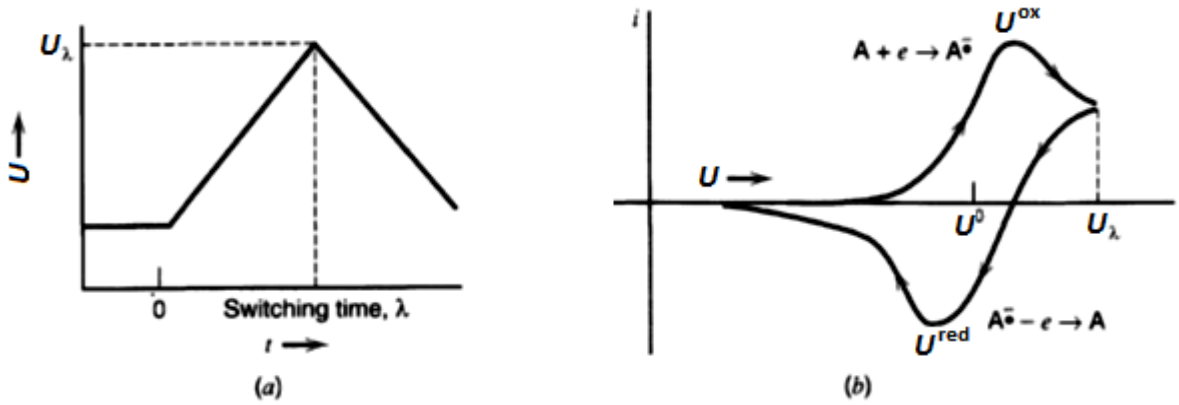

Figure 13 (a) Cyclic potential sweep over time (b) resulting CV showing the current response versus applied potential. Figure taken from reference [173] and modified.

Cyclic voltammograms give access to information about the location of U_0 of a redox reaction, the energetic positions of HOMOs (highest occupied molecular orbital) and LUMOs (lowest occupied molecular orbital) [174], the reversibility of a reaction, the adsorption/desorption processes and whether multiple reaction steps are involved and the approximate kinetics of chemical reactions [175]. A complete analysis of a CV to obtain kinetic information is complex and gives only semi-qualitative results because the electrode surfaces deviates from ideal, flat geometry which could lead to apparent electro-catalytic effects [176].

In general the peak separation ΔU (the difference in potential position of the oxidation and the reduction peak) of U^{red} and U^{ox} is a good approximation to obtain kinetics of a redox-reaction on non-porous electrodes. The fastest one-electron redox-reactions exhibit a peak-separation of 59 mV which is independent of the applied scan-rate [176].

The equilibrium of a redox reaction is described by the Nernst equation (23):

$$U = U^0 + \frac{R \cdot T}{n \cdot F} ln \frac{a(Ox)}{a(Red)} = U^0 + 2.3026 \frac{R \cdot T}{n \cdot F} log \frac{a(Ox)}{a(Red)} \qquad (23)$$

with the relative activities of the oxidized a(Ox) and the reduced a(Red) species at equilibrium. In applications the activity is often replaced by the concentration c of the redox-active species for simplification and the standard potential is replaced to the formal potential $U^{0'}$. The Nernst equation is a useful expression to calculate and predict the respond of a system to changes of the concentration or electrode potential [177].

Electrochemical reversibility is defined by the ratio of the electron transfer constant k_0 and mass transfer. The latter is dependent on the scan rate and the electrochemical reversibility parameter Λ can be described by following equation [173]:

$$\Lambda = \frac{k_0}{\left(\frac{D \cdot n \cdot F \cdot v}{R \cdot T}\right)^{1/2}} \qquad (24)$$

For ranges of $\Lambda \geq 15$ ($k_0 \geq 0.3\ v^{1/2}$ cm s^{-1}) an electrochemical system is defined as reversible, for ranges $15 \geq \Lambda \geq 10^{-2(1+\alpha)}$ ($0.3\ v^{1/2} \geq k_0 \geq 2\ 10^{-5}\ v^{1/2}$ cm s^{-1}) as quasi-reversible and for

ranges of $\Lambda \leq 10^{-2(1+\alpha)}$ ($k_0 \leq 2\ 10^{-5}\ v^{1/2}$ cm s^{-1}) as totally irreversible [173]. The applied scan rate is an important parameter and determines the speed the potential is scanned and has an effect on the monitored CV. The higher the scan rate, the smaller is the size of the diffusion layer and higher currents are monitored (see Figure 14 (a)). The flux to the electrode is smaller at slow scan rates than at fast rates and the current is proportional to flux towards the electrode. The Randles–Sevcik equation (25) describes for electrochemically reversible electron transfer processes how the peak current I_{peak} increases linearly with the square root of the scan rate v and can be used to calculate the diffusion coefficient D [177].

$$I_{\text{peak}} = 0.4463 \cdot n \cdot F \cdot A \cdot c \cdot \left(\frac{n \cdot F \cdot v \cdot D}{R \cdot T}\right)^{\frac{1}{2}} \qquad (25)$$

If the position of the current maximum occurs at the same voltage for all scan rates, as it is nearly the case in Figure 14 (a), the electron transfer reactions are often referred to be reversible. An indication for irreversible or quasi-reversible processes is that the peak currents for reduction and oxidation shift to different potentials with scan rate.

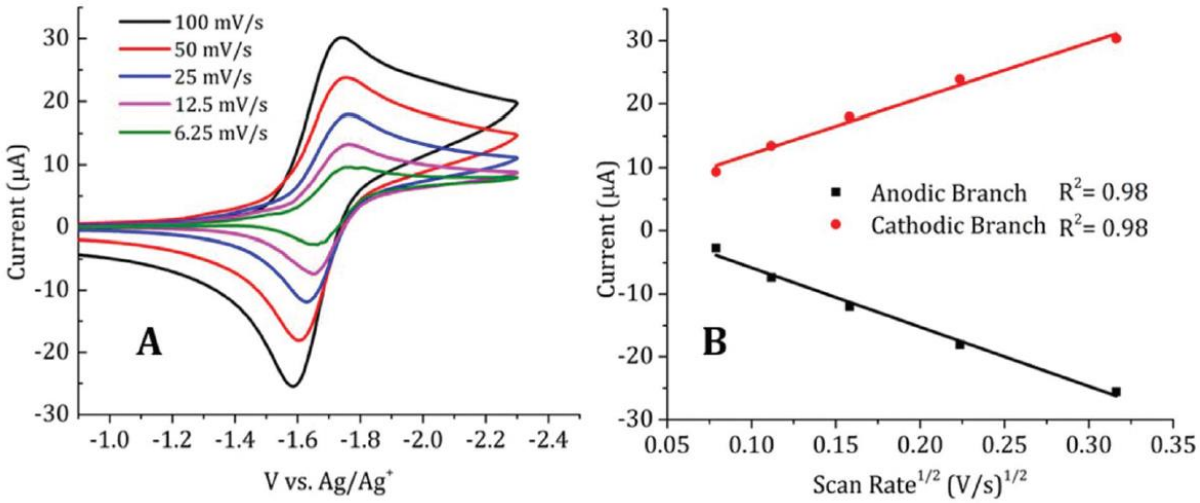

Figure 14 (a) Cyclic voltammetry of 33 mM poly(para-nitrostyrene) in 0.1 M $TBAPF_6$ at various scan rates, Pt disk working electrode (0.04 cm2) (b) Randles–Sevcik plot. Figure taken from ref. [178].

A plot of peak current versus square root of scan rate is called Randles-Sevcik plot and an example can be seen in Figure 14 (b). If the plot shows a linear curve, the diffusion coefficient can be obtained from the slope.

By using CV it is also possible to determine the double layer capacity. Therefore, CVs in a blank electrolyte are conducted which can be seen in Figure 15. The investigated region is between around 425 mV to 675 mV vs. SHE at different scan rates because in this range no Faradaic reactions occur, only the charging of the double layer of the electrode/electrolyte boundary proceeds and a rectangular voltammogram is obtained.

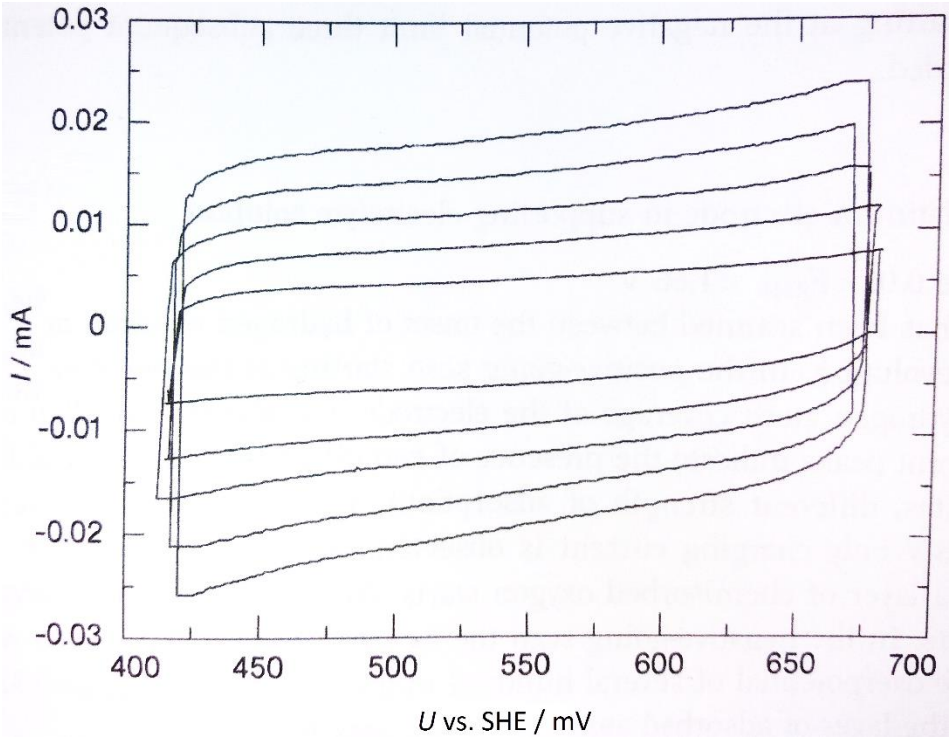

Figure 15 CVs of a platinum electrode (3 cm^2) in contact with an aqueous electrolyte solution of 0.05 M H_2SO_4 in the double-layer region, scan rate = 20 to 100 mV s^{-1}. Figure taken from ref. [175].

The currents observed at the same potential at various scan rates are obtained and a plot of these currents versus the scan rates yields a linear curve. The slope is equivalent to the double layer capacity. The behaviour of the double layer is similar to that of a plate condenser. By dividing the obtained double layer capacity by the literature value for the double layer capacity for an ideally flat surface of 20 µF cm^{-2}, the roughness factor of the electrode can be calculated [175].

The electron transfer constant k_0 for a quasi-reversible reactions can be obtained from the peak separation by using the methodology published by Nicholson [179]: from the data the peak separation is extracted and from the obtained value a dimensionless value Ψ can be determined (see ref. [179]). The rate constant can be obtained from Ψ when the peak separation is between 61 and 212 mV by the following equation [175]:

$$\Psi = \left({}^{D_{\mathrm{ox}}}/_{D_{\mathrm{red}}}\right)^{\alpha/2} \cdot k_0 \cdot \left[(R \cdot T)^{\frac{1}{2}} \cdot (n \cdot F \cdot v \cdot D_{\mathrm{ox}})^{\frac{1}{2}}\right] \quad (26)$$

3.2 Electrochemical impedance spectroscopy

Electrochemical impedance spectroscopy (EIS) is a technique where the current response is observed with an AC potential. For more than a century, EIS has been used to investigate, inter alia, corrosion processes, adsorption properties and to test the properties of batteries and fuel cells [180]. EIS is based on the fundamental property that the complex resistance *Z*, the impedance, of a parallel combination of a resistor and a capacitor is frequency dependent [176]. Because the resistance follows Ohm's law, a representation of the opposition force to electrical currents in AC circuits is the impedance, which includes phase angles not equal to zero and capacitive and inductive effects [180]. In an EIS experiment with three-electrode set-up, a sinusoidal voltage is applied. The electrode is perturbed from equilibrium and the impedance will arise from the Ohmic resistance R_{Ohm}, the double layer capacitance C_{DL}, the charge transfer resistance R_{CT} (and the Warburg element Z_{w}). The polarization of the electrode in solution can be described as the charge transfer resistance and the double layer capacitance in parallel plus an Ohmic resistance in series [176]. A Randles circuit is shown in the inset in Figure 16. The impedance for a single electrochemical reaction on a flat surface can be described by following equation [176]:

$$Z = R_{Ohm} + \frac{R_{CT}}{1 + i \cdot 2\pi \cdot f \cdot R_{CT} \cdot C_{DL}} \quad (27)$$

with frequency of the sine-wave *f* and imaginary number *i*. The real *Z*' and imaginary *Z*'' parts of the impedance are expressed by the following equations:

$$Z' = R_{Ohm} + \frac{R_{CT}}{1 + \omega^2 \cdot {R_{CT}}^2 \cdot {C_{DL}}^2} \quad (28)$$

$$Z'' = \frac{{R_{CT}}^2 \cdot C_{DL} \cdot \omega}{1 + \omega^2 \cdot {R_{CT}}^2 \cdot {C_{DL}}^2} \quad (29)$$

with angular frequency ω.

Figure 16 shows a Nyquist plot, whereas the imaginary part Z'' ($-Im(Z)$) is plotted against the real part Z' ($Re(Z)$) of the impedance.

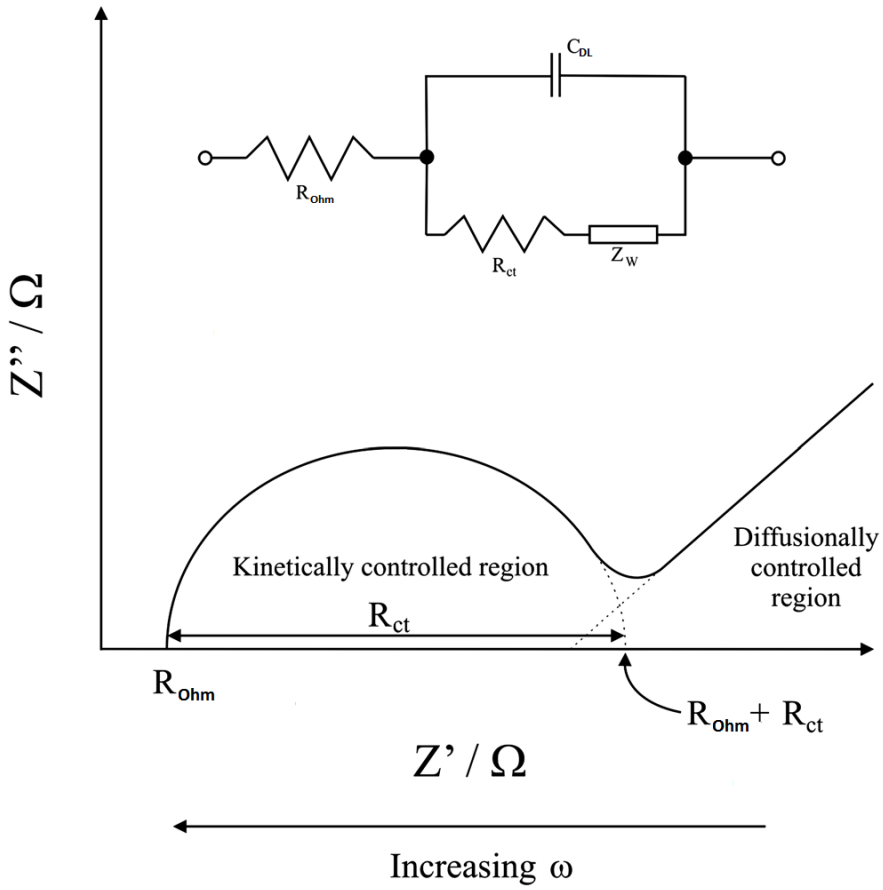

Figure 16 Nyquist plot and simple Randles equivalent circuit for an electrochemical cell. Figure taken from reference [180] and modified.

The Nyquist plot is a representation that allows to determine R_{Ohm} and R_{CT}. For high frequencies (f ~ 10^5 Hz) the quotient is zero and therefore $Z = R_{Ohm}$. The physical explanation for that is that at high frequencies C_{DL} is shorted and R_{CT} is bypassed because not enough charge is transferred to fully charge the capacitor which is therefore blocking. R_{CT} can be calculated by the width of the semicircle because at low frequencies (f ~ 1 Hz) $Z \approx R_{Ohm} + R_{CT}$. Is the measured semicircle depressed due to heterogeneity of the electrode, the C_{DL} can be replaced by a constant phase element (CPE) [176]. The chosen frequency range should meet the dynamic response of the system under investigation, usually across the range of mHz to kHz, sometimes up to MHz with an amplitude of around 5 mV to 50 mV [181].

At low frequencies Warburg contributions due to mass-transport limitations can be seen and the Warburg element Z_W reflects the diffusion of the ions in solution during an electrochemical reaction. In the Nyquist plot the Warburg impedance appears as a diagonal

line of 45° and is defined by equation:

$$|Z_W| = \sqrt{2} \cdot \sigma / \omega^{1/2} \quad (30)$$

and the Warburg coefficient σ for a reversible reaction is given by [182]:

$$\sigma = \frac{R \cdot T}{\sqrt{2} \cdot A \cdot c \cdot F^2 \cdot D^{1/2}} \quad (31)$$

A Bode plot shows frequency information whereas the logarithm to base ten of the absolute impedance and the phase angle ϕ (ϕ = $\tan^{-1}(Re(Z)/Im(Z))$ plotted against the logarithm to base ten of the frequency (see Figure 17).

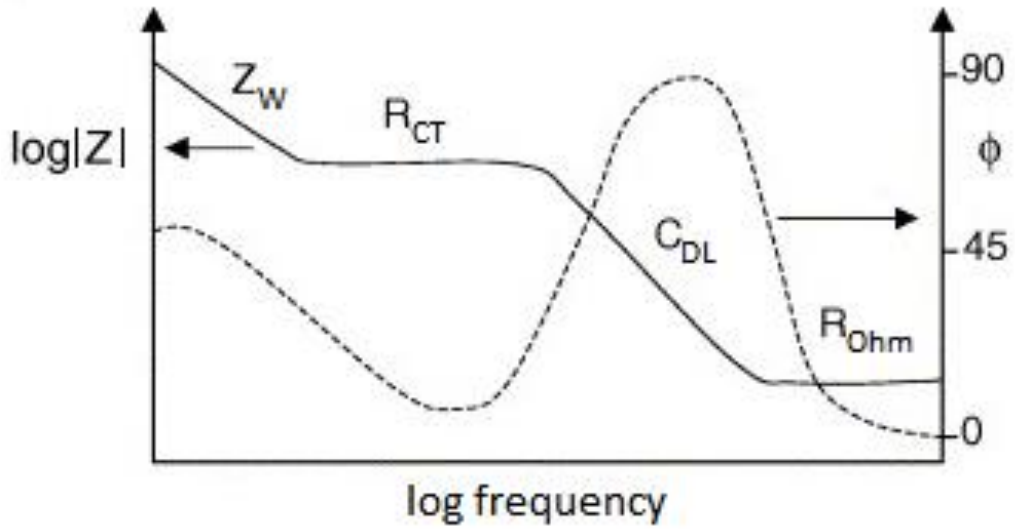

Figure 17 Bode Plot showing impedance behaviour of a simple electrochemical cell involving a single Faradaic process. Figure taken from reference [183] and modified.

The Bode plot is less intuitive because of the double-logarithmic scale but can be useful to obtain capacitive and inductive effects.

In this work values for R_{Ohm}, R_{CT} and C_{DL} are obtained by fitting experimental curves to equivalent circuits. To obtain reliable data the investigated redox species should be present in equilibrium ($c_{ox} = c_{red}$) and the resting potential U_{OCV} should be equal to U_0. Are the aforementioned criteria met, EIS is a quick, trustworthy method to determine k_0 [176].

3.3 CHRONOAMPEROMETRY

Chronoamperometry (CA) is a technique that uses sudden electrode potential steps (PSs) applied to the WE which is in contact with a solution containing the redox species under investigation to perturb the electrode potential from U_0 (or any other potential relative to a reference potential) and the flowing current-time dependence is measured. Initially the measured current is large and only limited by Ohmic resistance of the electrolyte solution and for charging the EDL.

The Butler-Volmer equation describes dependency of the current I of the applied over-potential. Equation (32) shows the Butler-Volmer equation derived by Erdey-Gruz and Volmer [15]:

$$I = I_0 \left(exp\left[\frac{\alpha_a \cdot n \cdot F}{R \cdot T} \cdot \eta \right] - exp\left[-\frac{\alpha_c \cdot n \cdot F}{R \cdot T} \cdot \eta \right] \right) \qquad (32)$$

with over-potential η, anodic/cathodic transfer coefficient $\alpha_{a/c}$ which is a measure of the symmetry of the energy barrier and diffusion coefficient for redox species $D_{ox/red}$. At high positive (negative) over-potentials the Butler-Volmer equation simplifies to equation (33) and only the anodic (cathodic) branch of equation has to be considered.

$$I = I_0 \left(exp\left[\frac{\alpha_a \cdot n \cdot F}{R \cdot T} \cdot \eta \right] \right) \text{ and } I = -I_0 \left(exp\left[-\frac{\alpha_c \cdot n \cdot F}{R \cdot T} \cdot \eta \right] \right) \qquad (33)$$

An exponential relationship between current and over-potential is obtained and the over-potential can be considered as logarithmically dependent on the current. A graph where log current density is plotted versus over-potential is known as Tafel plot (Figure 18) and from the slope the transfer coefficient $\alpha_{a/c}$ and from the intersection with the y-axis the exchange current I_0 can be obtained which directly proportional to the electron transfer constant k_0. This approximation is applicable for small currents only because at high currents transport limitation becomes dominant over charge transfer limitations [175].

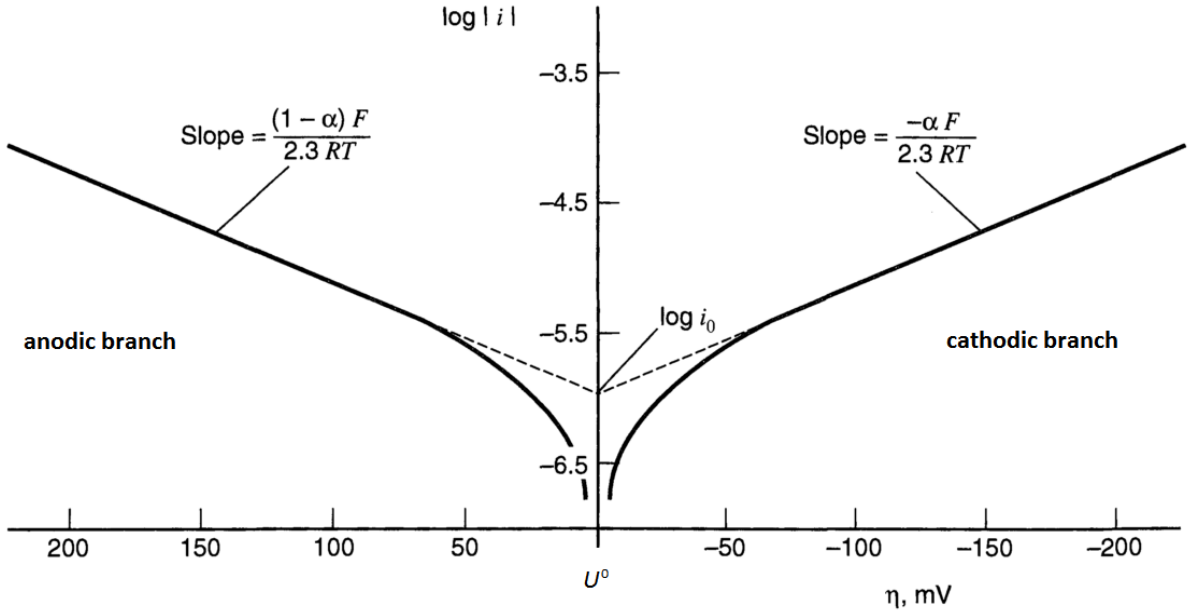

Figure 18 Tafel plots for anodic and cathodic branches of the current - over-potential curve for O + e^- ⇌ R with a = 0.5, T = 298 K, and I_0 = 10^{-6} A cm^{-2}. Figure taken from [173] and modified.

Initially of the PS the electrochemical double layer is charged but is only significant during the initial period of typically a few milliseconds. A non-Faradaic current I_{NF} contributes in the initial phase and afterwards a decreasing Faradaic current I_F can be measured as a concentration gradient develops on the electrode surface and the mass transport can be observed since the diffusion layer grows continuously with time. The time-dependence of I_F is described by the following equations (34) and (35) for short times [176]:

$$I_F = I_0 \left(exp\left[\frac{a_a \cdot n \cdot F}{R \cdot T} \cdot \eta \right] - exp\left[-\frac{a_c \cdot n \cdot F}{R \cdot T} \cdot \eta \right] \right) \cdot \left(1 - 2\lambda \sqrt{\frac{t}{\pi}} \right) \qquad (34)$$

$$\lambda = \frac{I_0}{n \cdot F} \left(\frac{1}{c_{ox} \cdot \sqrt{D_{ox}}} exp\left[\frac{a_a \cdot n \cdot F}{R \cdot T} \cdot \eta \right] + \frac{1}{c_{red} \cdot \sqrt{D_{red}}} exp\left[\frac{a_c \cdot n \cdot F}{R \cdot T} \cdot \eta \right] \right) \qquad (35)$$

An example of a PS and the resulting current response versus $t^{1/2}$ with extrapolation of the exchange current I_0 for a VO_2^+/VO^{2+} solution can be seen in Figure 19.

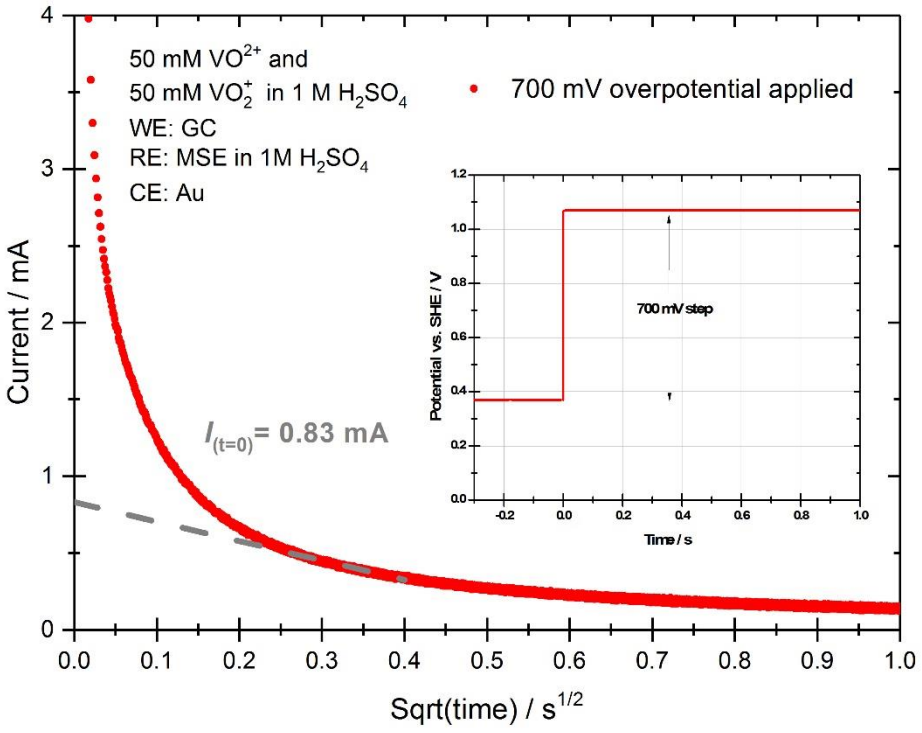

Figure 19 Chronoamperometric experiment and resulting current-(square root of)time response for +700 mV over-potential of 50 mM VO_2^+/VO^{2+} in 1 M sulphuric acid with extrapolation of I_0. The inset shows the potential step of +700 mV over-potential versus time.

The I_{NF} decays exponentially with the cell time constant R_uC_{DL}, with uncompensated resistance R_u, and the full establishment of a PS requires around 5 R_uC_{DL}, hence, a PS must last at least 10 R_uC_{DL} for sufficient quality of produced data. The cell time constant is dependent of the size of the electrode, hence, the lower limit of experimental time scale is also determined of the size of the electrode [173]. The fastest measurable redox-reactions given by Yeager and Kuta, assuming a fast potentiostat and a concentrated supporting electrolyte (around 1 M) [176], can be described by following equation [184]:

$$k_{0,\max} \leq 2.5 \cdot \left(D/\tau_{\mathrm{pot}}\right)^{1/2} \qquad (36)$$

with potentiostat response time τ_{pot}. With τ_{pot} = 50 10^{-6} s and D = 10^{-6} cm^2 s^{-1} the fastest measurable redox-reactions have a rate of $k_{0,max}$ = 0.35 cm s^{-1} [176].

The Cottrell equation (37) [185] describes the resulting current on a planar electrode following a large over-potential in a reversible redox reaction as a function of $t^{-1/2}$:

$$I = \frac{n \cdot F \cdot A \cdot c \cdot \sqrt{D}}{\sqrt{\pi \cdot t}} \qquad (37)$$

In a Cottrell-plot the measured current is plotted versus $t^{-1/2}$ to obtain the concentration, the diffusion coefficient, number of transferred electrons or the surface area from the slope.

CHAPTER 4. ANION EFFECTS ON THE REDOX KINETICS OF POSITIVE ELECTROLYTE OF THE ALL-VANADIUM REDOX FLOW BATTERY

4.1 INTRODUCTION

As described in chapter two major effort has been made to improve the VRFB system. Compared to other energy storage systems, the VRFB offers essential advantages: VRFB has a low self-discharge, long lifetime and high cycle stability [49,50]. Another advantage is that power and capacity can be scaled independently. Even with regard to safety aspects, the VRFB does not pose any major risks, as its components are not flammable and less toxic than other elements employed for redox flow batteries. In contrast to iron / chromium or zinc / bromine RFBs, the advantage of the VRFB is that by using purely vanadium ions in catholyte and anolyte, no cross-contamination of both circuits occurs by diffusion of vanadium ions through the membrane which would cause irreversible loss of capacity. One of the remaining problematic challenges is the low power density (< 0.1 W cm^{-2}) due to slow kinetics of the VO^{2+}/VO_2^+ redox reaction. The electron transfer constant k_0 of aforementioned redox reaction is 1 - 3 10^{-6} cm s^{-1} on carbon electrodes [3] which indicates that the power density is limited by the charge transfer resistance. In addition, it was shown by Gattrell *et al.* that the redox reaction is not a simple electron transfer, but indeed a combination of two chemical (de-/protonation) reactions and an electron transfer [186,187]. The sequence of these steps is not fixed but their contribution depends on the applied over-potential and other parameters. To complicate things further, a deposition of vanadium oxides on carbon electrodes from the electrolyte has been observed [2,186,188]. To increase the power density of the VRFB catalysis of the vanadium reactions is desirable. However, it was shown that in contrast to the V^{2+}/V^{3+} redox reaction, the VO^{2+}/VO_2^+ couple is not catalyzed by oxygen functional groups on carbon electrodes [2–5]. Therefore, homogeneous catalysis by replacing the commonly employed sulphate ions with phosphate ions is now investigated. In this study it is shown that transferring the system from 1 M sulphuric acid to 1 M phosphoric acid the electron transfer constant k_0 is increased. This observation is confirmed by chronoamperometry, electrochemical impedance spectroscopy as well as qualitatively by cyclic voltammetry and symmetric flow cell tests.

4.2 EXPERIMENTAL

4.2.1 ELECTROLYTE

To prepare a solution of 50 mM VO^{2+} and 50 mM VO_2^+, 25 mM vanadium pentoxide (V_2O_5) and 50 mM vanadyl sulphate ($VOSO_4$) were added to the supporting electrolyte (1 M sulphuric acid, 1 M phosphoric acid, 0.5 M sulphuric acid / 0.5 M phosphoric acid) and heated to reflux until completely dissolved. After cooling to RT (21°C) the solutions were used.

4.2.2 NUCLEAR MAGNETIC RESONANCE SPECTROSCOPY

NMR spectra were recorded at room temperature with Bruker Avance III at a frequency of 300 MHz.

4.2.3 ELECTROCHEMICAL MEASUREMENTS

CVs, EIS and CA were conducted with a Bio-Logic SP-300 in a custom-built glass cell at RT (21°C). The used cell comprised a three-electrode set-up (mercurous sulphate reference electrode (MSE in 1 M sulphuric acid, 0.674 V vs. SHE), gold counter electrode, glassy carbon working electrode (surface area A = 0.02 cm^2). For CV, CA and EIS experiments the geometric surface area was used to calculate the current density j from the current I. The concentration of the solutions was 50 mM VO^{2+} and 50 mM VO_2^+ in various electrolytes for CV, CA and EIS. Before each experiment nitrogen was passed through the solution and the working electrode was polished with 0.05 µm polishing alumina. Between each potential step the working electrode was polished again. The over-potential was applied in 50 mV steps in the range from ± 50 to ± 1000 mV. For the data analysis, the transients were fit in the time regime from 0.25 to 0.40 $s^{1/2}$ in a current versus square-root of time plot. To conduct EIS the open circuit potential (OCP) was perturbed with a 10 mV amplitude in a frequency range from 40 kHz to 100 mHz. The data were fitted with EC-Lab. Cyclic voltammetry was carried out with a scan rate of 100 mV s^{-1}.

4.2.4 RFB CELL TESTS

For flow cell tests a C Flow LAB 5x5 cell was used in conjunction with a Reglo ICC pump. GFD graphite felts (50 x 50 x 4.6 mm^3) from SGL Carbon were used as electrodes. The half-cells were separated by a Nafion N117 membrane. Before each battery test, the electrodes were heat-treated at 400°C for 12 h in laboratory atmosphere and the membrane was boiled in 1 M sulphuric acid for 30 min. Initially, both electrolyte tanks contained the same electrolyte, 50 mM VO^{2+} and 50 mM VO_2^+ in 1 M sulphuric or 1 M phosphoric acid, respectively, so that only the catholyte of a VRFB was investigated. The experiments were conducted within an acrylic box at RT and both electrolyte tanks contained 60 mL of electrolyte and were continuously purged with nitrogen. The battery was charged and discharged by the potentiostat Bio-Logic SP-300 with currents from 25 to 2000 mA. The cut off potentials were ±1.0 V.

4.3 RESULTS

4.3.1 NUCLEAR MAGNETIC RESONANCE SPECTROSCOPY

^{51}V NMR spectra were recorded to investigate the effect of the anion of the supporting electrolyte on chemical environment of the VO_2^+ ion. Vanadium is diamagnetic and susceptible for NMR in the oxidation states (-III, d^8), (-I, d^6) and (+V, d^0). Vanadium (+IV, d^1) is paramagnetic under normal conditions and cannot be observed [189]. As shown in Figure 20, the peak of VO_2^+ ion in 1 M sulphuric acid appears at -543.81 ppm and in 1 M phosphoric acid the peak is located at -556.81 ppm. When vanadium pentoxide is dissolved in a mixture of both supporting electrolytes, 0.5 M each, the peak appears between these, at - 550.56 ppm. This result indicates, that the coordinating environment of the VO_2^+ ion changes with the supporting electrolyte and the containing anions.

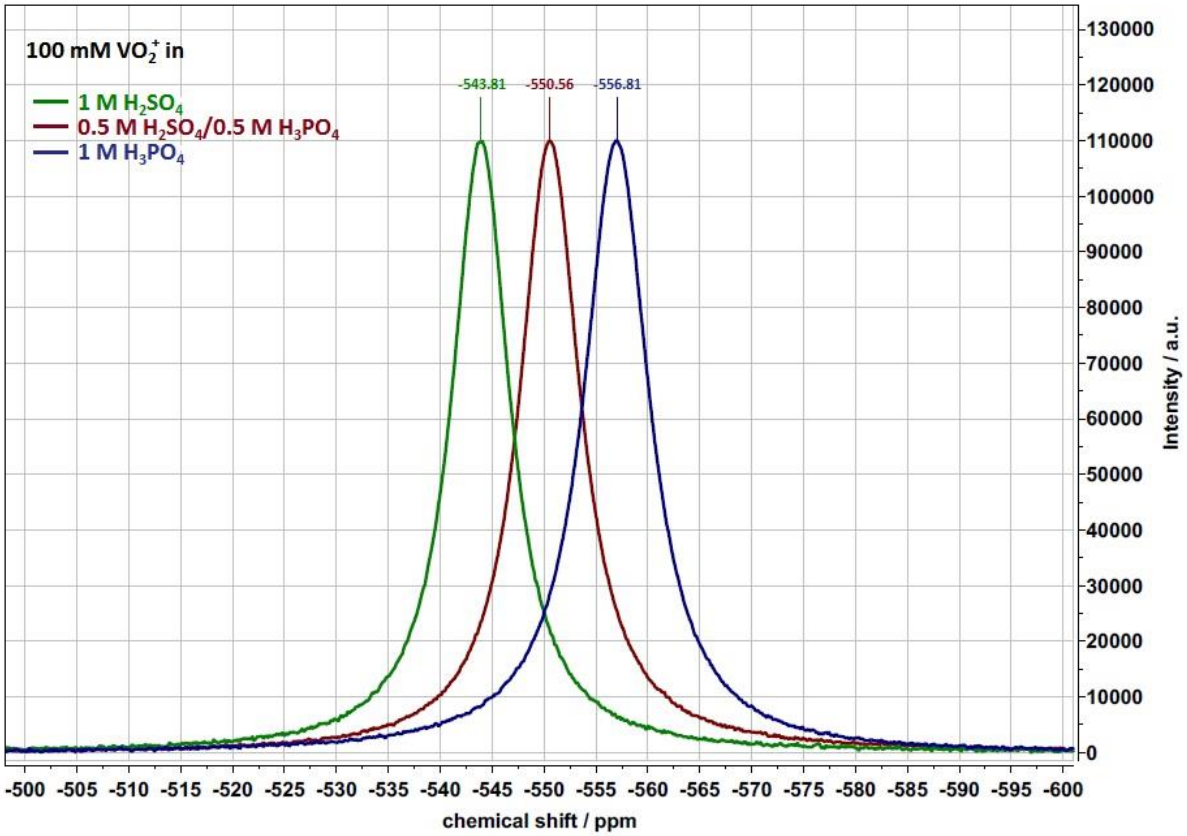

Figure 20 ^{51}V NMR spectra of 50 mM V_2O_5 dissolved in three different supporting electrolytes.

Around *pH* 1 vanadium (V) is present as the vanadyl cation VO_2^+ which has a *cis*-dioxo structure and the formation of the pseudo-octahedral species $[VO_2(H_2O)_4]^+$ is assumed [190]. In sulphuric acid and phosphoric acid the formation of sulphate/phosphate-compounds that still contain the octahedral *cis*-VO_2 is suggested. Gresser *et al*. showed that phosphate and pyrophosphate anions form anhydrides with vanadate and heteropolyvanadate ions as well as cyclic di-anhydrides can be formed [191]. The difference in chemical shift observed for the three supporting electrolytes suggests that both sulphate and phosphate anion interact with the VO_2^+ ion and that the result is a different vanadium-anion compounds in each solvent. The chemical shift is very sensitive to the chemical environment. It is assumed that in the mixed electrolyte the VO_2^+ ion undergoes a rapid anion exchange and appears as a single peak at the average chemical shift. This phenomenon occurs when ions or molecules transform quickly between two states and the total magnetization, which does not dephase notably, emerges from all ions [192].

4.3.2 Cyclic voltammetry

Figure 21 shows CVs of 50 mM VO^{2+} and 50 mM VO_2^+ in 1 M sulphuric acid (red), 1 M phosphoric acid (black) and in 0.5 M sulphuric acid / 0.5 M phosphoric acid (green). Apparent characteristic standard potentials calculated from the mean of anodic and cathodic peak potential are similar in all electrolytes, but differ greatly from the tabulated standard potential of U^{Θ} = 1.00 V vs. SHE [193] (see Table 4). This might be due to the assymetry in the electron transfer reactions.

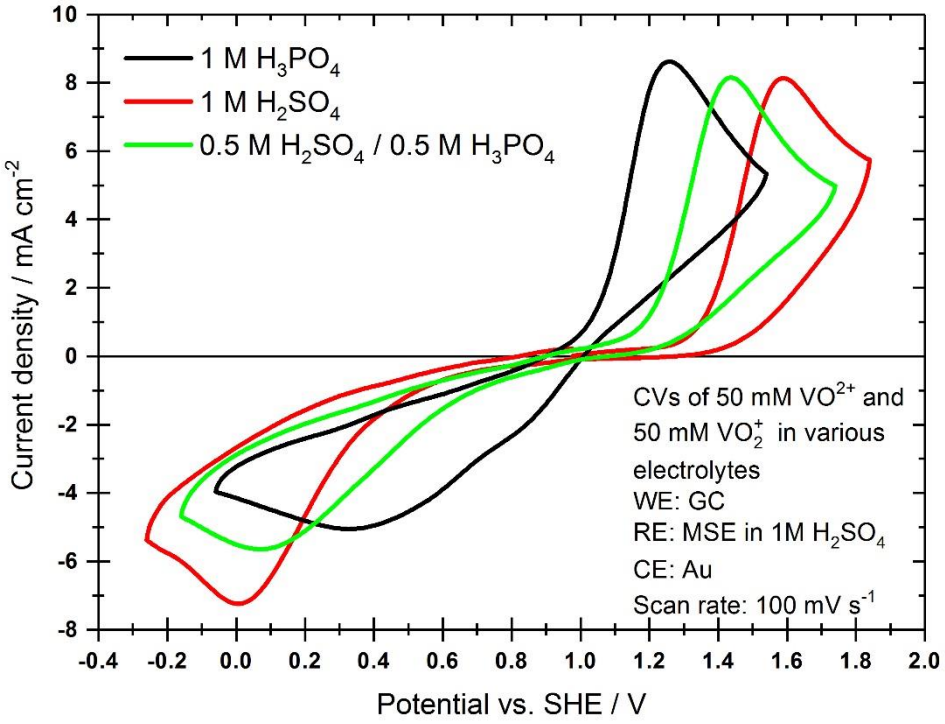

Figure 21 CVs of 50 mM VO^{2+} and 50 mM VO_2^+ in various electrolytes at a scan rate of 100 mV s^{-1}.

The anodic and cathodic peak potentials vary with electrolyte as shown in Table 4. The smallest peak separation can be found in 1 M phosphoric acid and the largest in 1 M sulphuric acid. The mixed electrolyte shows an intermediate separation. This may indicate that the kinetics of the redox reaction are faster in 1 M phosphoric acid than in the other electrolytes because on flat electrodes a smaller peak separation suggests a higher electron transfer constant [3,173].

Table 4 Parameters extracted from CVs of 50 mM VO^{2+} and 50 mM VO_2^+ in various electrolytes.

Electrolyte	apparent U^{Θ} / V vs. SHE	U_{peak}^{ox}/ V vs. SHE	U_{peak}^{red}/ V vs. SHE	Peak separation / V
1 M H_2SO_4	0.824	1.590	0.058	1.532
1 M H_3PO_4	0.793	1.257	0.328	0.929
0.5 M H_2SO_4 / 0.5 M H_3PO_4	0.752	1.437	0.067	1.370

4.3.3 Electrochemical impedance spectroscopy

EIS was recorded for all three electrolytes and Nyquist plots and one representative Bode plot are shown in Figure 22.

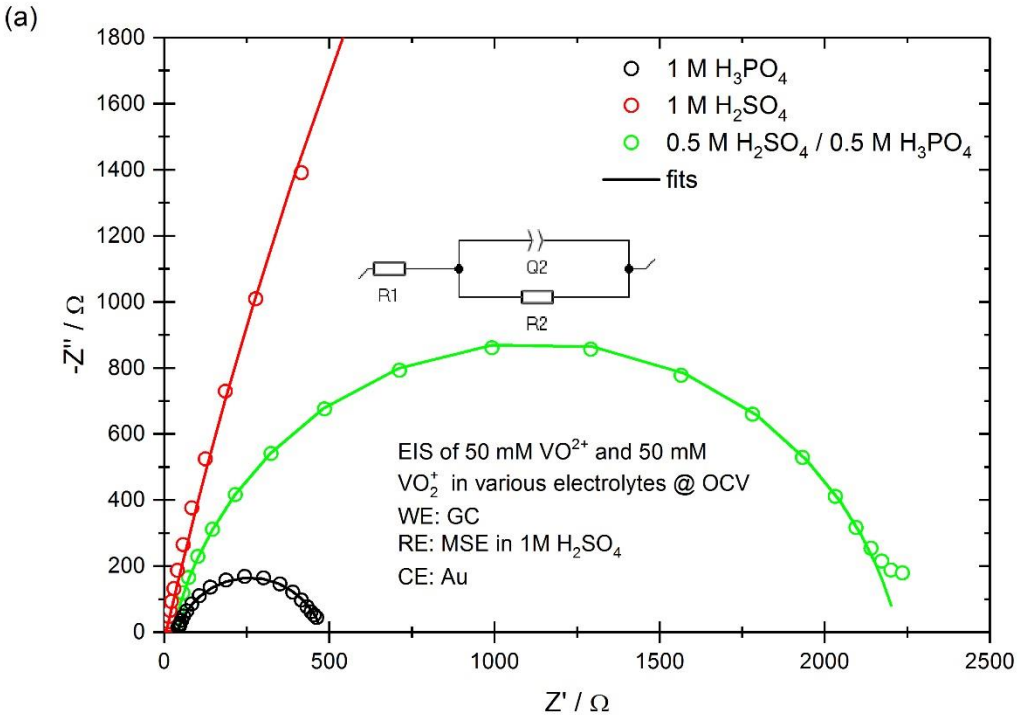

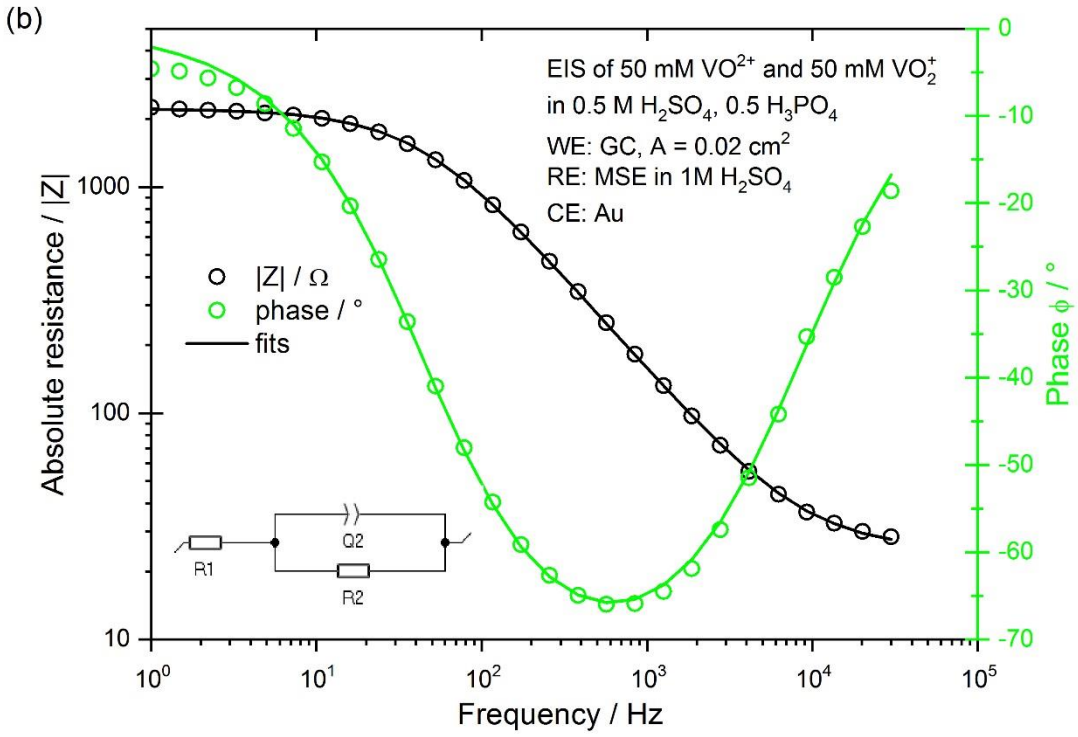

Figure 22 (a) Nyquist plot of 50 mM VO^{2+} and 50 mM VO_2^+ in various electrolytes. For clarity, only the data points recorded at high frequencies are shown for the spectrum in 1 M H_2SO_4. (b) Bode plot of 50 mM VO^{2+} and 50 mM VO_2^+ in 0.5 M H_2SO_4 / 0.5 M H_3PO_4. The recorded data points were fitted to the Randles circuit shown as inset.

By fitting the experimental spectra to the Randles circuit the parameters listed in Table 5 are obtained. The double layer capacitance C_{DL} is calculated from the constant phase element Q by the formula given by Hirschhorn *et al.* for a surface distribution [194]:

$$C_{\mathrm{DL}} = Q^{1/\alpha}\left(\left(R_{\mathrm{Ohm}} \cdot R_{\mathrm{CT}}\right) \Big/ \left(R_{\mathrm{Ohm}} + R_{\mathrm{CT}}\right)\right)^{(1-a)/a} \qquad (38)$$

with constant phase element parameter α. The electron transfer constant k_0 is given by rearranging equation (8).

As shown in Table 5, R_{CT} is 67 times higher in the sulphuric than in the phosphoric acid system. In the mixed acid electrolyte R_{CT} is 13 higher than in phosphoric acid and five times lower than in sulphuric acid. The calculated capacitances are similar for all electrolytes.

Table 5 Fitted parameters of EIS of 50 mM VO^{2+} and 50 mM VO_2^+ in various electrolytes.

	1 M H_3PO_4	**1 M H_2SO_4**	**0.5 M H_2SO_4 / 0.5 M H_3PO_4**
R_{Ohm} / Ω m^2	7.84 10^{-5}	1.21 10^{-5}	5.03 10^{-5}
R_{CT} / Ω m^2	8.81 10^{-4}	0.06	4.42 10^{-3}
α	0.824	0.856	0.858
Q / $Fs^{(\alpha-1)}$	5.74 10^{-6}	3.58 10^{-6}	3.61 10^{-6}
C_{DL} / F	4.36 10^{-7}	4.32 10^{-7}	4.57 10^{-7}
j_0 / A m^{-2}	29.34	0.44	5.87
k_0 / cm s^{-1}	6.09 10^{-4}	9.15 10^{-6}	1.21 10^{-4}

4.3.4 Symmetric flow cell - charge discharge tests

Charge and discharge experiments in a symmetric cell with 50 mM VO^{2+} and 50 mM VO_2^+ in 1 M sulphuric acid and 1 M phosphoric acid in both tanks were conducted with various currents to compare the over-voltages and determine the charge transfer constant k_0.

Figure 23 shows the charge/discharge curves for both systems. Due to high over-voltages, currents of 1000 and 2000 mA could not be applied on the sulphuric acid system.

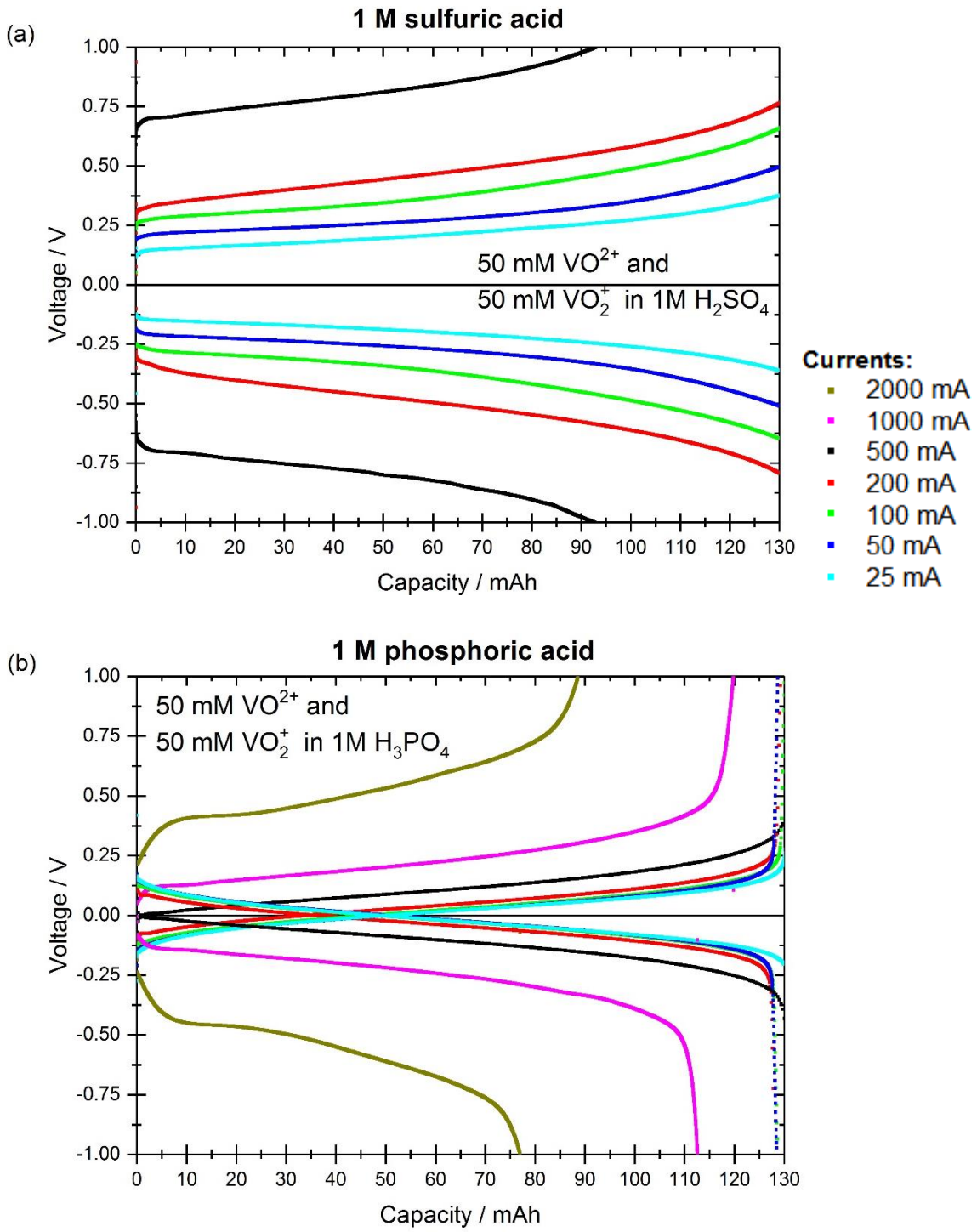

Figure 23 Charge/discharge test with SGL-GFD 4.6 electrode, Nafion N117 membrane and 60 mL 50 mM VO^{2+} and 50 mM VO_2^+ in (a) 1 M H_2SO_4 and (b) 1 M H_3PO_4.

At a SOC of 50%, when half of the full capacity for the respective cycle was reached, the voltage was determined for each applied current. The full capacity is determined as the capacity that is present at that point where the slope of the curve significantly changes. Figure 24 shows a pseudo Tafel plot and the exchange current density j_0 corresponds to the

intersection with the ordinate.

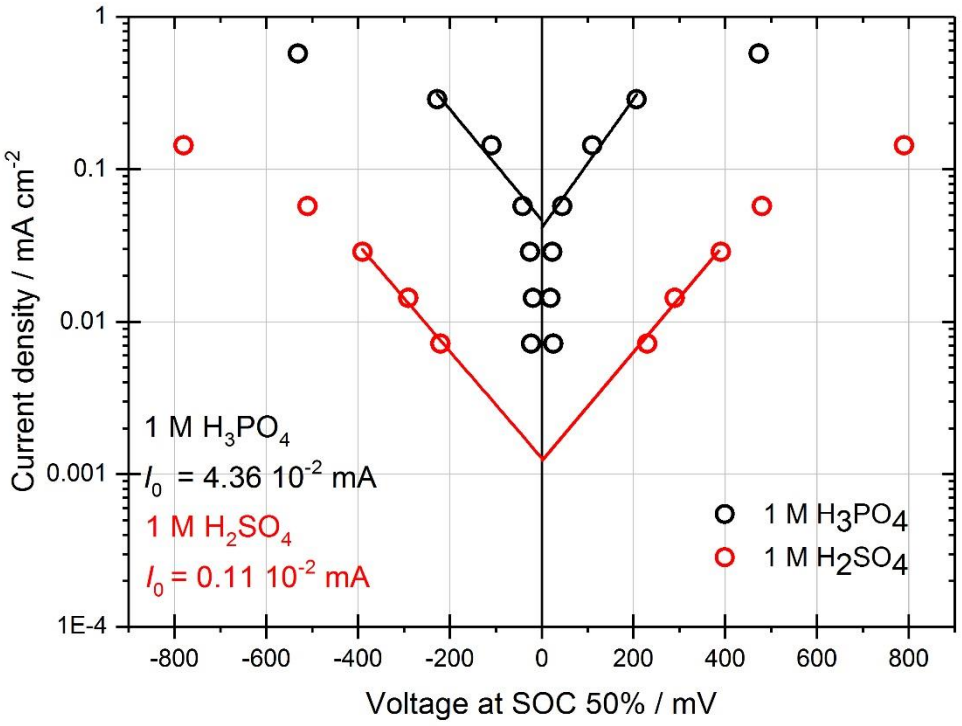

Figure 24 Pseudo Tafel plot obtained from evaluating the charge-discharge curves in Figure 23. The current density is calculated from the currents with surface area A^{DL} from the evaluation of the double layer capacitance C_{DL}.

In order to transform I_0 to k_0 the surface area has to be known. The Brunauer–Emmett–Teller (BET) surface area A^{BET} of the GFD electrodes per gram is given as 0.44 $m^2\ g^{-1}$ for untreated felts [195]. With the weight of the electrode m = (1.083 ± 0.015) g, A^{BET} = (4760 ± 66) cm^2. The value for the specific capacitance for graphite felts is a combination of the specific capacitance of the basal plane (bp) C_{DL}^{bp} = 3.2 10^{-6} F cm^{-2} and that of the edge plane (ep) c_{DL}^{ep} = 47.8 10^{-6} F cm^{-2} [196]. With heat treatment the proportion of edge planes increases [197,198]. Assuming that the electrode felts consist mostly of basal plane (94%) with a small contribution from the edge plane (6%) [196], the specific capacitance should be CDL = 0.94 C_{DL}^{bp} + 0.06 C_{DL}^{ep} = 5.9 10^{-6} F cm^{-2}. With the capacitance of the electrodes determined by EIS to be C_{DL} = 0.02055 F, the surface area of the electrode A^{DL} = 3483 cm^2. Using A^{DL} the exchange current density j_0 and thereby k_0 can be calculated from the I_0 values shown in Figure 24. In the symmetric cell, k_0 is 38 times larger in phosphoric acid

(k_0 = 9.05 10^{-5} cm s^{-1}) than in sulphuric acid (k_0 = 2.38 10^{-6} cm s^{-1}). In a full cell experiment as performed here, the R_{CT} is only part of the total resistance that leads to an over-voltage. Besides the kinetic activation represented by R_{CT} also the membrane resistance R_{mem}, the diffusion resistance R_{diff} contribute to and limit k_0.

4.3.5 CHRONOAMPEROMETRY

Figure 25 (a) shows exemplary CA experiments ±200 mV over-potential in 1 M sulphuric acid and 1 M phosphoric acid (see also Figure 19).

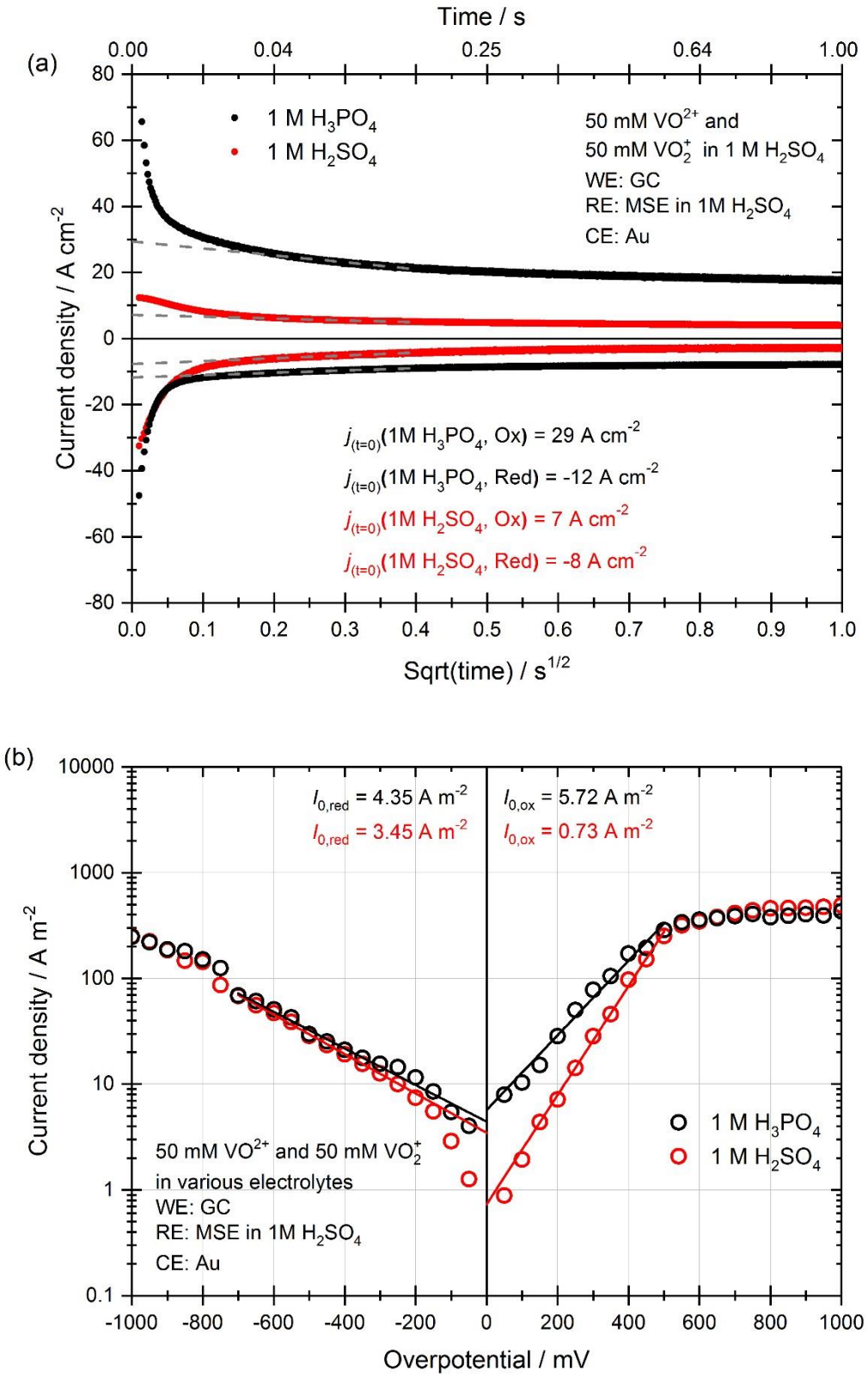

Figure 25 (a) Exemplary potentiostatic pulse experiments for 50 mM VO^{2+} and 50 mM VO_2^+ in 1 M sulphuric (red) and 1 M phosphoric acid (black). The applied potential pulse was ±200 mV. (b) Extrapolated faradaic current densities at $t \rightarrow 0$ s over the potential they were recorded at.

The current density response was plotted versus the square-root of time to extrapolate the Faradaic current at $t \rightarrow 0$. Current densities were j ($t \rightarrow 0$) determined for all over-potentials η from ±50 to ±1000 mV and are given in Figure 25 (b). The Tafel plot shows that the cathodic area the data points for both curves are almost identical regarding position and slope. Only at small over-potentials $|\eta| < 200$ mV, the extrapolated currents are significantly higher in 1 M phosphoric acid than in 1 M sulphuric acid. Hence, for a linear fit to η = 0 the resulting apparent cathodic exchange currents $I_{0,\mathrm{red}}$ are similar. The shape of the reduction branch for both electrolytes is consistent with the investigations of Gattrell *et al.* [187] who found a very low transfer coefficient of $\alpha_{\mathrm{cathodic}} = 0.15$. In Figure 25 (b) the cathodic transfer coefficients are $\alpha_{\mathrm{cathodic}}^{\mathrm{H_3PO_4}} \approx \alpha_{\mathrm{cathodic}}^{\mathrm{H_2SO_4}} = 0.11$ for η >200 mV and $\alpha_{\mathrm{cathodic}}^{\mathrm{H_2SO_4}} = 0.38$ for $\eta < 200$ mV. In the anodic area both curves differ in slope and magnitude for over-potentials $\eta < 500$ mV. In that region the current values measured in 1 M phosphoric acid are significantly higher than in 1 M sulphuric acid, and the transfer coefficients are $\alpha_{\mathrm{anodic}}^{\mathrm{H_2SO_4}}$= 0.31 and $\alpha_{\mathrm{anodic}}^{\mathrm{H_3PO_4}} = 0.21$. In the region η > 500 mV both curves exhibit a plateau on which the currents are the same for both electrolyte systems. Looking at the data points before the plateau and extrapolating back to zero over-potential the apparent anodic exchange current $I_{0,\mathrm{ox}}$ in the phosphoric acid system is about eight times higher than in the sulphuric acid system.

4.4 Discussion

CVs, EIS, CA and full cell tests on the VO^{2+}/VO_2^{+} redox couple in 1 M sulphuric acid, 1 M phosphoric acid and in a mixed electrolyte were conducted. All investigations indicate that electron transfer constant k_0 in the presence of PO_4^{3-} anions is higher than with SO_4^{2-} anions. A comparison of the results is shown in Table 6.

Table 6 Summary of all results obtained by CA, EIS and charge/discharge experiments.

	Determined from anodic branch CA	Determined from EIS at OCP	Determined from sym. flow cell
Electrolyte	k_0 / cm s^{-1}	k_0^{OCP}/ cm s^{-1}	k_0^{apparent}/ cm s^{-1}
1 M H_2SO_4	1.52 10^{-5}	9.15 10^{-6}	2.38 10^{-6}
1 M H_3PO_4	1.19 10^{-4}	6.09 10^{-4}	9.05 10^{-5}
0.5 M H_2SO_4 / 0.5 M H_3PO_4	----	1.21 10^{-4}	----

However, while there is an agreement in the fact that the reaction is faster in phosphoric acid, the determined acceleration compared to sulphuric acid varies greatly. EIS was measured at OCP at small over-potentials (amplitude 10 mV). At OCP k_0^{OCP} is 67 times larger in phosphoric acid than it is in sulphuric acid. The Tafel plot obtained from CA, Figure 25 (b), also shows a difference for the j ($t \rightarrow 0$) values in phosphoric acid and sulphuric acid for over-potentials -200 mV < η < 500 mV, with the largest difference around OCP. A suggestion is that there are two over-potential dependent reaction regimes, in the anodic as well as in the cathodic branch. For over-potentials -200 mV < η < 500 mV the data points indicate the reaction is faster in phosphoric acid than in sulphuric acid, for over-potentials outside of that region, $\eta <$ -200 mV and $\eta >$ 500 mV, the determined current values for the two systems coincide because in this region diffusional effects dominate and the diffusion-limited current in the order of 20 to 40 mA cm^{-2} is visible. Gattrell *et al.* have stated that both the oxidation and the reduction of VO^{2+}/VO_2^+ proceed via two chemical reactions (C) coupled to an electron transfer (E) [186,187]. The chemical reactions are proton transfer reactions. The set of equations proposed by Gattrell *et al*. [186,187] is presented in Figure 26. They have found that for both oxidation and reduction three possible reaction pathways exist and that they all contribute to the current, but that their contribution varies with over-potential. For the oxidation they found that the main contributors are the sequences electron transfer E-C-C (oxidation 1, red line) and C-E-C (oxidation 2, green line) [187]. Interestingly, the modelled C-E-C reaction is characterized by a plateau for $\eta >$ 150 mV. Looking at the data, it can be proposed that in the initial over-potential region (0 mV < η < 500 mV) Oxidation 1 (E-C-C) dominates which is then replaced by Oxidation 2 (C-E-C) mechanism at η > 500 mV as major

contributor. This change in reaction pathway can be concluded because at η > 500 mV the current in both electrolytes exhibits a plateau as modelled for the C-E-C mechanism described in [187]. Also the fact that at η > 500 mV the measured current densities are similar, whereas before that over-potential the current density in 1 M H_3PO_4 was larger, suggests that a new rate-limiting step (with the same rate in both electrolytes) determines the rate of electron transfer. This interpretation would suggest that the rate of the E-step is faster in phosphoric acid than in sulphuric acid, therefore enabling higher currents in the former system than in the latter when the E-step is the first reaction, but that the first C-step in the CEC reaction at high over-potentials is similar in both systems and rate-limiting.

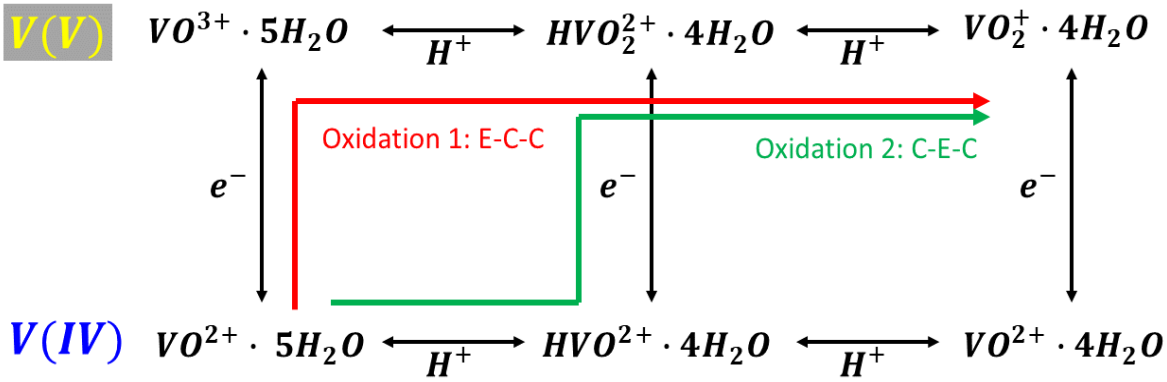

Figure 26 Possible reaction pathways for the VO^{2+}/VO_2^+ redox reaction according to [187]. The measured data suggests, that for the oxidation the reaction follows Oxidation 1 (red) at low over-potentials and Oxidation 2 (green) at high over-potentials. In the latter pathway the electron transfer step (E) is preceded by a proton exchange step (C) which appears to be rate limiting.

For the reduction of VO_2^+ Gattrell *et al*. assumed that the electron transfer takes place through a layer of adsorbed intermediates at high over-potential [186]. This was hypothesized on the basis of a low apparent transfer coefficient, like the one which was observed ($\alpha_{\text{cathodic}}^{H_3PO_4} \approx \alpha_{\text{cathodic}}^{H_2SO_4} = 0.11$, see Figure 25 (b)). Using the Marcus theory, the transfer coefficient and its applied potential dependence can be predicted. For low over-potentials and if no species is adsorbed on the electrode, the α value should be close to 0.5 [249]. In the case the α value is notably lower than 0.5 it may correspond to a concerted process or to a stepwise process which involves a slow electron transfer [250]. The presence of reaction intermediates was also postulated to explain EIS [2] and X-ray absorption fine structure [188] experiments. It therefore can be assumed that the electron transfer through this layer of adsorbed species is independent of electrolyte and limits the rate at high cathodic over-

potentials ($\eta < -200$ mV). As a consequence, the E-C-C reduction mechanism determines the rate only at the smallest over-potentials such 0 mV < η < -200 mV in CA.

The effects of phosphate additives on the stability of the positive electrolyte has been investigated by Ding *et al.* [199]*.* They showed that adding small amounts of phosphate, $c(NH_4H_2PO_4) \leq 0.2$ M, to the electrolyte (1.6 M VO_2^+ / 3 M H_2SO_4 solution at temperature of 50°C) improves the thermal stability and delays the precipitation time of VO_2^+. A charging and discharging test (1.6 M V^{3+}/VO^{2+} in 3.0 M H_2SO_4) has been conducted and has shown improved performance regarding long-term stability and energy efficiency (83%, 300 cycles) with 0.2 M $NH_4H_2PO_4$ additive [199]. The results also indicate that the introduction of phosphate reduces the over-potential within the cell, however, no quantitative values were obtained. Earlier heating/cooling studies from Zhang *et al.* showed that adding 3wt% Na_3PO_4 notably improves the thermal stability (-5 to 40°C) of 2 M V(III), V(IV) and V(V) in 5 M sulphate solution [109]. The time without precipitation at the aforementioned temperature range has been extended in case of all three investigated vanadium species by many days. In the experiments, it was observed that after a few days a precipitation occurs in the phosphoric acid solution which is re-dissolvable by heating to 70°C for 30 min.

4.5 Conclusion

As other researchers before, it can be concluded that the VO^{2+}/VO_2^+ redox reaction is an intricate combination of electron transfer and chemical reactions [2,186–188]. Previous experiments have clearly shown that the reaction is not catalysed by oxygen functional groups on the surface of carbon electrodes [2–4] which is in agreement with other research groups [58,200–203]. In this publication it was able to show that the electron transfer reaction part of the VO^{2+}/VO_2^+ redox reaction can be considerably accelerated when 1 M phosphoric acid is used as supporting electrolyte instead of 1 M sulphuric acid. However, it was also shown that the change in supporting electrolyte only accelerates the electron transfer part of the reaction. The coupled chemical reactions that limit the rate at high anodic over-potentials, or the electron transfer through a layer of reaction intermediates at cathodic over-potentials which seems to slow down the reaction, is independent of the employed anion. Nevertheless, in a laboratory scale flow cell that employed dilute vanadium electrolyte (100 mM vanadium), it was able to show that the over-voltages can be

significantly lower in phosphoric acid than compared to sulphuric acid. Considering that commercial VRFB electrolyte contains phosphoric acid as a stabilising agent, it can be worthwhile to explore the ideal ratio of H_2SO_4/H_3PO_4 in terms of kinetics and stability for technical and commercial systems.

CHAPTER 5. ASYMMETRIC POLYOXOMETALATE ELECTROLYTES FOR ADVANCED REDOX FLOW BATTERIES

5.1 INTRODUCTION

By now the champion and best explored RFB of the dissolved metal chemistries is the VRFB with its prodigious advantages described previously [39,55,67,204]. The main drawbacks of the VRFB are the sluggish kinetics of the V^{2+}/V^{3+} and the VO^{2+}/VO_2^{+}redox reactions which limit the current density and therefore the power density [3]. As shown in the previous chapter the electron transfer constant k_0 for the vanadium reactions are in the order of $k_0 = 10^{-6}$ cm s^{-1} and homogeneous and heterogeneous catalysis of the half-cell reactions could improve the system only slightly [6,205]. Other groups have shown that the positive effects on the V^{2+}/V^{3+} half-cell are not permanent because the low potential at which it is operated reduces the oxygen groups, thereby eliminating their catalytic effect [57,58]. Nevertheless, the VRFB uses the mature RFB chemistry, with large demonstration projects and commercial energy storage power stations built globally; for example the 200 MW/800 MW h power station in Dalian, China, for which the construction contract was signed in October 2016 [145]. Organic redox couples can be low cost and made from abundant elements, and they offer greater variability than metal ion redox couples due to their tuneable structure [7]. A great number of organic redox couples have been presented in recent years, with the capital cost of metal ion RFB chemistries being the main driver for their development [7,47,162,206]. As most studies have been restricted to laboratory cell operation, insights into scale-up with larger cell areas, bigger electrolyte volumes and long-term cycling are currently not available [7]. Another type of redox electrochemistry that can be employed in RFBs uses polyoxometalates. POMs form a class of discrete transition metal-oxide nanoclusters with promising properties and are described in the following sections.

5.2 POLYOXOMETALATES

Polyoxometalates are discrete early transition metal-oxide cluster anions, containing mostly vanadium, molybdenum and tungsten [207], and form a class of inorganic complexes of unmatched versatility and structural variation in symmetry and size with a length scale from 1 – 5 nm [208,209]. The first POM was the heteropolyacid $H_3[PW_{12}O_{40}] \cdot 6H_2O$ reported by Keggin in 1933, the archetype of the Keggin-ions [8,210]. POMs are clusters with unique structural

characteristics and diversity of electronic structures and many compounds were synthesised with Keggin, Wells-Dawson, Preyssler, and Lindquist type (see Figure 27). They are known in versatile applications such as catalysis, medicine, material science and can act as ligands to coordinate various transition metal ions because of their high electronic density [211].

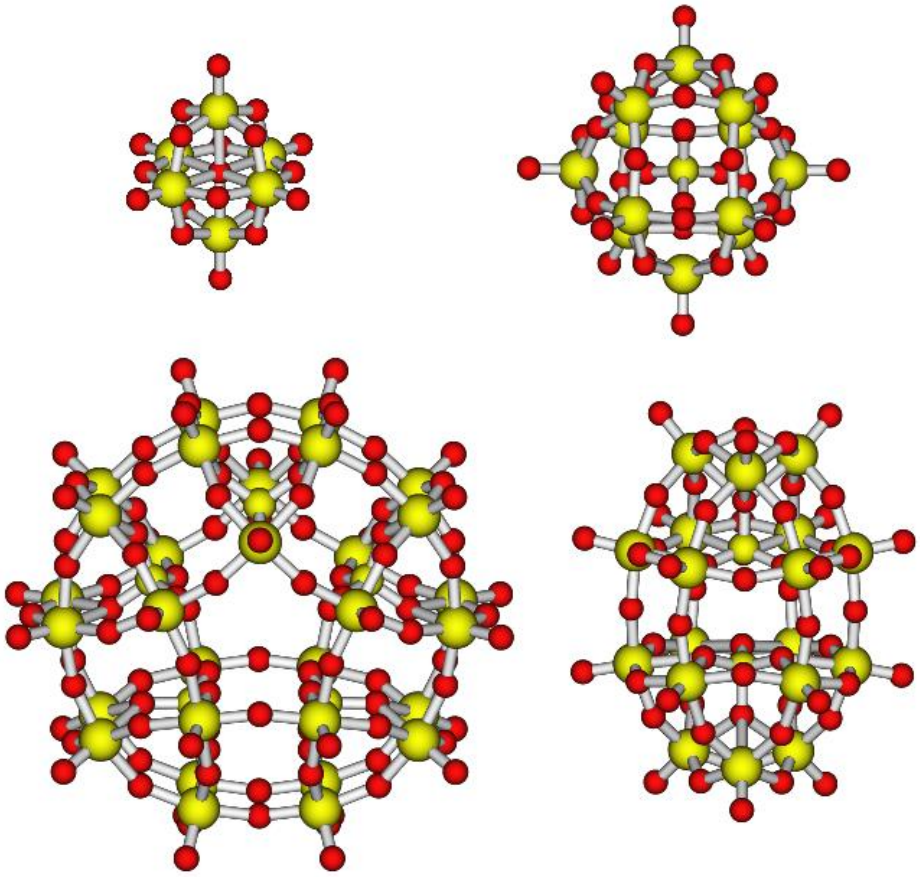

Figure 27 Molecular structures of polyoxometalate types (clockwise, from the upper left corner: Lindqvist, α-Keggin, α-Wells–Dawson, and Preyssler type; oxygen in red, other atoms in yellow). Figure taken from ref. [212].

The structure of the POMs can be described as linked MO_n polyhedra (with n = 4 – 6) that form two principal groups: the first group contains silicates or oxoanions of neighbouring main-group elements (B, Si, Ge, P, As, Sb, S, Se, Te, I) which form polymeric structures based on linked MO_4 tetrahedra; the second group is mainly characterized by MO_6 octahedra with short, terminal M=O bonds. Due to their low surface charge density extensive solution chemistry in aqueous and non-aqueous media is accessible because on the surface of the POM anions terminal (M=O) and bridging (M-O-M) oxygen are present whereas the bridging oxygen atoms are carriers of a greater negative charge and are often protonated. During the synthesis the POM forms itself commonly by self-assembly, although the exact mechanism is not fully understood [176].

POMs as new chemistry are promising candidates for RFBs as replacement for vanadium in the VRFB because as described in previous chapters the vanadium chemistry is limited. POMs offer the following properties:

1. Electrons added to POMs by reduction are often delocalised over several metal atoms [213] and this will facilitate fast electron transfer which enables high current densities [214]. Additionally, their hydrodynamic radius is quite large (some Ångströms) and the total solvent reorganization energy of POMs is small which predicts facile electron transfer according to Marcus theory [251];
2. POMs are anions and are bigger than solvated transition metals [215,216]. Therefore, POMs should not permeate through cation exchange membranes typically employed in RFBs;
3. Electron transfer by POMs is often coupled to cation or proton transfer [128]. Therefore, the net charge of the polyoxoanions does not change upon oxidation or reduction. This concept, often found in biological systems, avoids highly charged species and results in increased stability [217];
4. Some POMs are highly soluble, with the maximum concentration determined by the kind of POM, the electrolyte and also the present counterions [218]. Coupled with multi-electron transfers per molecule this can lead to high energy densities [133].

Other studies on POMs as the RFB electrolyte focused on symmetric chemistries, cells in which the same molecule was used as anolyte and catholyte [126,133,219]. A tri-vanadium substituted Keggin ion ($[SiV_3W^{VI}_9O_{40}]^{7-}$) has been tested in aqueous and non-aqueous solvents [126]. This system was only demonstrated for a small capacity (4 mAh) at a low POM concentration (20 mM) [126]. Much higher concentrations of 0.8 M were reached for an RFB employing $H_6[CoW_{12}O_{40}]$ as anolyte and catholyte [133]. While $H_6[CoW_{12}O_{40}]$ was well suited as the anolyte (the tungsten-ions transfer four electrons at an average potential of -0.1 V vs. SHE) the cobalt heteroatom transfers only one electron at 1.1 V vs. SHE. Therefore, to balance the charges in the two tanks the catholyte volume had to be four times larger than the anolyte volume. A capacity of 13.4 Ah L^{-1} was demonstrated for the anolyte, while the catholyte exhibited only 3.3 Ah L^{-1} [133]. Another symmetric POM RFB was presented by VanGelder *et al.* who employed a series of Lindqvist polyoxovanadate-alkoxide clusters as electroactive species in acetonitrile [219].

Because it is difficult to prepare a substituted POM that transfers more than three electrons at potentials suitable for a catholyte, an asymmetric POM chemistry for RFBs is proposed. In POMs, a trend was observed that with increasing electronegativity χ of the polyatom the redox potential decreases [220], and tungsten ($\chi = 2.36$) is the most electronegative metal that can be used as polyatom in POMs, and so $[SiW_{12}O_{40}]^{4-}$ (**SiW_{12}**) was used as anolyte. A ball-and-stick representation of the anion is shown in Figure 32 (b). Because of the low electronegativity of vanadium ($\chi = 1.63$), a polyoxovanadate anion was chosen as catholyte species: $[PV_{14}O_{42}]^{9-}$ (**PV_{14}**), shown in Figure 35 (b) [221]. The POMs have a similar structure (Keggin structure), with the difference that **PV_{14}** has two additional metal-oxygen caps. The following sections show the investigations of both electrolytes in detail and the flow battery studies of the new **PV_{14}**-**SiW_{12}**-System.

5.3 Materials and Methods

Tungstosilicic acid hydrate $H_4[SiW_{12}O_{40}] \cdot xH_2O$ and all other reagents and solvents were purchased from Sigma Aldrich and used without further purification.

5.3.1 Synthesis of PV_{14}

The hydrated sodium salt of $[PV_{14}O_{42}]^{9-}$ (**PV_{14}**), $Na_{4.75}H_{4.25}[PV_{14}O_{42}] \cdot NaCl \cdot 12H_2O$ was obtained by a modification of the preparation method by Selling *et al*. [222]. A suspension of $NaV0_3$ (14 eq.) in water was boiled to dissolve the salt. After cooling to RT (23°C) concentrated (85%) phosphoric acid (4 eq.) was added slowly to the metavanadate solution and the *pH* of the solution was adjusted to 2.3 with aqueous HCl. After stirring for three days, the *pH* was readjusted to 2.3 and after additional two day the *pH* was adjusted again. NaCl was added to obtain a total concentration of 3 M NaCl. The solution was cooled to 4°C for three days and crystals of **PV_{14}** were obtained by filtration. The product (dark-red powder) was dried under vacuum and the yield was 95% (on vanadium). The identity of **PV_{14}** was confirmed by dissolving the product in water and taking a ^{51}V NMR spectrum that showed the three distinct peaks of **PV_{14}** (^{51}V NMR, δ = -530.8, -585.1, -596.0 ppm and Figure 38 (a)).

Selling *et al*. measured the numbers of protons attached to **PV_{14}** anions in solution by ^{31}P and ^{51}V NMR.[222] They found that there are multiple $[H_xPV_{14}O_{42}]^{(9-x)-}$ species with x = 1 - 6 in a *pH* range from 1.5 < *pH* 6.5. The lower the *pH*, the higher the number of protons per **PV_{14}** polyoxoanion. As each of the species has its own pK_a value, it is assumed that **PV_{14}** can act as buffer. Therefore, a titration curve was measured during the formation of **PV_{14}** from $NaVO_3$ as shown in Figure 28. Initially, 300 g $NaVO_3$ were dissolved in 1 L of ultra-pure type 1 water (ELGA Option- Q) with 70 mL conc. phosphoric acid added dropwise. Then the *pH* was measured (Mettler Toledo, Lab 850 benchtop *pH* meter) while adding concentrated hydrochloric acid. The protons taken up per **PV_{14}** polyoxoanion *p* were calculated by subtracting the "free protons" H^+_{free} from the added protons H^+_{added}:

$$H^+_{\mathrm{added}} = c_{\mathrm{HCl}} \cdot V \quad (39)$$

$$H^+_{\mathrm{free}} = 10^{-pH} * (V + 1.07\ \mathrm{L}) \quad (40)$$

$$p = (H^+_{\mathrm{added}} - H^+_{\mathrm{free}}) \,/\, n_{\mathrm{PV_{14}}} \quad (41)$$

With concentration of concentrated HCl c_{HCl} = 12.1 M, volume of added aqueous HCl *V*, amount of **PV_{14}** $n_{\mathrm{PV_{14}}} = 0.176$ mol.

Figure 28 shows that the *pH* of the solution drops from *pH* 5.8 to *pH* 2.0 upon addition of 101 mL of concentrated HCl. The number of protons per **PV_{14}** rises linearly from 0 to 7.

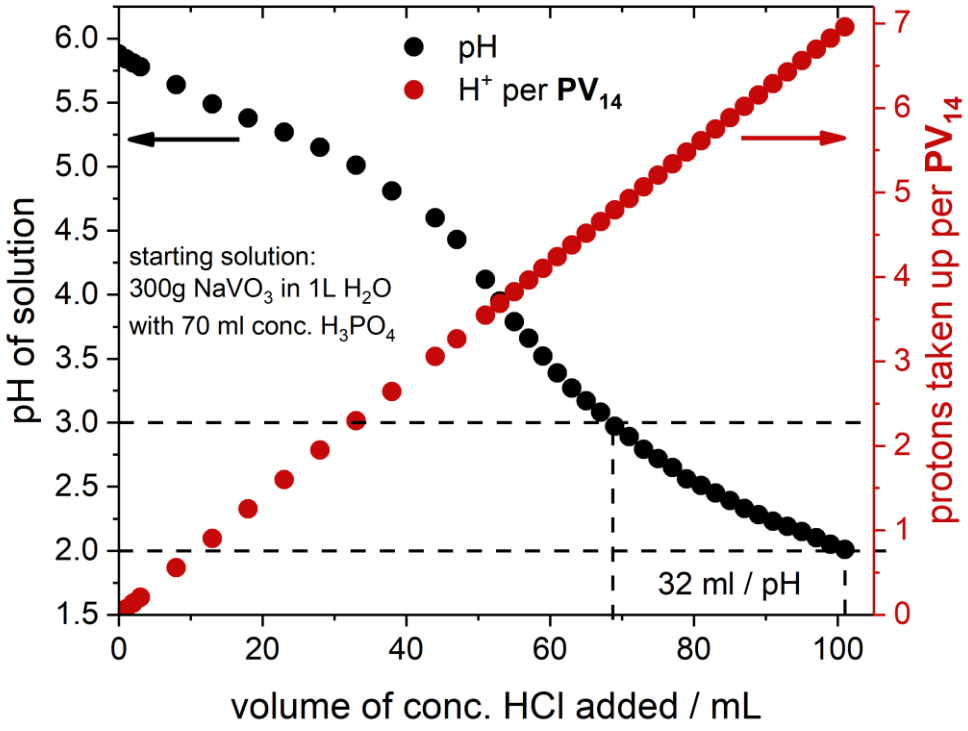

Figure 28 Titration curve measured during the synthesis of **PV_{14}**. The abscissa gives the volume of added HCl, the left ordinate (black data points) the measured *pH* values and the right ordinate the calculated number of protons taken up by each **PV_{14}** in solution.

The measured *pH* value exhibits two plateaus during the measurement, indicating that the **PV_{14}** solution acts as a buffer in these regions. Addition of 32 mL of concentrated hydrochloric acid changed the *pH* by one unit, from 3.0 to 2.0.

5.3.2 ^{51}V NMR AND IN-SITU NMR

^{51}V (I = 7/2, nat. abund. 99.76%) NMR spectra were measured at 78.94 MHz without proton decoupling on a Bruker Avance III 300 Spectrometer in 5 mm o.d. tubes at a temperature of 298K. Chemical shifts are relative to neat $VOCl_3$ as an external reference. 90º excitation pulses of 9.2 µs duration were used, and rapid T_1 relaxation as a result of the nuclear quadrupole led to line widths of 1000 – 2000 Hz. For the *in-situ* NMR measurements the spectral width was 1188 ppm and the FID was acquired into 1024 data points, leading to an acquisition time of 0.00546 s, so that with a relaxation delay of 0.001 s it was possible to acquire 2048 transients in less than 14 s. Measurements were made at intervals of

85 seconds over a period of 10 hours, and the individual FIDs were transformed into 32678 points after multiplication by a 50 Hz exponential window.

5.3.3 ELECTROCHEMISTRY

Three electrode measurements were performed at RT in custom-built glass cells with a polished glassy carbon working electrode (surface area A = 0.02 cm^2), a gold wire (diameter d = 0.5 mm) counter electrode and a Mercury/Mercurous Sulphate reference electrode in 1 M H_2SO_4 (MSE, 0.668 V vs. SHE). Prior to the measurements the electrolyte was purged with nitrogen, and the cell was kept under nitrogen pressure during the experiment. A Bio-Logic SP300 potentiostat was used for control and data acquisition.

Bulk electrolysis was conducted with a bulk electrolysis cell from BASi containing a reticulated vitreous carbon WE, platinum wire CE and an Ag/AgCl (in 3 M NaCl, 0.209 V vs. SHE) RE. Before the experiment, the solution was stirred and purged with nitrogen for 15 min. The solution was reduced with constant current of -50 mA until the desired amount of charge was reached. To reduce a solution of 30 mL with a concentration of 20 mM POM by 0.5 electrons per molecule, the added charge was 28.9455 C (total time = 9 min 39 s). During the reduction the solution was stirred and purged with nitrogen. After reduction the OCV was measured.

The flow battery experiments were conducted in a commercial cell (C-Tech 5 x 5, surface area A = 25 cm^2) at RT. Graphite felts (GFD, SGL Carbon) were used as electrodes and pre-treated at 400°C for 24 h in the laboratory atmosphere. In the cell the 4.6 mm thick electrodes were compressed to 3.5 mm. A cation exchange membrane (FUMASEP - F1040, thickness 40 µm) was employed and boiled in 1 M lithium chloride for 30 min before application. During the experiment the cell and the pump with tubing were kept in a polycarbonate box purged with nitrogen.

The stationary battery cell (A = 16 cm^2) was designed by Jochen Friedl and a schematic can be seen in Figure 29. The entire void space of the two half-cells was filled with carbon felt electrodes (GFD, SGL Carbon) which were heat-treated for activation before every experiment (24 h at 400°C). As proton exchange membrane, Nafion N117 was used and boiled in 1 M lithium chloride for 30 min before it was assembled. To ensure a good seal, the

two PTFE half-cell are supported by stainless-steel plates. During the experiment the cell was kept in a polycarbonate box purged with nitrogen.

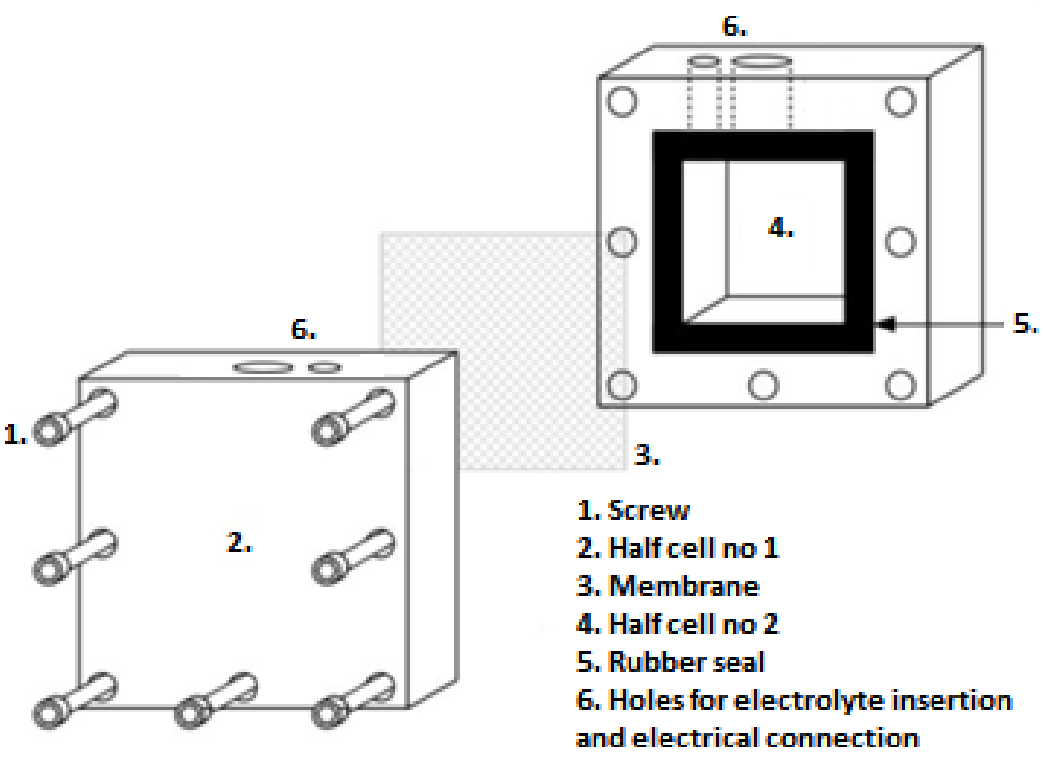

Figure 29 Schematic of the stationary battery cell designed by Jochen Friedl (by private communication).

5.4 Investigations of the anolyte, SiW_{12}

The redox properties are determined by the heteroatom in the Keggin ion and can be Si, P, As, Ge, W or Mo [223]. By varying those addenda ions the redox properties are modified and therefore it is possible to adjust parameter like ΔU [176]. The POM **SiW_{12}** was chosen because this molecule is able to transfer electrons at a low potential, hence, it is suitable as anolyte.

5.4.1 Cyclic voltammetry of SiW_{12} and pH stability

Stability of all redox species used is one of the main criteria for suitability as RFB electrolyte. As POMs are fairly complicated molecules, it is imperative to test whether they remain stable or possibly decompose. **SiW_{12}** is known to be a stable Keggin ion which exists in very acidic media and starts to decompose at *pH* 4.5 [224,225]. The decomposition mechanism of **SiW_{12}** to $[WO_4]^{2-}$ and $[SiO_4]^{4-}$ proceeds via the intermediates $[SiW_{11}O_{39}]^{8-}$ and $[SiW_9O_{34}]^{10-}$ [226]. Because the literature studies investigated the stability of **SiW_{12}** at low concentrations *c* (e.g. $c = 6\ 10^{-4}$ M in ref. [224]) it was looked at *pH* stability at a concentration more suitable for RFBs,

c = 0.1 M. The voltammetric response of $[SiW_{11}O_{39}]^{8-}$ and $[SiW_9O_{34}]^{10-}$ is clearly distinct from that of **SiW_{12}** [128], therefore CVs were employed as analytical tools to assess stability. It was determined that after 24 hours in electrolytes with $1 \leq pH \leq 6$ **SiW_{12}** at c = 0.1 M was undamaged (see Figure 30). *pH*-stability was assessed by preparing a series of 0.1 M solutions of **SiW_{12}** and adjusting their *pH* to values in the range 1 - 6 by addition of 3 M LiOH. These solutions were stored for 24 h and were then diluted to a common *pH* and concentration (1 mM) by addition of 1 M H_2SO_4. The CVs are shown in Figure 30 and indicate that exposure for 24 h to an electrolyte with *pH* up to 6 does not affect **SiW_{12}** detrimentally as the CV pattern is very similar for each curve, similar to the CV of freshly prepared **SiW_{12}** shown in Figure 30 and is in accord with CV data published in the literature [134,227,228].

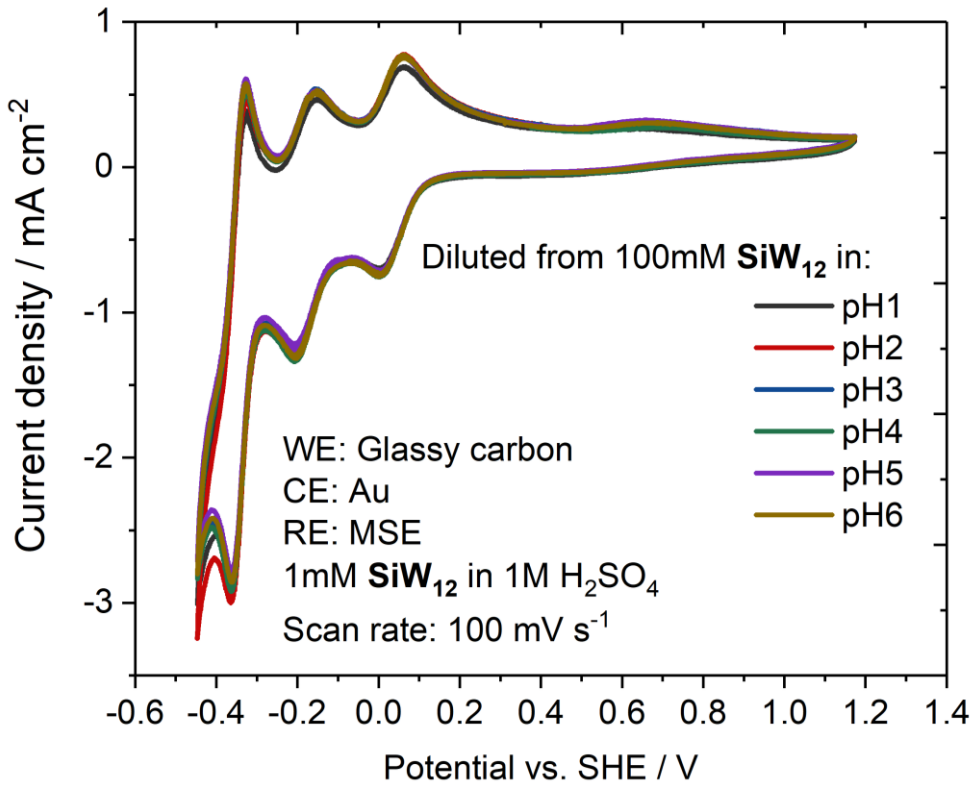

Figure 30 Cyclic voltammogram of 1 mM **SiW_{12}** after storage for 24 h in aqueous solution ranging in *pH* from 1- 6. Measured in 1 M H_2SO_4 aqueous solution.

The next Figure 31 (a) shows the CVs of 1 mM **SiW_{12}** in diluted aqueous HCl solution at various *pH* values. The first two waves correspond to single electron transfer and the third wave corresponds to a two electron transfer. What can be seen in the Pourbaix-diagram, Figure 31 (b), is that the first two one-electron waves are *pH*-independent, whereas the third

wave corresponds to a *pH*-dependent redox process and is shifted to more negative potentials with increasing *pH* which is in agreement with the literature [229].

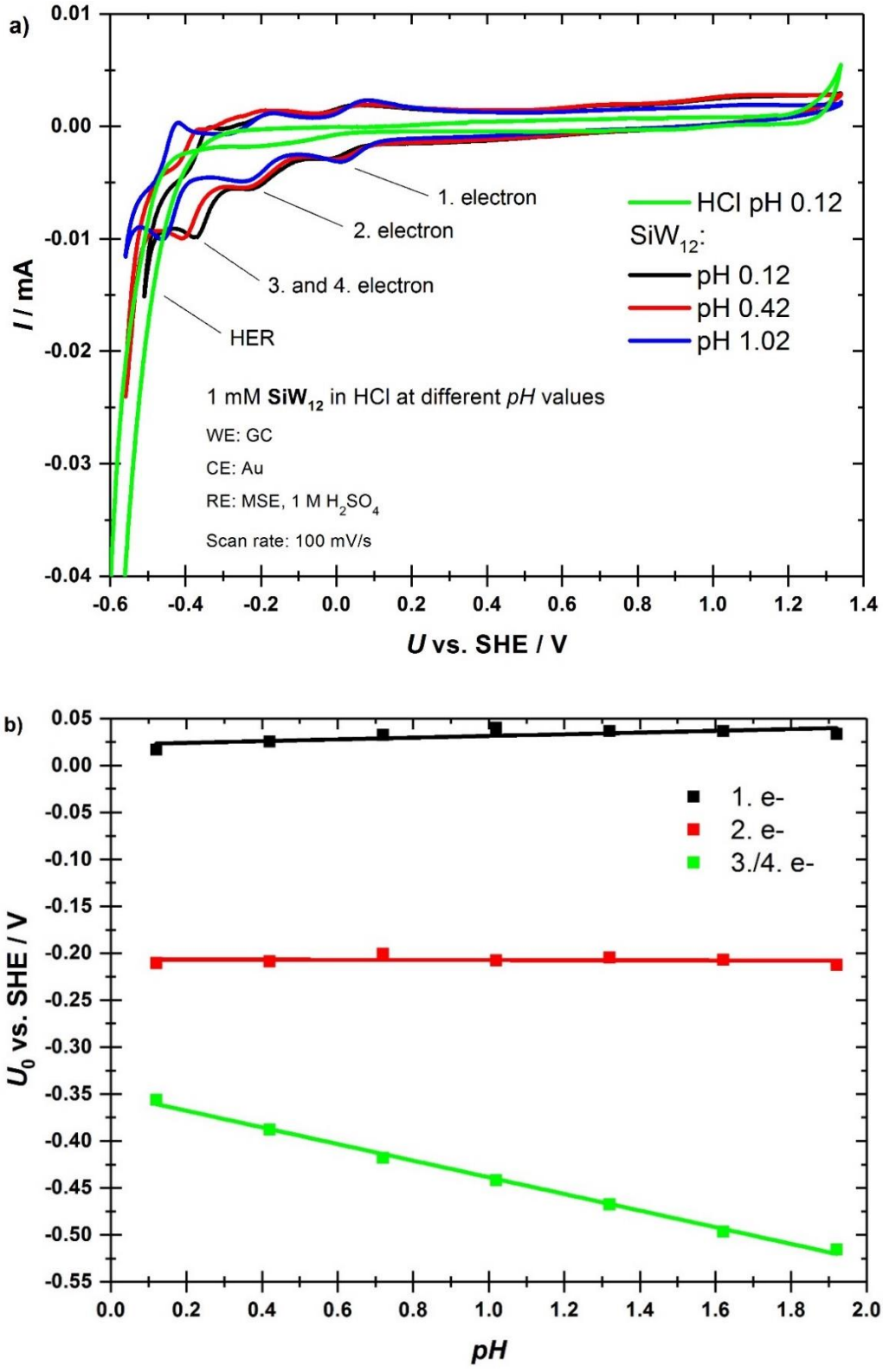

Figure 31 (a) Cyclic voltammograms of 1 mM **SiW₁₂** in diluted aqueous HCl at various *pH* values between 0.12 and 1.02, (b) Pourbaix-diagram of the first three redox processes of **SiW₁₂** as a function of *pH*.

Figure 32 compares a cyclic voltammogram of 1 mM **SiW_{12}** with a CV of 12 mM V^{3+} in 1 M H_2SO_4. This comparison is made because the anolyte of the VRFB contains V^{2+}/V^{3+} and **SiW_{12}** serves as its replacement in the negative half-cell. The electrodes are glassy carbon discs used after polishing. The CV of **SiW_{12}** exhibits the typical pattern of two one-electron redox reactions followed by one two-electron redox reaction which has been described in the literature [134,227,228].

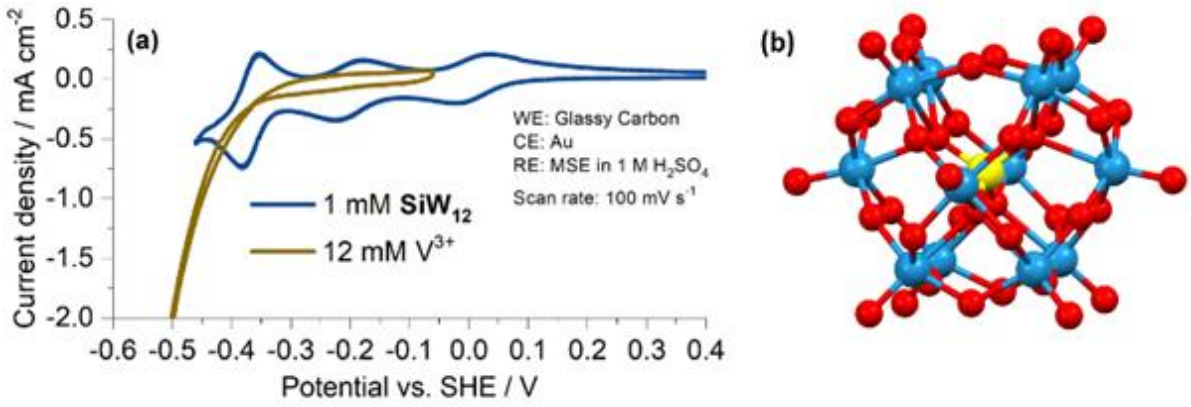

Figure 32 (a) Comparison of cyclic voltammograms of 1 mM **SiW_{12}** and 12 mM V^{3+} in 1 M H_2SO_4. These are the anolyte species of the presented all-POM RFB and the VRFB. (b) Ball-and-stick representation of **SiW_{12}**. Colour code: silicon – yellow; tungsten – blue; oxygen – red.

Determined equilibrium potentials U_0(**SiW_{12}**), peak potential separations ΔU and number of transferred electrons *n* for the three redox reactions of **SiW_{12}** at 100 mV s^{-1} are given in Table 7:

Table 7 Parameters of the **SiW_{12}** redox reactions determined from the CV shown in Figure 32 at 100 mV s^{-1}.

Redox reaction	*n*	$U_0(\mathbf{SiW_{12}})$/ V vs. SHE	ΔU / mV
SiW_{12}/SiW_{12}^{-}	1	0.01	57
$SiW_{12}^{-}/SiW_{12}^{2-}$	1	-0.21	56
$SiW_{12}^{2-}/SiW_{12}^{4-}$	2	-0.37	29

The determined values for ΔU are small, in fact they are close to the theoretical minimum for a one (59 mV) or a two (29.5 mV) electron redox reaction. The redox behaviour of **SiW_{12}** is well investigated and the 1-1-2 electron redox pattern has been reported by many

authors [134,227,228]. In this study, the reduction of **SiW_{12}** was restricted to the first two electron transfers because at potentials in the vicinity of the third redox wave the POM irreversibly modifies the electrode which leads to its decomposition and catalysis of the HER [130].

The V^{2+}/V^{3+} redox reaction is a sluggish reaction and exhibits significant current only on oxidised carbon materials, on the polished glassy carbon electrode used here the current is negligible [2,58,200,201]. The current which is associated with the reduction of V^{3+} and the subsequent reoxidation of V^{2+} is very small, current from the hydrogen evolution reaction appears to be larger. Figure 33 compares the previously shown CV of 12 mM V^{3+} in 1 M H_2SO_4 on a polished GC electrode with a CV of 12 mM V^{3+} on a GC electrode which has been electrochemically oxidised.

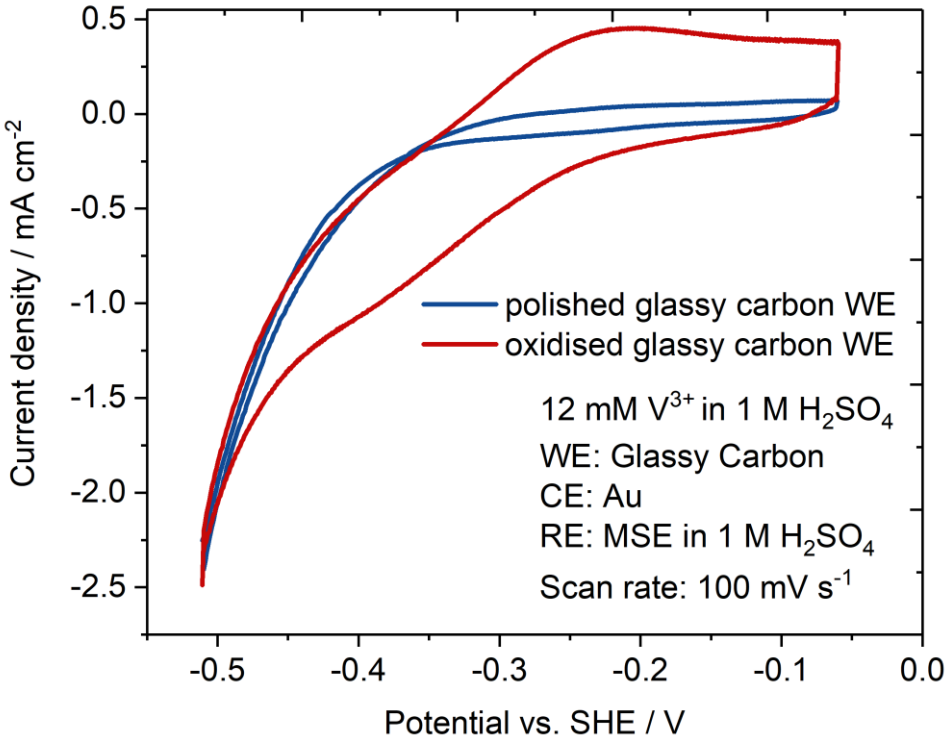

Figure 33 Comparison of the V^{2+}/V^{3+} redox reaction on a polished and on an oxidised (2 V vs. SHE for 10 s in 1 M H_2SO_4) glassy carbon working electrode.

For this the potential of the GC electrode was stepped to 2 V vs. SHE for 10 s in 1 M H_2SO_4. The much higher current on the oxidised GC indicates that the electrochemical pre-treatment produced a catalytic electrode surface. This is in accordance with other studies that attributed catalytic properties for the V^{2+}/V^{3+} redox reaction to oxygen functional groups [2,58,200,201]. The reason for this catalytic effect is most likely a bridge activated electron

transfer, as for Fe^{2+}/Fe^{3+} [17,230,231]. This has consequences for the VRFB in which the evolution of hydrogen decreases the Coulombic efficiency [62].

With standard potentials of $U_{0,1}$(**SiW_{12}**) = 0.01 V vs. SHE and $U_{0,2}$(**SiW_{12}**) = -0.21 V vs. SHE, the first two redox reactions of the POM are positive of the measured standard potential of the V^{2+}/V^{3+} redox reaction $U_0(V^{2+}/V^{3+})$ = -0.29 V vs. SHE. However, the peak separations and the comparable current density, despite a twelve-fold higher concentration for the V^{3+}, suggest that the electron transfer for **SiW_{12}** is much faster than for V^{2+}/V^{3+}. For the latter the literature gives values on GC of $k_0^{V^{2+}/V^{3+}}$ = 10^{-6} cm s^{-1} [3].

5.4.2 Electrochemical impedance spectroscopy of SiW_{12}

In order to determine the redox kinetics of **SiW_{12}** electrochemical impedance spectroscopy measurements were performed in 1 M H_2SO_4 with 20 mM **SiW_{12}**. This solution was reduced by 0.5 electrons per **SiW_{12}** polyoxoanion by bulk electrolysis. The solution then contained 10 mM **SiW_{12}** and 10 mM **SiW_{12}^-** and the measured open circuit potential was equal to the standard potential of $\boldsymbol{U_{SiW_{12}}^{\theta,1}}$ = 0 V vs. SHE for the first reduction. EIS was measured at the OCP with an amplitude of 10 mV from 1 MHz to 100 mHz. The obtained spectra were fitted to a Randles circuit (shown in Figure 34) with added inductance accounting for the inductivity of the setup [3].

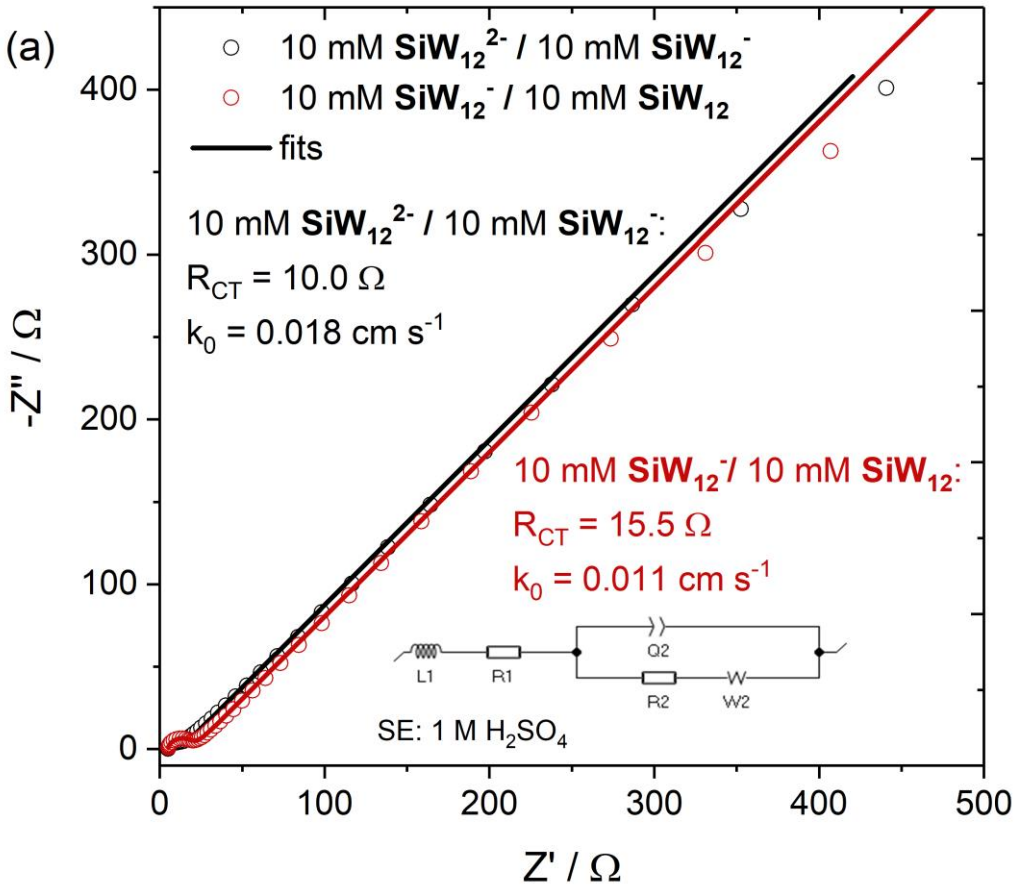
(a)
10 mM SiW12 2- / 10 mM SiW12 -
10 mM SiW12 - / 10 mM SiW12
fits
10 mM SiW12 2- / 10 mM SiW12 -:
RCT = 10.0 Ω
k0 = 0.018 cm s-1
10 mM SiW12 -/ 10 mM SiW12:
RCT = 15.5 Ω
k0 = 0.011 cm s-1
L1
R1
Q2
R2
W
W2
SE: 1 M H2SO4
-Z'' / Ω
Z' / Ω
0
100
200
300
400
500

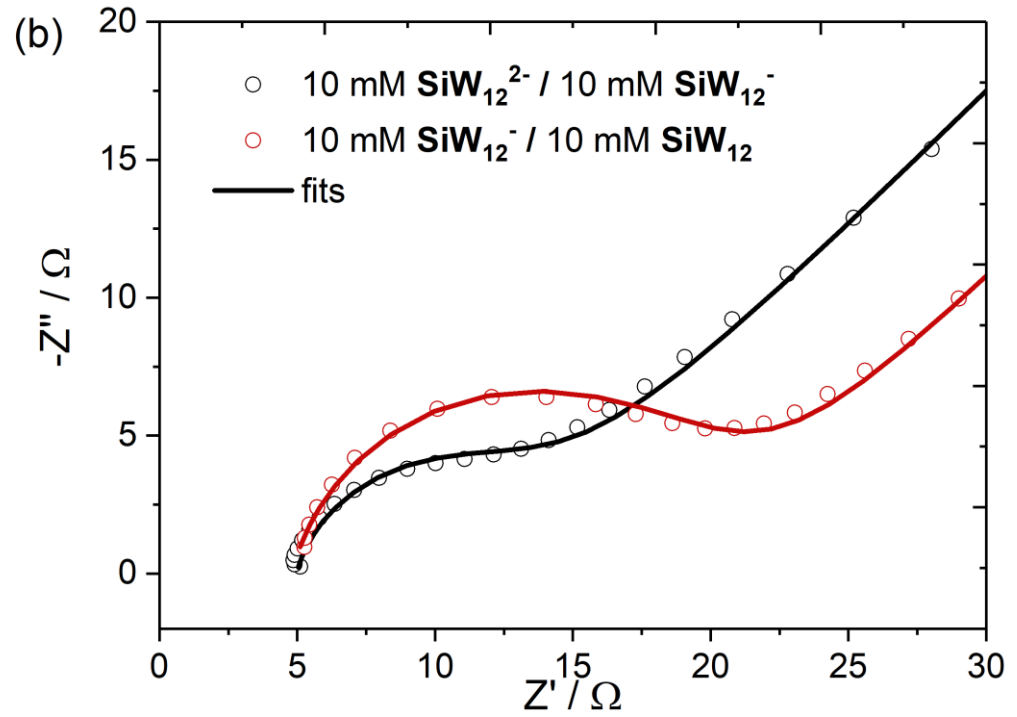
(b)
10 mM SiW12 2- / 10 mM SiW12 -
10 mM SiW12 - / 10 mM SiW12
fits
-Z'' / Ω
Z' / Ω
0
5
10
15
20
25
30

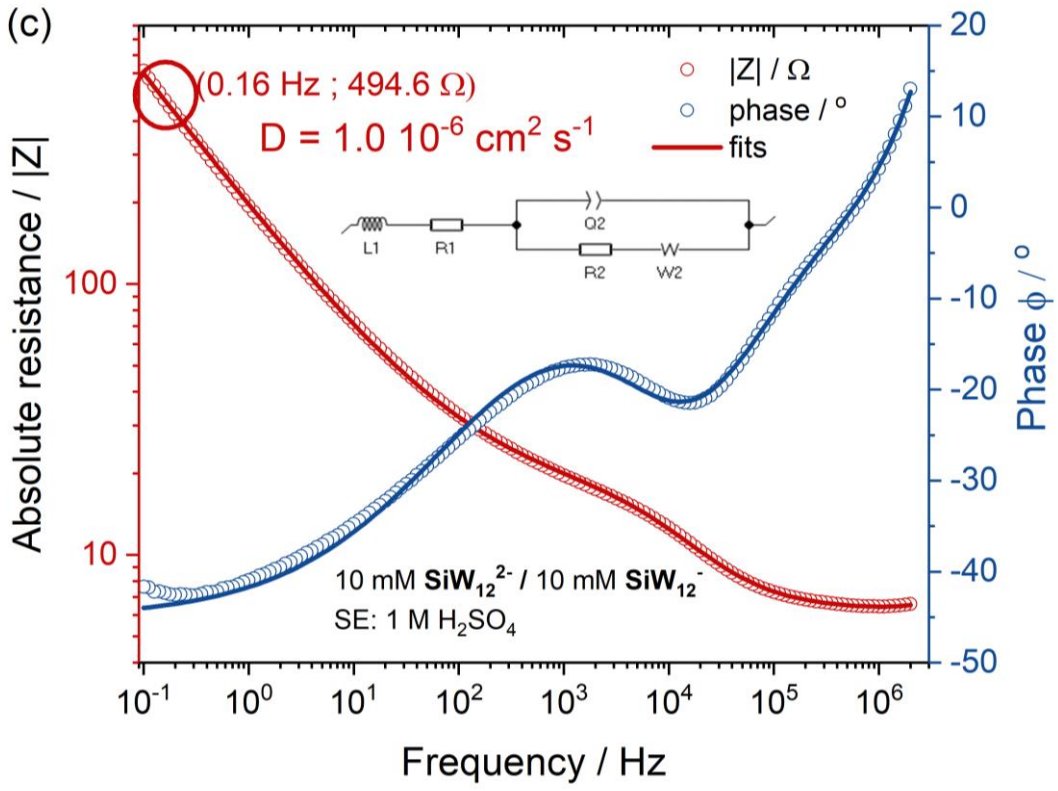

Figure 34 Electrochemical impedance spectroscopy measurements of the first two redox reactions of **SiW_{12}**. (a) Nyquist plots of 10 mM **SiW_{12}**/10 mM **SiW_{12}^-** and 10 mM **SiW_{12}^-**/ 10 mM **SiW_{12}^{2-}** with fits and the used equivalent circuit shown. (b) Detail of (a) showing the semicircle. (c) Bode plot of 10 mM **SiW_{12}^-**/10 mM **SiW_{12}^{2-}** with fits. (Experiments were conducted by Jochen Friedl and Faye Cording).

The electron transfer constant k_0 was then calculated from the charge transfer resistance R_{CT} obtained from the fit. All fitted parameters are given in Table 8, the double layer capacitance was calculated from the constant phase element with the formula given by Hirschorn *et al.* for a surface distribution.[194]

Table 8 Parameters for first two redox reactions of **SiW_{12}** determined by fitting the experimental data to the equivalent circuit given in Figure 34 or by reading the impedance at 0.16 Hz.

Redox reaction	R_{Ohm} / Ω	R_{CT} / Ω	CPE / F $s^{(a-1)}$	a (*)	k_0 / cm s^{-1}	C_{DL} / µF	|Z| at 0.16 Hz/Ω	D / cm^2 s^{-1}
SiW_{12}/SiW_{12}^-	4.8	15.5	$2.6\ 10^{-6}$	0.85	0.011	0.31	510	$1.0\ 10^{-6}$
SiW_{12}^-/SiW_{12}^{2-}	4.6	10.0	$21.2\ 10^{-6}$	0.76	0.018	1.0	494	$1.1\ 10^{-6}$

(*) constant phase element parameter

The measurement described above was repeated to measure the kinetics of the second electron transfer of **SiW_{12}**; 1.5 electrons were added to fully oxidised **SiW_{12}**, the composition of the solution is then 10 mM **SiW_{12}^{-}** and 10 mM **SiW_{12}^{2-}** and the OCP was $U_{\mathrm{SiW_{12}}}^{\theta,1}$ = -0.21 V vs. SHE. Nyquist plots for both measurements with their fits are shown in Figure 34 (a) and Figure 34 (b). R_{Ohm} is very similar for both measurements, the double layer capacitance C_{DL} is lower for **SiW_{12}/SiW_{12}^{-}** than for **SiW_{12}^{-} /SiW_{12}^{2-}** . For the latter measurement a specific capacitance C_{DL} = 14 10^{-6} F cm^{-2} is reasonable for a glassy carbon electrode [17].

The determined electron transfer constants are in the order of $k_0 \approx 10^{-2}$ cm s^{-1}. It appears that the second redox reaction **SiW_{12}^{-} /SiW_{12}^{2-}** is faster than the first redox reaction **SiW_{12}/SiW_{12}^{-}**. To the best of my knowledge, this has not been investigated in the literature and could be an interesting research topic.

Diffusion coefficients D was determined from the magnitude of the admittance ($1/|Z|$) at a frequency of 0.16 Hz. The calculations yield a very similar diffusion coefficient for **SiW_{12}^{-} /SiW_{12}^{2-}** and **SiW_{12}/SiW_{12}^{-}** at D = 1.1 10^{-6} cm^2 s^{-1} and D = 1.1 10^{-6} cm^2 s^{-1} respectively. The literature value for D of $[SiW_{12}O_{40}]^{4-}$ in 0.9 M Na_2SO_4, 0.1 M H_2SO_4 at 25°C is higher at 2.6 10^{-6} cm^2 s^{-1} [134].

Electrochemical impedance spectroscopy (see Figure 34 and Table 8) shows that the transfer of the first redox wave, **SiW_{12}/SiW_{12}^{-}**, proceeds at a rate of k_0 = 1.1 10^{-2} cm s^{-1} and for the second redox wave, **SiW_{12}^{-}/SiW_{12}^{2-}**, k_0 = 1.8 10^{-2} cm s^{-1} was measured. Therefore, the kinetics of **SiW_{12}** are significantly more facile than those of V^{2+}/V^{3+}. The diffusion coefficient of **SiW_{12}** was also determined by EIS to be approximately $D \approx 10^{-6}$ cm^2 s^{-1}. Inserting this value into the Stokes-Einstein equation,

$$D = \frac{k_B \cdot T}{6\pi \cdot \eta \cdot r} \qquad (42)$$

with k_B Boltzmann's constant, η dynamic viscosity [232] and r hydrodynamic radius of spherical particle, gives a value of r = 2 nm for **SiW_{12}.** This is larger than the crystallographic radius ($r \approx 0.5$ nm), but this makes sense as the hydration shell of the charged molecule has to be considered, too [134].

5.5 Investigations of the catholyte, PV_{14}

The POM **PV_{14}** was chosen because this molecule is able to transfer electrons at a high potential, hence, it is suitable as catholyte.

5.5.1 Electrochemical Investigations of the catholyte, PV_{14}

Figure 35 compares a CV of 1 mM **PV_{14}** recorded in 1 M LiCl at *pH* 2.3 with a CV of 14 mM VO_2^+ in 1 M H_2SO_4. This comparison is made because the catholyte of the VRFB contains VO^{2+}/ VO_2^+ and **PV_{14}** serves as its replacement in the positive half-cell.

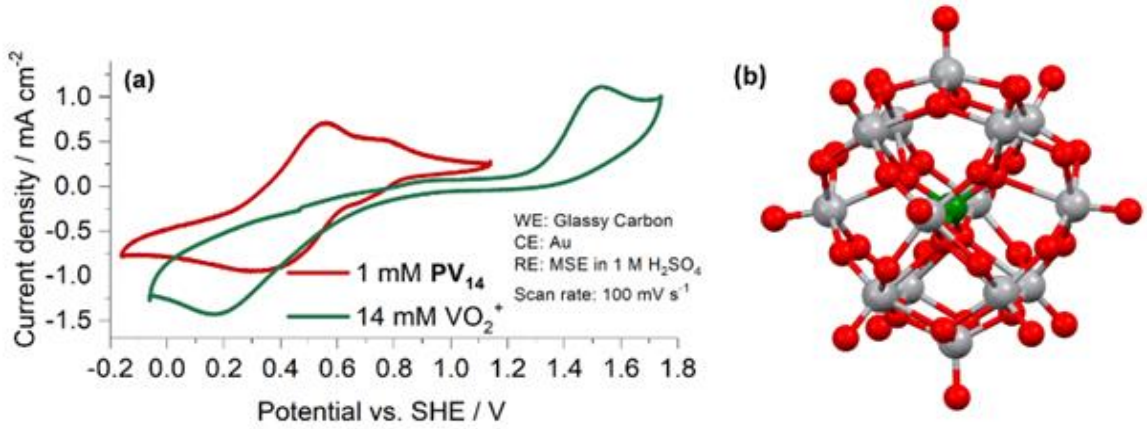

Figure 35 (a) Comparison of Cyclic voltammograms of 1 mM **PV_{14}** and 14 mM VO_2^+, the catholyte species of the presented all-POM RFB and the VRFB. VO_2^+ was measured in 1 M H_2SO_4, **PV_{14}** in 1 M LiCl at *pH* 2.3 (b) Ball-and-stick representation of **PV_{14}**. Colour code: phosphorus – green; vanadium – silver; oxygen – red.

Because **PV_{14}** is less investigated than **SiW_{12},** a more detailed study is presented here. The **PV_{14}** redox waves are multi-electron transitions, the overlap of many redox reactions makes it difficult to determine exact standard potentials and peak separations. Comparison with 14 mM VO_2^+ shows that 1 mM **PV_{14}** reaches similar peak current densities.

For the VO^{2+}/VO_2^+ redox reaction with standard potential $U_0(VO^{2+}/VO_2^+)$ = 1.0 V vs. SHE [204] the peak separation is 1.37 V at 100 mV s^{-1}, which is typical for very sluggish redox reactions ($k_0^{VO^{2+}/VO_2^+}$ = 10^{-6} cm s^{-1} [3,6,186,187]). Figure 36 (a) shows five CVs of 20 mM **PV_{14}** at scan rates from 10 mV s^{-1} to 250 mV s^{-1}. **PV_{14}** exhibits a multi-electron redox reaction in the range from 0.2 – 0.7 V vs. SHE. Both the oxidation wave and the reduction wave consist of (at least) two individual peaks, labelled Ox. 1, Ox. 2, Red. 1 and Red. 2 in Figure 36a. The peaks Ox. 2 and Red. 2 are the most pronounced for all scan rates, their arithmetic mean gives an

approximate standard potential U_0(**PV$_{14}$**) = 0.60 V vs. SHE. The peak potential positions shift only minimally with scan rate, Ox. 2 shifts 13 mV higher from 0.01 V s^{-1} to 0.25 V s^{-1}, during the same change in scan rate the potential position of Red. 2 decreases by 18 mV s^{-1}. However, because it is unknown how many electrons are transferred during each peak a kinetic assessment is difficult.

In order to determine the number of electrons *n* transferred in the redox waves the peak current densities of Ox. 2 and Red. 2 are plotted over the square root of the scan rate in Figure 36 (b). The data points for oxidation reaction and reduction reaction are on a straight line for smaller scan rates, but for 0.1 V s^{-1} and 0.25 V s^{-1} they fall below those lines. This indicates a limitation in the rate of electron transfer, such as slower preceding chemical reaction.

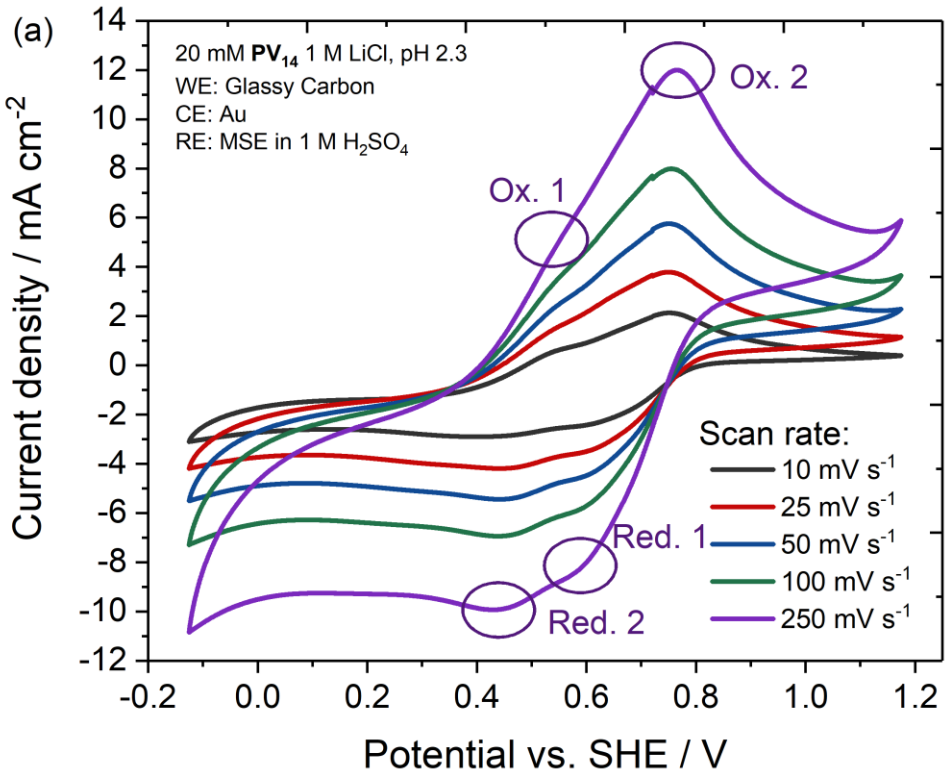

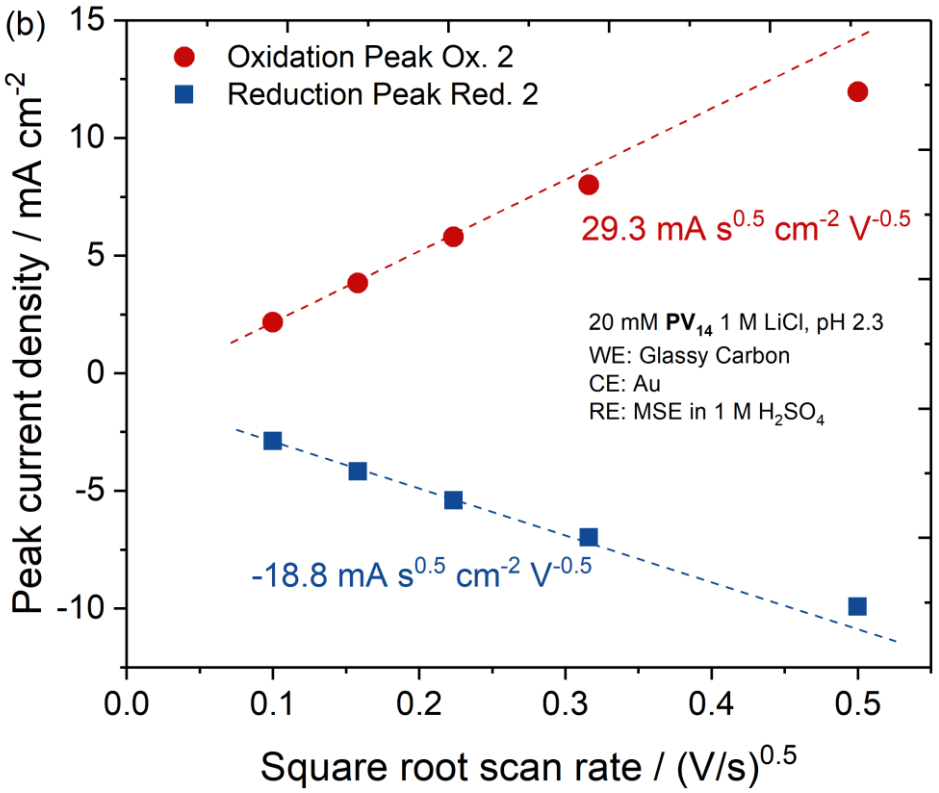
(b)
Oxidation Peak Ox. 2
Reduction Peak Red. 2
29.3 mA s^0.5 cm^-2 V^-0.5
20 mM PV14 1 M LiCl, pH 2.3
WE: Glassy Carbon
CE: Au
RE: MSE in 1 M H2SO4
-18.8 mA s^0.5 cm^-2 V^-0.5
Peak current density / mA cm^-2
Square root scan rate / (V/s)^0.5

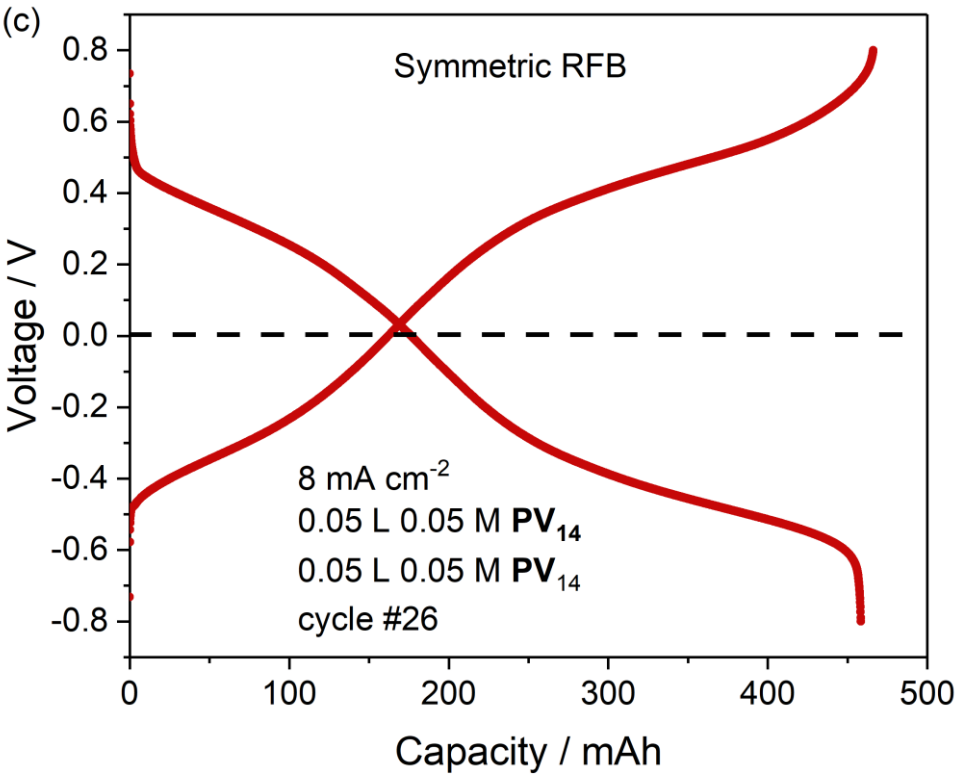
(c)
Symmetric RFB
8 mA cm^-2
0.05 L 0.05 M PV14
0.05 L 0.05 M PV14
cycle #26
Voltage / V
Capacity / mAh

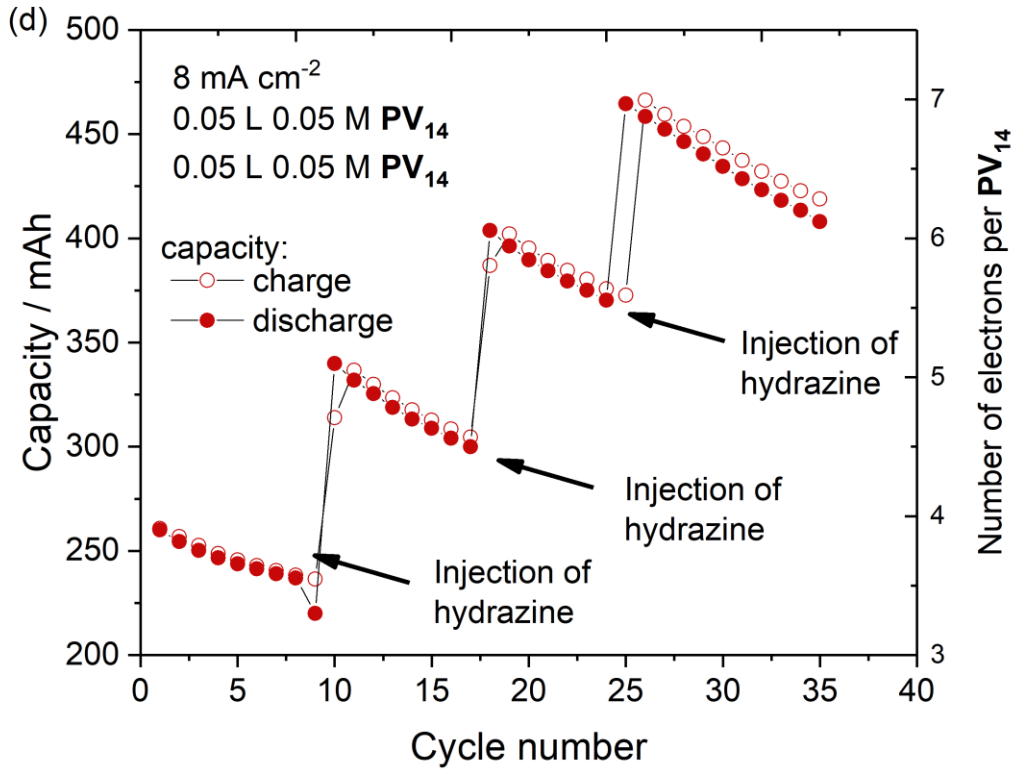

Figure 36 Electrochemical investigation of **PV_{14}**. (a) Cyclic Voltammograms of 20 mM **PV_{14}** with various scan rates. Observed peaks are labelled. (b) Peak current density vs. square root of scan rate for peaks Ox. 2 and Red. 2. (c) A charge-discharge curve for a symmetric flow cell with **PV_{14}** (d) Discharge capacity over cycle number for the symmetric flow cell.

The determined slopes allow to determine *n* with the Randles-Sevcik equation (25), if the diffusion coefficient is known. The diffusion coefficient of **PV_{14}**, determined in section 5.5.5, was inserted into equation (25). The calculation yields that during the oxidation n^{ox} = 5.5 electrons are transferred, during the reduction n^{red} = 3.6 in the investigated peaks. The imbalance between n^{red} and n^{ox} can be explained by the larger peak current of Red. 1 than Ox. 1 as additional electrons are transferred. However, n^{red} and n^{ox} are only rough estimates, the baseline of the preceding peaks (Ox. 1 and Red. 1) are not been taken into account, the inserted value for *D* most likely comes with a large error, and non-integer values for *n* do not make sense. However, it is clear from the analysis that indeed multiple electrons are transferred during the redox waves in shown Figure 36 (a).

To confirm that multiple electrons can be transferred per **PV_{14}** polyoxoanion, a symmetrical flow cell was set up. Both tanks of the cell, anolyte and catholyte, were 0.05 M **PV_{14}** solution. Hydrazine was added to one tank to reduce the **PV_{14}** in it. The electrons generated by this

chemical reduction are then transferred from one tank to the other during the charge and discharge of the battery. Because the amount of **PV_{14}** is known, the reached capacity *Q* is a direct measure for the number of electrons transferred per molecule *n*:

$$Q = n\,V\,c \qquad (43)$$

with *V* volume of the tanks and *c* concentration of **PV_{14}**. One cycle of the symmetric battery is shown in Figure 36 (c). As can be seen, the charge and discharge curves (at 8 mA cm^{-2} / 200 mA) are symmetrical around zero cell voltage, as expected for a symmetrical flow cell. Multiple additions of hydrazine increased the capacity with each injection. The maximum number of electrons transferred was *n* = 7, higher numbers were not tested. This result confirmed the findings of Figure 36 (a) and Figure 36 (b), that the redox reactions of **PV_{14}** are multi-electron. The capacity of the symmetric flow battery faded quickly, at approximately 5 mAh per cycle, which is attributed to re-oxidation of reduced **PV_{14}** species, as the tanks were not purged with nitrogen during the experiment.

5.5.2 Investigation of proton coupled electron transfer of PV_{14}

One aspect that arises from the use of **PV_{14}** in the catholyte of an RFB is that the electron exchange is coupled to a proton transfer. To confirm that behaviour, the polyoxovanadate was reduced and oxidized in a flow battery while the *pH* was measured in the tank. The other half-cell consisted of an excess of Fe^{2+}. The result is shown in Figure 37. Upon reduction the *pH* increases, as **PV_{14}** takes up electrons and protons. This behaviour is reversible and depends on the concentration of **PV_{14}** as expected.

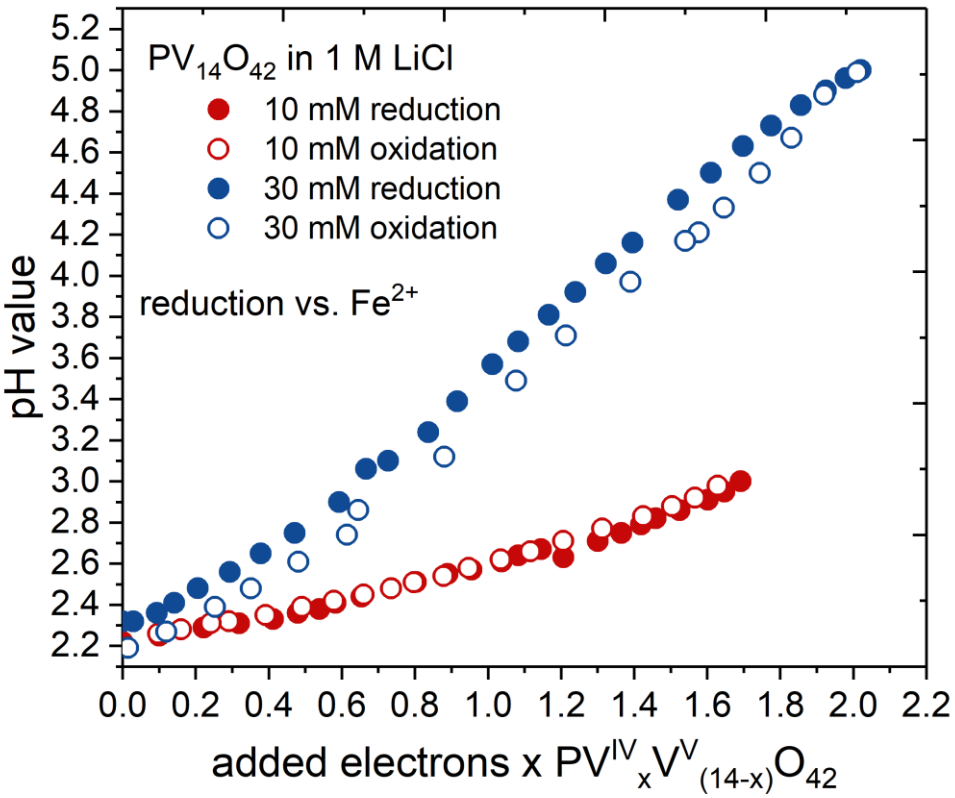

Figure 37 Evolution of *pH* value during reduction and oxidation of **PV$_{14}$** against an excess of Fe^{2+}. The measurement is shown for two concentrations: 10 mM (red circles) and 30 mM (blue circles) **PV$_{14}$** for reduction and oxidation.

In Figure 37 the evolution of the *pH* value for an electrolyte in which **PV$_{14}$** is reduced is shown. Upon reduction **PV$_{14}$** takes up electrons and protons. Thus for a solution with fixed volume the *pH* rises from 2.3 to 3.0 in a 10 mM **PV$_{14}$** electrolyte and to *pH* 5 in a 30 mM **PV$_{14}$** electrolyte upon reduction by two electrons. Subsequent oxidation of **PV$_{14}$** returns the *pH* to its initial value. It is assumed that this experiment worked without destroying the **PV$_{14}$** because the POMs served as buffer solution. This is suggested by the titration curve recorded while synthesising **PV$_{14}$** by addition of conc. HCl (compare Figure 28). A solution with *pH* 2, which corresponds to a hydronium ion concentration of $c_{H_3O^+}$ = 0.02 M, cannot supply the required protons to allow 0.03 M **PV$_{14}$** to take up two protons per molecule. Therefore, **PV$_{14}$** must release protons with increasing *pH*, a phenomenon that counteracts the consumption of protons during the proton coupled electron transfer (PCET). This buffer effect is in line with research from Selling *et al*. who found that there are multiple

$[H_xPV_{14}O_{42}]^{(9-x)-}$ species with x = 1-6 in a *pH* range from 1.5 < *pH* 6.5, each species with its own pK_a value [222].

5.5.3 ^{51}V NMR INVESTIGATION OF PV_{14} TO MEASURE PH STABILITY

Selling *et al*. showed by ^{51}V NMR that **PV_{14}** in solution is in equilibrium with free vanadium (VO_2^+) and decavanadate ($[V_{10}O_{28}]^{6-}$).[222] **PV_{14}** is the dominant vanadium species at around *pH* 2.3, more acidic conditions favour VO_2^+, whereas higher *pH* values see most vanadium incorporated in $[V_{10}O_{28}]^{6-}$. **PV_{14}** undergoes PCET and therefore changes the *pH* value of its electrolyte when being oxidised or reduced (Figure 37). This might be expected to shift the *pH* of the electrolyte to a value outside of the stability range of **PV_{14}**. While it was stated that the transformation of **PV_{14}** to $[V_{10}O_{28}]^{6-}$ at high *pH* and to VO_2^+ at low *pH* is a slow process, the exact time dependence was not given.[222] Therefore, the time-dependence of the transformations was determined as shown in Figure 38.

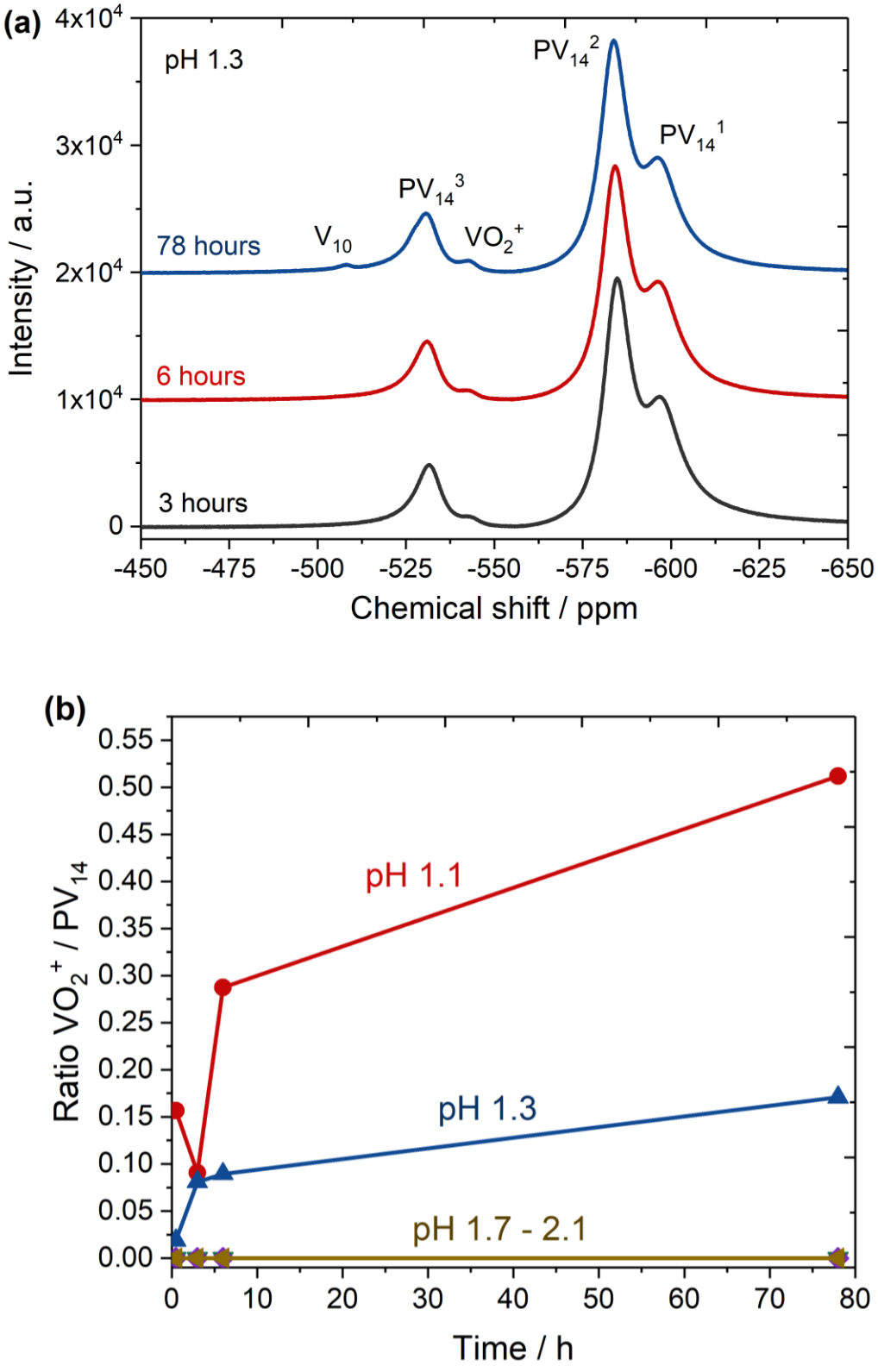

Figure 38 (a) Typical ^{51}V NMR spectra for 50 mM **PV_{14}** in water with *pH* 1.3: 3 hours after adjusting the *pH* (black curve), after 6 hours (red curve) and after 78 hours (blue curve). (b) Development of VO_2^+ to **PV_{14}** ratio evaluated over time. The three lines for *pH* 1.7, 1.9 and 2.1 overlap.

The *pH* stability of **PV_{14}** was measured by ^{51}V NMR. For this purpose, spectra in electrolytes ranging in *pH* from 1.1 to 2.1 were recorded immediately after adjusting the *pH*, and again after 3, 6 and 78 hours. The ratio of free vanadium (VO_2^+) to **PV_{14}** was determined by integrating the intensities of the peaks labelled PV_{14}^3 and VO_2^+. The signal PV_{14}^3 arises from two vanadium sites in **PV_{14}**, and so its integrated intensity was divided by 2 for comparison with the single vanadium site in VO_2^+. In electrolytes with *pH* from 2.3 to 1.7 ^{51}V NMR shows no indication of vanadium species other than **PV_{14}** after 78 hours. At *pH* 1.3 17% of the vanadium is present as free vanadium, and after 78 hours, at *pH* 1.1 this is increased to 51%. Figure 38 (b) shows that the transformation is not instantaneous but builds up over time. Therefore, in an RFB electrolyte a *pH* value of 1.7 can be tolerated permanently, and even lower values are permissible for short periods of time. This dynamic equilibrium of vanadium species, first described by Selling *et al.*, endows **PV_{14}** with self-repairing properties [222]. This is demonstrated in Figure 39 which shows ^{51}V NMR spectra of various vanadium species.

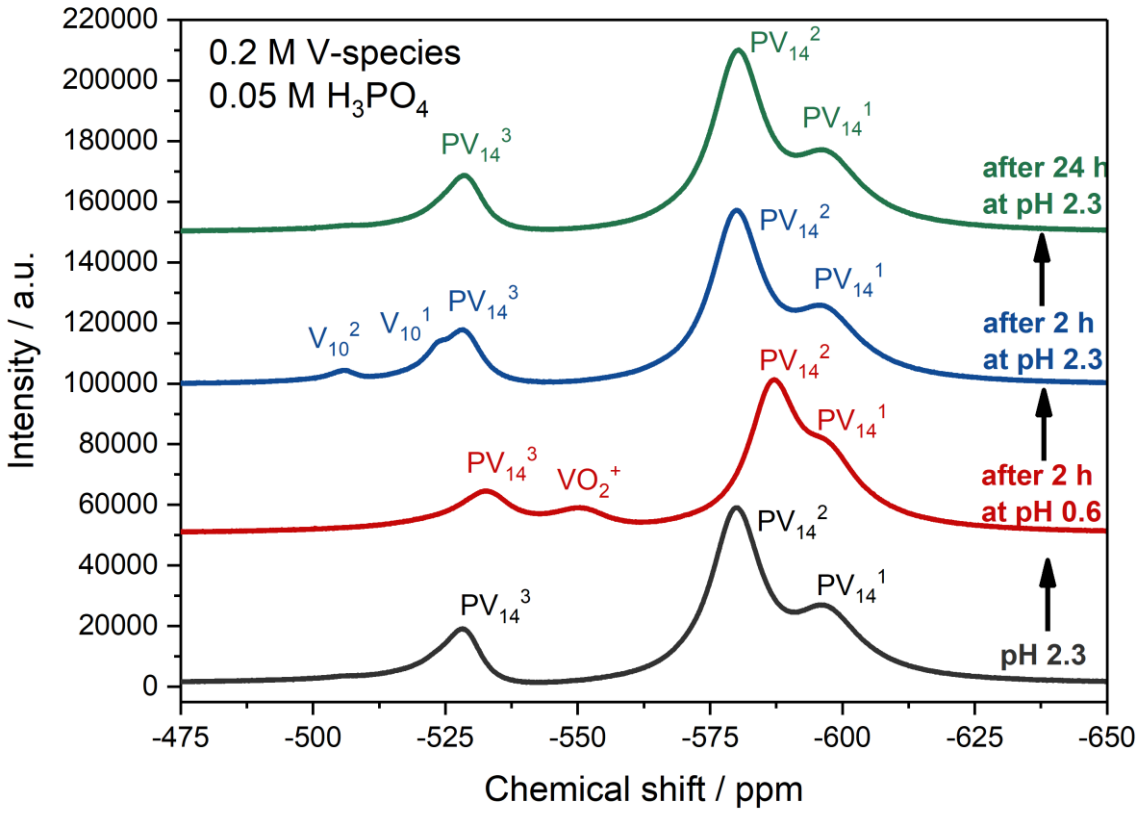

Figure 39 Evolution of ^{51}V NMR spectra of 0.2 M vanadium species in 0.05 M H_3PO_4 initially at *pH* 2.3.

Initially, at *pH* 2.3 (grey spectrum), three peaks are present. These can be attributed to the three vanadium positions in **PV_{14}** [222]; PV_{14}^3 stems from the two vanadium atoms in the cap, PV_{14}^1 from the 4 vanadium atoms in the plane of the phosphorous ion in the centre, and PV_{14}^2 from the remaining eight. Reducing the *pH* to 0.6 with HCl (red curve) leads to a shift of the vanadium species equilibrium towards free vanadium, its peak emerges at -550 ppm in the spectrum. At *pH* 0.6 PV_{14}^1, PV_{14}^2 and PV_{14}^3 are located at more negative chemical shifts than at *pH* 2.3, an effect that has been reported before [222]. Successive increase of *pH* to 2.3 showed that the VO_2^+ peak had vanished after two hours, however peaks for $[V_{10}O_{28}]^{6-}$ have appeared (blue curve). Remeasuring this solution after 24 hours yields a spectrum that contains only **PV_{14}** (green curve), the molecule has reassembled. It is plausible that the formation of **PV_{14}** from VO_2^+ proceeds via $[V_{10}O_{28}]^{6-}$ as intermediate, because a few synthesis protocols for **PV_{14}** start with decavanadate [233,234].

5.5.4 In-situ ^{51}V NMR of PV_{14}

Because there is a fluent transition between VO_2^+, $[V_{10}O_{28}]^{6-}$ and **PV_{14}**, *in-situ* ^{51}V NMR to detect whether the **PV_{14}** molecule is stable upon reduction (and therefore acts as the actual electron carrier in the RFB) was performed. Alternatively, **PV_{14}** could disintegrate upon reduction, potentially due to a local change in *pH*, into a V(IV)-containing species and reassemble when re-oxidised. Using *in-situ* ^{51}V NMR, the chemical composition of 50 mM **PV_{14}** was monitored during reduction and oxidation in the NMR spectrometer (Figure 40 (a)). Figure 40 (c) shows a schematic of the self-made *in-situ* NMR cell.

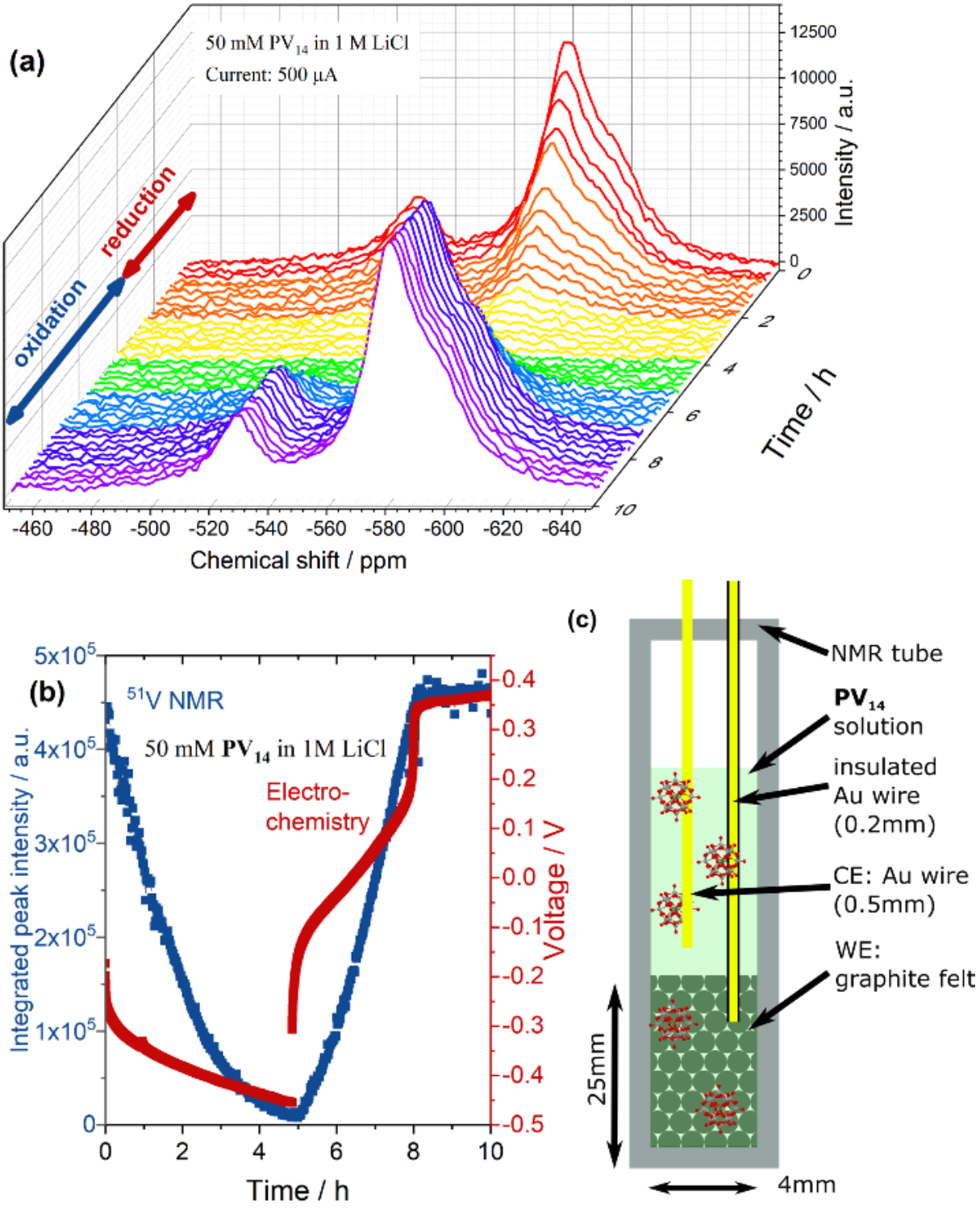

Figure 40 (a) ^{51}V NMR spectra of **PV_{14}** recorded in a NMR tube during an electrochemical experiment. In the graph, time proceeds from the back (red curve) to the front of the plane (blue curve). The time during which a reducing or an oxidizing current were applied are marked. (b) Integrated intensity of all three vanadium peaks (left, blue) and measured voltage (red, right). (c) Schematic of the *in-situ* NMR cell.

A carbon felt (GFD, SGL carbon) working electrode was contacted with a partly insulated gold wire (0.2 mm diameter), another gold wire served as counter- and reference electrode (0.5 mm diameter). The carbon felt assumed a cylindrical shape of diameter 4 mm and height 25 mm. The volume of electrolyte contained in the porous electrode was estimated to (0.30 ± 0.05) mL. Therefore, with a concentration of 50 mM, a charge of Q^{theo}= (1.4 ± 0.2) C (≙ (0.40 ± 0.07) mAh) has to be transferred to reduce the **PV_{14}** within the electrode by one electron. Figure 40 (a) shows spectra recorded during the reduction and oxidation of **PV_{14}** inside the *in-situ* NMR cell. The first plot is the red spectrum at t = 0 h, then every tenth recorded spectrum is shown until t = 10 h (36000 s, blue line). During the reduction phase with a current of 500 µA the three peaks typically observed for **PV_{14}** decreased until their integrated intensity was close to zero after t = 5 h (18000 s, as shown in Figure 40 (b), blue data). The charge transferred during this time was Q = -2.4 mAh (≙ 6 ± 1 electrons per **PV_{14}**). At this point a positive current of 500 µA was applied and the peaks began to re-appear until at t = 8.3 h the integrated peak intensities reached a plateau at their original values prior to the reduction. During this interval Q = 1.6 mAh (≙ 4 ± 0.7 electrons per **PV_{14}**) were transferred. The interpretation is as follows:

1. Peak intensity decreases upon reduction because diamagnetic V(V) is transformed to paramagnetic V(IV).[235] The fact that all three peaks of the **PV_{14}** lose intensity simultaneously indicates that the added electrons are delocalized, therefore influencing all three vanadium positions;
2. As estimated above, the charge transferred per **PV_{14}** polyoxoanion corresponds to the addition of six electrons when its intensity in the ^{51}V NMR spectrum vanished entirely. Re-oxidation was completed after removing four electrons from each polyoxoanion. The absence of a separator in the NMR tube is a likely reason for this imbalance. During reduction, reduced species diffuses out of the working electrode volume into the supernatant region, and these are replaced by fully oxidised **PV_{14}**. These molecules can also be reduced so that the number of electrons added during reduction is likely higher than the number which would be needed without diffusion. Similarly, in the oxidation phase, less **PV_{14}** can be re-oxidised, because some of the reduced species is able to diffuse away from the working electrode. Therefore, less electrons are removed from the polyanions during the oxidation than would be possible without diffusion.

The conclusion is that **PV_{14}** can be reversibly reduced and oxidised. Taking the error from diffusion into account, it was estimated that the ^{51}V NMR signal disappears after approximately five ((6 + 4) /2 = 5) electrons have been added to the 14 vanadium ions of the POM.

5.5.5 Electrochemical impedance spectroscopy of PV_{14}

In order to determine the redox kinetics of **PV_{14}** electrochemical impedance spectroscopy measurements were performed in 1 M LiCl with 20 mM **PV_{14}**. The experiments were performed and analysed in the same way as for **SiW_{12}** (see section 5.4.2). This solution was reduced by 0.5 electrons per **PV_{14}** molecule by bulk electrolysis and contained then 10 mM **PV_{14}** and 10 mM **PV_{14}^{-}**. The measured open circuit potential was $\boldsymbol{U}_{\mathbf{PV_{14}}}^{\boldsymbol{\theta,1}}$ = 0.75 V vs. SHE for the first reduction. This measurement was repeated to measure the kinetics of the second ($\boldsymbol{U}_{\mathbf{PV_{14}}}^{\boldsymbol{\theta,2}}$ = 0.67 V vs. SHE), third ($\boldsymbol{U}_{\mathbf{PV_{14}}}^{\boldsymbol{\theta,3}}$ = 0.54 V vs. SHE) and fourth electron ($\boldsymbol{U}_{\mathbf{PV_{14}}}^{\boldsymbol{\theta,4}}$ = 0.24 V) transfer of **PV_{14}**. Therefore, 1.5, 2.5 and 3.5 electrons were added to fully oxidised **PV_{14}** to obtain the desired compositions (see Table 9). The obtained spectra were fitted to a Randles circuit and Nyquist plots for all measurements with their fits are shown in Figure 41 (a) and (b).

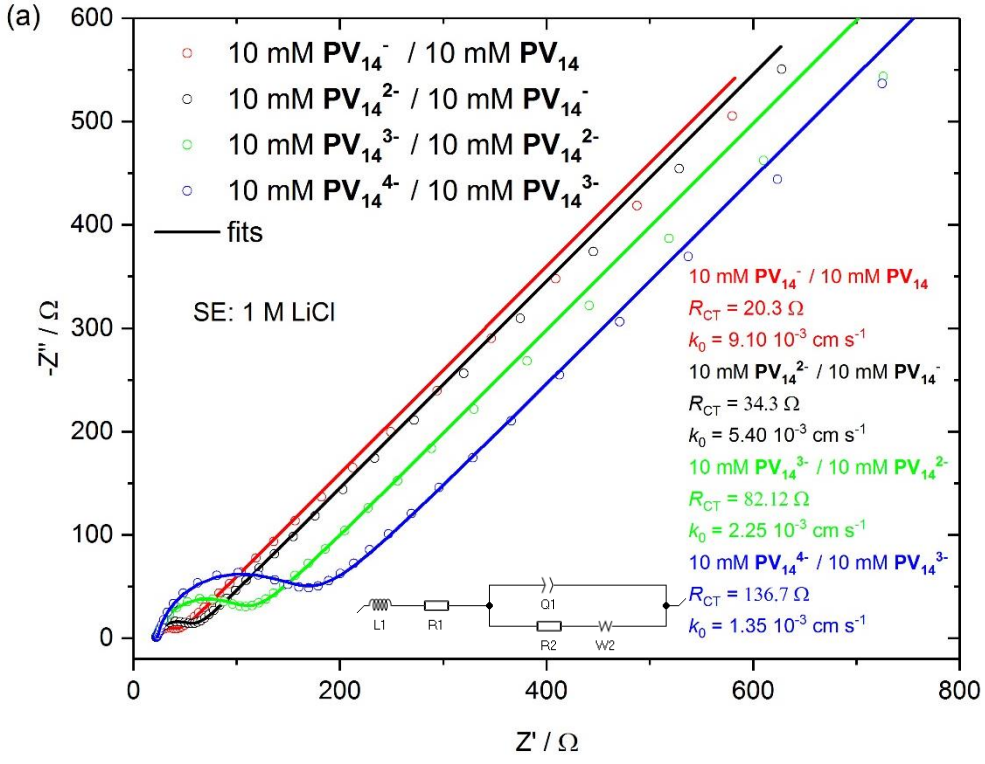

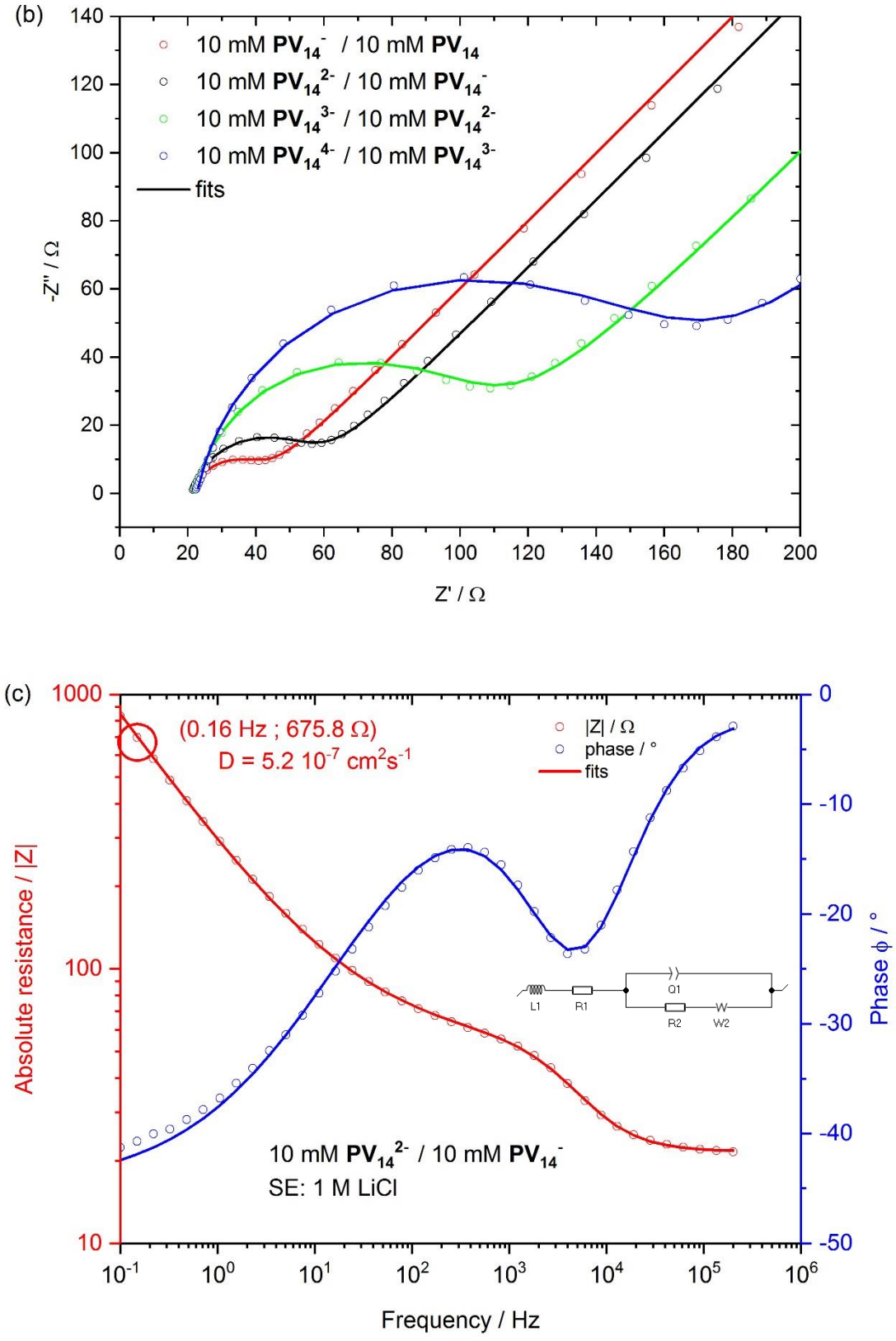

Figure 41 Electrochemical impedance spectroscopy measurements of the first four redox reactions of **PV_{14}**. (a) Nyquist plots of 10 mM **PV_{14}**/10 mM **PV_{14}^-**, 10 mM **PV_{14}^-**/10 mM **PV_{14}^{2-}**, 10 mM **PV_{14}^{2-}**/10 mM **PV_{14}^{3-}** and 10 mM **PV_{14}^{3-}**/10 mM **PV_{14}^{4-}** with fits and the used equivalent circuit shown. (b) Detail of (a) showing the semicircles. (c) Bode plot of 10 mM **PV_{14}^-**/10 mM **PV_{14}^{2-}** with fits. (Experiments conducted by Felix Pfanschilling).

All fitted parameters are given in Table 9. R_{ohm} and the double layer capacitance C_{DL} are very similar for all measurements. The determined electron transfer constants are between $k_0 \approx 9\ 10^{-3} - 1\ 10^{-3}$ cm s^{-1}, slightly lower as for **SiW_{12}**. It appears that the electron transfer constants decrease with reduction of the **PV_{14}** molecule. k_0 for the first redox reaction of **PV_{14}** is very similar to the first redox reaction of **SiW_{12}** and the fourth redox reaction of **PV_{14}** is roughly one order of magnitude slower than the first one.

Table 9 Parameters for first four redox reactions of **PV_{14}** determined by fitting the experimental data to the equivalent circuit given in Figure 41 or by reading the impedance at 0.16 Hz.

	R_{Ohm} / Ω	R_{CT} / Ω	CPE / F $s^{(a-1)}$	α (*)	k_0 / cm s^{-1}	C_{DL} / µF	|Z| at 0.16 Hz/Ω	D / cm^2 s^{-1}
PV_{14}/ PV_{14}^-	21.4	20.3	$5.6\ 10^{-6}$	0.87	0.009	1.32	625	$5.9\ 10^{-7}$
PV_{14}^-/ PV_{14}^{2-}	21.6	34.3	$4.4\ 10^{-6}$	0.89	0.005	1.27	677	$5.2\ 10^{-7}$
PV_{14}^{2-}/ PV_{14}^{3-}	22.4	82.1	$3.9\ 10^{-6}$	0.89	0.002	1.22	883	$3.4\ 10^{-7}$
PV_{14}^{3-}/ PV_{14}^{4-}	22.8	136.7	$4.4\ 10^{-6}$	0.88	0.001	1.28	1036	$2.7\ 10^{-7}$

(*) constant phase element parameter

Electrochemical impedance spectroscopy (see Figure 41 and Table 9) shows that the transfer of the first redox wave, **PV_{14}/ PV_{14}^-** proceeds at a rate of $k_0 = 9\ 10^{-3}$ cm s^{-1} which is significantly more facile than the VO^{2+}/VO_2^+ redox reaction.

The calculated diffusion coefficients D lead to similar values for all reduction states in the order of $D = 10^{-7}$ cm^2 s^{-1} which is reasonable for large molecules. The radius of **PV_{14}** calculated by equation (42) with the hydrodynamic viscosity of 1 M LiCl [236] gives a value of r = 3 nm which is bigger than the radius of **SiW_{12}** r = 2 nm. That can be explained because of the higher negative charge and therefore bigger solvation shell of **PV_{14}**.

5.6 Battery studies of the PV_{14}-SiW_{12}-System

5.6.1 Cross-over studies

One prerequisite for an asymmetric RFB is that the redox shuttles do not penetrate the membrane. The crossover of Fe^{2+}, as archetype for a small transition metal ion, was compared to that of **SiW_{12}** for two commercial membranes, Nafion N117 (thickness 183 µm)

and Fumatech's FUMASEP F-1040 (thickness 40 µm). As the direct comparison of 100 mM Fe^{2+} and 100 mM **SiW_{12}** (Figure 42) showed, the small cation Fe^{2+} easily crosses both tested membranes. The cross-over studies were performed by separating two half-cells each with a volume of 32 cm^3 by a membrane with a surface area of 16 cm^2. One of the half-cells contained a concentration *c* of 100 mM of the species under investigation (Fe^{2+} or **SiW_{12}**) in 1 M H_2SO_4, the electrolyte in the other half-cell was *c* = 20 mM of V^{3+} in the case of Fe^{2+} and *c* = 20 mM of Fe^{2+} in the case of **SiW_{12}**. The half-cell with the high concentration was stirred. In the half-cell with the lower concentration a working-, counter- and reference electrode were used to measure CVs periodically. The measured peak currents for Fe^{2+} and **SiW_{12}** were then converted to concentrations and plotted as seen in Figure 42.

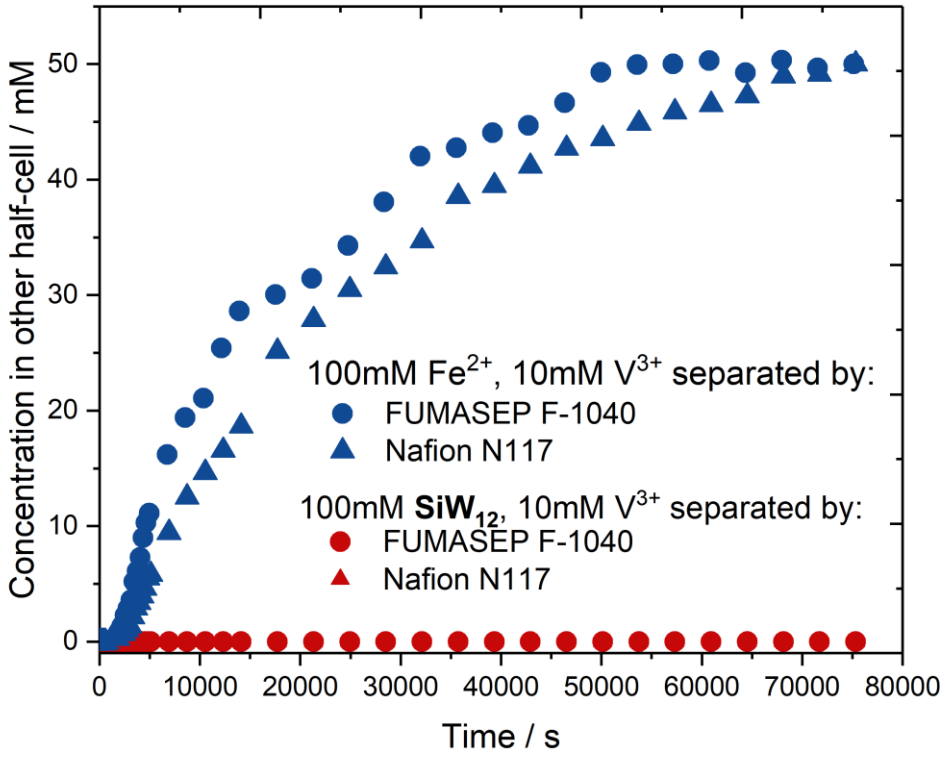

Figure 42 Time dependent concentration of Fe^{2+} (blue data) and **SiW_{12}** (red data) measured by CVs in a half-cell that did not contain these species at *t* = 0 s. (Conducted by Erasmus student).

The half-cell that initially was devoid of Fe^{2+} and was separated by the membrane from a half-cell with 100 mM Fe^{2+}, contained half of the initial concentration (50 mM) of Fe^{2+} after 19 h; the two half-cells had become equilibrated. In the case of the larger anion **SiW_{12}**, both

membranes prevented crossover during the 20 h of monitoring. The inhibition of crossover for the POM can be explained in two ways. First, size exclusion: From x-ray diffraction in solution it is known that the 12 tungsten atoms of **SiW_{12}** form a roughly spherical unit with unit cell of volume $(0.5\ nm)^3$.[216] With terminal oxygen atoms and hydration shell the diameter of the solvated polyoxoanion is likely to exceed 2 nm, as calculated from the Stokes-Einstein equation (42) from the diffusion coefficient. Conductive channels in Nafion membranes were determined to be of variable size from 1 - 100 nm [237,238]. Narrow points in the channel might therefore restrict the movement of the **SiW_{12}** species as they are of similar size. Second, electrostatic repulsion: Both investigated membranes are based on perfluorosulfonic acid ionomers and are therefore cation-conducting membranes. The negatively charged SO_3^- groups in the membrane might repel the $[SiW_{12}O_{40}]^{4-}$ anion, thus preventing it from crossing the separator.

5.6.2 Full cell RFB test

The flow cell studies were performed in a laboratory flow cell with electrode area 5 x 5 cm^2; a detailed description of the setup is given in section 5.3.3. The composition of the anolyte was 0.2 M **SiW_{12}** in 1 M LiCl, and the starting *pH* was adjusted to 1.6 from 0.6. The catholyte comprised 0.1 M **PV_{14}** in 1 M LiCl. Prior to starting the tests, the catholyte was reduced by addition of hydrazine (35% in water) while it was purged with nitrogen. The *pH* was then adjusted to 2.0 from 2.6 by addition of aqueous HCl (1 M). With four electrons per **PV_{14}** molecule added, and each tank containing 60 mL of electrolyte, the theoretical capacity Q^{theo} is:

$$Q^{\text{theo}} = n \cdot V \cdot c \ \cdot F \qquad (44)$$

$$Q^{\text{anolyte}} = 2 \cdot 0.06\ \text{L} \cdot 0.2\ \text{M} \cdot F = 640\ \text{mAh} \qquad (45)$$

$$Q^{\text{catholyte}} = 4 \cdot 0.06\ \text{L} \cdot 0.1\ \text{M} \cdot F = 640\ \text{mAh} \qquad (46)$$

with theoretical capacity of anolyte and catholyte Q^{anolyte} and $Q^{\text{catholyte}}$.

Electrochemical impedance spectroscopy was employed at an open circuit voltage of 1 V with an amplitude of 10 mV and in a frequency range 10 kHz $\leq f \leq$ 50 mHz. The resulting Nyquist plot is shown in Figure 43.

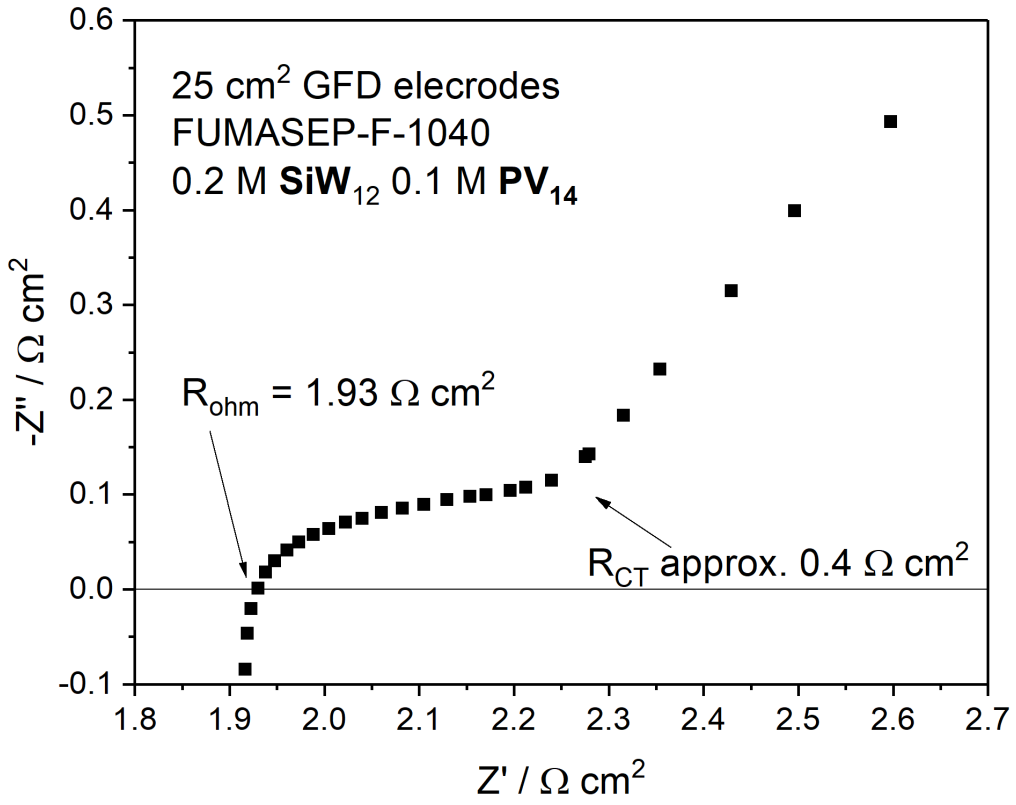

Figure 43 Nyquist spectrum of the flow cell after 155 cycles at an open circuit voltage of 1 V with values for R_{Ohm} and R_{CT} given.

The area specific resistance at high frequencies caused by the Ohmic losses in the current collector, the electrodes and the ionic resistance in the membrane was relatively high for an aqueous system, R_{Ohm} = 1.93 Ω cm^2 (Nyquist plot in Figure 43, for comparison see values in [168]). Typical charge and discharge curves at three different current densities are shown in Figure 44 (a). All curves exhibit two distinct plateaus. These stem from the two redox processes of **SiW$_{12}$** (compare Figure 32). For 30 mA cm^{-2} the theoretical capacity of Q^{theo} = 640 mAh is almost reached at discharge (Q^{exp} = 612 mAh). Coulombic efficiencies are about 94% for each cycle and are slightly higher for higher current densities. The voltage efficiency was 65% at 30 mA cm^{-2}, attributed mainly to the Ohmic losses R_{Ohm} and not to the kinetics of the redox couples. This is based on the three electrode measurements which found high k_0 values for **SiW$_{12}$** in the order of 10^{-2} cm s^{-1} and the Nyquist plot shown in Figure 43 in which the R_{CT} ≈ 0.4 Ω cm^{-2} when R_{Ohm} = 1.93 Ω cm^2.

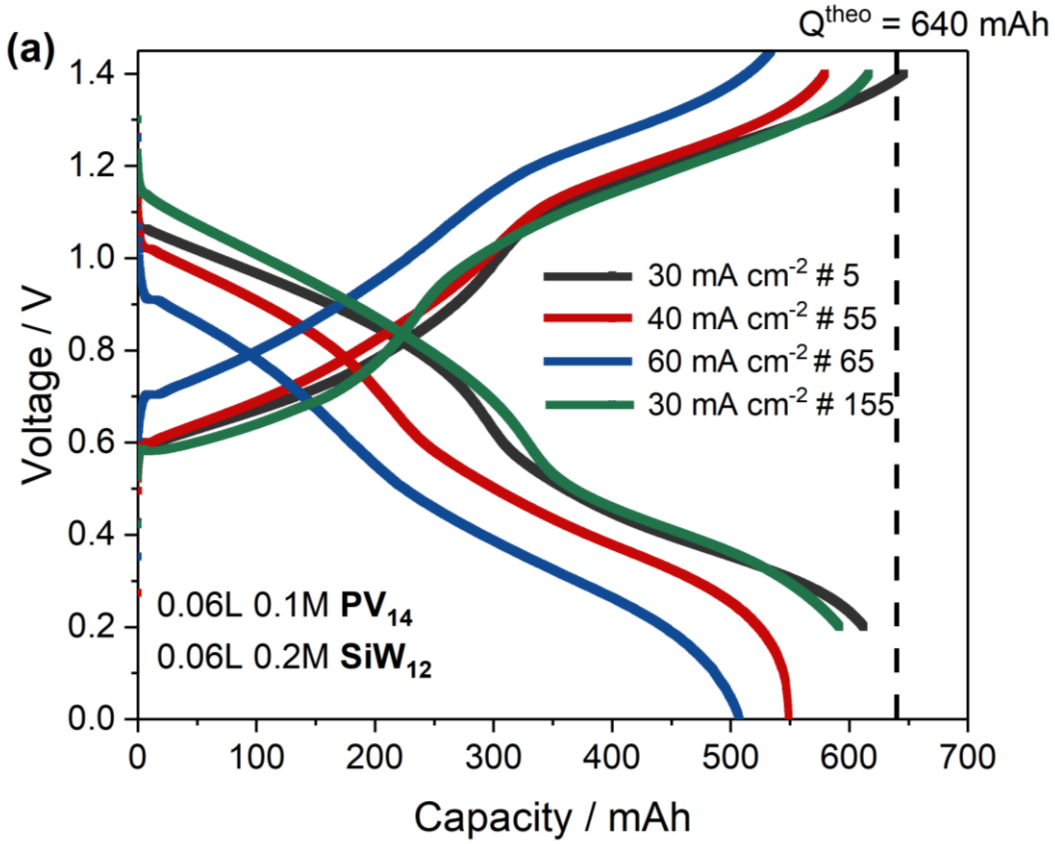
(a)
Q^{theo} = 640 mAh
30 mA cm^{-2} # 5
40 mA cm^{-2} # 55
60 mA cm^{-2} # 65
30 mA cm^{-2} # 155
0.06L 0.1M PV_{14}
0.06L 0.2M SiW_{12}
Voltage / V
Capacity / mAh

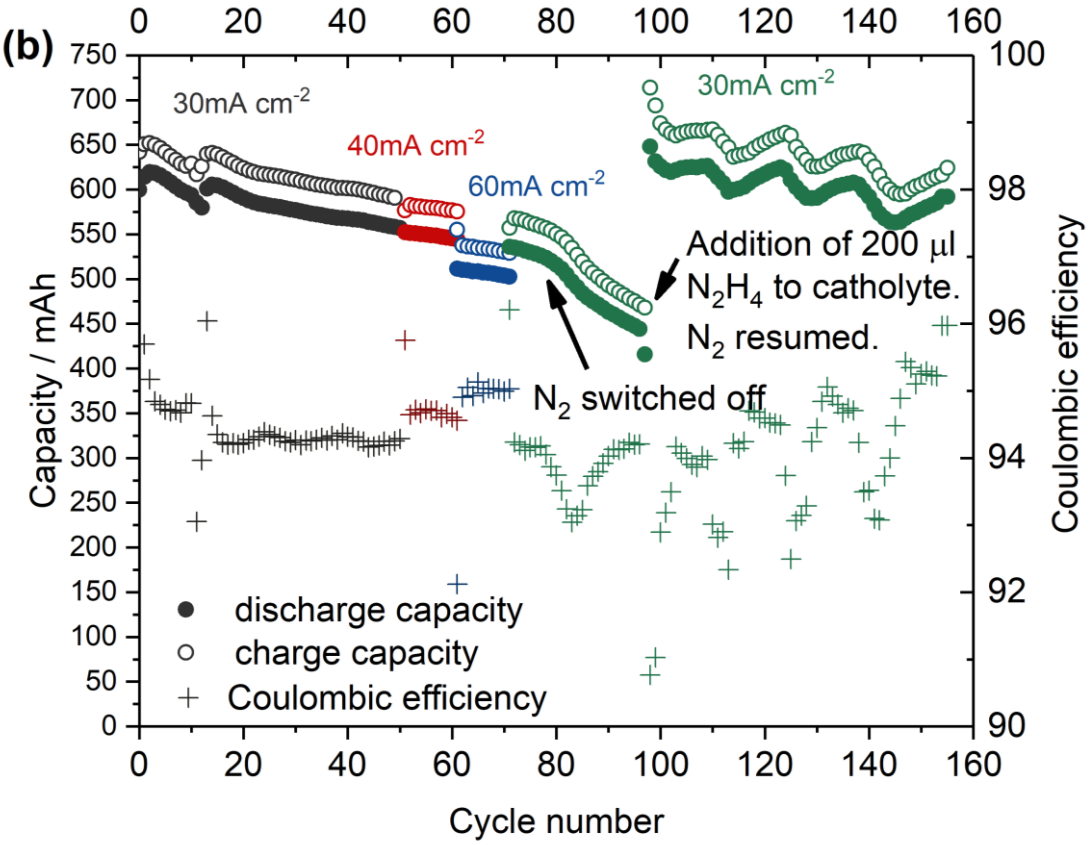
(b)
30mA cm^{-2}
40mA cm^{-2}
60mA cm^{-2}
30mA cm^{-2}
Addition of 200 µl N_2H_4 to catholyte.
N_2 resumed.
N_2 switched off
discharge capacity
charge capacity
Coulombic efficiency
Capacity / mAh
Coulombic efficiency
Cycle number

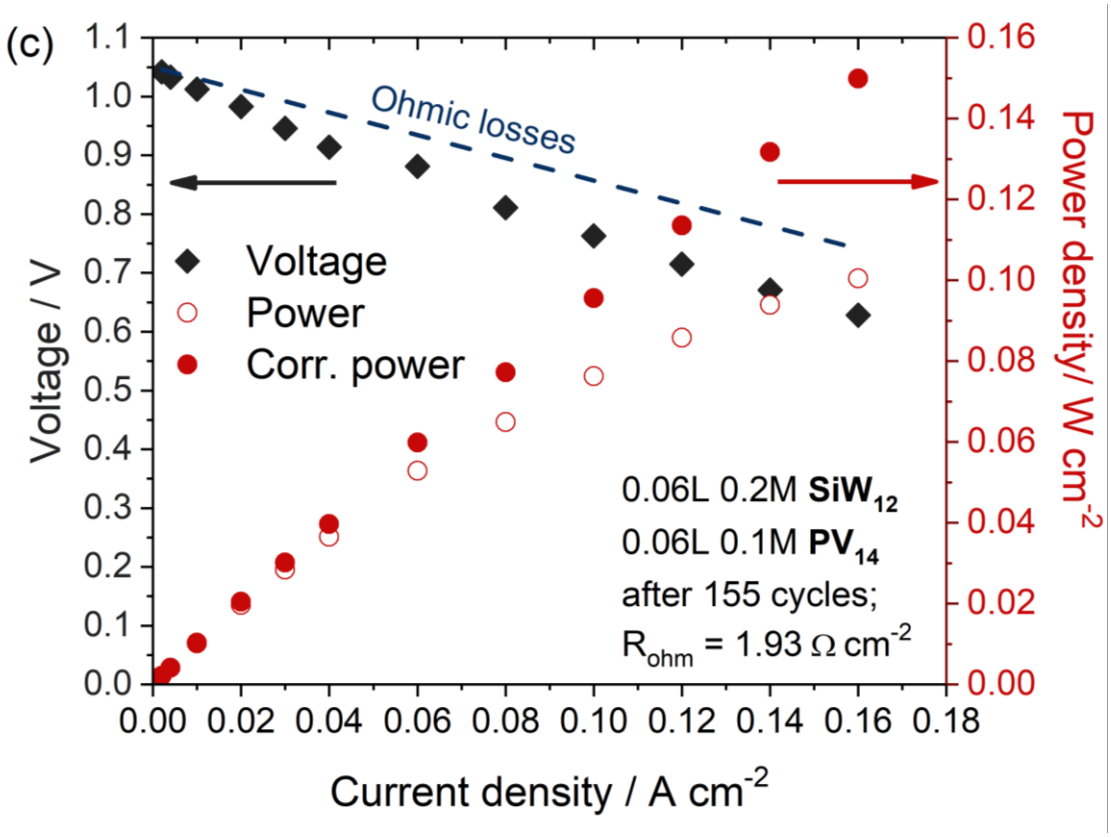

Figure 44 Flow cell studies on a cell using 0.2 M **SiW_{12}** as anolyte and 0.1 M **PV_{14}** as catholyte in 1 M LiCl. (a) Typical charge and discharge curves for cycle number 5 at 30 mA cm^{-2} (grey curves), number 55 at 40 mA cm^{-2} (red curves), number 65 at 60 mA cm^{-2} (blue curves) and the last cycle (number 155) at 30 mA cm^{-2} (green curves). (b) Charge (open circle) and discharge (full circle) capacity for cycles 1-155 with current density indicated. Coulombic efficiencies are given as + symbol (c) Rate test for RFB starting at an open circuit voltage of 1.05 V. The left ordinate gives the discharge voltage, the right ordinate the achieved power density. The voltage drop due to R_{Ohm} is shown by a broken line.

This cell was cycled for 14 days, completing 155 charge and discharge cycles. The measured capacities are shown in Figure 44 (b). For 50 cycles a current density of 30 mA cm^{-2} was applied (grey markers), followed by ten cycles with 40 mA cm^{-2} (red markers) and 60 mA cm^{-2} (blue markers) each. Then the initial current density of 30 mA cm^{-2} (green markers) was reapplied to show that ageing has a negligible effect on the battery. From cycle 20 to cycle 71 the capacity remained relatively stable and decayed with 1 mAh/cycle. Relative to the highest achieved discharge capacity (619 mAh in cycle 2), this equals a capacity decay of 0.16% per cycle.

Chemical oxidation of reduced **SiW_{12}** and reduced **PV_{14}** by the oxygen in the atmosphere is the most likely reason for the observed capacity fade. To test this hypothesis, the nitrogen gas purge of the battery containment was stopped at cycle 80, thus permitting the ingress of

atmospheric oxygen. From cycle 85 to 97 an increased capacity fade of 3.5 mAh/cycle or 0.56%/cycle was measured, suggesting that the measured capacity fade is due oxidation by oxygen [239]. During cycle 98, 200 µL of hydrazine were added to the catholyte and the nitrogen purging was resumed. This addition of a reducing agent replenished the full capacity of the RFB: Cycle 98 had a discharge capacity of 648 mAh, which even exceeded the theoretical capacity. To achieve this, **SiW_{12}** can partly access its third, two-electron redox reaction, and **PV_{14}** can take up more than 4 electrons per anion. Figure 36 (d) shows the charge and discharge of a symmetric RFB that operates with **PV_{14}** in both electrolytes. The curves indicate that **PV_{14}** can store at least seven electrons. After the hydrazine injection, the cell test was continued to reach a total operation time of 14 days and the capacity fade continued to be 0.16%/cycle. The capacity oscillates in a day/night cycle, maxima in capacity are separated by 24 hours. It is known from other experiments that the day-night cycle is mainly influenced by temperature changes. The columbic efficiency oscillates with the same periodicity as the capacities.

After the 155th cycle the cell was charged to reach an open circuit voltage of 1.05 V, then the cell was discharged at a certain current rate for 2 mAh, and immediately after that charged for 2 mAh. This was done for current densities from 2 mA cm^{-2} to 160 mA cm^{-2}. The discharge voltage and power at these current densities are shown in Figure 44 (c). The maximum achieved power density was 100 mW cm^{-2} at 160 mA cm^{-2}. At this current density 73% of the voltage drop is caused by the Ohmic resistance of the cell (R_{ohm} = 1.93 Ω cm^{-2}).

A ^{51}V NMR spectrum of the catholyte was obtained after the 155 charge and discharge cycles shown in Figure 44 at a moment when it was fully charged. The *pH* of the solution was 1.2. This spectrum is shown in Figure 45 and is very similar to the spectra shown in Figure 38 (a).

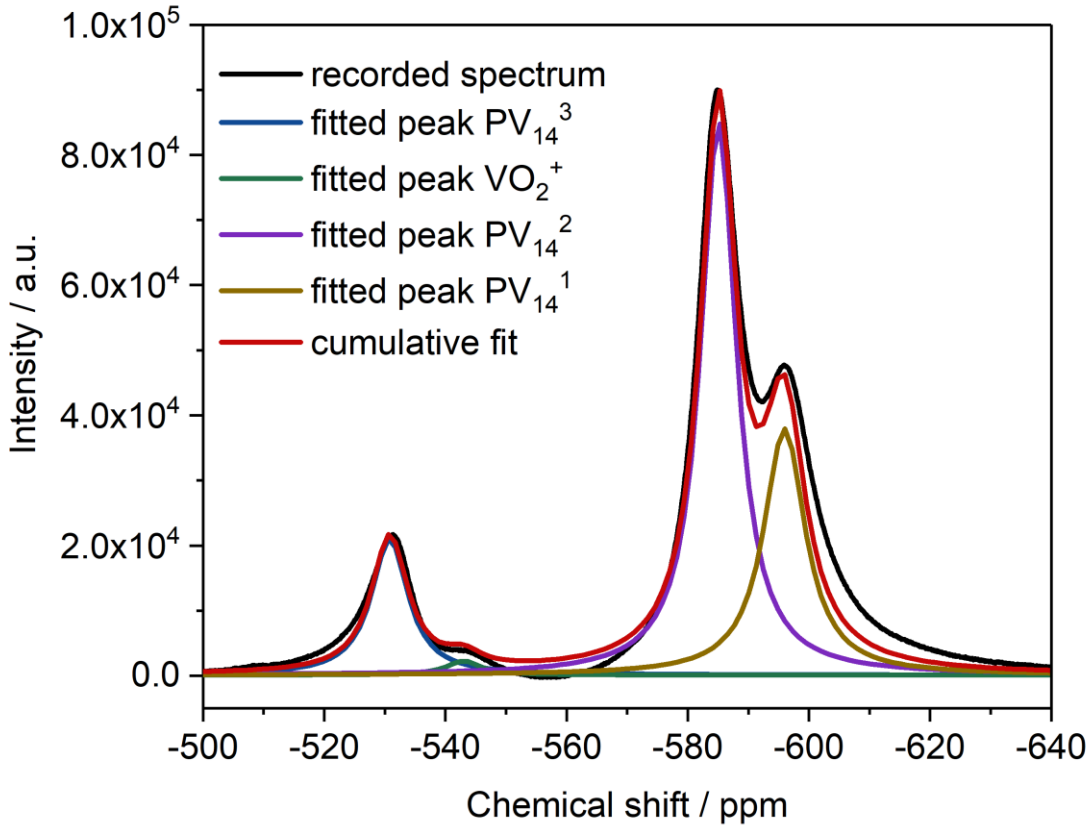

Figure 45 ^{51}V NMR spectra of the catholyte after 155 charge and discharge cycles which took 14 days. The individual contributions were fitted to Lorentzian curves.

Most of the vanadium is present as **PV_{14}**, however, a contribution from VO_2^+ at -544 ppm is also visible. Fitting of the peaks and data analysis revealed that the ratio of VO_2^+ to PV_{14}^3 signals is 0.10, and therefore the presence of VO_2^+ is as expected for the measured *pH*. This indicates, that degradation due to electrochemical processes does not contribute to the decomposition of **PV_{14}.** A ^{51}V NMR spectrum of the anolyte after 155 charge and discharge cycles gave no signal, indicating that no vanadium containing species had crossed through the membrane.

Table 10 Peak positions and integrated intensities for the curves fitted to the ^{51}V spectrum shown in Figure 45.

Peak	Chemical shift / ppm	Integrated Intensity	Ratio to PV_{14}^3
PV_{14}^3	-530.8	240000	1.0
VO_2^+	-543.0	23500	0.1
PV_{14}^2	-585.1	960000	4.0
PV_{14}^1	-596.0	495000	2.1

5.7 Discussion

In this study an asymmetric all-POM RFB utilising **SiW_{12}** as anolyte and **PV_{14}** as catholyte is presented. Four hypotheses regarding the suitability of POMs for RFBs were tested.

1. It was shown that electron transfer using **SiW_{12}** is fast. An electron transfer in the order of $k_0 = 10^{-2}$ cm s^{-1} was determined by EIS which is four orders of magnitude faster than that of the vanadium redox reactions employed in the VRFB.[3] The simultaneous decrease of the three **PV_{14}** peaks in the *in-situ* ^{51}V NMR spectrum (Figure 40) also indicates that added electrons are delocalised. The loss in voltage of the battery cell was mostly determined by the Ohmic drop and not by charge transfer resistances.
2. In cross-over studies, two types of commercial cation exchange membranes prevented **SiW_{12}** from crossing over into an adjacent half-cell (Figure 42). After 14 days of RFB operation no vanadium was found in the anolyte by ^{51}V NMR. Electrostatic repulsion between the SO_3^- groups of the membranes and the polyoxoanions, and limited transport of the POMs (1 nm) through membrane channels of comparable size (1-100 nm) are likely causes of this prevention of cross-over [216,237,238].
3. *In-situ* ^{51}V NMR showed that **PV_{14}** was stable during reduction and oxidation (Figure 40). Furthermore, the decavanadate also spontaneously reassembled after decomposition in excessively acidic or alkaline solvents when the *pH* was restored to 2.3 (Figure 39).
4. With concentrations of 0.1 M for **PV_{14}** and 0.2 M for **SiW_{12}**, the RFB had a capacity of 10.7 Ah L^{-1} and was able to reach this theoretical value reliably with minimal capacity loss (0.16% per cycle). The capacity loss was due to ingress of atmospheric oxygen and not due to instability of the redox shuttles. In VRFBs capacity decays of 2%/cycle [57] or 75% after 50 cycles [5] have been reported. For the metal-free anthraquinone-bromine RFB an average capacity fade of 0.8%/cycle was reported [135]. In addition, the full capacity of the all-POM RFB could be restored by adding a reducing agent to the catholyte.

The above four points illustrate the potential for POMs as designable redox shuttles for flow batteries. There are several possible avenues for improvement:

Energy density: Two approaches are available to increase the capacity: First, to utilise more electrons per molecule. It was able to show that **PV_{14}** can be reduced by as many as seven electrons (Figure 36 (d)), whereas during battery operation the molecule was reduced by only four electrons. The limit to this needs to be explored. From its CV it is clear that **SiW_{12}** can be reduced by four electrons (Figure 32 (a)), two more than are currently utilised in the battery anolyte. However, in order for these two additional electrons to be used the decomposition reaction of **SiW_{12}** at low potential must be understood and prevented [228]. Second, the concentration of the POMs could be increased. For $H_4SiW_{12}O_{40}$, the maximum concentration at room temperature measured was 0.875 M.

Power density: The asymmetric POM-RFB reached a power density of 100 mW cm^{-2} at an open circuit voltage of 1.05 V. For commercial VRB systems power densities of 50 – 300 mW cm^{-2} (at 1.40 – 1.60 V) are reported [240]. The Ohmic drop causes 73% of the voltage loss, and this should therefore be improved with the highest priority. When correcting for the Ohmic drop a power density of 150 mW cm^{-2} can be achieved (shown in Figure 44 (c)). Common RFBs are operated in highly acidic conditions, and therefore protons can be used to transfer the charge across the membrane. Since the asymmetric POM-RFB operates in only mildly acidic conditions, it is necessary to use Li cations for charge transport, and it can be assumed that Li transport leads to a lower conductivity than proton transport (Li^+: 38.7 S cm^2 mol^{-1}, H^+: 349.6 S cm^2 mol^{-1} at 298 K in water [241]). Thinner membranes, or separators working on the basis of size exclusion should be tested to take advantage of the large size of the POMs.

5.8 Options to improve the new POM battery system/increase energy density

5.8.1 Lead additive to the anolyte

As described in section 5.4.1, the reduction of **SiW_{12}** was restricted to the first two electron transfers because at low potentials the POM irreversibly modifies the electrode which leads to its decomposition of the POM and catalysis of the HER [130]. An access of four than two electrons per molecule **SiW_{12}** would double the energy density of the anolyte. An approach to make that feasible is to shift the HER to more negative potential and to inhibit the decomposition reaction of the POM at low potential. The idea is to significantly exceed the decomposition voltage of water by increasing the over-voltage for hydrogen on the

electrode surface. One example for an application that makes use of the strong increase in hydrogen overvoltage is the lead acid battery. The overvoltage of hydrogen on lead is so high that the HER only occurs at an acid concentration of more than 4 M at a noticeable rate [242]. In the following experiments a lead additive was added to the anolyte with the idea that the addition of lead to the electrolyte is followed by the subsequent deposit of metallic lead onto the negative electrode and therefore increases the over-potential for the HER significantly. Hence, four instead of two electrons would be usable instead of just two (see also Figure 31). Figure 46 (a) and (b) shows the results of stationary battery cell tests of 0.01 M **SiW_{12}** as anolyte and 0.02 M **PV_{14}** as catholyte, initially reduced with hydrazine by two electrons, in 1 M LiCl with (b) and without (a) lead additive.

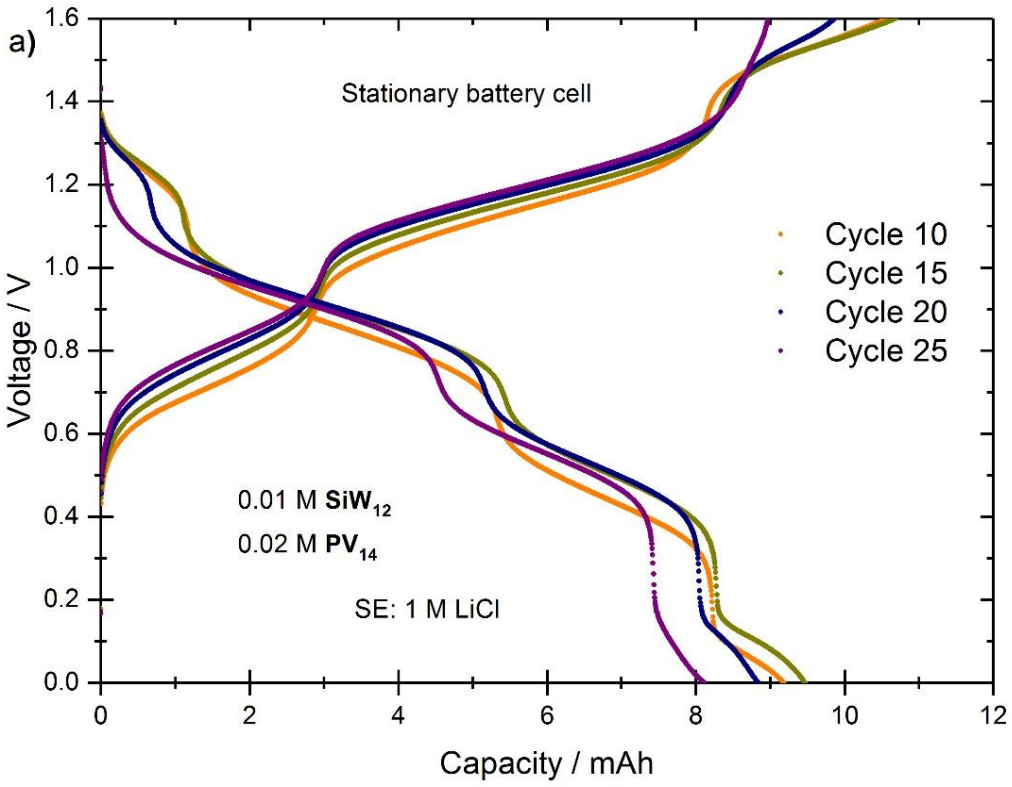

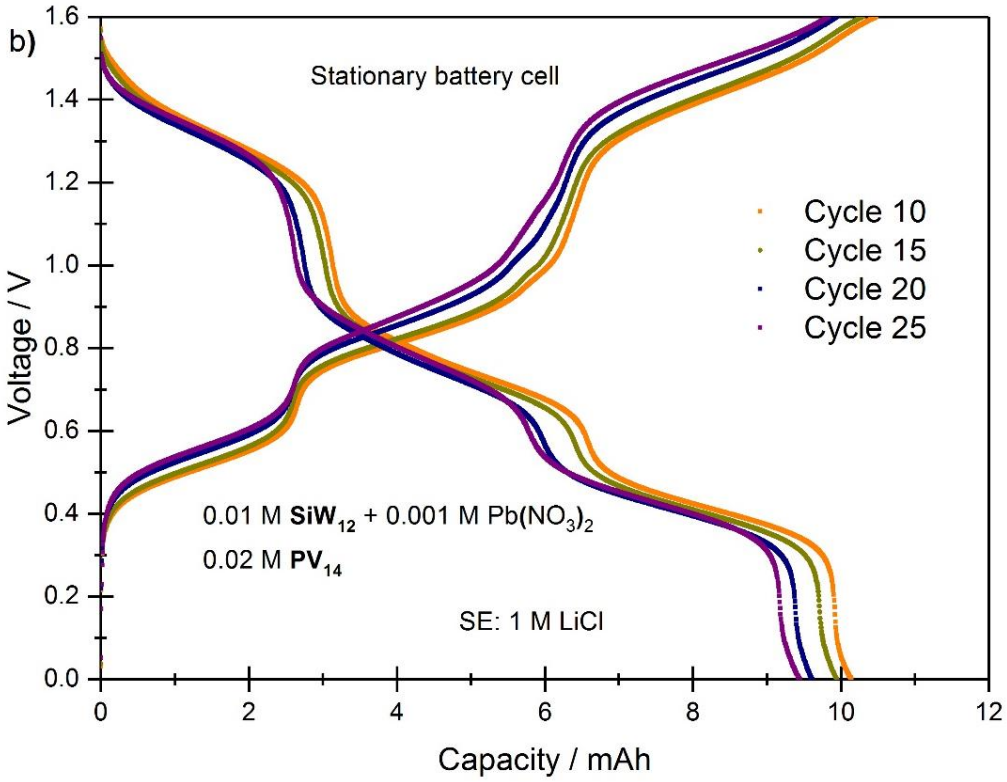

Figure 46 Stationary battery cell studies and Typical charge and discharge curves, I = 1.25 mA cm^{-2}, of selected cycles using (a) 10 ml 0.01 M **SiW_{12}** as anolyte and 10 ml 0.02 M **PV_{14}** as catholyte in 1 M LiCl and (b) 10 ml 0.01 M **SiW_{12}** as anolyte and 10 ml 0.02 M **PV_{14}** with 0.001 m lead(II)nitrate as catholyte in 1 M LiCl.

Figure 46 (a) shows selected cycles for the stationary battery test of the POM system without lead additive. The theoretical capacity is 10.7 mAh but the maximum capacity reached is lower and decreases with cycle. Cycle 10 and 15 show the three expected plateaus that stem from the first, second and third/fourth electron. Afterwards the shape of the curves change and the length of the third plateau decreases and disappears completely at cycle 25. This is indicative for an irreversible decomposition of **SiW_{12}** because the last cycle shows the pattern of a two electron transfer instead of four electrons in the beginning. Figure 46 (b) shows selected cycles for the stationary battery test of the POM system with 1 mM lead additive. The maximum capacity is higher and decreases less with ongoing cycling. The curves show three plateaus and the shape does not change which indicates that the **SiW_{12}** does not decompose during cycling. The lead additive makes four instead of two electrons of the anolyte accessible what leads to an increase of the energy density of the battery by a factor of two. This result shows a significant improvement of the POM system

and should be transferred from the stationary cell test into a RFB to increase the energy density of the anolyte.

5.8.2 Increase of solubility of the catholyte

To reach a higher energy density of the battery another approach is to increase the solubility of the catholyte. The used catholyte **PV_{14}** has a lower solubility than the anolyte and limits the energy density.

Investigations show that the sodium, potassium, rubidium and cesium ions all are weakly hydrated with only a single shell of water molecules. Because the lithium cation is much smaller than the sodium cation it is more strongly hydrated, most probably with a second hydration shell present [243], hence, its hydration energy and solubility is higher. **PV_{14}** is present $Na_{4.75}H_{4.25}[PV_{14}O_{42}] \cdot NaCl \cdot 12H_2O$ as it is synthesised using sodium metavanadate as starting material and recrystallized in sodium chloride solution, leads to a maximum concentration of 0.2 M L^{-1}. The idea is to increase the solubility by exchanging the sodium cation by the smaller lithium cation, therefore, a new synthesis route was developed. The new **Li-PV_{14}** was synthesised under similar conditions as the (see section 5.3.1) **Na-PV_{14}**. Instead of $NaVO_3$, $LiVO_3$ was used and **Li-PV_{14}** was obtained without further purification by precipitation due to high solubility and a ^{51}V NMR spectrum was recorded. Figure 47 shows the ^{51}V NMR spectra of **Na-PV_{14}** and **Li-PV_{14}** for comparison.

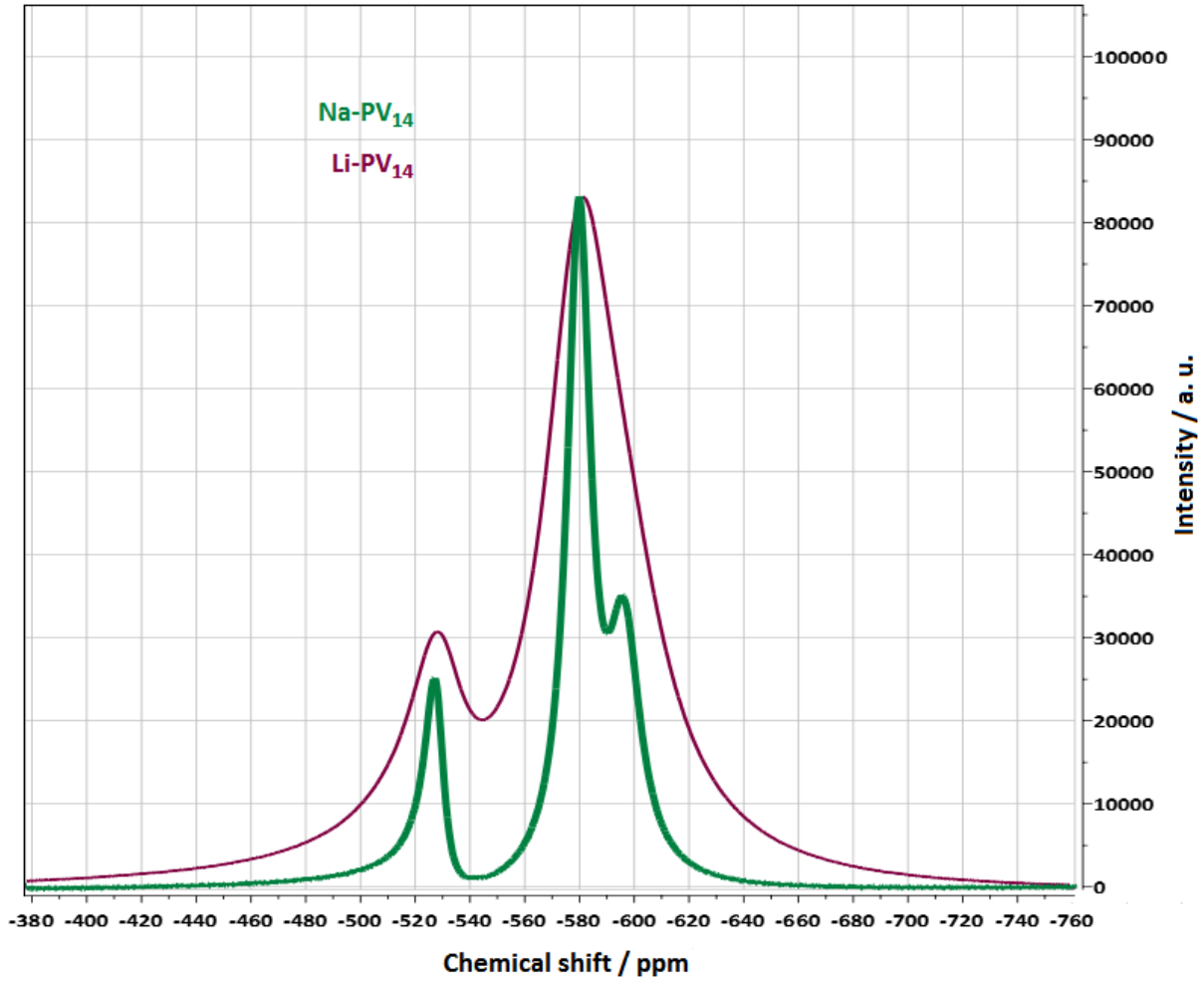

Figure 47 ^{51}V NMR spectra of **Na-PV$_{14}$** (green line) and **Li-PV$_{14}$** (red line) in water.

The peaks of **Li-PV$_{14}$** appear at the same chemical shift as those for **Na-PV$_{14}$**. The peaks are broader which leads to a superimposition and disappearance of the third peak at -596 ppm with Li^+ as counter ion. The broadening of ^{51}V NMR spectra of pentavalent vanadium compounds is usually due to the quadrupole moment of this nucleus, although chemical exchange cannot be completely ruled out. The quadrupolar broadening depends upon the local symmetry at vanadium and the molecular tumbling rate. The latter will be affected by the temperature, the effective dynamic radius (which may depend upon ion pairing - hence the difference between the Li and Na samples) and concentration. Spectral simulations were conducted by Prof. William McFarlane and an approximate doubling of the ^{51}V line width can make the third signal “vanish”. No side products like $[V_{10}O_{28}]^{6-}$ are visible. The new synthesis was successful and it was possible to obtain a new POM which has not been published in literature so far. Using $LiVO_3$ as starting material leads to a 3.5-fold concentration of **Li-PV$_{14}$**

with 0.7 M L^{-1} compared to **Na-PV_{14}**. Figure 48 shows an overview about the cation effect on the solubility of the polyoxometalates **PV_{14}** and **SiW_{12}**.

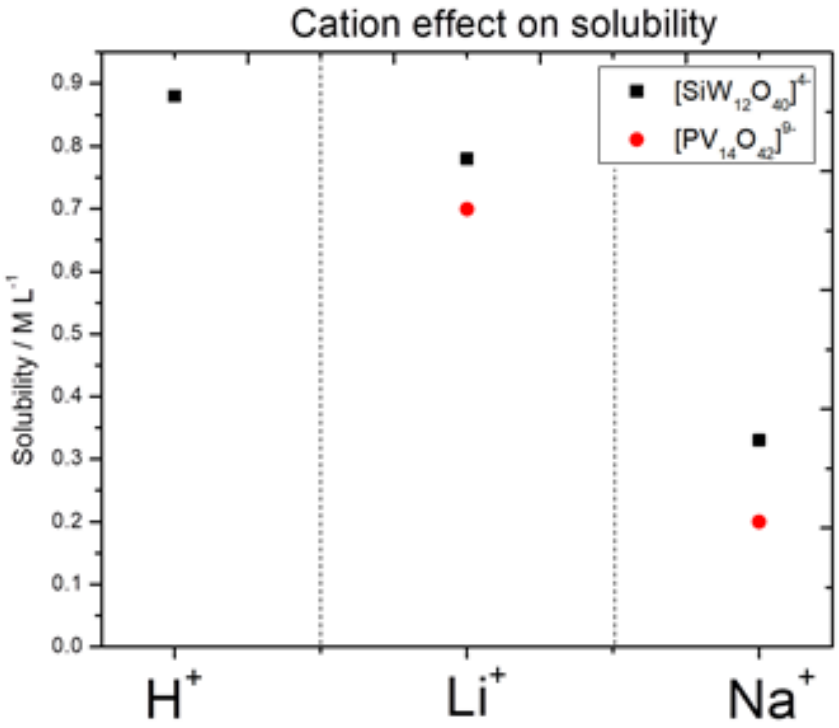

Figure 48 Cation effect on the solubility of the polyoxometalates **PV_{14}** and **SiW_{12}**.

Flow cell tests were conducted applying 0.06 L 0.1 M **SiW_{12}** as anolyte and 0.06 L 0.05 M **Li-PV_{14}** as catholyte in 1 M LiCl and applying 0.06 L 0.6 M **SiW_{12}** as anolyte and 0.06 L 0.3 M **Li-PV_{14}** as catholyte. Initially the catholyte was reduced chemically with hydrazine by four electrons per molecule **Li-PV_{14}** and the anolyte was applied in its oxidised form. One selected charge and discharge curve per concentration is shown in Figure 49. The red curve shows the result for the low concentration and the blue curve the results for the high concentration. The theoretical capacity for both systems is shown as vertical line.

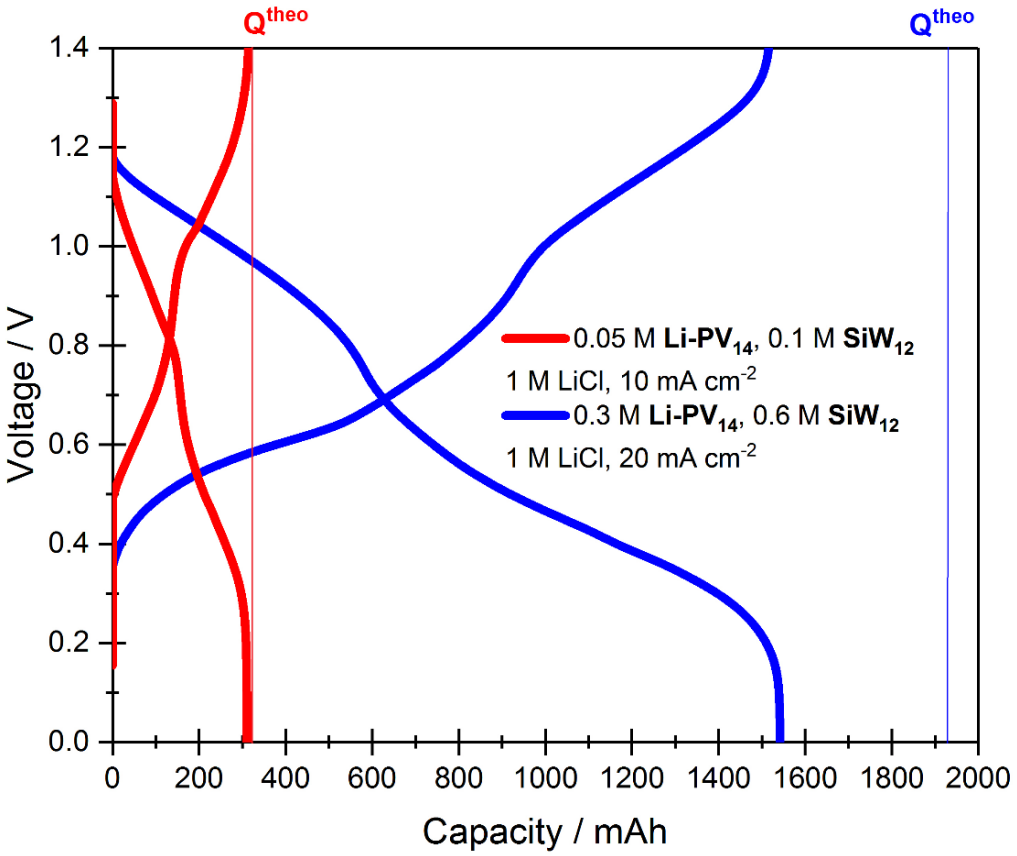

Figure 49 charge and discharge curves of flow cell studies on a cell using (red curve) 0.06 L 0.1 M **SiW_{12}** as anolyte and 0.06 L 0.05 M **Li-PV_{14}** as catholyte initially reduced with hydrazine by four electrons in 1 M LiCl, (blue curve) 0.06 L 0.6 M SiW_{12} as anolyte and 0.06 L 0.3 M **Li-PV_{14}** as catholyte initially reduced with hydrazine by four electrons in 1 M LiCl. The theoretical capacity for both systems are shown by a vertical line.

The applied current density was 10 mA cm^{2-} for the low concentration and 20 mA cm^{2-} for the high concentration. Both curves exhibit two distinct plateaus, which stem from the two redox processes of **SiW_{12}** (compare Figure 32). For the RFB test with 0.05 M **Li-PV_{14}** the reached discharge capacity was 312 mAh which is 97% of theoretical value (Q^{theo} = 322 mAh) and for the RFB test with 0.3 M **Li-PV_{14}** the reached discharge capacity was 1542 mAh which is 80% of theoretical value (Q^{theo} = 1930 mAh). For high concentration $Q^{discharge}$ does not match Q^{theo} because a too fast chemical reduction with hydrazine before the experiment could lead to a decomposition of the POM. Before application of reduced **Li-PV_{14}** the electrolyte was filtered to remove precipitated side products which leads to a decrease in total concentration of the catholyte. A possibility to improve that is to reduce the catholyte electrochemically before the experiment to avoid decomposition. These flow cell

experiments show that it is possible to replace the **Na-PV_{14}** successfully by **Li-PV_{14}** and therefore to increase the concentration to 0.7 M L^{-1} which enhances the energy density by a factor of 3.5.

5.9 Conclusion

As described in previous chapters, overall-improvements of the VRFB system are limited by the sluggish kinetics of the V^{2+}/V^{3+} and VO^{2+}/VO_2^+ redox reaction. This chapter presented a new class of redox electrolyte, polyoxometalates, which combines the tuneability of organic molecules with the stability of metal ions to overcome the limitations of the VRFB. The main feature of the investigated POMs is that the kinetics of the electron transfer are 1000 times faster than the kinetics of the VRFB. This is a great benefit because k_0 is proportional to the power density and this enhancement is a milestone in RFB research, opening new avenues for large-scale energy storage. Research in the field of new electrodes and cell design should be carried out to tailor and optimize their properties to the facile kinetics of POMs. Crossover studies showed that no crossover into the other half-cell occurs during long-time cycling which improves the lifetime of RFBs enormously. Hence, thinner membranes or separators could be applied for this system which would lower the cost of the battery system because membranes are implicated as substantial contributors to the capital cost of VRFBs [46]. Investigations regarding new membranes should be carried out and should be optimized for the new POM system. *In-situ* ^{51}V NMR experiments were conducted and showed that **PV_{14}** is stable during reduction and oxidation. For this experiment a self-made electrochemical cell was built inside a NMR tube with an inner diameter of only 4 mm. This novel set-up enables electrochemical *in-situ* investigations and offers a deeper insight into electrochemical processes in general. This application could be useful tool for the investigation of other systems, too. Options to improve the all-POM battery system in terms of the energy density were discussed and initial experiments showed promising results. A lead additive was given to the anolyte which significantly enlarged the hydrogen overvoltage with the aim to make four instead of two electrons per **SiW_{12}** molecule accessible. Initial stationary battery cell tests showed a stable cycling behaviour with a two-fold energy density of the anolyte. Further investigations regarding the optimum of lead concentration should be conducted and, for instance, SEM analysis should be carried out to investigate the

lead deposition on the electrode surface. Furthermore, a new synthesis method using lithium metavanadate instead of sodium metavanadate was successfully conducted which lead to an exchange of the counter cation in **PV_{14}** from Na^+ to Li^+. Hence, the maximum concentration of the catholyte could be increased by a factor of 3.5 and initial flow battery tests with a three times higher concentration of the catholyte and showed promising results. Some precipitation during the chemical reduction of **Li-PV_{14}** was observed, prior the flow battery tests. Investigations regarding the initial reduction of the catholyte should be conducted in the future to provide a higher concentration and therefore a higher energy density of the system. These results are worth carrying out further experiments to optimize the system. The newly developed system can be regarded as a model system for POM RFBs and offers many advantages compared to the commercially available VRFB. To improve the system further, more suitable POMs for the application symmetric and asymmetric RFBs should be investigated and research regarding new cell design should be focussed on. Main criteria should be costs of the chemicals and number of transferred electrons per molecule.

CHAPTER 6. DISCUSSION AND OUTLOOK

This work shows possibilities to improve the energy and power density of RFBs. The main drawbacks of the VRFB are the sluggish kinetics of the V^{2+}/V^{3+} and the VO^{2+}/VO_2^+ redox reactions which limit the current density and therefore the power density [3]. The power density is proportional to the electron transfer constant k_0 which indicates that the power density of the VRFB is limited by the charge transfer resistance. As described in previous chapters many attempts have been made to improve the application RFB, for instance, by heterogeneous catalysis. Since it was shown in the literature that the VO^{2+}/VO_2^+ redox reaction cannot be catalyzed by oxygen functional groups on carbon electrodes [2–5] homogeneous catalysis was conducted in this work to enhance the kinetics VO^{2+}/VO_2^+ redox reaction. The kinetics of the VO^{2+}/VO_2^+ redox reaction have been investigated in 1M sulphuric and 1 M phosphoric acid by cyclic voltammetry, chronoamperometry, electrochemical impedance spectroscopy and flow battery. The transfer of the system from 1 M sulphuric acid to 1 M phosphoric acid increases the electron transfer constant k_0 up to 67 times. At higher over-potentials the determined currents match for the two electrolytes. This over-potential dependent difference in electron transfer constant is explained by variable contributions from three reaction mechanisms for the oxidation of VO^{2+} to VO_2^+, and by the presence of adsorbed intermediates for the reduction of VO_2^+, which means that the complex reaction mechanism is a combination of electron transfer and chemical reaction. In a laboratory scale flow cell that employed dilute vanadium electrolyte, it was possible to show that the over-voltages can be significantly lower in phosphoric acid as compared to sulphuric acid. This study shows that the redox kinetics of the VO^{2+}/VO_2^+ can be considerably accelerated by altering the chemical environment of the vanadium ions, and that this effect can also be transferred into a flow battery [6]. Despite all efforts made in recent years to improve the VRFB system its potential for further optimization is limited because of low k_0.

The idea in this work was to overcome the limitations of the system with a new chemistry. A new class of redox electrolyte which combines the tuneability of organic molecules with the stability of metal ions was suggested to improve the remaining disadvantages and two polyoxometalates, were investigated in detail. It was shown that these POMs exhibit facile redox kinetics (electron transfer constant $k_0 \approx 10^{-2}$ cm s^{-1} for $[SiW_{12}O_{40}]^{4-}$, which is four

orders of magnitude faster than V^{2+}/V^{3+} and VO_2^+/VO^{2+}), thereby enabling high power densities; in addition, they feature multi-electron transfer, realizing a high capacity per molecule; they do not cross cation exchange membranes, eliminating self-discharge through the separator and capacity fade; and they are chemically and electrochemically stable as shown by *in-situ* NMR. The catholyte species even spontaneously reassembles when destroyed by adverse solvent conditions. In flow battery studies the theoretical capacity (10.7 Ah L^{-1}) could be achieved under operating conditions. The cell showed a capacity fade of 0.16% per cycle due to oxidation by oxygen when the cell was cycled for 14 days with current densities from 30 to 60 mA cm^{-2} (155 cycles). The Coulombic efficiency was 94% during cycling. Very small losses occurred due to residual oxygen in the system. The voltage efficiency (~65% at 30 mA cm^{-2}) was mainly affected by Ohmic rather than kinetic losses.

Options to improve the all-POM battery system were discussed and initial experiments showed promising results concerning the improvement of the energy density. A lead additive was given to the anolyte to significantly enlarge the hydrogen overvoltage with the idea to make four instead of two electrons per **SiW_{12}** molecule accessible. Initial stationary battery cell tests show a stable cycling behaviour with a 2-fold energy density of the anolyte. Furthermore, a new synthesis was successfully developed to exchange the counter cation in **PV_{14}** from Na^+ to Li^+ with the idea to increase the solvation energy and thus the maximum concentration of the catholyte. Solubility studies show a 3.5-fold higher solubility of the new **Li-PV_{14}** compared to **Na-PV_{14}**. Initial flow battery tests were conducted with a three times higher concentration of the catholyte and show promising results. The results are worth carrying out further experiments to optimize the system.

The main feature of the POMs is that the kinetics of the electron transfer are 1000 times faster than the kinetics of the VRFB. This enhancement is a milestone in RFB research, opening new avenues for large-scale energy storage. Crucial to technology and breakthrough, however, are the cost per kWh stored, also in terms of the target by the ARPA-e of DOE to limit the capital cost to US$100 per kWh for widespread adoption (see Chapter 2). Important are investment costs, maintenance costs and lifetime. The price for vanadium for example has increased drastically during the last years which can be seen in Figure 50.

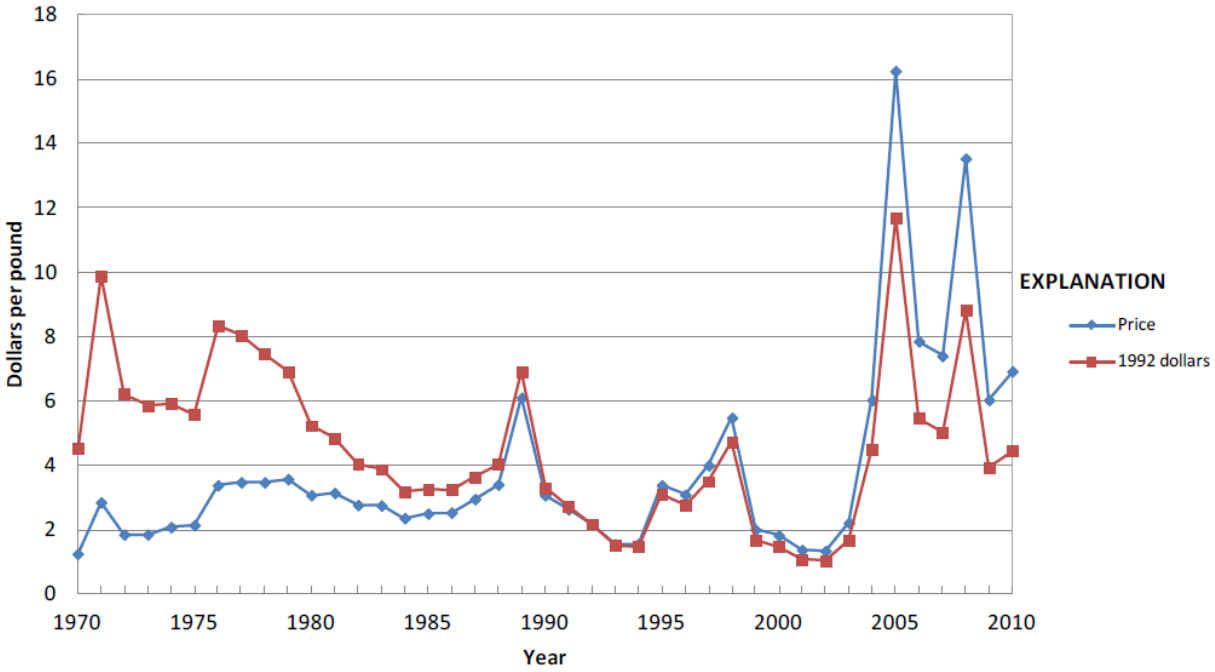

Figure 50 Annual average vanadium pentoxide price (min. 98%, anhydrous), including (blue) and excluding (red) the inflation [244].

The current price (September 2018) for vanadium is $19.65 per pound vanadium [245] which makes vanadium an expensive element. As shown in section 2.8 the capital cost for the VRFB was calculated to US$400 kWh, which is clearly a big leap to the target of the ARPA-e of DOE, to get a general idea.

In the case of **PV_{14}**, only four of the 14 vanadium contained are used and in the case of **SiW_{12}** only four (six with lead additive, see section 5.8.1) tungsten are used, which represents only a small part of the theoretically usable amount of electrons per molecule, which is unfavourable in terms of cost. One way to improve this and to address more vanadium/tungsten is to increase the potential window in water or by using organic solvents to make more electrons per molecule accessible. Stability and solubility tests of POMs in non-aqueous media should be carried out. The advantages and challenges of aqueous and non-aqueous systems are summarised in Table 2. Another aspect is that tungsten is a quite heavy element (183.84 u), which is disadvantageous in terms of gravimetric energy density.

However, the capabilities of POMs as redox active species in RFBs are undeniable due to their multiple redox centres and fast kinetics, hence, energy and power density can be addressed but other elements such as manganese, molybdenum or zinc are cheaper (see U.S. Geological Survey data bank) and less heavy, thus, lower the cost, get closer to the

target of US$100 per kWh and would improve the gravimetric factors. The investigated **PV_{14}** - **SiW_{12}** system shows promising results as POM-RFB and can be considered as a model system to investigate and understand new POMs in the future with regard to technical application. New POMs that contain the aforementioned elements should be electrochemically investigated to test their suitability for RFB application.

Due to the promising results in laboratory scale, SIEMENS AG conducted an upgrade of the investigated chemistry in technical scale for commercial application [246]. A long term study (continuous cycling of the battery for 88 days) conducted with a large commercial cell (surface area 1400 cm^2, J. Schmalz GmbH, see Figure 51 for set-up). An electrolyte solution with 1.5 L 80 mM **SiW_{12}** was prepared as anolyte, a solution of 1.5 L 80 mM reduced **PV_{14}** was used as catholyte. The initial discharge capacity was 4.70 Ah (72% of C_{theo} = 6.4 Ah). This discrepancy in capacitance can be explained by a lack of pre-reduced **PV_{14}**.

Figure 51 Photograph of the 1400 cm^2 cell with periphery (tanks, pumps, tubing) and containment.

During cycling the *pH* was measured (see Figure 52 (a)). The concentration of hydronium ions in the anolyte (green line) does not change significantly during one cycle, but the *pH* in

the catholyte (blue line) drops during charge and increases during discharge due to PCET. Figure 52 (b) compares the previously shown 10th cycle to the 1000th cycle. The latter was recorded 1508 h or 63 days after the former. As can be seen in the graph the general shape of the charge and discharge curves is not changed, exhibiting similarly high efficiencies η_{CE}^{1000} = 99.2% and η_{EE}^{1000} = 85.1%.

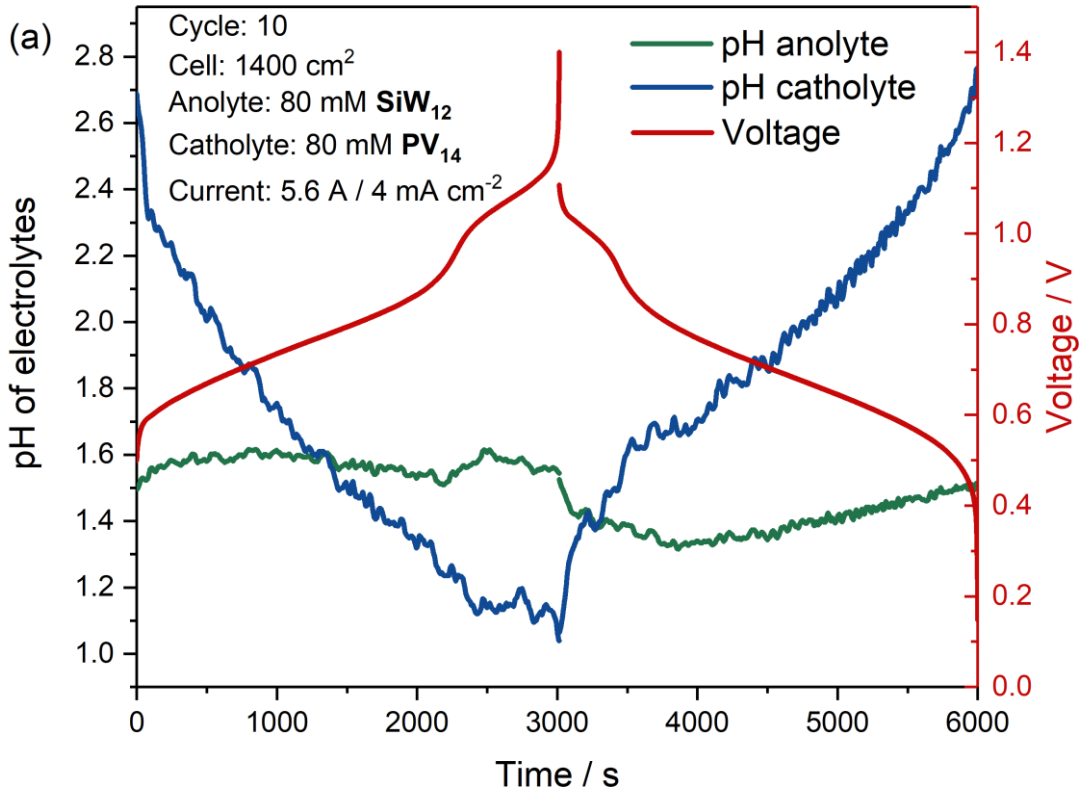

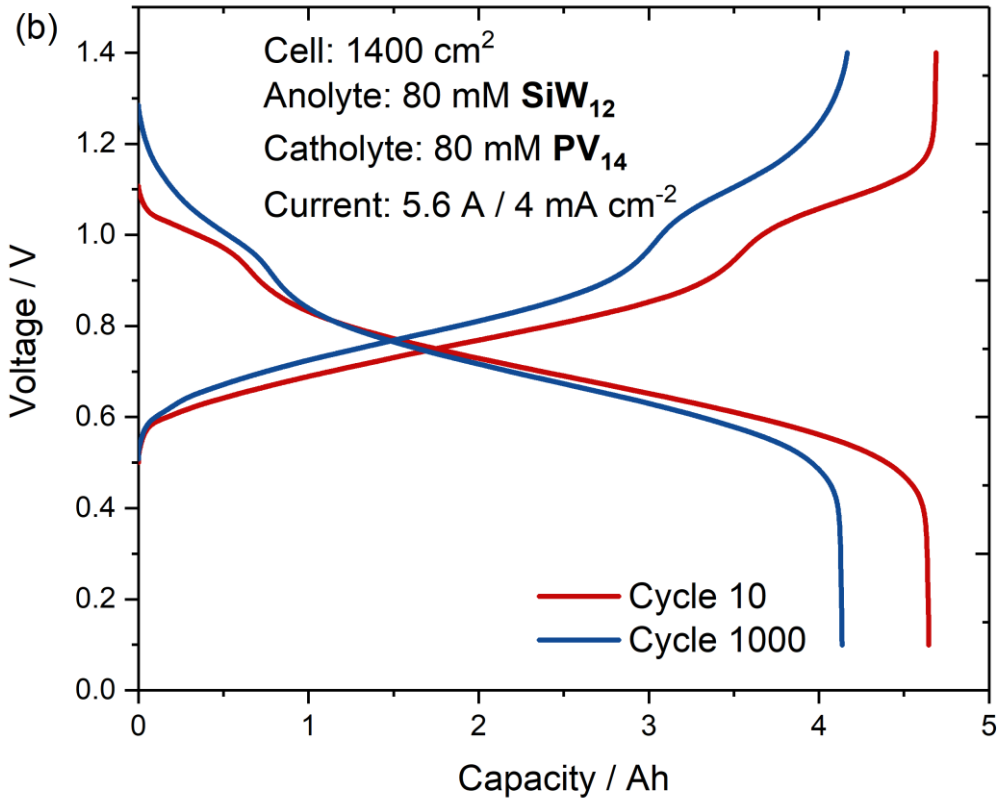

Figure 52 Cycling behaviour of the 1400 cm^2 cell conducted by SIEMENS. (a) Recorded observables of the 10th charge-discharge cycle over time. Measured *pH* values of anolyte (green line) and catholyte (blue line) are shown, as well as the cell voltage (red line). (b) Direct comparison of cycle 10 and cycle 1000. Cycle 1000 was recorded 63 days after the 10th cycle.

The long-term cycling behaviour of the 1400 cm^2 cell is shown in Figure 53. The changes in pH of anolyte and catholyte are given in Figure 53 (a). The *pH* of the catholyte is stable, the *pH* of the anolyte increases slightly from 1.5 to 2 during 1400 cycles. The *pH* sensors stopped working several times during the experiment, for these durations no *pH* data can be shown. Figure 53 (b) shows the capacity retention (red data) and the current density (blue line) of the 1400 cm^2 cell during 1400 cycles. The discharge capacity dropped from Q_{dch}^{1}= 4.70 Ah to Q_{dch}^{1000}= 3.95 Ah, which equals an average capacity loss of 0.53 mAh per cycle. When the current density was increased from 4 mA cm^{-2} to 43 mA cm^{-2} (cycles 185 to 240) the discharge capacity dropped to Q_{dch} ≈ 3.2 Ah. Figure 53 (c) shows the η_{CE} (black data) and the η_{EE} (red data). The Coulombic efficiency was nearly 100% over all 1400 cycles with the energy efficiency only dropping from 86.1% to 85.1% over the same period of time. While the electrolytes proved to be electrochemically stable (both ^{51}V NMR and cyclic voltammetry

showed that the polyoxoanions in the electrolyte were not damaged during the battery operation and that the molecules had not crossed the membrane), an average capacity loss of 0.01% per cycle was experienced that stems from residual oxygen in the system, avoidable in an industrial system.

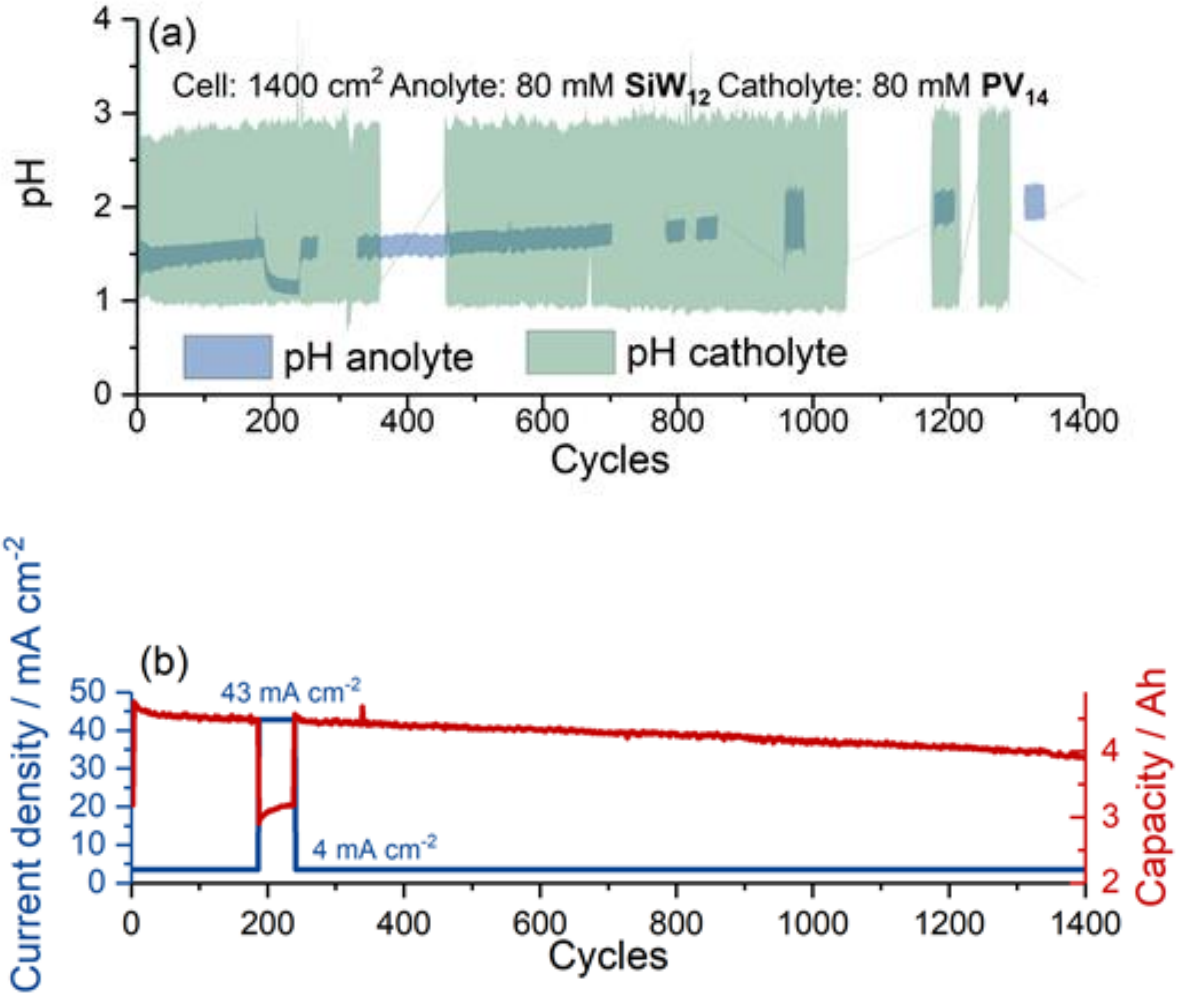

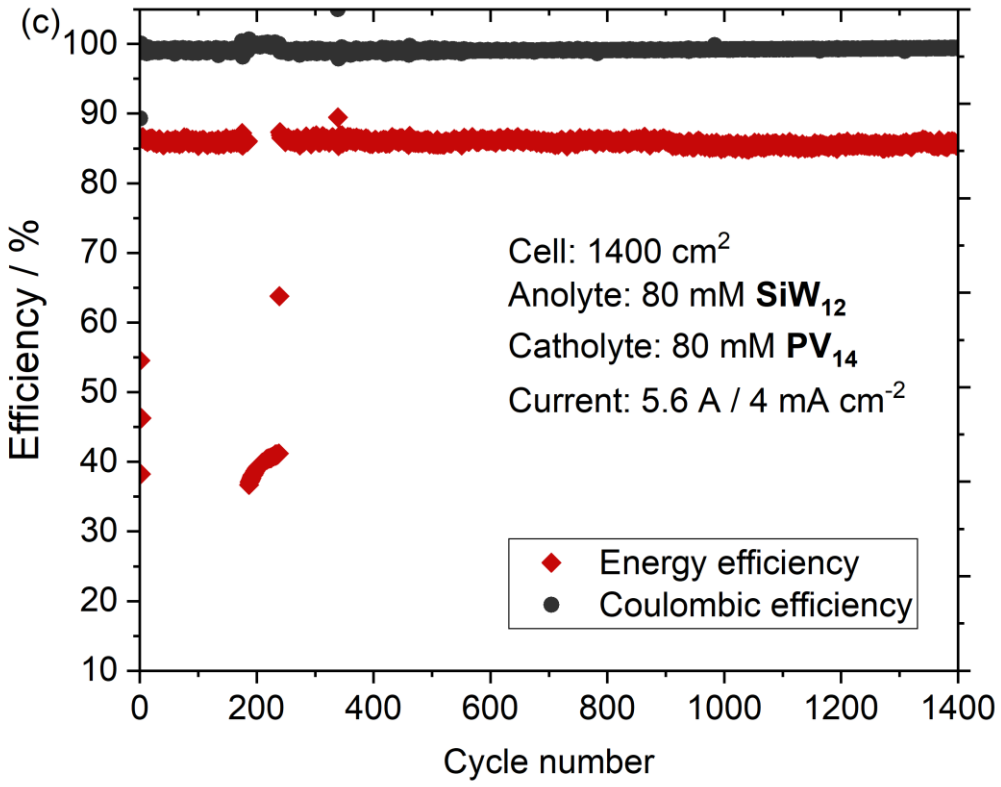

Figure 53 Long-term behaviour of the 1400 cm^2 cell conducted by SIEMENS. (a) *pH* of anolyte and catholyte over cycle number (b) capacity retention and current density. (c) Coulombic and energy efficiency. Data analysed by Jochen Friedl.

The obtained Coulombic efficiency of the **SiW_{12}-PV_{14}** system in the 1400 cm^2 cell is higher than for typical VRFB cells (η_{CE}^{VRFB}= 90% [50,247,248]). While the VRFB loses charge through cross-mixing of the electrolytes and by the parasitic HER, the POM system experiences no cross-over and the HER has not been observed due to the potentials in the anolyte compartment, which means a very big advantage.

The results obtained by SIEMENS AG confirm the results presented in this thesis and proof the suitablity of POMs as nano-sized electron shuttles for RFB. POMs offer an enormous variation in topology, size, electronic properties and elemental composition [8] which is pioneering and opens doors to further research opportunities especially in the field of RFBs. To find further suitable POMs for the application symmetric and asymmetric RFBs, a large number of molecules should be investigated with focus on costs and number of transferred electrons.

CHAPTER 7. BIBLIOGRAPHY

1 M. V. Holland-Cunz, F. Cording, J. Friedl and U. Stimming, *Front. Energy*, 2018, **12**, 198–224.

2 H. Fink, J. Friedl and U. Stimming, *J. Phys. Chem. C*, 2016, **120**, 15893–15901.

3 J. Friedl and U. Stimming, *Electrochim. Acta*, 2017, **227**, 235–245.

4 J. Friedl, C. M. Bauer, A. Rinaldi and U. Stimming, *Carbon*, 2013, **63**, 228–239.

5 I. Derr, A. Fetyan, K. Schutjajew and C. Roth, *Electrochim. Acta*, 2017, **224**, 9–16.

6 M. V. Holland-Cunz, J. Friedl and U. Stimming, *J. Electroanal. Chem.*, 2017, 0–1.

7 P. Leung, A. A. Shah, L. Sanz, C. Flox, J. R. Morante, Q. Xu, M. R. Mohamed, C. Ponce de León and F. C. Walsh, *J. Power Sources*, 2017, **360**, 243–283.

8 M. T. Pope and A. Müller, *Angew. Chemie Int. Ed.*, 1991, **30**, 34–48.

9 J. Friedl, M. V. Holland-Cunz, F. Cording, F. L. Pfanschilling, C. Wills, W. McFarlane, B. Schricker, R. Fleck, H. Wolfschmidt and U. Stimming, *Energy Environ. Sci.*, 2018, **11**, 3010–3018.

10 Z. Yang, J. Zhang, M. C. W. Kintner-Meyer, X. Lu, D. Choi, J. P. Lemmon and J. Liu, *Chem. Rev.*, 2011, **111**, 3577–3613.

11 G. J. Offer, D. Howey, M. Contestabile, R. Clague and N. P. Brandon, *Energy Policy*, 2010, **38**, 24–29.

12 S. Ramachandran and U. Stimming, *Energy Environ. Sci.*, 2015, **8**, 3313–3324.

13 B. Scrosati and J. Garche, *J. Power Sources*, 2010, **195**, 2419–2430.

14 M. Armand, *Nature*, 2008, **451**, 652–657.

15 K. J. Vetter, *Electrochemical Kinetics - Theoretical and Experimental Aspects*, Academic Press Inc., New York/London, English Ed., 1967.

16 J. Friedl and U. Stimming, in *Energie: Forschung und Konzepte*, ed. H. Bruhns, Arbeitskreis Energie (AKE) in der Deutschen Physikalischen Gesellschaft, 2014.

17 R.L. McCreery, *Chem. Rev.*, 2008, **108**, 2646–2687.

18 U. Fischer, R. Saliger, V. Bock, R. Petricevic and J. Fricke, *J. Porous Mater.*, 1997, **4**, 281–285.

19 O. Barbieri, M. Hahn, A. Herzog and R. Kötz, *Carbon*, 2005, **43**, 1303–1310.

20 J. P. Tessonnier, D. Rosenthal, T. W. Hansen, C. Hess, M. E. Schuster, R. Blume, F. Girgsdies, N. Pfänder, O. Timpe, D. S. Su and R. Schlögl, *Carbon*, 2009, **47**, 1779–1798.

21 F. Béguin, V. Presser, A. Balducci and E. Frackowiak, *Adv. Mater.*, 2014, **26**, 2219–2251.

22 V. Ruiz, C. Blanco, E. Raymundo-Piñero, V. Khomenko, F. Béguin and R. Santamaría, *Electrochim. Acta*, 2007, **52**, 4969–4973.

23 M. P. Marder, *Condensed Matter Physics*, John Wiley & Sons, Inc., Hoboken, 2nd edn., 2010.

24 J. Janek and W. G. Zeier, *Nat. Energy*, 2016, **1**, 1–4.

25 D. Lin, Y. Liu and Y. Cui, *Nat. Nanotechnol.*, 2017, **12**, 194–206.

26 W. Xu, J. Wang, F. Ding, X. Chen, E. Nasybulin, Y. Zhang and J. G. Zhang, *Energy Environ. Sci.*, 2014, **7**, 513–537.

27 J. Friedl and U. Stimming, *Electrochim. Acta*, 2013, **101**, 41–58.

28 W. Schmickler and E. Santos, *Interfacial electrochemistry*, Springer, Berlin, 2nd edn., 2010.

29 J. Zhang, M. B. Vukmirovic, Y. Xu, M. Mavrikakis and R. R. Adzic, *Angew. Chemie - Int. Ed.*, 2005, **44**, 2132–2135.

30 J. Greeley, I. E. L. Stephens, A. S. Bondarenko, T. P. Johansson, H. A. Hansen, T. F. Jaramillo, J. Rossmeisl, I. Chorkendorff and J. K. Nørskov, *Nat. Chem.*, 2009, **1**, 552–556.

31 J. K. Nørskov, J. Rossmeisl, A. Logadottir, L. Lindqvist, J. R. Kitchin, T. Bligaard and H. Jónsson, *J. Phys. Chem. B*, 2004, **108**, 17886–17892.

32 R. J. Marshall and F. C. Walsh, *Surf. Technol.*, 1985, **24**, 45–77.

33 F. C. Walsh and D. Pletcher, in *Developments in Electrochemistry: Science Inspired by Martin Felischmann.*, eds. D. Pletcher, Z. Q. Tian and D. E. Williams, Hoboken: John Wiley & Sons, 2014, pp. 95–111.

34 A. M. Bond, T. L. E. Henderson, D. R. Mann, T. F. Mann, W. Thormann and C. G. Zoski, *Anal. Chem.*, 1988, **60**, 1878–1882.

35 B. R. Chalamala, T. Soundappan, G. R. Fisher, M. R. Anstey, V. V. Viswanathan and M. L. Perry, *Proc. IEEE*, 2014, **102**, 976–999.

36 L. F. Arenas, C. Ponce de León and F. C. Walsh, *J. Energy Storage*, 2017, **11**, 119–153.

37 L. Thaller, *Electrically rechargeable redox flow cell*, US Patent 3996064A, 1976.

38 R. Remick, P. Ang, B. Hearn, S. Kalafut and T. Speckman, *Electrically rechargeable anionically active reduction-oxidation electrical storage-supply system*, US Patent 4485154, 1984.

39 M. Skyllas-Kazacos, M. Rychcik, R. G. Robins and A. G. Fane, *J. Electrochem. Soc.*, 1986, **133**, 1057–1058.

40 H. S. Lim, A. M. Lackner and R. C. Knechtli, *J. Electrochem. Soc.*, 1977, **124**, 1154–1157.

41 M. L. Perry, R. M. Darling and R. Zaffou, *ECS Trans.*, 2013, **53**, 7–16.

42 A. A. Akhil, G. Huff, A. B. Currier, B. C. Kaun, D. M. Rastler, S. B. Chen, A. L. Cotter, D. T. Bradshaw and W. D. Gauntlett, *DOE / EPRI 2013 Electricity Storage Handbook in Collaboration with NRECA*, Sandia National Laboratories, 2013.

43 S. Eckroad, *Vanadium Redox Flow Batteries: An In-Depth Analysis*, Palo Alto, CA: Electric Power Research Institute, 2007.

44 L. Livermore, N. Labs, L. Livermore, N. Labs, E. Independence, A. Curtright, J. Apt, W. Generation and R. Guttromson, arpa-e GRIDS Program Overview. 2010, https://arpa-e.energy.gov/sites/default/files/documents/files/GRIDS_ProgramOverview.pdf.

45 M. Zhang, M. Moore, J. S. Watson, T. a. Zawodzinski and R. M. Counce, *J. Electrochem.*

Soc., 2012, **159**, A1183–A1188.

46 V. Viswanathan, A. Crawford, L. Thaller, D. Stephenson, S. Kim, W. Wang, G. Coffey, P. Balducci, Z. Gary, L. Li and V. Sprenkle, *Estimation of Capital and Levelized Cost for Redox Flow Batteries*, The Electrochemical Society, 2012.

47 J. Noack, N. Roznyatovskaya, T. Herr and P. Fischer, *Angew. Chemie - Int. Ed.*, 2015, **54**, 9776–9809.

48 F. Pan and Q. Wang, *Molecules*, 2015, **20**, 20499–20517.

49 A. Z. Weber, M. M. Mench, J. P. Meyers, P. N. Ross, J. T. Gostick and Q. Liu, *J. Appl. Electrochem.*, 2011, **41**, 1137–1164.

50 C. Ponce de León, A. Frías-Ferrer, J. González-García, D. A. Szánto and F. C. Walsh, *J. Power Sources*, 2006, **160**, 716–732.

51 Y. Zhao, Y. Ding, Y. Li, L. Peng, H. R. Byon, J. B. Goodenough and G. Yu, *Chem. Soc. Rev.*, 2015, **44**, 7968–7996.

52 G. L. Soloveichik, *Chem. Rev.*, 2015, **115**, 11533–11558.

53 L. H. Thaller, *Electrically rechargeable redox flow cell*, US Patent 3996064, 1976.

54 E. Sum and M. Skyllas-Kazacos, *J. Power Sources*, 1985, **15**, 179–190.

55 M. Rychcik and M. Skyllas-Kazacos, *J. Power Sources*, 1987, **19**, 45–54.

56 S. S. Hosseiny, M. Saakes and M. Wessling, *Electrochem. commun.*, 2011, **13**, 751–754.

57 I. Derr, M. Bruns, J. Langner, A. Fetyan, J. Melke and C. Roth, *J. Power Sources*, 2016, **325**, 351–359.

58 M. A. Miller, A. Bourke, N. Quill, J. S. Wainright, R. P. Lynch, D. N. Buckley and R. F. Savinell, *J. Electrochem. Soc.*, 2016, **163**, A2095–A2102.

59 V. Yufit, B. Hale, M. Matian, P. Mazur and N. P. Brandon, *J. Electrochem. Soc.*, 2013, **160**, A856–A861.

60 M. C. Tucker, V. Srinivasan, P. N. Ross and A. Z. Weber, *J. Appl. Electrochem.*, 2013, **43**,

637–644.

61 H. Hewa Dewage, B. Wu, A. Tsoi, V. Yufit, G. Offer and N. Brandon, *J. Mater. Chem. A*, 2015, **3**, 9446–9450.

62 R. Schweiss, A. Pritzl and C. Meiser, *J. Electrochem. Soc.*, 2016, **163**, A2089–A2094.

63 A. A. Shah, H. Al-Fetlawi and F. C. Walsh, *Electrochim. Acta*, 2010, **55**, 1125–1139.

64 J. Weber, Z. Samec and V. Marecek, *J. Electroanal. Chem.*, 1978, **89**, 271–288.

65 B. Jonshagen and P. Lex, *Power Eng. J.*, 1999, **13**, 142–148.

66 M. Duduta, B. Ho, V. C. Wood, P. Limthongkul, V. E. Brunini, W. C. Carter, Y.-M. Chiang, W. Craig Carter and Y.-M. Chiang, *Adv. Energy Mater.*, 2011, **1**, 511–546.

67 Q. Huang and Q. Wang, *ChemPlusChem*, 2015, **80**, 312–322.

68 Q. Huang, H. Li, M. Grätzel and Q. Wang, *Phys. Chem. Chem. Phys.*, 2013, **15**, 1793–1797.

69 F. Pan, J. Yang, Q. Huang, X. Wang, H. Huang and Q. Wang, *Adv. Energy Mater.*, 2014, **4**, 1400567.

70 E. Zanzola, C. R. Dennison, A. Battistel, P. Peljo, H. Vrubel, V. Amstutz and H. H. Girault, *Electrochim. Acta*, 2017, **235**, 664–671.

71 W. Wang, S. Kim, B. Chen, Z. Nie, J. Zhang, G. G. Xia, L. Li and Z. Yang, *Energy Environ. Sci.*, 2011, **4**, 4068–4073.

72 K. Izutsu, *Electrochemistry in nonaqueous solutions*, Wiley-VCH GmbH & Co., Weinheim, 2002.

73 Q. Liu, A. E. S. Sleightholme, A. A. Shinkle, Y. Li and L. T. Thompson, *Electrochem. commun.*, 2009, **11**, 2312–2315.

74 A. E. S. Sleightholme, A. A. Shinkle, Q. Liu, Y. Li, C. W. Monroe and L. T. Thompson, *J. Power Sources*, 2011, **196**, 5742–5745.

75 Y. Matsuda, K. Tanaka, M. Okada, Y. Takasu, M. Morita and T. Matsumura-Inoue, *J.*

Appl. Electrochem., 1988, **18**, 909–914.

76 Z. Li, S. Li, S. Liu, K. Huang, D. Fang, F. Wang and S. Peng, *Electrochem. Solid-State Lett.*, 2011, **14**, A171–A173.

77 K. Gong, Q. Fang, S. Gu, S. F. Y. Li and Y. Yan, *Energy Environ. Sci.*, 2015, **8**, 3515–3530.

78 C. G. Zoski, *Handbook of electrochemistry*, Elsevier B.V., Amsterdam, 2007.

79 X. Wei, W. Xu, M. Vijayakumar, L. Cosimbescu, T. Liu, V. Sprenkle and W. Wang, *Adv. Mater.*, 2014, **26**, 7649–7653.

80 M. Armand and J.-M. Tarascon, *Nature*, 2008, **451**, 652–7.

81 J. O. Metzger, *Angew. Chemie*, 1998, **110**, 3145–3148.

82 H. Greim, *Occupational Toxicants: Critical Data Evaluation for MAK Values and Classfication of Carcinogens, Band 19, The MAK-Collection for Occupational Health and Safety. Part 1: MAK Value Documentations (DFG)*, Wiley-VCH Verlag GmbH & Co. KGaA, Weinheim, 2003.

83 Toxicology Data Network. U.S. National Library of Medicine. 2017-7, https://toxnet.nlm.nih.gov.

84 A. Ejigu, P. A. Greatorex-Davies and D. A. Walsh, *Electrochem. commun.*, 2015, **54**, 55–59.

85 E. P. Roth and C. J. Orendorff, *Interface*, 2012, **21**, 45–50.

86 J. Friedl, I. I. E. Markovits, M. Herpich, G. Feng, A. A. Kornyshev and U. Stimming, *ChemElectroChem*, 2016, **71**, 311–315.

87 A. M. O'Mahony, D. S. Silvester, L. Aldous, C. Hardacre and R. G. Compton, *J. Chem. Eng. Data*, 2008, **53**, 2884–2891.

88 T. M. Anderson and H. D. P. Iii, Ionic Liquid Flow Batteries. 2015-6, https://www.osti.gov/scitech/biblio/1256242.

89 H. D. Pratt, J. C. Leonard, L. A. M. Steele, C. L. Staiger and T. M. Anderson, *Inorganica Chim. Acta*, 2013, **396**, 78–83.

90 H. Prifti, A. Parasuraman, S. Winardi, T. M. Lim and M. Skyllas-Kazacos, *Membranes (Basel).*, 2012, **2**, 275–306.

91 S. Maurya, S.-H. Shin, Y. Kim and S.-H. Moon, *RSC Adv.*, 2015, **5**, 37206–37230.

92 Z. Tang, *Characterization Techniques and Electrolyte Separator Performance Investigation for All Vanadium Redox Flow Battery. Dissertation for the Doctoral Degree*, Knoxville: University of Tennessee, 2013.

93 T. Mohammadi and M. Skyllas Kazacos, *J. Power Sources*, 1996, **63**, 179–186.

94 T. Mohammadi and M. Skyllas-Kazacos, *J. Memb. Sci.*, 1995, **98**, 77–87.

95 T. Mohammadi, S. C. Chieng and M. Skyllas Kazacos, *J. Memb. Sci.*, 1997, **133**, 151–159.

96 Z. Yuan, Y. Duan, H. Zhang, X. Li, H. Zhang and I. Vankelecom, *Energy Environ. Sci.*, 2015, **9**, 22–24.

97 T. Janoschka, N. Martin, U. Martin, C. Friebe, S. Morgenstern, H. Hiller, M. D. Hager and U. S. Schubert, *Nature*, 2015, **527**, 78–81.

98 K. J. Cathro, K. Cedzynska, D. C. Constable and P. M. Hoobin, *J. Power Sources*, 1986, **18**, 349–370.

99 H. S. Yang, J. H. Park, H. W. Ra, C. S. Jin and J. H. Yang, *J. Power Sources*, 2016, **325**, 446–452.

100 S. Higashi, S. W. Lee, J. S. Lee, K. Takechi and Y. Cui, *Nat. Commun.*, 2016, **7**, 11801.

101 M. Rychcik and M. Skyllas-Kazacos, *J. Power Sources*, 1988, **22**, 59–67.

102 M. Ulaganathan, V. Aravindan, Q. Yan, S. Madhavi, M. Skyllas-Kazacos and T. M. Lim, *Adv. Mater. Interfaces*, 2016, **3**, 1500309.

103 M. Skyllas-Kazacos, *J. Electrochem. Soc.*, 1996, **143**, L86.

104 L. Li, S. Kim, W. Wang, M. Vijayakumar, Z. Nie, B. Chen, J. Zhang, G. Xia, J. Hu, G. Graff, J. Liu and Z. Yang, *Adv. Energy Mater.*, 2011, **1**, 394–400.

105 S. Roe, C. Menictas and M. Skyllas-Kazacos, *J. Electrochem. Soc.*, 2016, **163**, A5023–A5028.

106 M. Skyllas-Kazacos and M. Kazacos, *Stabilised electrolyte solutions, methods of preparation thereof and redox cells and batteries containing stabilised electrolyte*, European Patent EP0729648, 1995.

107 Y. Lei, S. Q. Liu, C. Gao, X. X. Liang, Z. X. He, Y. H. Deng and Z. He, *J. Electrochem. Soc.*, 2013, **160**, A722–A727.

108 F. Chang, C. Hu, X. Liu, L. Liu and J. Zhang, *Electrochim. Acta*, 2012, **60**, 334–338.

109 J. Zhang, L. Li, Z. Nie, B. Chen, M. Vijayakumar, S. Kim, W. Wang, B. Schwenzer, J. Liu and Z. Yang, *J. Appl. Electrochem.*, 2011, **41**, 1215–1221.

110 S. Li, K. Huang, S. Liu, D. Fang, X. Wu, D. Lu and T. Wu, *Electrochim. Acta*, 2011, **56**, 5483–5487.

111 T. D. Nguyen, A. Whitehead, G. G. Scherer, N. Wai, M. O. Oo, A. Bhattarai, G. P. Chandra and Z. J. Xu, *J. Power Sources*, 2016, **334**, 94–103.

112 A. A. Shinkle, A. E. S. Sleightholme, L. T. Thompson and C. W. Monroe, *J. Appl. Electrochem.*, 2011, **41**, 1191–1199.

113 A. A. Shinkle, A. E. S. Sleightholme, L. D. Griffith, L. T. Thompson and C. W. Monroe, *J. Power Sources*, 2012, **206**, 490–496.

114 A. A. Shinkle, T. J. Pomaville, A. E. S. Sleightholme, L. T. Thompson and C. W. Monroe, *J. Power Sources*, 2014, **248**, 1299–1305.

115 J. D. Saraidaridis, B. M. Bartlett and C. W. Monroe, *J. Electrochem. Soc.*, 2016, **163**, A1239–A1246.

116 Q. Liu, A. A. Shinkle, Y. Li, C. W. Monroe, L. T. Thompson and A. E. S. Sleightholme, *Electrochem. commun.*, 2010, **12**, 1634–1637.

117 M. A. Goulet and E. Kjeang, *J. Power Sources*, 2014, **260**, 186–196.

118 M. A. Goulet, O. A. Ibrahim, W. H. J. Kim and E. Kjeang, *J. Power Sources*, 2017, **339**,

80–85.

119 S. Ressel, A. Laube, S. Fischer, A. Chica, T. Flower and T. Struckmann, *J. Power Sources*, 2017, **355**, 199–205.

120 M. Skyllas-Kazacos, *J. Power Sources*, 2003, **124**, 299–302.

121 F. C. Walsh, *Pure Appl. Chem.*, 2001, **73**, 1819–1837.

122 EA Technology, Review of electrical energy storage technologies and systems and of their potential for the UK, 2004, http://www.wearemichigan.com/JobsAndEnergy/documents/file15185.pdf.

123 B. Li, Z. Nie, M. Vijayakumar, G. Li, J. Liu, V. Sprenkle and W. Wang, *Nat. Commun.*, 2015, **6**, 6303.

124 T. Janoschka, N. Martin, M. D. Hager and U. S. Schubert, *Angew. Chemie - Int. Ed.*, 2016, **55**, 14427–14430.

125 J. Winsberg, T. Hagemann, S. Muench, C. Friebe, B. Häupler, T. Janoschka, S. Morgenstern, M. D. Hager and U. S. Schubert, *Chem. Mater.*, 2016, **28**, 3401–3405.

126 H. D. Pratt, N. S. Hudak, X. Fang and T. M. Anderson, *J. Power Sources*, 2013, **236**, 259–264.

127 H. D. Pratt, W. R. Pratt, X. Fang, N. S. Hudak and T. M. Anderson, *Electrochim. Acta*, 2014, **138**, 210–214.

128 J. Friedl, R. Al-Oweini, M. Herpich, B. Keita, U. Kortz and U. Stimming, *Electrochim. Acta*, 2014, **141**, 357–366.

129 A. Kremleva, P. A. Aparicio, A. Genest and N. Rösch, *Electrochim. Acta*, 2017, **231**, 659–669.

130 L. Nadjo, B. Keita, *Mater. Chem. Phys.*, 1989, **22**, 77–103.

131 J. B. Christian, S. P. E. Smith, M. S. Whittingham and H. D. Abruña, *Electrochem. commun.*, 2007, **9**, 2128–2132.

132 J. Friedl, C. Bauer, R. Al-Oweini, D. Yau Wai Yu, U. Kortz, H. Hoster and U. Stimming,

Investigation on Polyoxometalates for the Application in Redox Flow Batteries. In: 222th ECS Meet., Honululu, HI, 2012, http://ma.ecsdl.org/content/MA2012-02/51/3551.short, 2011.

133 Y. Liu, S. Lu, H. Wang, C. Yang, X. Su and Y. Xiang, *Adv. Energy Mater.*, 2017, **7**, 2–7.

134 M. T. Pope and G. M. Varga, *Inorg. Chem.*, 1966, **5**, 1249–1254.

135 B. Huskinson, M. P. Marshak, C. Suh, S. Er, M. R. Gerhardt, C. J. Galvin, X. Chen, A. Aspuru-Guzik, R. G. Gordon and M. J. Aziz, *Nature*, 2014, **505**, 195–198.

136 Q. Chen, M. R. Gerhardt, L. Hartle and M. J. Aziz, *J. Electrochem. Soc.*, 2015, **163**, A5010–A5013.

137 Q. Chen, M. R. Gerhardt and M. J. Aziz, *J. Electrochem. Soc.*, 2017, **164**, A1126–A1132.

138 Q. Chen, L. Eisenach and M. J. Aziz, *J. Electrochem. Soc.*, 2016, **163**, A5057–A5063.

139 T. J. Carney, S. J. Collins, J. S. Moore and F. R. Brushett, *Chem. Mater.*, 2017, **29**, 4801–4810.

140 K. Lin, Q. Chen, M. R. Gerhardt, L. Tong, S. B. Kim, L. Eisenach, A. W. Valle, D. Hardee, R. G. Gordon, M. J. Aziz and M. P. Marshak, *Science*, 2015, **349**, 1529–1532.

141 K. Lin, R. Gómez-Bombarelli, E. S. Beh, L. Tong, Q. Chen, A. Valle, A. Aspuru-Guzik, M. J. Aziz and R. G. Gordon, *Nat. Energy*, 2016, **1**, 16102.

142 F. M. Rabiul Islam, K. Al Mamun and M. T. O. Amanullah, *Smart Energy Grid Design for Island Countries*, Springer, Cham, 2017.

143 D. A. Johnson and M. A. Reid, *J. Electrochem. Soc.*, 1985, **132**, 1058–1062.

144 A. W. Nice, *NASA Redox System Development Project Status. In: 4th Battery and Electrochemical Contractors Conference*, Washington, 1981.

145 H. Zhang, *Development and Application of High Performance VRB Technology. In: IFBF 2017 International Flow Battery Forum*, Manchester, UK, 2017.

146 D. P. Scamman, G. W. Reade and E. P. L. Roberts, *J. Power Sources*, 2009, **189**, 1220–1230.

147 P. R. Morrissey, *Int. J. Ambient Energy*, 2000, **21**, 213–220.

148 P. K. Leung, C. P. De León and F. C. Walsh, *Electrochem. commun.*, 2011, **13**, 770–773.

149 Y. R. Dong, H. Kaku and K. Hanafusa, *ECS Trans.*, 2015, **69**, 59–67.

150 Y. K. Zeng, T. S. Zhao, X. L. Zhou, L. Wei and H. R. Jiang, *J. Power Sources*, 2016, **330**, 55–60.

151 J. Cheng, L. Zhang, Y. S. Yang, Y. H. Wen, G. P. Cao and X. D. Wang, *Electrochem. commun.*, 2007, **9**, 2639–2642.

152 M. Morita, Y. Tanaka, K. Tanaka, Y. Matsuda and T. Matsumura-Inoue, *Bull. Chem. Soc. Jpn.*, 1988, 61, 2711–2714.

153 M. H. Chakrabarti, E. P. L. Roberts, C. Bae and M. Saleem, *Energy Convers. Manag.*, 2011, **52**, 2501–2508.

154 P. J. Cappillino, H. D. Pratt, N. S. Hudak, N. C. Tomson, T. M. Anderson and M. R. Anstey, *Adv. Energy Mater.*, 2014, **4**, 2–6.

155 B. Hwang, M. S. Park and K. Kim, *ChemSusChem*, 2015, **8**, 310–314.

156 D. Zhang, H. Lan and Y. Li, *J. Power Sources*, 2012, **217**, 199–203.

157 Y. Xu, Y. Wen, J. Cheng, G. Cao and Y. Yang, *Electrochem. commun.*, 2009, **11**, 1422–1424.

158 B. Yang, L. Hoober-Burkhardt, F. Wang, G. K. Surya Prakash and S. R. Narayanan, *J. Electrochem. Soc.*, 2014, **161**, A1371–A1380.

159 S. H. Oh, C. W. Lee, D. H. Chun, J. D. Jeon, J. Shim, K. H. Shin and J. H. Yang, *J. Mater. Chem. A*, 2014, **2**, 19994–19998.

160 *nanoFlowcell Holdings Ltd, nanoFlowcell® Flow Cells are the Energy of the Future, WhichWill Change Electric MobilityWorldwide, 87th Geneva Mot. Show*, 2017.

161 D. R. Weinberg, C. J. Gagliardi, J. F. Hull, C. F. Murphy, C. A. Kent, B. C. Westlake, A. Paul, D. H. Ess, D. G. McCafferty and T. J. Meyer, *Chem. Rev.*, 2012, **112**, 4016–4093.

162 R. Dmello, J. D. Milshtein, F. R. Brushett and K. C. Smith, *J. Power Sources*, 2016, **330**, 261–272.

163 B. Schwenzer, J. Zhang, S. Kim, L. Li, J. Liu and Z. Yang, *ChemSusChem*, 2011, **4**, 1388–1406.

164 E. Wiedemann, A. Heintz and R. N. Lichtenthaler, *J. Memb. Sci.*, 1998, **141**, 215–221.

165 C. Ding, H. Zhang, X. Li, T. Liu and F. Xing, *J. Phys. Chem. Lett.*, 2013, **4**, 1281–1294.

166 E. S. Beh, D. De Porcellinis, R. L. Gracia, K. T. Xia, R. G. Gordon and M. J. Aziz, *ACS Energy Lett.*, 2017, **2**, 639–644.

167 M. Vijayakumar, M. S. Bhuvaneswari, P. Nachimuthu, B. Schwenzer, S. Kim, Z. Yang, J. Liu, G. L. Graff, S. Thevuthasan and J. Hu, *J. Memb. Sci.*, 2011, **366**, 325–334.

168 R. Darling, K. G. Gallagher, J. A. Kowalski, S. Ha and F. R. Brushett, *Energy Environ. Sci.*, 2014, **7**, 3459–3477.

169 U. S. Department of Energy Headquarters Advanced Research Projects Agency – Energy (ARPA-E), Grid-Scale Rampable Intermittent Dispatchable Storage (GRIDS). 2010, https://www. osti.gov/scitech/biblio/1046668.

170 J. Winsberg, T. Hagemann, T. Janoschka, M. D. Hager and U. S. Schubert, *Angew. Chemie - Int. Ed.*, 2017, **56**, 686–711.

171 Y. K. Zeng, T. S. Zhao, L. An, X. L. Zhou and L. Wei, *J. Power Sources*, 2015, **300**, 438–443.

172 T. E. Al-Salih and R. W. Al-Taha, *Der Pharma Chem.*, 2014, **6**, 42–50.

173 A. J. Bard and L. R. Faulkner, *Electrochemical Methods: Fundamentals and Applications. 2nd ed*, John Wiley and Sons, New York, 2001.

174 L. Leonat, G. Sbarcea and I. V. Branzoi, *U.P.B.Sci.Bull., Ser. B*, 2013, **75**, 111–118.

175 R. Holze, *Experimental Electrochemistry*, Wiley-VCH GmbH & Co., Weinheim, 2009.

176 J. Friedl, *Advanced Materials for Redox Flow Batteries, Dissertation for the Doctoral Degree*, Technischen Universität München, 2015.

177 N. Elgrishi, K. J. Rountree, B. D. McCarthy, E. S. Rountree, T. T. Eisenhart and J. L. Dempsey, *J. Chem. Educ.*, 2017, **95**, 197–206.

178 M. Burgess, K. Hernández-Burgos, K. J. Cheng, J. S. Moore and J. Rodríguez-López, *Analyst*, 2016, **141**, 3842–3850.

179 R. S. Nicholson, *Anal. Chem.*, 1965, **37**, 1351–1355.

180 E. P. Randviir and C. E. Banks, *Anal. Methods*, 2013, **5**, 1098–1115.

181 M. Olivier and M. Poelman, *Recent Res. Corros. Eval. Prot.*, 2013, **399**, 1–27.

182 R. Vedalakshmi, V. Saraswathy, H. W. Song and N. Palaniswamy, *Corros. Sci.*, 2009, **51**, 1299–1307.

183 C. Fernández-Sánchez, C. J. McNeil and K. Rawson, *TrAC - Trends Anal. Chem.*, 2005, **24**, 37–48.

184 E. Yaeger and J. Kuta, in *Phys. Chem. An Adv. Treatise. Vol. IXA Electrochem.*, ed. H. Eyring, Academic Press, New York/London, 1970, pp. 346–451.

185 F. G. Cottrell, *Zeitschrift für Phys. Chemie*, 1903, **42U**, 385–431.

186 M. Gattrell, J. Qian, C. Stewart, P. Graham and B. MacDougall, *Electrochim. Acta*, 2005, **51**, 395–407.

187 M. Gattrell, J. Park, B. MacDougall, J. Apte, S. McCarthy and C. W. Wu, *J. Electrochem. Soc.*, 2004, **151**, A123.

188 J. Maruyama, T. Shinagawa, A. Hayashida, Y. Matsuo, H. Nishihara and T. Kyotani, *ChemElectroChem*, 2016, **3**, 650–657.

189 G. A. Webb, *Annual Reports on NMR Spectroscopy Band 62*, Academic Press Inc., 2007.

190 S. E. O'Donnell and M. T. Pope, *J. Chem. Soc. Dalt. Trans.*, 1976, 2290.

191 M. J. Gresser, A. S. Tracey and K. M. Parkinson, 1986, 6229–6234.

192 M. P. Williamson, *Prog. Nucl. Magn. Reson. Spectrosc.*, 2013, **73**, 1–16.

193 International Union of pure and applied Chemistry, *Standard Potentials in Aqueous Solution*, CRC Press, New York, 1985.

194 B. Hirschorn, M. E. Orazem, B. Tribollet, V. Vivier, I. Frateur and M. Musiani, *Electrochim. Acta*, 2010, **55**, 6218–6227.

195 R. Schweiss, T. Oelsner, F. Dörfler, A. Davydov and S. Wöhner, in *International Flow Battery Forum 2011*, 2011, pp. 44–45.

196 T. J. Rabbow and A. H. Whitehead, *Carbon*, 2017, **111**, 782–788.

197 T. J. Rabbow, M. Trampert, P. Pokorny, P. Binder and A. H. Whitehead, *Electrochim. Acta*, 2015, **173**, 17–23.

198 T. J. Rabbow, M. Trampert, P. Pokorny, P. Binder and A. H. Whitehead, *Electrochim. Acta*, 2015, **173**, 17–23.

199 C. Ding, X. Ni, X. Li, X. Xi, X. Han, X. Bao and H. Zhang, *Electrochim. Acta*, 2015, **164**, 307–314.

200 A. Bourke, R. P. Lynch and D. N. Buckley, *ECS Trans.*, 2013, **53**, 59–67.

201 A. Bourke, N. Quill, R. P. Lynch and D. N. Buckley, *ECS Trans.*, 2014, **61**, 15–26.

202 R. Schweiss, C. Meiser, F. Wei and T. Goh, *ChemElectroChem*, 2017, 1–7.

203 J. Langner, M. Bruns, D. Dixon, A. Nefedov, C. Wöll, F. Scheiba, H. Ehrenberg, C. Roth and J. Melke, *J. Power Sources*, 2016, **321**, 210–218.

204 M. Skyllas-Kazacos, L. Cao, M. Kazacos, N. Kausar and A. Mousa, *ChemSusChem*, 2016, 1–24.

205 M. H. Chakrabarti, N. P. Brandon, S. A. Hajimolana, F. Tariq, V. Yufit, M. A. Hashim, M. A. Hussain, C. T. J. Low and P. V. Aravind, *J. Power Sources*, 2014, **253**, 150–166.

206 J. Friedl, M. A. Lebedeva, K. Porfyrakis, U. Stimming and T. W. Chamberlain, *J. Am. Chem. Soc.*, 2018, **140**, 401–405.

207 M. T. Pope and A. Müller, *Polyoxometalate Chemistry From Topology via Self-Assembly to Applications*, Kluwer Academic Publishers, New York, Boston, Dordrecht,

London, Moscow, 2001.

208 T. Yamase and M. T. Pope, *Polyoxometalate Chemistry for Nano-Composite Design*, Kluwer Academic Publishers, New York, Boston, Dordrecht, London, Moscow, 2002.

209 S. G. Mitchell, T. Boyd, H. N. Miras, D. L. Long and L. Cronin, *Inorg. Chem.*, 2011, **50**, 136–143.

210 J. F. Keggin, *Nature*, 1933, **131**, 908–909.

211 H. Yang, S. Gao, J. Lü, B. Xu, J. Lin and R. Cao, *Inorg. Chem.*, 2010, **49**, 736–744.

212 R. Brodbeck and D. Andrae, in *Wagner S., Steinmetz M., Bode A., Brehm M. (eds) High Performance Computing in Science and Engineering*, Springer, Berlin, Heidelberg, Garching/Munich, 2007.

213 M. Kozik, N. Casan-Pastor, C. F. Hammer and L. C. W. Baker, *J. Am. Chem. Soc.*, 1988, **110**, 7697–7701.

214 E. L. Bominaar, C. Achim, S. a. Borshch, J.-J. Girerd and E. Münck, *Inorg. Chem.*, 1997, **36**, 3689–3701.

215 I. K. Song, M. S. Kaba, K. Nomiya, R. G. Finke and M. a. Barteau, *J. Mol. Catal. A Chem.*, 2007, **262**, 216–226.

216 H. A. Levy, P. A. Agron and M. D. Danford, *J. Chem. Phys.*, 1959, **30**, 1486–1488.

217 M. H. V Huynh and T. J. Meyer, *Chem. Rev.*, 2007, **107**, 5004–5064.

218 S. Herrmann, J. T. Margraf, T. Clark and C. Streb, *Chem. Commun.*, 2015, **51**, 13702–13705.

219 L. E. VanGelder, A. M. Kosswattaarachchi, P. L. Forrestel, T. Cook and E. Matson, *Chem. Sci.*, 2018, **9**, 1692–1699.

220 I. K. Song and M. A. Barteau, *J. Mol. Catal. A Chem.*, 2004, **212**, 229–236.

221 C. Streb, in *Polyoxometalate-Based Assemblies and Functional Materials*, ed. Y.-F. Song, Springer, Oxford, 2017, pp. 31–47.

222 A. Selling, I. Andersson, L. Pettersson, C. M. Schramm, S. L. Downey and J. H. Grate, *Inorg. Chem.*, 1994, **33**, 3141–3150.

223 S. Himeno and M. Takamoto, *J. Electroanal. Chem.*, 2002, **528**, 170–174.

224 A. Jürgensen and J. B. Moffat, *Catal. Letters*, 1995, **34**, 237–244.

225 P. Souchay, *Ions minéraux condensés*, Masson et Cie, Paris, 1969.

226 D. L. Kepert and J. H. Kyle, *J. Chem. Soc. Dalt. Trans.*, 1978, 137–141.

227 M. Sadakane and E. Steckhan, *Chem. Rev.*, 1998, **98**, 219–238.

228 B. Keita and L. Nadjo, *J. Electroanal. Chem. Interfacial Electrochem.*, 1987, **227**, 77–98.

229 P. Gomez-Romero, *Solid State Ionics*, 1997, **101**, 243–248.

230 Z. Nagy, N. C. Hung and R. M. Yonco, *J. Electrochem. Soc.*, 1989, **136**, 895.

231 N. G. Hung and Z. Nagy, *J. Electrochem. Soc.*, 1987, **134**, 2215–2220.

232 F. H. Rhodes and C. B. Barbour, *Ind. Eng. Chem.*, 1923, **15**, 850–852.

233 V. F. Odyakov, E. G. Zhizhina and R. I. Maksimovskaya, *Appl. Catal. A Gen.*, 2008, **342**, 126–130.

234 V. F. Odyakov, E. G. Zhizhina, Y. A. Rodikova and L. L. Gogin, *Eur. J. Inorg. Chem.*, 2015, **2015**, 3618–3631.

235 X. Lu, W. D. Johnson and J. Hook, *Environ. Sci. Technol.*, 1998, **32**, 2257–2263.

236 K. Tanaka and R. Tamamushi, *Zeitschrift fur Naturforsch. - Sect. A J. Phys. Sci.*, 1991, **46**, 141–147.

237 E. Aleksandrova, R. Hiesgen, K. A. Friedrich and E. Roduner, *Phys. Chem. Chem. Phys.*, 2007, **9**, 2735–2743.

238 J. Chou, E. W. McFarland and H. Metiu, *J. Phys. Chem. B*, 2005, **109**, 3252–3256.

239 B. Rausch, M. D. Symes, G. Chisholm and L. Cronin, *Science (80-.).*, 2014, **345**, 1326–1330.

240 J. Noack, P. Fischer, P. Hussinger, N. Roznyatovskaya, M. Küttinger, D. Karabelli, M. Schäffer, J. Tübke and K. Pinkwart, *Redox-flow-Batterien für Netze mit fluktuierenden erneuerbaren Energiequellen*, Karlsruhe, 2016.

241 TU Braunschweig, http://www.pci.tu-bs.de/aggericke/PC2/Kap_0/Elektrolyte.htm, (accessed 4 December 2018).

242 Peter Paetzold, *Einführung in die Allgemeine Chemie*, SpringerVieweg+Teubner, Wiesbaden, 2nd edn., 2013.

243 J. Mähler and I. Persson, *Inorg. Chem.*, 2012, **51**, 425–438.

244 *U.S. Geological Survey, Metal Prices in the United States through 2010: U.S. Geological Survey Scientific Investigations Report 2012–5188, U.S. Geological Survey, 2013*, .

245 *Mineral Industry Surveys, Mineral Industry Surveys: Vanadium in September 2018, U.S. Geological Survey, 2018*, .

246 J. Friedl, M. V. Holland-Cunz, R. Fleck, B. Schricker, H. Wolfschmidt and U. Stimming, *Upscaling of an asymmetric Polyoxometalate Redox Flow Battery.* Submitted.

247 A. M. Pezeshki, R. L. Sacci, G. M. Veith, T. A. Zawodzinski and M. M. Menchd, *J. Electrochem. Soc.*, 2016, **163**, X13–X13.

248 M. Skyllas-Kazacos and F. Grossmith, *J. Electrochem. Soc.*, 1987, **134**, 2950–2953.

249 Allen J. Bard, György Inzelt, Fritz Scholz, *Electrochemical Dictionary*, Springer-Verlag, Berlin Heidelberg, 2nd edn., 2012.

250 John Emsley, Frank Hibbert, Hiizu Iwamura, Hans-Gert Korth, Jean-Michel Savéant, Reiner Sustmann, *Advances in Physical Organic Chemistry,* ed. D. Bethell, Academic Press Limited, London, 1990, Volume 26.

251 R. A. Marcus, Elektronentransferreacktionen in der Chemie -Theorie und Experiment (Nobel-Vortrag), *Angew. Chemie*, 1993, **8**, 1161-72.